universität wien

DISSERTATION / DOCTORAL THESIS

Titel der Dissertation / Title of the Doctoral Thesis

Applications of a Rigid Source of Entangled Photons

verfasst von / submitted by

Dipl.-Ing. Matthias Fink

angestrebter akademischer Grad / in partial fulfilment of the requirements for the degree of

Doktor der Naturwissenschaften (Dr. rer. nat.)

Wien, 2020 / Vienna 2020

Studienkennzahl lt. Studienblatt / degree programme code as it appears on the student record sheet:	A 796 605 411
Dissertationsgebiet lt. Studienblatt / field of study as it appears on the student record sheet:	Physik
Betreut von / Supervisor:	emer. o. Univ.-Prof. Dr. DDr. h. c. Anton Zeilinger

Abstract

Quantum key distribution has recently experienced an increase in public interest due to the first intercontinental exchange of quantum-encrypted messages. Many related disciplines are benefiting from this fascination as well as from the technological progress that accompanies such satellite experiments. Exemplary for this is the photon source presented here, which was developed with the high demands of satellite missions in mind. Using this new tool, we conducted three independent experiments.

In our first experiment we proved the stability of the source under severe stress in a centrifuge and a drop tower. This impressively demonstrated the technical maturity of quantum optics outside the laboratories and beyond trifilar air-suspended tables. Thus, for the first time, the opportunity arose to systematically test photonic quantum entanglement in accelerated reference frames.

In the second experiment we constructed a gyroscope based on two-photon interference. With this fiber optic sensor the absolute rotation with respect to inertial space was measured with a precision beyond the shot-noise limit.

In the last of the three experiments conducted we send the photon pairs generated by the source over a 1.2 km-long free-space link through turbulent air across Vienna. Using a receiver designed for this purpose, we investigated the visibility of second-order interference, which is a process of fundamental importance for the implementation of quantum repeaters in future networks.

Vorwort

Die Quantenkryptographie erfährt in jüngster Zeit einen Zuwachs an öffentlichem Interesse aufgrund des ersten interkontinentalen Austauschs von quantenverschlüsselten Nachrichten. Von dieser Faszination und dem technologischen Fortschritt, welchen derartige Satellitenexperimente mit sich bringen, profitieren viele angrenzende Fachgebiete. Beispielhaft dafür ist die hier vorgestellte Photonenquelle, die im Hinblick auf die hohen Anforderungen von Satellitenmissionen entwickelt wurde. Mit diesem Werkzeug in Händen führen wir drei voneinander unabhängige Experimente durch.

Zuerst stellen wir die Stabilität der Quelle unter enormer Belastung in einer Zentrifuge und einem Fallturm unter Beweis. Wir demonstrieren dabei eindrücklich, dass verschränkte Photonen auch abseits von luftgefederten Labortischen zum Einsatz gebracht werden können, und suchen systematisch nach Abweichungen von der Standardtheorie der Quantenmechanik in unterschiedlich stark beschleunigten Bezugssystemen.

Für ein zweites Experiment konstruieren wir ein auf Zwei-Photonen Interferenz basierendes Gyroskop, mit dem wir die Absolutrotation bezüglich des Inertialraumes mit einer Präzision vermessen, welche mit klassischem Licht mit vergleichbarer Intensität wegen des fundamentalen Schrotrauschens der einzelnen Photonen nicht erreicht werden kann.

Abschließend schicken wir die von der Quelle erzeugten Photonenpaare über eine Distanz von 1.2 km durch den städtischen Nachthimmel von Wien. Mit einem eigens dafür konstruierten Empfänger untersuchen wir die Sichtbarkeit von Interferenz zweiter Ordnung welche von fundamentaler Bedeutung für die technische Realisierung von Zweigstellen in zukünftigen Quantennetzwerken ist.

Contents

Abstract iii

Vorwort v

1 Introduction 1

2 Fundamentals 5

2.1 Qubits . . . 5
2.2 Mutually Unbiased Bases (MUB) . . . 6
2.3 Projection Operators . . . 6
2.4 Quantum Measurement . . . 9
2.5 Mixed States . . . 10
2.5.1 Entangled Photons . . . 13
2.6 EPR and Local Hidden Variables . . . 15
2.7 Verification of Entanglement . . . 18
2.8 Two-Photon Interference . . . 21
2.8.1 Hong-Ou-Mandel Interference . . . 21
2.8.2 NOON states . . . 23
2.8.3 Two-Photons Interference in Polarization Modes . . . 27

3 Detection and Data Analysis 29

3.1 Single-Photon Detectors . . . 29
3.2 Time Tagging . . . 30
3.3 Coincidences . . . 31
3.4 Accidental Coincidences . . . 32
3.5 Coincidence Search . . . 33
3.6 Mean Time Delay Tracking . . . 34

4 Entangled Photon Source 37

4.1 Spontaneous Parametric Down-Conversion . . . 37
4.1.1 Quasi-Phase-Matching . . . 38
4.1.2 Joint Spectral Amplitude . . . 39
4.1.3 Temporal Correlation . . . 41

4.2 Experimental Setup . . . 43
4.2.1 Pump Laser . . . 43
4.2.2 Crystal . . . 44
4.2.3 Fiber Coupling and Walk-off Compensation . . . 47
4.2.4 Alignment . . . 49
4.3 Performance . . . 50
4.3.1 Brightness and Heralding Efficiency . . . 50
4.3.2 Spectrum . . . 50
4.3.3 Two-Photon Interference . . . 51

5 Entanglement in Accelerated Reference Frames 55
5.1 Introduction . . . 55
5.2 Experimental Setup . . . 56
5.2.1 Generation of Polarization-Entangled Photons . . . 56
5.2.2 Verification of Entanglement . . . 57
5.3 Drop Tower . . . 60
5.4 Centrifuge . . . 62
5.5 Conclusion . . . 64

6 Entanglement-Enhanced Optical Gyroscope 67
6.1 Introduction . . . 67
6.2 Methods . . . 69
6.2.1 Sagnac Effect . . . 69
6.2.2 Experimental Setup . . . 70
6.2.3 Optical Setup . . . 71
6.3 Results . . . 74
6.4 Precision Beyond the Shot-Noise Limit . . . 77
6.4.1 Estimation Based on Fitting Parameters . . . 77
6.4.2 Estimation Based on Residuals . . . 78
6.5 Loss . . . 80
6.6 Conclusion . . . 84

7 Two-Photon Interference and Transmission in Presence of Atmospheric Turbulence 87
7.1 Introduction . . . 87
7.2 Methods . . . 88
7.2.1 Optical Setup . . . 88
7.2.2 Free-Space Link . . . 90
7.2.3 Count Rate Normalization . . . 92

7.2.4 Stochastic and Deterministic Loss 93
7.3 Results 94
7.3.1 Setup Performance 94
7.3.2 HOM Interference 96
7.4 Conclusion 97

8 Summary and Outlook **101**

Bibliography **104**

Appendices **115**

A HOM Interference Coincidence Count Rate **117**

B First Author Publications **123**

C List of Publications **137**

Acknowledgements **139**

1 Introduction

Entanglement, as predicted by quantum mechanics, refers to correlations between subsystems of a compound quantum state. This collective behavior of the entangled state is maintained even in situations where interaction or information exchange between the individual constituents can be excluded [1]. The question, therefore, arises as to how such correlations are sustained. This question is not answered by quantum mechanics, however, this phenomenon is described very precisely. Einstein, Podolsky, and Rosen therefore drew the conclusion that quantum mechanics is an incomplete description of reality [2]. Attempts to extend this scientific theory by hidden-variables [3] in order to explain this "spooky action at a distance" could be ruled out experimentally [4, 5, 6] using Bell-like inequalities [7]. From today's perspective, such states are called non-local, suggesting that they refuse to fit into our concepts of space and time. However, due to the quantum mechanical description of entangled systems, we are able to provide accurate predictions and use them in various applications.

In quantum cryptography, entangled photons come into use as they can be transmitted over long distances and possess properties such as polarization that are hardly influenced by the environment. Their correlations in polarization leads to identical measurement results in distant observers. This allows the generation of a symmetric digital key which can be used to encrypt secret messages [8]. Rather than relying on a messenger in the classical sense, this concept depends on a natural phenomenon described in quantum mechanics as the no-cloning theorem [9]. In times of global data exchange, this technology can be utilized to protect the right to privacy of communications as enshrined in the Universal Declaration of Human Rights*. For a future global quantum network, optical free-space links are a necessary ingredient in order to overcome large distances [11]. Approaching this ambitious goal, the first intercontinental quantum key distribution via a satellite link has recently been demonstrated [12], leading to an increased public interest in this topic.

However, quantum optical effects are not only used in space, but also underground. Quantum metrology uses non-classical states of light in optical sensors in order to im-

*Article 12 of The Universal Declaration of Human Rights [10]: *"No one shall be subjected to arbitrary interference with his privacy, family, home or correspondence, nor to attacks upon his honour and reputation. Everyone has the right to the protection of the law against such interference or attacks."*

prove their precision. In this way, an improvement of the resolution in the detection of gravitational waves could be achieved with LIGO using squeezed states of light [13]. Such effects can also be achieved with so-called NOON states [14]. The collective behavior of this state consisting of N photons causes all photons to be in one of two paths; it is uncertain in which path all photons are in [15]. Such path-entangled states are used in interferometric measurements and provide a signal that oscillates N times faster than the signal obtained from independent photons with respect to a relative phase between the paths [16]. This effect is called super-resolution and may lead to precision which beats the shot-noise limit (SNL). This is remarkable since this limit cannot be undercut by measurements with classical states of light whose signal is perturbed by the fundamental quantization noise of the individual photons.

Entanglement is a resource for emerging applications such as quantum metrology and quantum cryptography, which are just making a leap from the laboratory into practice. In these promising applications, entanglement at the push of a button is required without worrying about its formation or stability. Outside a laboratory environment, unfavorable conditions such as temperature fluctuations, vibrations, dust, or atmospheric turbulence prevail for precision experiments. For this reason, we developed a mobile plug-and-play testbed for quantum entanglement which is easy to use and can withstand adverse conditions. The result of our efforts is a crate containing a small quantum laboratory, including all necessary optical and electronic equipment. The two-photon state generated by the autarkic unit can be used with much versatility. This state can be described as a NOON state in polarization modes which shows super resolution in polarization measurements. By means of a polarizing beam splitter, this state can be converted into a path-entangled two-photon state and deployed in conventional interferometers. The random splitting at a beam splitter cube allows the generation of a polarization-entangled state in post-selection. Using this tool, we conducted three independent experiments.

1) Entanglement in Accelerated Reference Frames

The stable performance of our mobile quantum laboratory will be verified under severe stress in a drop tower and a centrifuge experiment, experiencing uniform acceleration ranging from 0.03 g to up to 30 g. During these experiments we generate polarization-entangled photons, whose entanglement is verified within the autarkic crate. This is the first systematic test of a non-local state in accelerated reference frames to demonstrate the extent to which such a gray area of theory between quantum mechanics and relativity can be accessed with state-of-the-art quantum optics hardware.

2) Entanglement Enhanced Optical Gyroscope

A fiber optic gyroscope measures the absolute rotation with respect to inertial space by utilizing the Sagnac effect. By integrating a fiber-coil-based Sagnac interferometer, our crate is turned into a device which can be operated with NOON states. The super-resolution provided by such two-photon state enables us to achieve sub-SNL precision in measuring absolute rotation. Subsequently, we will discuss the impact of photonic loss within the fiber and prerequisites for possible applications.

3) Two-Photon Interference and Transmission despite Atmospheric Turbulence

A facility suitable for optical free-space connections in urban areas was established. The receiver module will be used to impose a polarization-dependent time delay on the received photons. This facility can be utilized for the verification of polarization- and hyper-entangled photons after transmission through turbulent air across Vienna [17]. With the photon pairs generated by the source of the crate and sent via a 1.2 km-long free-space link, we will examine the second-order interference visibility of the collinear transmitted photons. Such two-photon interference is a process of fundamental importance for quantum repeaters dealing with photons protected by the no-cloning theorem. This experiment represents a vital next step toward approaching the implementation of such nodes in future quantum networks.

2 Fundamentals

The experiments in the following chapters are based on the phenomenon of quantum entanglement. This chapter provides a brief introduction to this topic to better understand the potential for technical applications of these intriguing quantum states. A more detailed introduction can be found in the book "*Entangled Systems*" by Jürgen Audretsch [18].

Using the simplest two-level quantum system, the qubit, we will discuss quantum mechanical notions such as pure and mixed states as well as quantum measurements. Next, we illustrate the experimental test of non-locality by means of the Einstein, Podolsky, and Rosen paradox and Bell's inequality. Following "*Relations between Entanglement Witnesses and Bell Inequalities*" by Hyllus *et al.* [19], we then show that the entanglement of the photon state used in the later experiments can be verified by just two measurement settings. In the last section of the chapter, two-photon interference, which is of fundamental importance for many applications in quantum optics, will be introduced briefly.

2.1 Qubits

The state of a quantum system is represented by a vector of dimension $\mathcal{D}$, residing in a complex vector space called Hilbert space $\mathcal{H}^{\mathcal{D}}$. A prototypical example of a two-dimensional Hilbert space is formed by polarization vectors $|p\rangle \in \mathcal{H}^2$

$$|p\rangle = \begin{pmatrix} a \\ b \end{pmatrix} = (\overline{a}, \overline{b})^\dagger = \langle p|^\dagger \qquad\qquad a, b \in \mathbb{C} \tag{2.1}$$

with a scalar product

$$\langle p|p\rangle = (\overline{a}, \overline{b}) \begin{pmatrix} a \\ b \end{pmatrix} = (\overline{a}a + \overline{b}b). \tag{2.2}$$

The vectors

$$|\mathrm{H}\rangle = \begin{pmatrix} 1 \\ 0 \end{pmatrix} \qquad \text{and} \qquad |\mathrm{V}\rangle = \begin{pmatrix} 0 \\ 1 \end{pmatrix} \tag{2.3}$$

denote horizontal and vertical polarization and form a basis in $\mathcal{H}^2$. Any polarization state $|p\rangle$ can be written as a linear superposition of the basis vectors

$$|p\rangle = a\,|\mathrm{H}\rangle + b\,|\mathrm{V}\rangle \tag{2.4}$$

with the norm $\||p\rangle\| = \sqrt{\langle p|p\rangle} = \sqrt{|a|^2 + |b|^2} = 1$ and $a, b \in \mathbb{C}$. Such two-dimensional quantum states are referred to as qubits, which can be seen by assigning $|\mathsf{O}\rangle \equiv |\mathrm{H}\rangle$ and $|\mathsf{I}\rangle \equiv |\mathrm{V}\rangle$ to the basis vectors. In the case of $a = 1$ ($a = 0$), such a qubit $|Q_{bit}\rangle = a\,|\mathsf{O}\rangle + b\,|\mathsf{I}\rangle$ carries the classical information 0 (1), respectively. The advantageous difference to a classical bit is the ability of the qubit to be in a linear superposition of $|\mathsf{O}\rangle$ and $|\mathsf{I}\rangle$.

2.2 Mutually Unbiased Bases (MUB)

Besides $|\mathrm{H}\rangle$ and $|\mathrm{V}\rangle$, there are two other common sets of basis vectors, the diagonal and anti-diagonal polarization

$$|\mathrm{D}\rangle = \frac{1}{\sqrt{2}}(|\mathrm{H}\rangle + |\mathrm{V}\rangle) \qquad \text{and} \qquad |\mathrm{A}\rangle = \frac{1}{\sqrt{2}}(|\mathrm{H}\rangle - |\mathrm{V}\rangle) \tag{2.5}$$

and the right-hand and left-hand circular polarization

$$|\mathrm{R}\rangle = \frac{1}{\sqrt{2}}(|\mathrm{H}\rangle - \mathbb{i}\,|\mathrm{V}\rangle) \qquad \text{and} \qquad |\mathrm{L}\rangle = \frac{1}{\sqrt{2}}(|\mathrm{H}\rangle + \mathbb{i}\,|\mathrm{V}\rangle). \tag{2.6}$$

Each of the states $\{|\mathrm{H}\rangle, |\mathrm{V}\rangle\}$, $\{|\mathrm{D}\rangle, |\mathrm{A}\rangle\}$, and $\{|\mathrm{R}\rangle, |\mathrm{L}\rangle\}$ can be projected onto a state of another set with a probability of 1/2. Such sets of basis vectors are called mutually unbiased. In a Hilbert space of dimension $\mathcal{D} = 2$, a maximum number of three mutually unbiased bases can be found [20, 21]. Such MUBs are of fundamental importance in quantum cryptography. A qubit can be coded in any of these vector sets. If a qubit is prepared in the DA basis in the state $|\mathsf{I}\rangle_{\mathrm{DA}} \equiv |\mathrm{A}\rangle$, this information can only be extracted by a measurement in the corresponding basis. A measurement in the HV basis yields a random result of $|\mathsf{O}\rangle_{\mathrm{HV}} \equiv |\mathrm{H}\rangle$ or $|\mathsf{I}\rangle_{\mathrm{HV}} \equiv |\mathrm{V}\rangle$ with a probability of 1/2 each.

2.3 Projection Operators

The most fundamental measurements in quantum mechanics are projective measurements. Such projections onto normalized states (e.g.: $|b\rangle$) are described by projection operators

$$\widehat{\Pi} = |b\rangle\langle b| = \begin{pmatrix} b^1 \\ b^2 \\ \vdots \\ b^{\mathcal{D}} \end{pmatrix} \left(\overline{b^1}, \overline{b^2}, \cdots, b^{\mathcal{D}}\right) = \begin{bmatrix} b^1\overline{b^1} & b^1\overline{b^2} & \cdots & b^1\overline{b^{\mathcal{D}}} \\ b^2\overline{b^1} & b^2\overline{b^2} & \cdots & b^2\overline{b^{\mathcal{D}}} \\ \vdots & \vdots & \ddots & \vdots \\ b^{\mathcal{D}}\overline{b^1} & b^{\mathcal{D}}\overline{b^2} & \cdots & b^{\mathcal{D}}\overline{b^{\mathcal{D}}} \end{bmatrix}, \tag{2.7}$$

with the eigenvector $|b\rangle$ associated with the eigenvalue 1 and a set of linearly independent eigenvectors $\{|b^{\perp}\rangle\}$ associated with the eigenvalue 0. The probability to detect system $|q\rangle$ in state $|b\rangle$ can be calculated via $\langle q|\,\widehat{\Pi}\,|q\rangle$. After projection, the system is described by the eigenvector of the operator $|b\rangle$. Any further projection ($\widehat{\Pi}^2 = \widehat{\Pi}^n = \widehat{\Pi}$) of the state results in $|b\rangle$ with unit probability.

A projection of polarization states can be achieved by means of a polarizer. If the transmission axis of such a polarizer is oriented horizontally, the corresponding projection operator is represented by $\widehat{\Pi}_{\mathrm{H}} = |\mathrm{H}\rangle\langle\mathrm{H}|$. Thus, the probability of measuring $|p\rangle$ (see Equation 2.4) in mode $|\mathrm{H}\rangle$ is $\langle p|\,\widehat{\Pi}_{\mathrm{H}}\,|p\rangle = \langle p|\,|\mathrm{H}\rangle\langle\mathrm{H}|\,|p\rangle = \overline{a}a = |a|^2$.

In a two-dimensional Hilbert space, a projection onto any normalized state $|p\rangle$ corresponds to a (complex) Hermitian 2×2 matrix $\widehat{\Pi} = \widehat{\Pi}^{\dagger}$ with

$$\mathrm{Tr}\left(\widehat{\Pi}\right) = \mathrm{Tr}\left(|p\rangle\langle p|\right) = \langle\mathrm{H}|\,|p\rangle\langle p|\,|\mathrm{H}\rangle + \langle\mathrm{V}|\,|p\rangle\langle p|\,|\mathrm{V}\rangle = \overline{a}a + \overline{b}b = 1. \tag{2.8}$$

The trace is invariant with respect to a change of basis. Such operators may be expressed in terms of the Pauli matrices $\widehat{\sigma}_i$, which together with the unit matrix $\widehat{\sigma}_0$ form a basis of the four-dimensional real vector space of all complex Hermitian 2×2 matrices.

$$\widehat{\sigma}_0 = \begin{bmatrix} 1 & 0 \\ 0 & 1 \end{bmatrix} \quad \widehat{\sigma}_1 = \begin{bmatrix} 0 & 1 \\ 1 & 0 \end{bmatrix} \quad \widehat{\sigma}_2 = \begin{bmatrix} 0 & -\mathbb{i} \\ \mathbb{i} & 0 \end{bmatrix} \quad \widehat{\sigma}_3 = \begin{bmatrix} 1 & 0 \\ 0 & -1 \end{bmatrix} \tag{2.9}$$

These fundamental Pauli operators have properties relevant for further calculation:

$$\mathrm{Tr}\left(\widehat{\sigma}_0\right) = 2 \tag{2.10}$$

$$\mathrm{Tr}\left(\widehat{\sigma}_i\right) = 0 \tag{2.11}$$

$$\widehat{\sigma}_{\mu}^2 = \widehat{\sigma}_0 \tag{2.12}$$

$$\widehat{\sigma}_i\widehat{\sigma}_j = \delta_{ij}\widehat{\sigma}_0 + \mathbb{i}\epsilon_{ijk}\,\sigma_k \tag{2.13}$$

$$[\widehat{\sigma}_i, \widehat{\sigma}_j] = \widehat{\sigma}_i\widehat{\sigma}_j - \widehat{\sigma}_j\widehat{\sigma}_i = 2\mathbb{i}\epsilon_{ijk}\widehat{\sigma}_k, \tag{2.14}$$

with Latin indices $\in [1, 2, 3]$, Greek indices $\in [0, 1, 2, 3]$, and the Levi-Civita sym-

bol* denoted by ϵ_{ijk}. With the Pauli representation each projection operator can be expressed in terms of the vector components n_i on the Poincaré sphere (see Figure 2.2)

$$\widehat{\Pi} = \frac{1}{2}\sum_{\mu=0}^{3} n_\mu \widehat{\sigma}_\mu = \frac{n_0}{2}\widehat{\sigma}_0 + \sum_{i=1}^{3}\frac{n_i}{2}\widehat{\sigma}_i \tag{2.15}$$

Since the trace of a projection operator (Equation 2.8) equals one

$$\mathrm{Tr}\left(\widehat{\Pi}\right) = \frac{n_0}{2}\mathrm{Tr}\left(\widehat{\sigma}_0\right) + \sum_{i=0}^{3}\frac{n_i}{2}\mathrm{Tr}\left(\widehat{\sigma}_i\right) = \frac{n_0}{2}\mathrm{Tr}\left(\widehat{\sigma}_0\right) = n_0 = 1, \tag{2.16}$$

Equation 2.15 reduces to

$$\widehat{\Pi} = \frac{1}{2}\left(\widehat{\sigma}_0 + n_i\widehat{\sigma}_i\right), \tag{2.17}$$

where we have used the Einstein notation of summation over identical indices. Two projectors $\widehat{\Pi}_l = |b_l\rangle\langle b_l|$ and $\widehat{\Pi}_k = |b_k\rangle\langle b_k|$ are orthogonal to each other with respect to the trace product of matrices $\mathrm{Tr}\left(\widehat{\Pi}_l\widehat{\Pi}_k\right) = \delta_{l,k}$ iff $\langle b_l|b_k\rangle = \delta_{l,k}$. From the orthogonality of tow projectors

$$\begin{aligned}
\mathrm{Tr}\left(\widehat{\Pi}_l\,\widehat{\Pi}_k\right) &= \frac{1}{4}\mathrm{Tr}\left(\left(\widehat{\sigma}_0 + n_i\widehat{\sigma}_i\right)\,\left(\widehat{\sigma}_0 + m_j\widehat{\sigma}_j\right)\right)\\
&= \frac{1}{4}\mathrm{Tr}\left(\left(\widehat{\sigma}_0 + m_j\widehat{\sigma}_j + n_i\widehat{\sigma}_i + n_i m_j\widehat{\sigma}_i\widehat{\sigma}_j\right)\right)\\
&= \frac{1}{4}\left(2 + 0 + 0 + 2n_i m_j\delta_{i,j}\right)\\
&= \frac{1}{2}\left(1 + n_i m_i\right)\\
&= \frac{1}{2}\left(1 + \vec{n}.\vec{m}\right)
\end{aligned} \tag{2.18}$$

it follows that the vectors $\vec{n}.\vec{m} = -1$ are antiparallel and normalized $\|\vec{n}\|^2 = \|\vec{m}\|^2 = 1$. Table 2.1 shows projectors corresponding to common basis vectors and their decomposition into Pauli matrices.

Using the Pauli representation, it can easily be proven that projections on basis vectors of different sets do not commute:

*$\epsilon_{ijk} = \begin{cases} +1 & \text{if } (i,j,k) \text{ is an even permutation of (1,2,3)} \\ -1 & \text{if } (i,j,k) \text{ is an odd permutation of (1,2,3)} \\ 0 & \text{else} \end{cases}$

Projector	Bracket	Matrix	Pauli Decomposition	$\vec{n} = (n_1, n_2, n_3)$
$\widehat{\Pi}_{\mathrm{H}}$	$\lvert\mathrm{H}\rangle\langle\mathrm{H}\rvert$	$\begin{bmatrix} 1 & 0 \\ 0 & 0 \end{bmatrix}$	$\frac{1}{2}(\widehat{\sigma}_0 + \widehat{\sigma}_3)$	$(0, 0, 1)$
$\widehat{\Pi}_{\mathrm{V}}$	$\lvert\mathrm{V}\rangle\langle\mathrm{V}\rvert$	$\begin{bmatrix} 0 & 0 \\ 0 & 1 \end{bmatrix}$	$\frac{1}{2}(\widehat{\sigma}_0 - \widehat{\sigma}_3)$	$(0, 0, -1)$
$\widehat{\Pi}_{\mathrm{D}}$	$\lvert\mathrm{D}\rangle\langle\mathrm{D}\rvert$	$\frac{1}{2}\begin{bmatrix} 1 & 1 \\ 1 & 1 \end{bmatrix}$	$\frac{1}{2}(\widehat{\sigma}_0 + \widehat{\sigma}_1)$	$(1, 0, 0)$
$\widehat{\Pi}_{\mathrm{A}}$	$\lvert\mathrm{A}\rangle\langle\mathrm{A}\rvert$	$\frac{1}{2}\begin{bmatrix} 1 & -1 \\ -1 & 1 \end{bmatrix}$	$\frac{1}{2}(\widehat{\sigma}_0 - \widehat{\sigma}_1)$	$(-1, 0, 0)$
$\widehat{\Pi}_{\mathrm{R}}$	$\lvert\mathrm{R}\rangle\langle\mathrm{R}\rvert$	$\frac{1}{2}\begin{bmatrix} 1 & -\mathbb{i} \\ \mathbb{i} & 1 \end{bmatrix}$	$\frac{1}{2}(\widehat{\sigma}_0 + \widehat{\sigma}_2)$	$(0, 1, 0)$
$\widehat{\Pi}_{\mathrm{L}}$	$\lvert\mathrm{L}\rangle\langle\mathrm{L}\rvert$	$\frac{1}{2}\begin{bmatrix} 1 & \mathbb{i} \\ -\mathbb{i} & 1 \end{bmatrix}$	$\frac{1}{2}(\widehat{\sigma}_0 - \widehat{\sigma}_2)$	$(0, -1, 0)$

Table 2.1 Projectors onto common basis vectors and their decomposition into Pauli matrices.

$$
\begin{aligned}
\left[(\widehat{\sigma}_0 + \widehat{\sigma}_i), (\widehat{\sigma}_0 \pm \widehat{\sigma}_j)\right] &= \widehat{\sigma}_0 \pm \widehat{\sigma}_j + \widehat{\sigma}_i \pm \widehat{\sigma}_i\widehat{\sigma}_j - \widehat{\sigma}_0 - \widehat{\sigma}_i \mp \widehat{\sigma}_j \mp \widehat{\sigma}_j\widehat{\sigma}_i && (2.19)\\
&= \pm[\widehat{\sigma}_i\widehat{\sigma}_j] && (2.20)\\
&= \pm 2\mathbb{i}\epsilon_{ijk}\widehat{\sigma}_k && (2.21)\\
&\neq 0 \quad \forall i \neq j. && (2.22)
\end{aligned}
$$

Due to Heisenberg's uncertainty principle, any pair of observables represented by non-commuting operators cannot be measured simultaneously with high accuracy. In other words, an observer chooses one measurement basis and gains knowledge of the result. At the same time, however, he completely loses the possibility of knowing the result of a complementary measurement.

2.4 Quantum Measurement

As mentioned above, the projector $|b\rangle\langle b|$ has two eigenvalues $\lambda = \{0, 1\}$ which are associated with the measurement results

- $\lambda = 1 \iff$ "System is in state $|b\rangle$".
- $\lambda = 0 \iff$ "System is not in state $|b\rangle$"

In general, measurements in quantum mechanics are represented by Hermitian operators called observables $\widehat{O} = \widehat{O}^{\dagger}$. These operators associate a state with a number that is the expectation value of a repeated measurement $\langle p| \widehat{O} |p\rangle \in \mathbb{R}$. Such observables can be decomposed into orthogonal projection operators

$$\widehat{O} = \sum_{i=1}^{\mathcal{D}} b_i |b_i\rangle\langle b_i| = \sum_{i=1}^{\mathcal{D}} b_i \widehat{\Pi}_i \tag{2.23}$$

with eigenvectors $|b_i\rangle$ and real eigenvalues $b_i \in \mathbb{R}$. The set $\{|b_i\rangle\}$ with $i \in [1, ..., \mathcal{D}]$ is an orthonormal basis of $\mathcal{H}^{\mathcal{D}}$.

A measurement with a polarizing beam splitter (PBS) can thus be described by the observable $\widehat{O}_{\mathrm{HV}} = |\mathrm{H}\rangle\langle\mathrm{H}| - |\mathrm{V}\rangle\langle\mathrm{V}|$, where we assign the results +1 and -1 to horizontally and vertically polarized photons, respectively. Decomposing the projectors into Pauli matrices results in $\widehat{O}_{\mathrm{HV}} = \widehat{\Pi}_{\mathrm{H}} - \widehat{\Pi}_{\mathrm{V}} = \frac{1}{2}(\widehat{\sigma}_0 + \widehat{\sigma}_3 - \widehat{\sigma}_0 + \widehat{\sigma}_3) = \widehat{\sigma}_3$. A generalized polarization measurement is obtained by manipulating the polarization in front of the PBS, for example, by half-wave plates or quarter-wave plates. The associated operator reads as follows

$$\widehat{O}_{\vec{n}} = \widehat{\Pi} - \widehat{\Pi}^{\perp} = \frac{1}{2}(\widehat{\sigma}_0 + n_i\widehat{\sigma}_i - \widehat{\sigma}_0 + n_j\widehat{\sigma}_j) = n_j\widehat{\sigma}_j \tag{2.24}$$

where $\vec{n}$ describes the measurement setting.

2.5 Mixed States

With state vectors, any coherent superposition of states can be represented; such states are called pure states. In contrast, there are states that are not pure, known as mixed states. The constituents of such incoherent state mixture have an undefined phase relation, which is a condition that cannot be specified by a state vector (of the same dimension). Averaging over such an undefined phase causes decoherence known as the loss of interference visibility. Such a circumstance can be captured by describing the state in dependence of an unknown property, which is averaged during the measuring process.

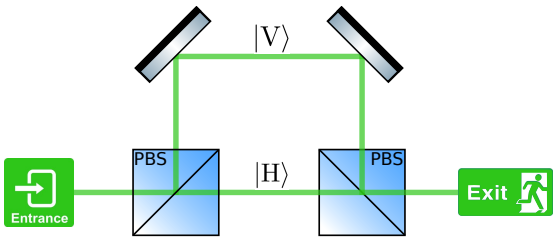


Figure 2.1 Unbalanced Mach–Zehnder interferometer with polarizing beam splitter cubes (PBS).

To illustrate this, imagine a diagonally polarized photon $|\mathrm{D}\rangle = \frac{1}{\sqrt{2}}(|\mathrm{H}\rangle + |\mathrm{V}\rangle)$ passing through an interferometer (see Figure 2.1). The photon is either transmitted or reflected by the first polarizing beam splitter cube (PBS). Consequently, we find the photon with a probability of 1/2 horizontally polarized in the lower path. It is just as likely that the photon is in the upper path and vertically polarized. A potentially H-polarized photon is transmitted by the second beam splitter, while a V-polarized photon would be reflected somewhat later due to the path-length difference. One way or another, at the end the photon is certainly in the "Exit" path but the polarization state of the photon depends on the path-length difference of the interferometer:

- If the path-length difference is zero, the coherent superposition of the two modes leads to $\frac{1}{\sqrt{2}}(|\mathrm{H}\rangle + |\mathrm{V}\rangle) = |\mathrm{D}\rangle$.
- If the path-length difference is greater than the coherence length of the photon, the photon is either in state $|\mathrm{H}\rangle$ or $|\mathrm{V}\rangle$ with a probability of 1/2 each.

In a Hilbert space extended by the temporal information early $|\mathrm{e}\rangle$ and late $|\mathrm{l}\rangle$, the state of the second case could also be written as $\frac{1}{\sqrt{2}}(|\mathrm{H}\rangle \otimes |\mathrm{e}\rangle + |\mathrm{V}\rangle \otimes |\mathrm{l}\rangle)$ [22]. Note that such a distinction is impossible if the temporal information of the photon in the entrance is unknown. A polarization measurement discarding the timing reveals an average over all possible arrival times. In the first of the two cases there is only one possible arrival time for which polarization D is obtained. In the second case we find a mixed state which cannot be denoted by a polarization state vector alone. Describing such a state by its response to projections

$$\widehat{\rho}_{\mathrm{HV}}^{\mathrm{mixed}} = \frac{1}{2}\left(|\mathrm{H}\rangle\langle\mathrm{H}| + |\mathrm{V}\rangle\langle\mathrm{V}|\right). \tag{2.25}$$

leads to a notation of the mixed state that is independent of the additional property, which can thus be of arbitrary nature. However, this notation, called the density matrix, uniquely defines the state of polarization. Pure states can also be specified by means of density matrices

$$\widehat{\rho}_{\mathrm{D}}^{\mathrm{pure}} = |\mathrm{D}\rangle\langle\mathrm{D}| = \frac{1}{2}\left(|\mathrm{H}\rangle\langle\mathrm{H}| + |\mathrm{H}\rangle\langle\mathrm{V}| + |\mathrm{V}\rangle\langle\mathrm{H}| + |\mathrm{V}\rangle\langle\mathrm{V}|\right). \tag{2.26}$$

In general, any $\widehat{\rho}$ can be decomposed into orthogonal projectors

$$\widehat{\rho} = \sum_{i=1}^{\mathcal{D}} P_i \, |b_i\rangle\langle b_i| = \sum_{i=1}^{\mathcal{D}} P_i, \widehat{\Pi}_i \tag{2.27}$$

where P_i are the projection probabilities which add up to one. From $\sum_i P_i = 1$ it follows that for every valid state (mixed or pure) the trace of the density matrix

must be one $\mathrm{Tr}\,(\widehat{\rho}) = 1$. In a two-dimensional Hilbert space, density matrices can be decomposed into Pauli matrices (the reasoning is the same as for projectors)

$$\widehat{\rho} = \frac{1}{2}\left(\widehat{\sigma}_0 + s_i\widehat{\sigma}_i\right). \tag{2.28}$$

This means that all states can be uniquely characterized by s_i, where $\vec{s} = (s_1, s_2, s_3)$ is known as the Stokes vector. Table 2.2 shows the most common polarizations and their representation as a state vector, density matrix, and Stokes vector.

State Vector	$\widehat{\rho}$	(s_1, s_2, s_3)
$\|\mathrm{H}\rangle$	$\|\mathrm{H}\rangle\langle\mathrm{H}\|$	(0,0,1)
$\|\mathrm{V}\rangle$	$\|\mathrm{V}\rangle\langle\mathrm{V}\|$	(0,0,-1)
$\|\mathrm{D}\rangle$	$\frac{1}{2}\left(\|\mathrm{H}\rangle\langle\mathrm{H}\| + \|\mathrm{H}\rangle\langle\mathrm{V}\| + \|\mathrm{V}\rangle\langle\mathrm{H}\| + \|\mathrm{V}\rangle\langle\mathrm{V}\|\right)$	(1,0,0)
$\|\mathrm{A}\rangle$	$\frac{1}{2}\left(\|\mathrm{H}\rangle\langle\mathrm{H}\| - \|\mathrm{H}\rangle\langle\mathrm{V}\| - \|\mathrm{V}\rangle\langle\mathrm{H}\| + \|\mathrm{V}\rangle\langle\mathrm{V}\|\right)$	(-1,0,0)
$\|\mathrm{R}\rangle$	$\frac{1}{2}\left(\|\mathrm{H}\rangle\langle\mathrm{H}\| - \mathbb{i}\,\|\mathrm{H}\rangle\langle\mathrm{V}\| + \mathbb{i}\,\|\mathrm{V}\rangle\langle\mathrm{H}\| + \|\mathrm{V}\rangle\langle\mathrm{V}\|\right)$	(0,1,0)
$\|\mathrm{L}\rangle$	$\frac{1}{2}\left(\|\mathrm{H}\rangle\langle\mathrm{H}\| + \mathbb{i}\,\|\mathrm{H}\rangle\langle\mathrm{V}\| - \mathbb{i}\,\|\mathrm{V}\rangle\langle\mathrm{H}\| + \|\mathrm{V}\rangle\langle\mathrm{V}\|\right)$	(0,-1,0)

Table 2.2 Common polarizations and their representation as a state vector, density matrix $\widehat{\rho}$, and Stokes vector $\vec{s} = (s_1, s_2, s_3)$

The expectation value of an observable can be calculated via $\mathrm{Tr}\left(\widehat{\rho}\,\widehat{O}\right)$. The projection $\widehat{\Pi}$ of a state defined by $\vec{s}$ yields a probability of

$$\begin{aligned}
\mathrm{Tr}\left(\widehat{\rho}\,\widehat{\Pi}\right) &= \frac{1}{4}\mathrm{Tr}\left(\left(\widehat{\sigma}_0 + s_i\widehat{\sigma}_i\right)\,\left(\widehat{\sigma}_0 + n_j\widehat{\sigma}_j\right)\right) \\
&= \frac{1}{4}\mathrm{Tr}\left(\widehat{\sigma}_0 + n_j\widehat{\sigma}_j + n_i\widehat{\sigma}_i + s_i n_j\widehat{\sigma}_i\widehat{\sigma}_j\right) \\
&= \frac{1}{4}\left(2 + 0 + 0 + s_i n_j 2\delta_{i,j}\right) \\
&= \frac{1}{2}\left(1 + s_i n_i\right).
\end{aligned} \tag{2.29}$$

The states from the interferometer example $\widehat{\rho}_{\mathrm{D}}^{\mathrm{pure}} = 1/2(\widehat{\sigma}_0 + \widehat{\sigma}_1)$ and $\widehat{\rho}_{\mathrm{HV}}^{\mathrm{mixed}} = \widehat{\sigma}_0$ are represented by the Stokes vectors $\vec{s}_{\mathrm{D}}^{\,\mathrm{p}} = (1, 0, 0)$ and $\vec{s}_{\mathrm{HV}}^{\,\mathrm{m}} = (0, 0, 0)$, and a projective measurement in path "Exit" of the interferometer result in

$$\mathrm{Tr}\left(\widehat{\rho}_{\mathrm{D}}^{\mathrm{pure}}\,\widehat{\Pi}\right) = \frac{1}{2}\left(1 + \vec{s}_{\mathrm{D}}^{\,\mathrm{p}}\vec{n}\right) = n_1 \tag{2.30}$$

$$\mathrm{Tr}\left(\widehat{\rho}_{\mathrm{HV}}^{\mathrm{mixed}}\,\widehat{\Pi}\right) = \frac{1}{2}\left(1 + \vec{s}_{\mathrm{HV}}^{\,\mathrm{m}}\vec{n}\right) = \frac{1}{2}. \tag{2.31}$$

The mixed state can be projected onto any pure state with a probability of 1/2. Such states are called maximally mixed. For $\widehat{\rho}_{\mathrm{D}}^{\mathrm{pure}} = |D\rangle\langle D|$ we find a unity projection

probability for the projector $\widehat{\Pi}_{\mathrm{D}} = |\mathrm{D}\rangle\langle\mathrm{D}|$ which corresponds to the vector $\vec{n} = (1, 0, 0)$. Of course, any other pure state can be projected onto itself with a probability of one. This insight can be used to classify pure states

$$\mathrm{Tr}\left(\widehat{\rho}^2\right) = \frac{1}{2}\left(1 + \|\vec{s}\|^2\right) \quad \begin{cases} = 1 & \text{pure state} \\ < 1 & \text{mixed state,} \end{cases} \tag{2.32}$$

where $\mathrm{Tr}\left(\widehat{\rho}^2\right)$ is called the purity of the state $\widehat{\rho}$. The set of Stokes vectors with a unit length represent the surface of a sphere known as the Poincaré sphere (see Figure 2.2). All vectors with $\|\vec{s}\|^2 < 1$ correspond to mixed states.

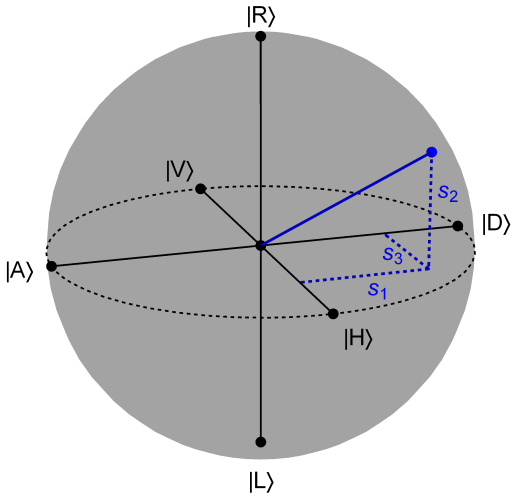


Figure 2.2 Poincaré sphere: Polarization state depicted as a Stokes vector on the Poincaré sphere.

2.5.1 Entangled Photons

Two quantum states $|\phi\rangle^A \in \mathcal{H}_A$ and $|\psi\rangle^B \in \mathcal{H}_{\mathrm{B}}$ can be considered as a composite quantum system, which is described by the product states $|\phi\rangle^{AB}_{\mathrm{sep}} = |\phi\rangle^A \otimes |\psi\rangle^B \in \mathcal{H}$ of the product space $\mathcal{H} = \mathcal{H}_A \otimes \mathcal{H}_{\mathrm{B}}$ [†]. Any state $|\phi\rangle^{AB}_{\mathrm{sep}} \in \mathcal{H}_A \otimes \mathcal{H}_{\mathrm{B}}$ that can be written as a direct tensor product of two state vectors is called product or separable state. However, the product space also includes non-separable states like

$$|\phi\rangle^{AB}_{\mathrm{ent}} = \frac{1}{\sqrt{2}}\left(|\phi\rangle^A \otimes |\psi\rangle^B + |\psi\rangle^A \otimes |\phi\rangle^B\right), \tag{2.33}$$

where the state of one photon depends on the state of the partner photon. Any state vector $|\phi\rangle^{AB} \in \mathcal{H}_A \otimes \mathcal{H}_{\mathrm{B}}$ that cannot be written as a direct product of two state vectors is said to be non-separable or entangled.

[†]with $\mathcal{D} = \mathcal{D}_{\mathrm{A}} \times \mathcal{D}_{\mathrm{B}}$ for finite-dimensional subspaces

In the following, we will largely refrain from explicitly writing the tensor product and denote such states using $|\phi\rangle^A \otimes |\psi\rangle^B = |\phi\rangle^A |\psi\rangle^B$. A basis in the product space of polarization states ($\mathcal{D} = 2 \times 2 = 4$) is formed by the set $\{|\Phi^+\rangle, |\Phi^-\rangle, |\Psi^+\rangle, |\Psi^-\rangle\}$ with

$$\left|\Phi^{\pm}\right\rangle = \frac{1}{\sqrt{2}}\left(|\mathrm{H}\rangle^A |\mathrm{H}\rangle^B \pm |\mathrm{V}\rangle^A |\mathrm{V}\rangle^B\right) \tag{2.34}$$

$$\left|\Psi^{\pm}\right\rangle = \frac{1}{\sqrt{2}}\left(|\mathrm{H}\rangle^A |\mathrm{V}\rangle^B \pm |\mathrm{V}\rangle^A |\mathrm{H}\rangle^B\right). \tag{2.35}$$

These four states are called Bell states, and each of them is maximally entangled. The corresponding density matrices are

$$\widehat{\rho}_{\Phi^{\pm}} = \left|\Phi^{\pm}\right\rangle\!\left\langle\Phi^{\pm}\right| = \frac{1}{4}\left(\widehat{\sigma}_0^{\mathrm{A}}\widehat{\sigma}_0^{\mathrm{B}} \pm \widehat{\sigma}_1^{\mathrm{A}}\widehat{\sigma}_1^{\mathrm{B}} \mp \widehat{\sigma}_2^{\mathrm{A}}\widehat{\sigma}_2^{\mathrm{B}} + \widehat{\sigma}_3^{\mathrm{A}}\widehat{\sigma}_3^{\mathrm{B}}\right) \tag{2.36}$$

$$\widehat{\rho}_{\Psi^{\pm}} = \left|\Psi^{\pm}\right\rangle\!\left\langle\Psi^{\pm}\right| = \frac{1}{4}\left(\widehat{\sigma}_0^{\mathrm{A}}\widehat{\sigma}_0^{\mathrm{B}} \pm \widehat{\sigma}_1^{\mathrm{A}}\widehat{\sigma}_1^{\mathrm{B}} \pm \widehat{\sigma}_2^{\mathrm{A}}\widehat{\sigma}_2^{\mathrm{B}} - \widehat{\sigma}_3^{\mathrm{A}}\widehat{\sigma}_3^{\mathrm{B}}\right), \tag{2.37}$$

where we have omitted the tensor product between the Pauli matrices $\widehat{\sigma}_\mu^{\mathrm{A}}$ and $\widehat{\sigma}_\nu^{\mathrm{B}}$ which act in subspace $\mathcal{H}_A$ and $\mathcal{H}_B$, respectively. Such entangled states have properties which are well defined for the composite system. Such properties, however, cannot be revealed by an observer of a single subsystem. For example, the composite polarization of $|\Psi^-\rangle$ is a pure state which is anti-correlated in all MUBs. Nevertheless, the polarization of the individual subsystems is described by a mixed state. To see this, we consider a projective measurement of the photon in subspace A. Such local polarization measurement is expressed by the operator $\widehat{\Pi}_{\vec{n}1} = |p\rangle^{AA}\langle p| \otimes \widehat{\mathbb{1}}^{\mathrm{B}} = 1/2(\widehat{\sigma}_0^{\mathrm{A}} + n_l\widehat{\sigma}_l^{\mathrm{A}}) \otimes \widehat{\sigma}_0^{\mathrm{B}}$ [‡].

$$\begin{aligned}
\mathrm{Tr}\left(\widehat{\Pi}_{\vec{n}1}\widehat{\rho}_{\Psi^-}\right) &= \frac{1}{2}\frac{1}{4}\mathrm{Tr}\left((\widehat{\sigma}_0^{\mathrm{A}}\widehat{\sigma}_0^{\mathrm{B}} + n_l\widehat{\sigma}_l^{\mathrm{A}}\widehat{\sigma}_0^{\mathrm{B}})(\widehat{\sigma}_0^{\mathrm{A}}\widehat{\sigma}_0^{\mathrm{B}} - \widehat{\sigma}_1^{\mathrm{A}}\widehat{\sigma}_1^{\mathrm{B}} - \widehat{\sigma}_2^{\mathrm{A}}\widehat{\sigma}_2^{\mathrm{B}} - \widehat{\sigma}_3^{\mathrm{A}}\widehat{\sigma}_3^{\mathrm{B}})\right) \\
&= \frac{1}{2}\frac{1}{4}\left(4 + n_l\, 4\delta_{l,0}\right) \\
&= \frac{1}{2}
\end{aligned} \tag{2.38}$$

The probability of the projection yields 1/2 for arbitrary measurement setting $\vec{n}$. Measuring the B subsystem instead of the A subsystem yields the same result $\mathrm{Tr}\left(\widehat{\Pi}_{1\vec{n}}\widehat{\rho}_{\Psi^-}\right) = 1/2$ with $\widehat{\Pi}_{1\vec{n}} = \widehat{\mathbb{1}}^{\mathrm{A}} \otimes |p\rangle^{BB}\langle p|$. So, if only one constituent is available for a local measurement, we have to conclude that the photon is in a mixed state.

After the projective measurement of the photon in subspace A, the composite system is in the product state

[‡] $\mathrm{Tr}\left(\widehat{\sigma}_\mu^{\mathrm{A}} \otimes \widehat{\sigma}_\nu^{\mathrm{B}}\right) = \widehat{\mathrm{Tr}}^{\mathrm{A}}\left(\widehat{\sigma}_\mu^{\mathrm{A}}\right)\widehat{\mathrm{Tr}}^{\mathrm{B}}\left(\widehat{\sigma}_\nu^{\mathrm{B}}\right)$

$$\begin{aligned}\sqrt{2}\,|p\rangle^{A\,A}\langle p|\;\left|\Psi^-\right\rangle &= \sqrt{2}\left(a\,|\mathrm{H}\rangle^A + b\,|\mathrm{V}\rangle^A\right)\left({}^A\langle \mathrm{V}|\,\overline{b} + {}^A\langle \mathrm{H}|\,\overline{a}\right)\;\left|\Psi^-\right\rangle \\ &= |p\rangle^A\left(-\overline{b}\,|\mathrm{H}\rangle^B + \overline{a}\,|\mathrm{V}\rangle^B\right) \\ &= |p\rangle^A\left|p^\perp\right\rangle^B, \end{aligned} \tag{2.39}$$

with $\left|p^\perp\right\rangle = -\overline{b}\,|\mathrm{H}\rangle + \overline{a}\,|\mathrm{V}\rangle$ and $\left\langle p\middle|p^\perp\right\rangle = 0$. The projection probability of a subsequent local measurement on the second subsystem can thus be predicted with a probability equal to one. The local measurement of the first subsystem thus affected the state of the second subsystem. Note that the above calculation is valid for projections onto arbitrary polarization measurements and any distance between the subsystems.

2.6 EPR and Local Hidden Variables

Einstein, Podolsky, and Rosen (EPR) formulated three key assumptions about physical theories [2]:

- **Locality:** *"if two systems no longer interact, no real change can take place in the second system in consequence of anything that may be done to the first system."*
- **Realism:** *"if, without in any way disturbing a system, we can predict with certainty (i.e., probability equal to unity) the value of a physical quantity, then there exists an element of reality corresponding to this quantity."*
- **Completeness:** *"every element of the physical reality must have a counterpart in the physical theory."*

An entangled photon pair in state $|\Psi^-\rangle$ can be used to show that these assumptions contradict quantum mechanics. For this purpose, the constituents of a pair must be separated by a large distance after generation. The current record holder is an experiment with the satellite Micius, which orbits the Earth at an altitude of 500 km [12]. The photon pairs generated at the satellite were transmitted to the ground stations in Delingha and Lijiang, which are separated by a distance of 1203 km. Under these circumstances, it can be assumed that the constituents of $|\Psi^-\rangle$ do not interact with each other when they arrive at the ground stations [1]. Based on the locality assumption we know that at this point, no manipulation of one photon can have a causal influence on the state of the other photon.

A local observer in Delingha, let's call her Alice, can choose any basis for the polarization measurement of the arriving photon. For example, if Alice chooses the HV basis, she gets one of two possible outcomes: Either the photon is in state $|\mathrm{H}\rangle$ or

$|\mathrm{V}\rangle$. If Alice detects an H polarized photon, she can predict with certainty that the partner photon of the observer Bob in Lijiang has to be V polarized. According to EPR (realism), the polarization of Bob's photon is an element of reality.

Alice, however, could have chosen a different basis for the polarization measurement. Let's say she chose the DA basis and got the result $|\mathrm{A}\rangle$. In that case, she could say with certainty that Bob's photon is D polarized. However, since Alice's basis choice cannot affect the photon of Bob (locality), both cases (Bob's photon is in state $|\mathrm{H}\rangle$, Bob's photon is in state $|\mathrm{D}\rangle$) must have been determined before splitting the photons (completeness).

However, we know from Equation 2.22 that the projectors $\widehat{\Pi}_\mathrm{V}$ and $\widehat{\Pi}_\mathrm{D}$ do not commute, which means that these properties cannot be determined simultaneously. EPR therefore concluded that "*the quantum-mechanical description of physical reality given by wave functions is not complete*". John Stewart Bell picked up on the idea that quantum mechanics should be supplemented with local hidden-variables (LHV) to restore the completeness [3].

To get an idea of a local hidden-variable, let us consider the following scenario. A photon with the polarization corresponding to the Stokes vector $\vec{s}$ is analyzed by means of a half-wave plate followed by a polarizing beam splitter ($\widehat{O}_{\vec{n}} = n_j\widehat{\sigma}_j$). After the measurement, the photon has one of the two polarizations $\pm\vec{n}$, corresponding to the measurement results $A(\vec{n}) = \pm 1$. Quantum mechanics merely describes that the state $\pm\vec{n}$ occurs with a probability of $\frac{1}{2}(1 \pm \vec{s}.\vec{n})$ and gives no reason why the respective state occurs. However, one could also imagine that the photon has an additional property. This local hidden variable can be considered as an additional Stokes vector $\vec{\lambda}$. With the knowledge of both Stokes vectors $\vec{\lambda}$ and $\vec{s}$, the measurement result $A_{\vec{\lambda}}(\vec{n})$ for any measurement settings $\vec{n}$ can be predicted with certainty[§].

By successively repeating the experiment with N photons, we observe the mean of the measurement series $\langle A\rangle = 1/N\sum_i^N A_i(\vec{n}) = \vec{s}.\vec{n}$, which is correctly predicted by quantum mechanics

$$\left\langle \widehat{O}_{\vec{n}} \right\rangle = \frac{1}{2}\mathrm{Tr}\left(\widehat{O}_{\vec{n}}(\widehat{\sigma}_0 + s_i\widehat{\sigma}_i)\right) = \vec{s}.\vec{n}. \tag{2.40}$$

This expectation value must also be reproduced by the LHV theory, so it is assumed that the vector $\vec{\lambda}$ is a random variable with a probability distribution of $\varrho(\vec{\lambda})$, where

$$\left\langle A_{\vec{\lambda}}(\vec{n})\right\rangle_{\vec{\lambda}} = \int \mathrm{d}\vec{\lambda}\ \varrho(\vec{\lambda})A(\vec{n},\vec{\lambda}) = \vec{s}.\vec{n} \tag{2.41}$$

and $\int \mathrm{d}\vec{\lambda}\ \varrho(\vec{\lambda}) = 1$ must hold.

[§]e.g .: $A_{\vec{\lambda}}(\vec{n}) = \mathrm{sign}\left(\vec{s}.\vec{n} + \vec{\lambda}.\vec{n}\right)$

Now the question arises whether with such an LHV theory the anti-correlations of the $|\Psi^-\rangle$ state can be explained or not. To this end, Bell developed an inequality that can falsify LHV theories [3]. Clauser, Horne, Shimony, and Holt (CHSH) have generalized Bell's theorem and proposed an explicit experiment [7]. Assuming LHV, the following equality holds

$$S_{\vec{\lambda}} = A_{\vec{\lambda}}(\vec{n})\left(B_{\vec{\lambda}}(\vec{m}) + B_{\vec{\lambda}}(\vec{m}')\right) + A_{\vec{\lambda}}(\vec{n}')\left(B_{\vec{\lambda}}(\vec{m}) - B_{\vec{\lambda}}(\vec{m}')\right) = \pm 2, \tag{2.42}$$

where $A_{\vec{\lambda}}(\vec{x}) = \pm 1$ and $B_{\vec{\lambda}}(\vec{x}) = \pm 1$ describe the measurement result of Alice and Bob with the measurement setting $\vec{x} \in \{\vec{n}, \vec{n}', \vec{m}, \vec{m}'\}$. It is evident that the equality holds since $B_{\vec{\lambda}}(\vec{m}) + B_{\vec{\lambda}}(\vec{m}')$ can give either ± 2 or 0. If $B_{\vec{\lambda}}(\vec{m}) + B_{\vec{\lambda}}(\vec{m}')$ equals plus or minus two, it follows that $B_{\vec{\lambda}}(\vec{m}) - B_{\vec{\lambda}}(\vec{m}')$ must be zero and vice versa. For the expected value $\langle S_{\vec{\lambda}} \rangle_{\vec{\lambda}}$, the inequality

$$-2 \leq \langle S_{\vec{\lambda}} \rangle_{\vec{\lambda}} \leq 2, \tag{2.43}$$

with

$$\begin{aligned}\langle S_{\vec{\lambda}} \rangle_{\vec{\lambda}} &= \int \varrho(\vec{\lambda}) S_{\vec{\lambda}} \, \mathrm{d}\vec{\lambda} \\ &= \langle A_{\vec{\lambda}}(\vec{n}) B_{\vec{\lambda}}(\vec{m}) \rangle_{\vec{\lambda}} + \langle A_{\vec{\lambda}}(\vec{n}) B_{\vec{\lambda}}(\vec{m}') \rangle_{\vec{\lambda}} + \langle A_{\vec{\lambda}}(\vec{n}') B_{\vec{\lambda}}(\vec{m}) \rangle_{\vec{\lambda}} - \langle A_{\vec{\lambda}}(\vec{n}') B_{\vec{\lambda}}(\vec{m}') \rangle_{\vec{\lambda}}\end{aligned}$$

holds, which is known as the CHSH variant of Bell's inequality [7]. The quantum mechanical expectation value of a polarization measurement (Equation 2.24) on both photons can be calculated with the operator $\widehat{O}_{\vec{n}\vec{m}} = \widehat{O}^{\mathrm{A}}_{\vec{n}} \otimes \widehat{O}^{\mathrm{B}}_{\vec{m}} = n_i \widehat{\sigma}^{\mathrm{A}}_i \otimes m_j \widehat{\sigma}^{\mathrm{B}}_j$ and yields

$$\begin{aligned}\mathrm{Tr}\left(\widehat{O}_{\vec{n}\vec{m}} \widehat{\rho}_{\Psi^-}\right) &= \frac{1}{4}\mathrm{Tr}\left((n_i m_j \widehat{\sigma}^{\mathrm{A}}_i \widehat{\sigma}^{\mathrm{B}}_j)(\widehat{\sigma}^{\mathrm{A}}_0 \widehat{\sigma}^{\mathrm{B}}_0 - \widehat{\sigma}^{\mathrm{A}}_1 \widehat{\sigma}^{\mathrm{B}}_1 - \widehat{\sigma}^{\mathrm{A}}_2 \widehat{\sigma}^{\mathrm{B}}_2 - \widehat{\sigma}^{\mathrm{A}}_3 \widehat{\sigma}^{\mathrm{B}}_3)\right) \\ &= \frac{1}{4} n_i m_j \; 4(-\delta_{i,1}\delta_{j,1} - \delta_{i,2}\delta_{j,2} - \delta_{i,3}\delta_{j,3}) \\ &= -n_i m_i \\ &= -\vec{n}.\vec{m}\end{aligned} \tag{2.44}$$

for the $|\Psi^-\rangle$ state. This results in an expected S value of

$$\begin{aligned}\langle S \rangle &= \left\langle \widehat{O}_{\vec{n}\vec{m}} \right\rangle + \left\langle \widehat{O}_{\vec{n}\vec{m}'} \right\rangle + \left\langle \widehat{O}_{\vec{n}'\vec{m}} \right\rangle - \left\langle \widehat{O}_{\vec{n}'\vec{m}'} \right\rangle \\ &= -\vec{n}.\vec{m} - \vec{n}.\vec{m}' - \vec{n}'.\vec{m} + \vec{n}'.\vec{m}'\end{aligned} \tag{2.45}$$

If the vectors are chosen to be on the Poincaré sphere and in the plane of linear polarization

$$\vec{n} = \begin{pmatrix} \sin\alpha_n \\ 0 \\ \cos\alpha_n \end{pmatrix} = \begin{pmatrix} 0 \\ 0 \\ 1 \end{pmatrix} \qquad \vec{n}' = \begin{pmatrix} \sin\alpha'_n \\ 0 \\ \cos\alpha'_n \end{pmatrix} = \begin{pmatrix} 1 \\ 0 \\ 0 \end{pmatrix}$$
$$\vec{m} = \begin{pmatrix} \sin\beta_m \\ 0 \\ \cos\beta_m \end{pmatrix} = \frac{1}{\sqrt{2}} \begin{pmatrix} 1 \\ 0 \\ 1 \end{pmatrix} \qquad \vec{m}' = \begin{pmatrix} \sin\beta'_m \\ 0 \\ \cos\beta'_m \end{pmatrix} = \frac{1}{\sqrt{2}} \begin{pmatrix} -1 \\ 0 \\ 1 \end{pmatrix}, \tag{2.46}$$

the expected value of S assumes a minimum of $\langle S\rangle = -2\sqrt{2}$ for the angles $\alpha_n = 0$, $\alpha'_n = \pi/2$, $\beta_m = \pi/4$, $\beta'_m = \pi/4$. This value is smaller than the lower limit of Bell's inequality and therefore cannot be explained with local hidden-variables.

Such a violation of Bell's inequality has been verified in a variety of experiments, but each experiment requires assumptions that provide loopholes for local realism. However, since all significant loopholes have been closed [4, 5, 6], there is reason to believe that local realism cannot properly describe nature.

2.7 Verification of Entanglement

The CHSH inequality is a useful tool for distinguishing between states whose correlated measurement results can be explained by local hidden-variables and states whose correlations cannot be explained in this way. However, an operator that allows a distinction between entangled and separable states is known as an entanglement witness.

As already mentioned, any pure state $|\phi\rangle^{AB} \in \mathcal{H}_A \otimes \mathcal{H}_\mathrm{B}$ that cannot be written as a direct product of pure states of the subspaces $|\phi\rangle^{AB}_{\mathrm{sep}} = |\phi\rangle^A \otimes |\psi\rangle^B$ is called entangled. A similar statement can be formulated for mixed states[¶] of the product space. Any bipartite density matrix $\widehat{\rho}$ acting on $\mathcal{H}_A \otimes \mathcal{H}_B$ is said to be separable iff it can be written in the form [23]

$$\begin{aligned} \widehat{\rho}_{\mathrm{sep}} &= \sum_i w_i \, \widehat{\rho}^{\mathrm{A}}_{(i)} \otimes \widehat{\varrho}^{\mathrm{B}}_{(i)} \\ &= \frac{1}{4} \sum_i w_i \, (\widehat{\sigma}^{\mathrm{A}}_0 + s_{j,(i)} \widehat{\sigma}^{\mathrm{A}}_j) \otimes (\widehat{\sigma}^{\mathrm{B}}_0 + r_{k,(i)} \widehat{\sigma}^{\mathrm{B}}_k), \end{aligned} \tag{2.47}$$

[¶]Any bipartite density matrix $\widehat{\rho}$ acting on $\mathcal{H}^2_A \otimes \mathcal{H}^2_B$ can be decomposed into Pauli matrices $\widehat{\rho} = \frac{1}{4}\left(t_{\mu,\nu} \widehat{\sigma}^{\mathrm{A}}_\mu \widehat{\sigma}^{\mathrm{B}}_\nu\right)$. For each valid state, the trace of the density matrix must be one $\mathrm{Tr}\,(\widehat{\rho}) = t_{0,0} = 1$.

with sets of Stokes vectors denoted by $s_{j,(i)} \in [s_{j,(1)}, s_{j,(2)}, \dots]$ and $r_{j,(i)} \in [r_{j,(1)}, r_{j,(2)}, \dots]$. The sum of the positive weights $w_i > 0$ is normalized to one $\sum_i w_i = 1$. Any state that cannot be written in this way is called inseparable or entangled. From the Horodecki family, we know that for every entangled state there exists an entanglement witness $\widehat{\mathcal{W}}$, which bears witness to this property.

Lemma 1. "*For any inseparable state* $\widehat{\rho}_{ent}$ *there exists Hermitian operator* $\widehat{\mathcal{W}}$ *such that*

$$\mathrm{Tr}\left(\widehat{\mathcal{W}}\widehat{\rho}_{\mathrm{ent}}\right) < 0 \qquad \text{and} \qquad \mathrm{Tr}\left(\widehat{\mathcal{W}}\widehat{\rho}_{\mathrm{sep}}\right) \geq 0 \tag{2.48}$$

for any separable $\widehat{\rho}_{sep}$." [24]

No separable state can violate a Bell inequality, but not every entangled state violates a Bell inequality [25]. Therefore, Bell inequalities are regarded as non-optimal entanglement witnesses. Figure 2.3 shows a schematic view of the different types of correlations and the distinctions which can be performed with entanglement witnesses and Bell inequalities.

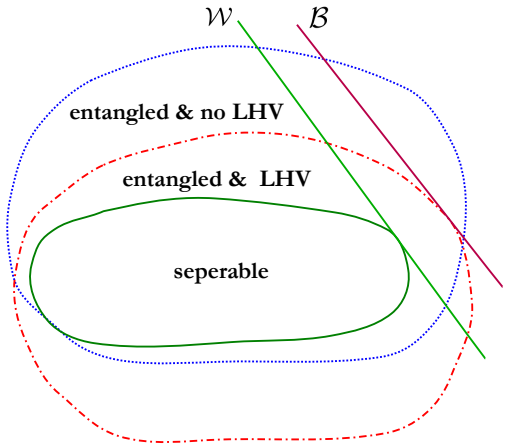


Figure 2.3 Schematic view of the different types of correlations: $\mathcal{W}$ and $\mathcal{B}$ denote the distinction which can be performed with an entanglement witness and a Bell inequality, respectively. Reprinted from "*Relations between Entanglement Witnesses and Bell Inequalities*", by Hyllus *et al.* [19].

In order to derive an optimal witness for the $|\Psi^-\rangle$ state, we follow the section "*From CHSH Inequalities to Optimal Witnesses* " in "*Relations between Entanglement Witnesses and Bell Inequalities*", by Hyllus *et al.* [19]. The observable, which corresponds to the measurement of an S value, is described by the Bell operator

$$\widehat{\mathcal{B}} = \left(n_i(m_j + m'_j) + n'_i(m_j - m'_j)\right)\widehat{\sigma}_i^{\mathrm{A}}\widehat{\sigma}_j^{\mathrm{B}}. \tag{2.49}$$

Applying the measurement setting described in Equation 2.46 shows that the same result can be obtained with measurements in the two mutually unbiased bases HV and DA denoted by the operator $\widehat{\mathcal{B}}_{\mathrm{HD}}$.

$$\widehat{\mathcal{B}}_{\mathrm{HD}} = \sqrt{2}\left(\widehat{\sigma}_1^{\mathrm{A}}\widehat{\sigma}_1^{\mathrm{B}} + \widehat{\sigma}_3^{\mathrm{A}}\widehat{\sigma}_3^{\mathrm{B}}\right). \tag{2.50}$$

For separable states, this operator yields an expectation value of

$$\mathrm{Tr}\left(\widehat{\mathcal{B}}_{\mathrm{HD}}\widehat{\rho}_{\mathrm{sep}}\right) = \sqrt{2}\sum_i w_i \left(s_{1,(i)}r_{1,(i)} + s_{3,(i)}r_{3,(i)}\right), \tag{2.51}$$

with a minimum value of $-\sqrt{2}$. Shifting this operator by the value $\sqrt{2}$ and multiplication with a factor $1/\sqrt{2}$ yields

$$\begin{aligned}\widehat{\mathcal{W}}_{\mathrm{HD}} &= \frac{1}{\sqrt{2}}\left(\sqrt{2}\,\widehat{\mathbb{1}}^{\mathrm{A}}\widehat{\mathbb{1}}^{\mathrm{B}} + \widehat{\mathcal{B}}_{\mathrm{HD}}\right)\\ &= \widehat{\sigma}_0^{\mathrm{A}}\widehat{\sigma}_0^{\mathrm{B}} + \widehat{\sigma}_1^{\mathrm{A}}\widehat{\sigma}_1^{\mathrm{B}} + \widehat{\sigma}_3^{\mathrm{A}}\widehat{\sigma}_3^{\mathrm{B}}\end{aligned} \tag{2.52}$$

This operator now has positive expectation values for all separable states $\mathrm{Tr}\left(\widehat{\mathcal{W}}_{\mathrm{HD}}\widehat{\rho}_{\mathrm{sep}}\right) > 0$ and yields negative values only for non-separable states, which describe an entanglement witness by definition [24]. Thus, we can prove the entanglement of $|\Psi^-\rangle$ by means of a negative expected value $\mathrm{Tr}\left(\widehat{\mathcal{W}}_{\mathrm{HD}}\widehat{\rho}_{\Psi^-}\right) = -1$.

At this point we want to introduce the horizontal/vertical and diagonal/anti-diagonal correlation operators $\widehat{\mathcal{V}}_{\mathrm{HV}} = -\widehat{\sigma}_3^{\mathrm{A}}\widehat{\sigma}_3^{\mathrm{B}}$ and $\widehat{\mathcal{V}}_{\mathrm{DA}} = -\widehat{\sigma}_1^{\mathrm{A}}\widehat{\sigma}_1^{\mathrm{B}}$, with expectation values corresponding to the experimental visibility in the respective basis. The visibility thus defined is positive for anti-correlated and negative for correlated states. However, with these operators, we can rewrite the entanglement witnesses as

$$\widehat{\mathcal{W}}_{\mathrm{HD}} = \widehat{\mathbb{1}}^{\mathrm{A}}\widehat{\mathbb{1}}^{\mathrm{B}} - \widehat{\mathcal{V}}_{\mathrm{HV}} - \widehat{\mathcal{V}}_{\mathrm{DA}}. \tag{2.53}$$

Experimentally the visibility can be accessed via $\mathcal{V}_{\mathrm{XY}} = \frac{N_{\mathrm{XY}}+N_{\mathrm{YX}}-N_{\mathrm{XX}}-N_{\mathrm{YY}}}{N_{\mathrm{XY}}+N_{\mathrm{YX}}+N_{\mathrm{XX}}+N_{\mathrm{YY}}}$, where N_{XY} is the number of coincident detection events between Alice's detector for polarization X and Bob's detector for polarization Y. The above equation reveals that visibility measurements satisfying $\widehat{\mathcal{V}}_{\mathrm{DA}}+\widehat{\mathcal{V}}_{\mathrm{HV}} > 1$ are sufficient criteria to prove the entanglement of the tested state.

2.8 Two-Photon Interference

Two-photon interference is of fundamental importance for many applications in quantum optics, such as the generation of NOON states, entanglement swapping, and quantum teleportation. In the following, we will first examine HOM interference and seamlessly connect this topic to NOON states. Therefore, we will mainly following Zhe-Yu Jeff Ou [26] and Jonathan P. Dowling [14].

Before we begin, we want to mention for the sake of completeness the creation (annihilation) operator $\hat{\mathsf{a}}^\dagger$ ($\hat{\mathsf{a}}$), which generates (eliminates) a photon when applied to a n-photon state $|\mathrm{n}\rangle$.

$$\hat{\mathsf{a}}^\dagger |\mathrm{n}\rangle = \sqrt{n+1}\,|n+1\rangle \tag{2.54a}$$

$$\hat{\mathsf{a}}\,|\mathrm{n}\rangle = \sqrt{n}\,|n-1\rangle \tag{2.54b}$$

We will indicate the vacuum state ($n = 0$) with $|\mathrm{Vac}\rangle$. The ladder operators also satisfy the known commutation relation

$$\left[\hat{\mathsf{a}}, \hat{\mathsf{a}}^\dagger\right] = 1 \tag{2.55}$$

and relate to the number operator via

$$\hat{N}\,|\mathrm{n}\rangle = \hat{\mathsf{a}}^\dagger\hat{\mathsf{a}}\,|\mathrm{n}\rangle = \mathrm{n}\,|\mathrm{n}\rangle\,. \tag{2.56}$$

2.8.1 Hong-Ou-Mandel Interference

Hong-Ou-Mandel (HOM) interference can be observed when two indistinguishable photons in different modes (a,b) of a beam splitter (BS) are superimposed [27]. Each photon is either reflected or transmitted to the output modes c and d. This process is described by the creation operator relation [28]

$$\hat{\mathsf{a}}_\mathrm{a}^\dagger = \frac{1}{\sqrt{2}}\left(\hat{\mathsf{a}}_\mathrm{c}^\dagger - \hat{\mathsf{a}}_\mathrm{d}^\dagger\right) \tag{2.57a}$$

$$\hat{\mathsf{a}}_\mathrm{b}^\dagger = \frac{1}{\sqrt{2}}\left(\hat{\mathsf{a}}_\mathrm{d}^\dagger + \hat{\mathsf{a}}_\mathrm{c}^\dagger\right), \tag{2.57b}$$

where $\hat{\mathsf{a}}_\mathrm{x}^\dagger$ denotes the creation operator of a photon in mode $\mathrm{x} \in \{\mathrm{a}, \mathrm{b}, \mathrm{c}, \mathrm{d}\}$. In Equation 2.57 we assumed a lossless beam splitter with 50% reflectance and 50% transmittance [29].

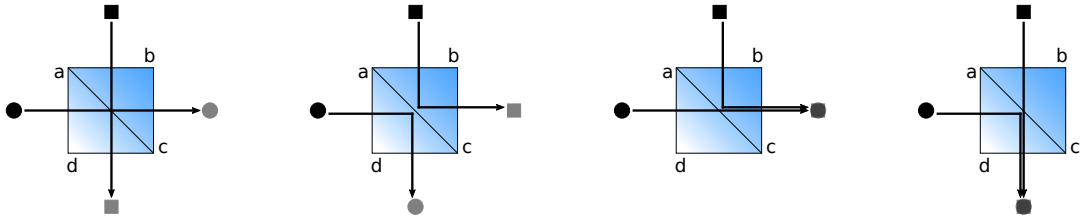


Figure 2.4 Lossless beam splitter: Four possible outcomes when two distinguishable photons incident on a beam splitter in separate input modes a and b.

There are four possible outcomes if two distinguishable photons (● / ■) are superimposed on the BS (see Figure 2.4). All four possibilities are described by the composed operator relation of both photons which reads

$$\hat{a}^\dagger_{a,\bullet}\hat{a}^\dagger_{b,\blacksquare} = \frac{1}{2}\left(\hat{a}^\dagger_{c,\bullet}\hat{a}^\dagger_{d,\blacksquare} - \hat{a}^\dagger_{d,\bullet}\hat{a}^\dagger_{c,\blacksquare} + \hat{a}^\dagger_{c,\bullet}\hat{a}^\dagger_{c,\blacksquare} - \hat{a}^\dagger_{d,\bullet}\hat{a}^\dagger_{d,\blacksquare}\right). \tag{2.58}$$

With a probability of 50% both photons are observed in the same mode, otherwise they are in separate modes. Interference of the two photons occurs only if they are indistinguishable. This can be seen by dropping the photon characterization (● / ■) in Equation 2.58:

$$\hat{a}^\dagger_a\hat{a}^\dagger_b = \frac{1}{2}\left(\hat{a}^\dagger_c\hat{a}^\dagger_d - \hat{a}^\dagger_d\hat{a}^\dagger_c + \hat{a}^\dagger_c\hat{a}^\dagger_c - \hat{a}^\dagger_d\hat{a}^\dagger_d\right) = \frac{1}{2}\left(\hat{a}^\dagger_c\hat{a}^\dagger_c - \hat{a}^\dagger_d\hat{a}^\dagger_d\right). \tag{2.59}$$

Consequently, the outcomes with one photon in each mode interfere destructively. Thus, both photons will always end up in the same output mode of the BS. This bunching effect is referred to as HOM interference.

$$\hat{a}^\dagger_a\hat{a}^\dagger_b\,|\mathrm{Vac}\rangle \xrightarrow{\mathrm{BS}} \frac{1}{2}\left(\hat{a}^\dagger_c\hat{a}^\dagger_c - \hat{a}^\dagger_d\hat{a}^\dagger_d\right)|\mathrm{Vac}\rangle \tag{2.60}$$

$$|1_a, 1_b\rangle \xrightarrow{\mathrm{BS}} \frac{1}{\sqrt{2}}\left(|2_c, 0_d\rangle - |0_c, 2_d\rangle\right) \tag{2.61}$$

The absence of coincidences in the output modes of such an experimental setup is a useful indicator for the indistinguishability of the superimposed photons. Imposing a temporal delay on one of the two photons before they reach the beam splitter causes distinguishability by means of their relative arrival time. Thus, random splitting is observed for delays which exceed the coherence time of the photons. Therefore, HOM interference can be used to measure the coherence length of photons. A more detailed study of this effect regarding partially distinguishable photons can be found in Appendix A.

2.8.2 NOON states

NOON states are a particular type of entangled state which are utilized in lithography and quantum metrology [30, 31]. In this section we will briefly introduce this type of multi-photon state.

The two-photon state resulting from the HOM interference describes a state in which both photons coexist in one of two modes, although it is uncertain which mode they are in (see Equation 2.61). Such a state can be generalized to a higher photon number of N

$$|\mathrm{NOON}\rangle = \frac{1}{\sqrt{2}}\frac{1}{\sqrt{N!}}\left((\hat{a}_c^\dagger)^N - (\hat{a}_d^\dagger)^N\right)|\mathrm{Vac}\rangle = \frac{1}{\sqrt{2}}\left(|N,0\rangle - |0,N\rangle\right) \tag{2.62}$$

Such path-entangled states are known as NOON state [32]. In the following, however, we will limit the calculations to the two-photon state relevant for the experiments of this thesis. Equation 2.61 describes such a NOON state with a photon number $N = 2$ in the spatial modes c and d. Superimposing these paths on a second beam splitter reverses the bunching process. Thus, the two photons are separated from each other in the output modes of the resulting interferometer.

$$\hat{a}_c^\dagger = \frac{1}{\sqrt{2}}\left(\hat{a}_e^\dagger + \hat{a}_f^\dagger\right) \tag{2.63a}$$

$$\hat{a}_d^\dagger = \frac{1}{\sqrt{2}}\left(\hat{a}_f^\dagger - \hat{a}_e^\dagger\right) \tag{2.63b}$$

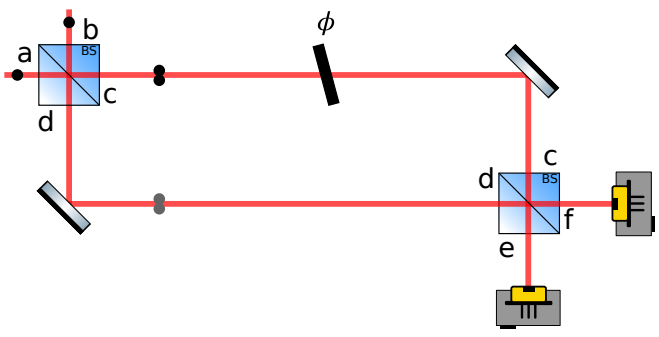


Figure 2.5 Mach–Zehnder interferometer: HOM interference of two photons at the first beam splitter generates a NOON state in modes c and d. The coincidence count rate of the detectors in modes e and f depends on the relative phase ϕ (see Equation 2.65).

However, this process depends on a relative phase ϕ between the two paths which is described by the operator $\hat{U}_c(\phi) = e^{i\hat{N}_c\phi}$, whereby $\hat{N}_c = \hat{a}_c^\dagger\,\hat{a}_c$ represents the photon

number operator in mode c.

$$\frac{1}{2}\left((\hat{\mathsf{a}}_{\mathrm{c}}^{\dagger})^2 - \mathrm{e}^{\mathrm{i}2\phi}(\hat{\mathsf{a}}_{\mathrm{d}}^{\dagger})^2\right)|\mathrm{Vac}\rangle \quad \xrightarrow{\mathrm{BS}} \quad \frac{1}{2}\left((\hat{\mathsf{a}}_{\mathrm{e}}^{\dagger})^2 + (\hat{\mathsf{a}}_{\mathrm{f}}^{\dagger})^2)\sin(\phi) + 2\hat{\mathsf{a}}_{\mathrm{e}}^{\dagger}\hat{\mathsf{a}}_{\mathrm{f}}^{\dagger}\cos(\phi)\right)|\mathrm{Vac}\rangle \tag{2.64a}$$

$$\frac{1}{\sqrt{2}}\left(|2,0\rangle - \mathrm{e}^{\mathrm{i}2\phi}|0,2\rangle\right) \quad \xrightarrow{\mathrm{BS}} \quad \frac{1}{\sqrt{2}}(|2,0\rangle + |0,2\rangle)\sin(\phi) + |1,1\rangle\cos(\phi) = |\mathrm{Out}_2\rangle \tag{2.64b}$$

$$R_{\mathrm{ef}} = |\langle 1,1|\mathrm{Out}_2\rangle|^2 = \cos^2(\phi) \tag{2.65a}$$

$$R_{\mathrm{ee}} + R_{\mathrm{ff}} = |\langle 2,0|\mathrm{Out}_2\rangle|^2 + |\langle 0,2|\mathrm{Out}_2\rangle|^2 = \sin^2(\phi) \tag{2.65b}$$

Equation 2.65 shows that the normalized coincidence count rate R_{ef} between the detectors in the output modes e and f varies periodically with the relative phase. The cases where both photons reach the same detector (R_{ee}, R_{ff}) can only be distinguished from single photons by means of photon-number-resolving detectors [33, 34, 35]. However, comparing this result with the situation of a single photon passing through the interferometer, shows that the detector count rate, in such a scenario, oscillates at half the frequency.

$$\frac{1}{\sqrt{2}}\left(\hat{\mathsf{a}}_{\mathrm{c}}^{\dagger} - \mathrm{e}^{\mathrm{i}\phi}\hat{\mathsf{a}}_{\mathrm{d}}^{\dagger}\right)|\mathrm{Vac}\rangle \quad \xrightarrow{\mathrm{BS}} \quad \frac{1}{2}\left(\hat{\mathsf{a}}_{\mathrm{e}}^{\dagger}\cos(\frac{\phi}{2}) + \hat{\mathsf{a}}_{\mathrm{f}}^{\dagger}\sin(\frac{\phi}{2})\right)|\mathrm{Vac}\rangle \tag{2.66a}$$

$$\frac{1}{\sqrt{2}}\left(|1,0\rangle - \mathrm{e}^{\mathrm{i}\phi}|0,1\rangle\right) \quad \xrightarrow{\mathrm{BS}} \quad |1,0\rangle\cos(\frac{\phi}{2}) + |0,1\rangle\sin(\frac{\phi}{2}) = |\mathrm{Out}_1\rangle \tag{2.66b}$$

$$R_{\mathrm{e}} = |\langle 1,0|\mathrm{Out}_1\rangle|^2 = \cos^2(\frac{\phi}{2}) \tag{2.67a}$$

$$R_{\mathrm{f}} = |\langle 0,1|\mathrm{Out}_1\rangle|^2 = \sin^2(\frac{\phi}{2}) \tag{2.67b}$$

The increased fringe oscillation frequency of the multi-photon state is called super-resolution. This effect provides a measurement advantage when the count rates are used to determine an unknown phase. Thereby the steeper slope of the function leads to a better phase resolution. In the following we want to characterize this measurement advantage quantitatively. In such an experiment, the expected count rates for both cases are

$$R_{\mathrm{e}} = M\cos^2(\frac{\phi}{2}) + B \tag{2.68a}$$

$$R_{\mathrm{ef}} = M/2\cos^2(\phi) + B \tag{2.68b}$$

with an average detected photon rate of M, including B phase-independent photons due to background (both measured in advance). Only half as many coincidences and therefore the same number of photons are detected. The inverse function of Equation 2.68 required for phase determination reads

$$\phi(R_\mathrm{e}) = 2\cos^{-1}\left(\sqrt{\frac{R_\mathrm{e}-B}{M}}\right) \tag{2.69a}$$

$$\phi(R_\mathrm{ef}) = \cos^{-1}\left(\sqrt{2\frac{R_\mathrm{ef}-B}{M}}\right) \tag{2.69b}$$

The error of the phase measurement results from the propagation of the uncertainty of the measured count rate $\Delta\phi(R) = |\partial\phi/\partial R|\sqrt{R}$. Such a system has maximum phase sensitivity at the Bisa point — at a count rate R^Bias — at which the unknown phase can be determined with an uncertainty of $\Delta\phi(R^\mathrm{Bias})$.

$$R_\mathrm{e}^\mathrm{Bias} = \sqrt{B(M+B)} \tag{2.70a}$$

$$R_\mathrm{ef}^\mathrm{Bias} = \sqrt{B(M/2+B)} \tag{2.70b}$$

$$\Delta\phi(R_\mathrm{e}^\mathrm{Bias}) = \frac{1}{\sqrt{M+2(B-\sqrt{B(M+B)})}} \tag{2.71a}$$

$$\Delta\phi(R_\mathrm{ef}^\mathrm{Bias}) = \frac{1}{\sqrt{2M+8(B-\sqrt{B(M/2+B)})}} \tag{2.71b}$$

In the limit of an infinitesimally small background we get the result

$$\lim_{B\to 0}\Delta\phi(R_\mathrm{e}^\mathrm{Bias}) = \Delta\phi_1^\mathrm{Min} = \frac{1}{\sqrt{M}} \tag{2.72a}$$

$$\lim_{B\to 0}\Delta\phi(R_\mathrm{ef}^\mathrm{Bias}) = \Delta\phi_2^\mathrm{Min}\frac{1}{\sqrt{2M}} \tag{2.72b}$$

The measurement precision obtained for single photons corresponds to the shot-noise limit (SNL) $\Delta\phi \geq \Delta\phi_\mathrm{SNL} = \frac{1}{\sqrt{M}}$, which cannot be violated with classical states of light. The precision achieved with the two-photon state, however, is improved by a factor of $\sqrt{2}$. Such sub-SNL precision is called super-sensitivity.

A more general calculation using quantum fisherman information [36] shows that the super-sensitivity scales with the photon number N of the NOON state used

$\Delta\phi_N^{\mathrm{Min}} = \frac{1}{\sqrt{N\,M}}$ [37]. The absolute minimum as predicted by the uncertainty principle $\frac{1}{M}$ can thus be achieved in the limit value of $N \mapsto M$. This Heisenberg limit retains its validity for arbitrary photon states. For the generation and detection of such high-NOON states ($N > 2$), however, more intricate experimental methods are necessary [15, 38].

A drawback of these NOON states is the high transmission η necessary for the sufficient detection of these states, i.e. all N photons of a state must be detected in order to obtain a valid signal. However, the probability for such an N-fold coincidence is proportional to η^N, rendering such an event increasingly unlikely with increasing N. We can therefore estimate the precision achieved in the presence of photon loss by $\Delta\phi_N^{\mathrm{Min}}(\eta) = \frac{1}{\sqrt{\eta^N N\,M}}$.

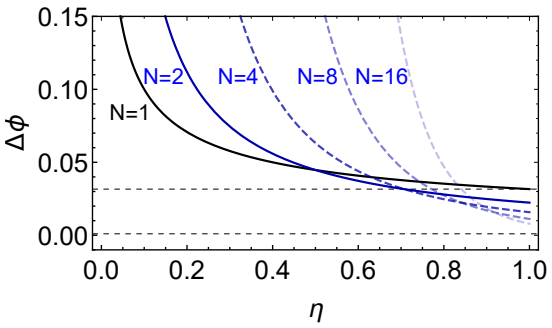


Figure 2.6 Measurement precision $\Delta\phi$ vs. transmission η: Achievable measurement precision $\Delta\phi_N^{\mathrm{Min}}(\eta) = \frac{1}{\sqrt{\eta^N N\,M}}$ in the presence of limited photon transmission η for NOON states with different photon number N and a mean photon rate of $M = 1000$. The shot-noise limit $\frac{1}{\sqrt{M}} = 0.032$ and Heisenberg limit $\frac{1}{M} = 0.001$ are depicted with a horizontal dashed line.

And so when using the same number of photons for the measurement, the advantage of a two-photon NOON state vanishes for a transmission probability of 0.5 or less ($\frac{1}{\sqrt{0.5^2 2\,M}} = \frac{1}{\sqrt{0.5M}}$). A more detailed study on this topic was conducted by Dorner *et al.*, who proposed the NOON "chopping" strategy in order to optimize NOON states with respect to losses [39, 40]. With this strategy, the photon number N is adapted to the total transmission of the system.

In general, there is a measurement advantage only for transmissions above a threshold dependent on N. If this threshold is not reached, more photons must be used at a higher N in order to achieve comparable precision. When comparing the same number of photons detected on average, a reduced phase noise can still be observed. However, there are several ways to achieve a certain resolution. In our comparison where we only consider the number of photons used, the loss, and the resulting quantization noise, NOON states have no advantage above a certain loss limit. However, if there are enough photons available for the measurement, it is decisive whether the additional photons have a detrimental effect on the resolution and whether they can be suppressed during signal recording. Therefore, we believe that NOON states can be advantageous for some applications even in case of loss scenarios beyond this threshold.

2.8.3 Two-Photons Interference in Polarization Modes

The photons being used in the later experiments are in a pair state with orthogonal polarization $\hat{a}_H^\dagger \hat{a}_V^\dagger |\mathrm{Vac}\rangle = |1_H, 1_V\rangle$. In the following we want to connect this state with the foregoing concepts. The basis transformation between the HV and DA basis is described by the operator relation

$$\hat{a}_H^\dagger = \frac{1}{\sqrt{2}} \left(\hat{a}_D^\dagger + \hat{a}_A^\dagger \right) \tag{2.73a}$$

$$\hat{a}_V^\dagger = \frac{1}{\sqrt{2}} \left(\hat{a}_D^\dagger - \hat{a}_A^\dagger \right), \tag{2.73b}$$

Rewriting $|1_H, 1_V\rangle$ in the DA basis shows that this two-photon state can be regarded as a NOON state in polarization modes.

$$\hat{a}_H^\dagger \hat{a}_V^\dagger |\mathrm{Vac}\rangle \xrightarrow{\text{DA-basis}} \frac{1}{2} \left(\hat{a}_D^\dagger \hat{a}_D^\dagger - \hat{a}_A^\dagger \hat{a}_A^\dagger \right) |\mathrm{Vac}\rangle \tag{2.74}$$

$$|1_H, 1_V\rangle \xrightarrow{\text{DA-basis}} \frac{1}{\sqrt{2}} \left(|2_D, 0_A\rangle - |0_D, 2_A\rangle \right) \tag{2.75}$$

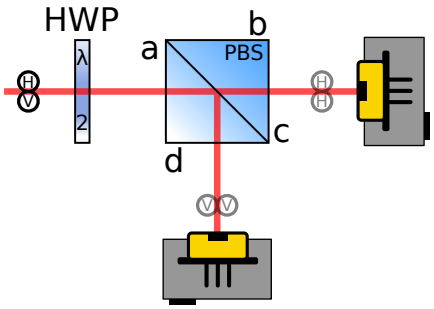


Figure 2.7 Polarization measurement: The two-photon state $|1_H, 1_V\rangle$ traverses an HWP followed by a PBS with single-photon detectors in each output mode (c,d).

By means of a polarizing beam splitter, a certain basis decomposition can be imposed on the photons. The polarization modes H and V with respect to the PBS are thus converted into spatial modes (aH $\mapsto$ cH, aV $\mapsto$ dV). This decomposition can be affected with the help of a half-wave plate. The resulting transformation is described by the relation

$$\hat{a}_{a,H}^\dagger = \cos(2\theta)\hat{a}_{c,H}^\dagger + \sin(2\theta)\hat{a}_{d,V}^\dagger \tag{2.76a}$$

$$\hat{a}_{a,V}^\dagger = \cos(2\theta)\hat{a}_{d,V}^\dagger - \sin(2\theta)\hat{a}_{c,H}^\dagger, \tag{2.76b}$$

with θ denoting the angle between the fast axis of the HWP and the horizontal axis of the PBS. In the output modes of the PBS we therefore expect the state

$$\hat{a}^{\dagger}_{a,H}\hat{a}^{\dagger}_{a,V}\left|\mathrm{Vac}\right\rangle \xrightarrow{\mathrm{HWP\&PBS}} \left(\cos(4\theta)\hat{a}^{\dagger}_{c,H}\hat{a}^{\dagger}_{d,V} - \frac{1}{2}\sin(4\theta)\left(\hat{a}^{\dagger}_{c,H}\hat{a}^{\dagger}_{c,H} - \hat{a}^{\dagger}_{d,V}\hat{a}^{\dagger}_{d,V}\right)\right)\left|\mathrm{Vac}\right\rangle \tag{2.77}$$

$$\left|1_{a,H}, 1_{a,V}\right\rangle \xrightarrow{\mathrm{HWP\&PBS}} \cos(4\theta)\left|1_{c,H}, 1_{d,V}\right\rangle - \frac{1}{\sqrt{2}}\sin(4\theta)\left(\left|2_{c,H}, 0_{d,V}\right\rangle - \left|0_{c,H}, 2_{d,V}\right\rangle\right) \tag{2.78}$$

Thus, at an angle of $\theta = \frac{\pi}{8}$ both photons enter the same output mode of the PBS. In this thesis, we will refer to this interference effect by "HOM interference in polarization modes". Moreover, in comparison to single photons

$$\left|1_{a,H}, 0_{a,V}\right\rangle \xrightarrow{\mathrm{HWP\&PBS}} \cos(2\theta)\left|1_{c,H}, 0_{d,V}\right\rangle + \sin(2\theta)\left|0_{c,H}, 1_{d,V}\right\rangle, \tag{2.79}$$

this NOON state in the polarization modes shows twice the fringe oscillation frequency with respect to HWP rotation and thus super-resolution in "polarization" measurements [41].

3 Detection and Data Analysis

Single-photon detectors are a very sensitive tool for detecting low intensities of light. Of course, in experiments these devices are very well protected against stray light, such as with spectral filters, but photons from background light cannot always be completely avoided. Something along the lines of a temporal filter is needed to sort out related detection events from the wealth of data. Such a process is carried out as part of the data evaluation.

The following chapter deals with the main features of the detectors and the data processing of their signal.

3.1 Single-Photon Detectors

Single-photon detectors used consist of silicon avalanche photodiodes (APD) implemented in an electrical circuit. Those APDs are reverse biased over breakdown voltage (Geiger mode). Free electrons in the semiconductor can be generated, inter alia, by incident photons. Those free electrons get accelerated by the bias voltage and can therefor trigger a self-sustaining avalanche of charge carriers (Geiger shower). The circuit lowers the bias voltage when an electrical current resulting from such an avalanche is registered. Consequently, the avalanche stops [42]. Thereafter, the bias voltage is restored and the detector is ready for the next event. In the time of reduced bias voltage, the detector is insensitive to incident photons. This so-called dead time t_{dead} leads to a decrease of the detection efficiency at higher count rates.

At the same time, the output voltage of the detector is raised for a short period of time to indicate the arrival of a photon. The time between the arrival of a photon and the rising edge of the output voltage is approximately normally distributed. The standard deviation of this varying delay, referred to as jitter σ_t, results in uncertainty of the registered time of arrival.

The detection efficiency η_{D} refers to the likelihood that an incoming photon will result in a rising edge in the output voltage. Besides photons thermal ionization can also produce free electrons. The resulting detector events cannot be distinguished from photon-induced events and result in the so-called dark count rate.

For experiments conducted in this thesis detectors from two different manufacturers were used. The technical specification of the detectors are summarized in Table 3.1.

Brand		Excelitas	AIT
Name		SPCM-800	QD800-pQI
Active Area	$\varnothing$	180 μm	500 μm
Detection Efficiency	η_D	64 %	50 %
Dark Count Rate	R_D	$<$ 600 Hz	200 Hz
Jitter	σ_t	350 ps	100 ps
Dead Time	t_dead	20 ns	10 μs

Table 3.1 Technical specification of the detectors used. The values are taken from the data sheet. With the AIT detector, the supply voltage and the cooling of the diode can be individually adjusted. Therefore, the given values could deviate substantially from the measured values.

Two filters (Semrock LL01-810, Thorlabs FGL665) were installed to prevent background light at the detectors. The spectral range above 1200 nm is not covered by the filters, since the detection efficiency becomes negligibly small at such long wavelengths (see Figure 3.1).

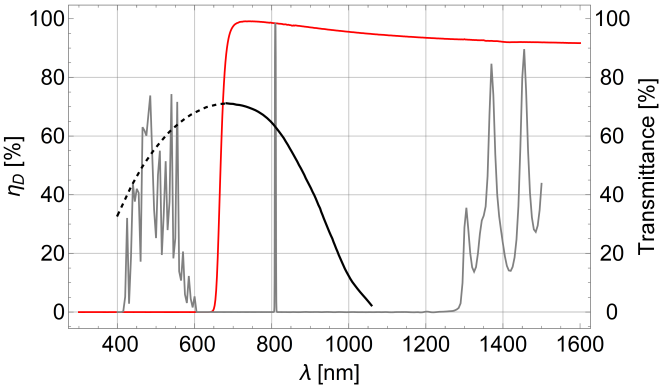


Figure 3.1 Typical photon detection efficiency η_D vs. wavelength λ. The black line is reprinted from the data sheet of the Excelitas detectors, extrapolated with a typical responsivity of a silicon APD. The gray (red) line shows the transmission of the Semrock LL01-810 (Thorlabs FGL665) filter.

3.2 Time Tagging

The output of the detectors is connected to a Time Tagging Module (TTM) manufactured by the Austrian Institute of Technology (TTM8000). This device provides eight channels that constantly monitor the output voltage of up to eight different detectors. The TTM has the ability to detect rising and falling edges of the voltage. In order to save capacity, the module was configured to only detect rising edges. The frequency of the internal clock is roughly 12.15 GHz which corresponds to $1/12.15 \times 10^{-9} = 82.3$ ps time bins. The module starts counting from zero whenever the power is turned on. The actual time is stored in a seven byte binary number which has an overflow every 68 days. This time value together with the channel and edge information is buffered

each time an event occurs and can be transferred to a PC via an Ethernet connection. The binary files produced in this way have a header of 30 bytes followed by successive time tags of eight bytes each. The time information is stored with little-endian in the first seven bytes of each tag, and the channel number is encoded in the first three bit of the last byte. The fourth bit of the last byte is one for rising or zero for falling edge events.

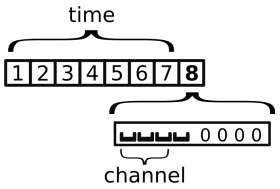


Figure 3.2 Structure of a time tag consisting of eight bytes, with the first seven bytes containing the time information. The channel number is encoded in the first three bit of the last byte. The fourth bit of the last byte is one or zero if a rising or falling edge was detected, respectively.

84	84	77	56	68	97	116	97	1	4	0	0	129	0	0
0	0	63	25	0	180	31	0	0	0	0	24	39	248	255
214	127	0	0	0	0	0	**16**	119	152	1	0	0	0	0
80	171	175	1	0	0	0	0	**80**	163	106	2	0	0	0
0	**80**	49	183	2	0	0	0	0	**80**	73	80	4	0	0

Table 3.2 Number example of a binary file. The first eight bytes of the binary file is the ASCII code for "TTM8Data". Overall, the header has 30 bytes (highlighted in gray), of which the last one has the value 255. Each odd time tag is highlighted in yellow. The time of the first tag is calculated as $(214+127\times256)\ 82.3\times10^{-12} = 2.693\,\text{ns}$. The channel information is in the last byte of each tag (bold). The number 16 results from the Bit-string $[00010000]_2 = 16$ and belongs to the channel 0 ($[01010000]_2 = 80 \leftrightarrow$ channel 2)

3.3 Coincidences

Two simultaneously generated photons are not always tagged simultaneously. There are several reasons for this, for example, the optical path length that the photons travel to the detectors may be different. Also, the cable length between the detectors and the TTM can cause a delay of the signal. The internal time delay of the detector can also vary with identical devices.

Two events occurring at detector D1 and D2 with a time difference $t_\Delta = t_{\text{D1}} - t_{\text{D2}}$, are called "coincident" if $|t_\Delta - t_\text{d}| < t_\text{coi}/2$ where t_coi is the coincidence window. The mean time delay between related time stamps t_d can be determined via cross-correlation of the arrival times, if t_d is stable for a sufficiently long period of time t_p [43]. The full width half maximum of the correlation function (t_FWHM) is determined by the timing

jitter of the detectors (σ_{tD1} and σ_{tD2})

$$t_{\mathrm{FWHM}} = 2\sqrt{2\log(2)}\,\sqrt{\sigma_{\mathrm{tD1}}^2 + \sigma_{\mathrm{tD2}}^2 + t_{\mathrm{coh}}^2} \tag{3.1}$$

and the coherence time t_{coh} of the photons. With the photon source used, the coherence time of the generated photons $t_{\mathrm{coh}} = 1.75\,\mathrm{ps}$ is much smaller than the jitter of the detectors and can be neglected. The correlation function measured with two AIT detectors (see Figure 3.3) results in $t_{\mathrm{FWHM}} = 822 \pm 10\,\mathrm{ps}$. This corresponds to a jitter of the detectors $\sigma_{\mathrm{AIT}} = 247 \pm 3\,\mathrm{ps}$, which is more than twice the value given in the data sheet. A second measurement with two Excelitas detectors resulted in a jitter of $\sigma_{\mathrm{Exc}} = 181 \pm 1\,\mathrm{ps}$, which is shorter by $\sim 150\,\mathrm{ps}$ than the value specified in the data sheet.

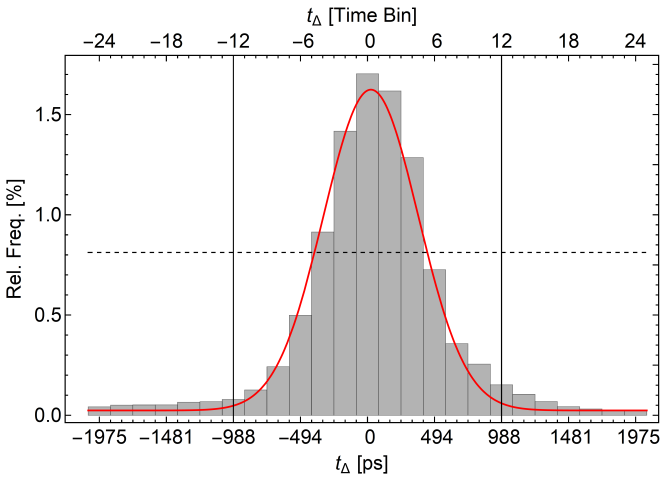


Figure 3.3 Histogram of t_Δ, measured with two AIT detectors. The red graph shows a Gaussian fit function with a standard deviation of $349 \pm 4\,\mathrm{ps}$ ($t_{\mathrm{FWHM}} = 822 \pm 10\,\mathrm{ps}$). The upper axis is plotted in units of TTM time bins, whereby one time bin corresponds to 82.3 ps. The horizontal lines indicate the coincidence window $t_{\mathrm{coi}} \simeq 2\,\mathrm{ns}$. The dashed line is half the maximum of the fit.

3.4 Accidental Coincidences

Uncorrelated detection events are caused by photon loss in the optical system, stray light, and dark counts. Such single events can occur independently at two different APDs within t_{coi} by accident. Such coincidences are called accidental coincidences or accidentals.

In a time period ΔT, two APDs detect a number of B_1 and B_2 single events. Thus, the mean photon number per coincidence window is $\overline{m}_i = B_i \frac{t_{\mathrm{coi}}}{\Delta T}$. The actual number k of photons arriving during a coincidence window follows a Poisson distribution

$$P(k, \overline{m}) = \frac{\overline{m}^k}{k!} \mathrm{e}^{-\overline{m}}. \tag{3.2}$$

The probability of detecting exactly one photon within t_{coi} in each of the two detectors, multiplied by the number of coincidence windows $n = \Delta T / t_{\mathrm{coi}}$, gives the expected

number of accidentals per ΔT. For small mean photon numbers $\overline{m} \ll 1$ the probability $P(1, \overline{m})$ can be approximated by the Taylor series $\overline{m}\mathrm{e}^{-\overline{m}} = \overline{m} + O(\overline{m}^2)$ *. Thus, the accidental rate per ΔT results in

$$R_{\mathrm{Acc}} = P(1, \overline{m}_1)\ P(1, \overline{m}_2)\ n \simeq B_1 \frac{t_{\mathrm{coi}}}{\Delta T}\ B_2 \frac{t_{\mathrm{coi}}}{\Delta T}\ \frac{\Delta T}{t_{\mathrm{coi}}} = B_1\ B_2\ \frac{t_{\mathrm{coi}}}{\Delta T}. \tag{3.3}$$

3.5 Coincidence Search

The amount of data produced by the TTM grows very quickly over time. If, for example, two detectors are used with a photon count rate of 400 kHz each, the file size after a 3-minute measurement time is $3 \cdot 60 \cdot 400 \times 10^3 \cdot 8$ Byte =576 MB. An algorithm based on the programming language C was developed to identify the few coincidences within this wealth of data in a time-saving manner.

The events detected during a short fraction of time t_{p} are written sequentially into an array **Event**$[i][n]$, with the row and column corresponding to the channel number $i \in [0, 1, \ldots, 7]$ and consecutive numbering n, respectively. The search for partner events of **Event**$[i][n]$ starts at the earliest possible time of a coincidence $u =$ **Event**$[i][n] + t_{\mathrm{d}} - t_{\mathrm{coi}}/2$, with the mean time delay t_{d} and the coincidence window t_{coi}. A loop looks for the smallest position m in channel j that satisfies $u <$ **Event**$[j][m]$. The events are considered coincidental if the deviation from the mean time delay $t_\Delta =$ **Event**$[j][m] -$ **Event**$[i][n] - t_{\mathrm{d}}$ is less than $t_{\mathrm{coi}}/2$. Such events are stored in an output file. Otherwise **Event**$[i][n]$ cannot have a partner in j sice $t_{\mathrm{dead}} > t_{\mathrm{coi}}$. Subsequently, this procedure is repeated for **Event**$[i+1][n]$. This process forms the central loop in the program (see Figure 3.4) and has to be repeated for each detector combination and time fragment.

For the coincidence search just described, the value t_{d} must be known. A very similar program can be used to find an unknown mean time delay. In this case, the central loop is repeatedly applied to the same fraction of the data, with different mean time delays $t_{d_l} = l\ t_{\mathrm{coi}}/2$, with $l \in \mathbb{Z}$. The delay which results in the highest number of coincidences can be used to calculate the mean time delay via $t_{\mathrm{d}} = t_{d_{Max}} + Mean(t_{\Delta_{Max}})$.

The deviation from the mean time delay t_Δ of each pair of events can be represented in a histogram (see Figure 3.3). The shape of the histogram is mainly determined by the jitter of the detector (see Equation 3.1) and can be approximated by a normal distribution.

*This approximation is always satisfied, if $t_{\mathrm{dead}} > t_{\mathrm{coi}}$.

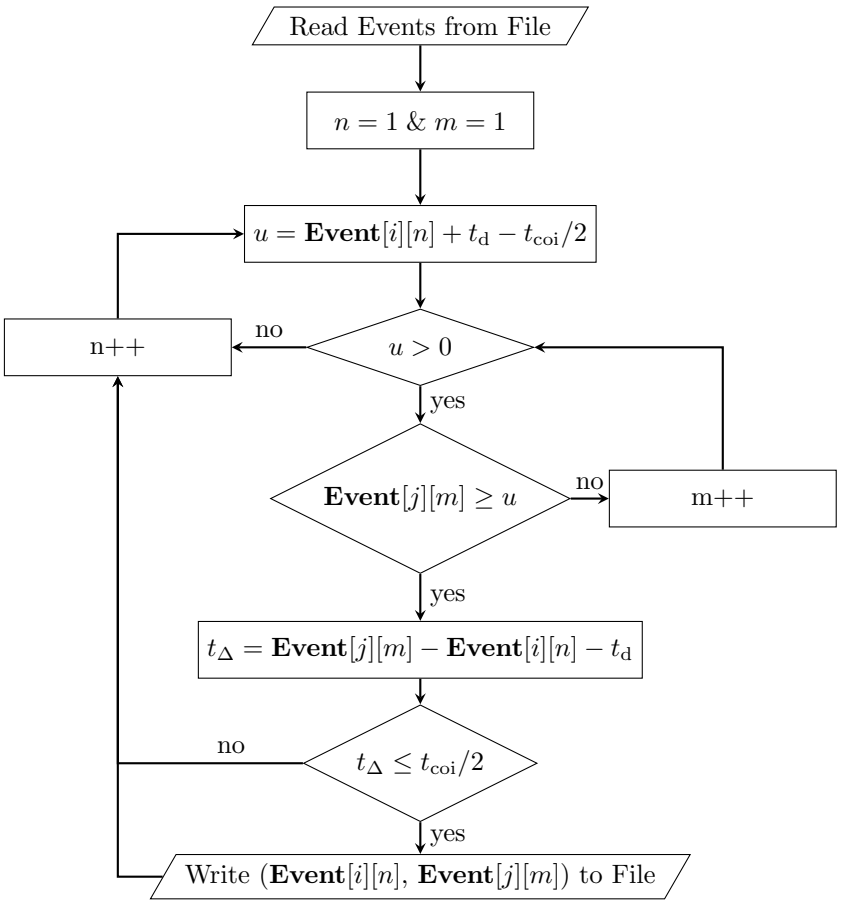


Figure 3.4 Flowchart of the central loop of the coincidence search program. The event times are sorted in an array $\mathbf{Event}[i][n]$, with the row and column corresponding to the detector/channel number $i \in [0, 1, \ldots, 7]$ and a consecutive numbering n, respectively.

3.6 Mean Time Delay Tracking

The mean time delay t_d does not change with time when all detectors are connected to the same TTM, since all of the data is handled in relation to the same clock. Therefore, it is sufficient to perform the delay search described above only once for a given experimental setup. For long distance experiments, several TTMs are needed.

The frequency deviation and drift of the internal clocks lead to a temporal variation of t_d, which must be considered in the coincidence search [43]. In this case, the delay search has to be performed for each time period t_p. In order to achieve an unadulterated result, the time delay t_d may not change by more than one time bin during t_p. The temporal variation of t_d is plotted in Figure 3.5 and can be approximated by a linear fit function with a slope of 280 ns/s (3402 time bins/s). This corresponds to one time bin every 294 μs ($t_p \overset{!}{<} 294\,\mu\mathrm{s}$).

The temporal delay of pair events is normally distributed around t_d with a stan-

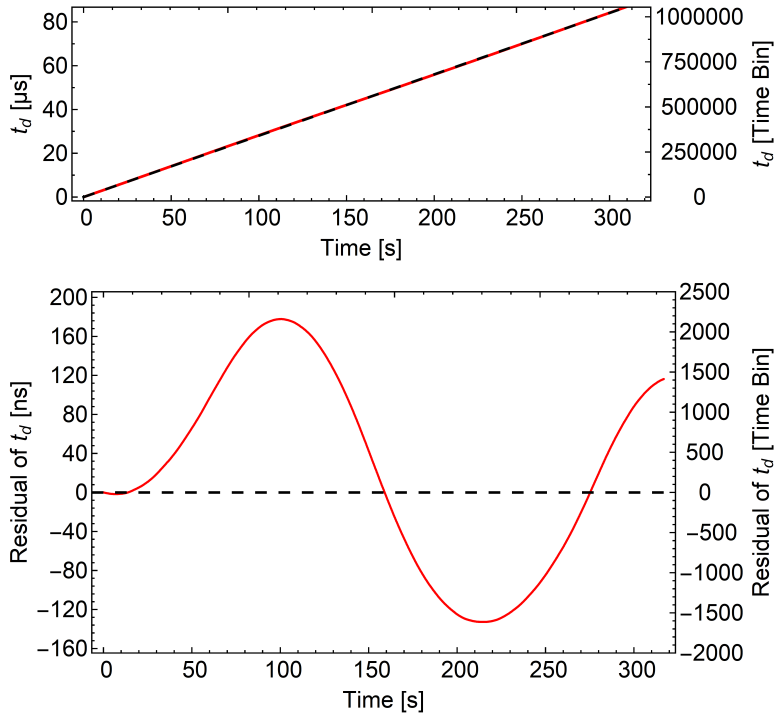


Figure 3.5 **Top:** Mean time delay t_d of pair events between two TTMs plotted over time (red line). The instability of the internal clocks leads to a temporal change of t_d. The black dashed line shows a linear fit with a slope of 280 ns/s (3402 time bins/s). **Bottom:** Residual of t_d over time (red line).

dard deviation of $\sqrt{\sigma_{\mathrm{tD1}}^2 + \sigma_{\mathrm{tD2}}^2}$. Thus, if N_{coi} coincidences are measured, t_d can be determined with an uncertainty of

$$\sigma_{t_\mathrm{d}} = \frac{1}{\sqrt{N_{coi}}} \sqrt{\sigma_{\mathrm{tD1}}^2 + \sigma_{\mathrm{tD2}}^2}. \tag{3.4}$$

The greater the photon loss along the optical link, the smaller the number of detected coincidences during t_p. As a result, the error of t_d becomes larger. In order to improve the stability t_p, two GPS clocks were used, one at each TTM. The electrical signal of these clocks is one pulse per second (PPS) which is synchronized to the GPS time. This signal is connected to a free channel of a TTM and appears in the stored binary files. During data evaluation, the assumption is that these signals occur simultaneously in both TTMs. The time between two consecutive PPS signals $\Delta t_{PPS} = t_{PPS_{m+1}} - t_{PPS_m} \sim 12.15 \times 10^9$ time bins as measured by the internal clock of the TTM, usually deviates from the expectation, because of the insufficient accuracy of the internal clock. A corrected time value for each event between two PPS signals can be calculated by

stretching each time bin by a factor of $(12.15 \times 10^9)/\Delta t_{PPS}$

$$\mathbf{EventCor}[i][n] = (\mathbf{Event}[i][n] - t_{PPS_m})\frac{12.15 \times 10^9}{\Delta t_{PPS}} + m\ (12.15 \times 10^9) \tag{3.5}$$

where m is the consecutive number of the PPS signals. The mean time delay t_d between corrected time stamps still varies in time due to instabilities of GPS clocks (see Figure 3.6).

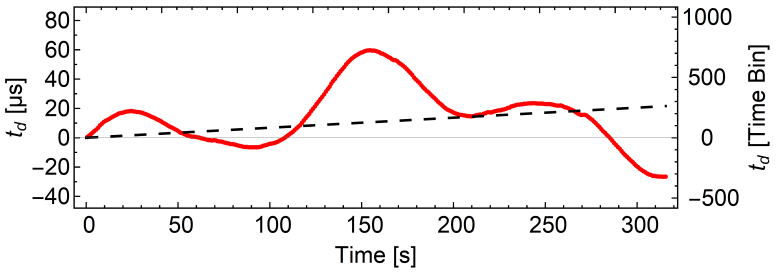


Figure 3.6 Mean time delay t_d between corrected time stamps of pair events between two TTMs plotted over time (red line). The instability of the PPS signal leads to a temporal change of t_d with a maximum slope of 2 ns/s (24 time bins/s). The black dashed line shows a linear fit with a slope of 69 ps/s (0.8 time bins/s).

With the corrected time the measured maximum value of the slope of t_d vs. time is 2 ns/s (24 time bins/s) which corresponds to one time bin every 41 ms ($t_p \overset{!}{<} 41$ ms). Thus, by using the GPS clocks, t_p can be increased by a factor of 140, which reduces the error of t_d by $\sim 1/12$ compared to the estimation without time correction.

4 Entangled Photon Source

For sophisticated experiments outside the usual laboratory environment, different sources of entangled photons are feasible [44]. The design of the source used focused on stability, robustness, and compactness [45, 46]. This source is minimalistic in terms of built-in optical components and dimensions, but provides entangled photons of excellent purity and suitable brightness.

Energy-time entangled photons are generated via spontaneous parametric down-conversion (SPDC) in a collinear type II configuration. Next, both photons are coupled into one polarization-maintaining fiber in order to compensate for the mean longitudinal walk-off between the H and V polarized photons of a pair. Thereafter both photons are indistinguishable except for their orthogonal polarization. As we will see in the following chapters, polarization-entangled photon pairs or path-entangled NOON states can be generated from such states with little additional effort.

In the course of this chapter, the functionality and performance of the source used will be discussed.

4.1 Spontaneous Parametric Down-Conversion

A very practical and versatile way of creating entangled photons is spontaneous parametric down-conversion. To induce this effect, a nonlinear crystal is pumped by a strong coherent field. Due to the non-linear polarization response of the atoms in the crystal, the pump field is disturbed and modes with different angular frequency appear. The description of this process using classical optics states that such modification of the pump field only happens if a signal field is present in addition to the pump field [47]. This process is called parametric amplification because it transfers energy from the strong pump field into the weak signal field and creates a third idler field. However, quantum mechanics states that signal and idler fields can occur spontaneously, i.e. both fields are initially in their respective vacuum states [26]. So, for no apparent reason and at a random time, a photon of the pump mode decays into two photons. The time a photon pair occurs is basically unknown, but if one of the photons is detected at a given time, the detection time of the partner photon can be predicted. Such biphoton states are in a coherent superposition of possible emission times and therefore energy-time entangled [48, 49].

For the SPDC process to be efficient, several conditions must be met. These are discussed in more detail below.

4.1.1 Quasi-Phase-Matching

We distinguish between different types of SPDC according to the phase-matched polarizations of the involved fields. In type I phase matching the signal and idler photons have the same polarization. However, in the source used, the photons of a pair have orthogonal polarization, referred to as type II phase-matched SPDC. The arrangement can be chosen such that signal and idler fields are horizontally and vertically polarized and collinear with the pump beam. For the sake of simplicity, we also assume only one angular frequency ω_p in the pump field, which is a reasonable assumption in view of our narrow-linewidth pump laser.

Since SPDC is a coherent process, the non-linear polarization response from different regions of the crystal contributes to the resulting biphoton state [50]. An efficient downconversion process is achieved if the individual contributions interfere constructively. Phase difference between those contributions result from different refractive indices $n(\omega)$ experienced by the three interacting fields within the birefringent material. The conservation of energy

$$\omega_\mathrm{p} = \omega_\mathrm{H} + \omega_\mathrm{V} \tag{4.1}$$

is satisfied for various frequencies ω_H and ω_V of the horizontally polarized signal and vertically polarized idler fields. The crystal is chosen so that the phase mismatch $\Delta k = k_\mathrm{p}(\omega_\mathrm{p}) - k_\mathrm{H}(\omega_\mathrm{H}) - k_\mathrm{V}(\omega_\mathrm{V})$ of the propagation constants $k(\omega) = 2\pi n(\omega)/\lambda$ is zero for certain frequencies ($\omega_\mathrm{p} = 2\omega_0,\ \omega_\mathrm{H} = \omega_0,\ \omega_\mathrm{V} = \omega_0$). The phase-matching condition $\Delta k = 0$ is not satisfied if the angular frequencies deviate from these values ($\omega_\mathrm{H} = \omega_0 + \Omega, \omega_\mathrm{V} = \omega_0 - \Omega$). Consequently, the phase difference after propagation over a distance $L_\mathrm{coh} = \pi/\Delta k$ is equal to π and the contributions thus interfere destructively. Such frequencies are suppressed if the length of the crystal L is greater than L_coh.

In periodically poled crystals with a poling period Λ, the sign of the nonlinear polarization response is inverted periodically after a distance $L_\mathrm{coh} = \Lambda/2$. Consequently, a destructive interference that normally appears at such a propagation distance is converted into constructive interference [51]. Thus, for collinear SPDC in a periodically poled crystal, only frequency combinations with small effective wave vector mismatching $|\Delta k| < 2\pi/L$ with

$$\Delta k(\omega_\mathrm{H}, \omega_\mathrm{V}) = k_\mathrm{p}(\omega_\mathrm{H} + \omega_\mathrm{V}) - k_\mathrm{H}(\omega_\mathrm{H}) - k_\mathrm{V}(\omega_\mathrm{V}) - \frac{2\pi}{\Lambda} \tag{4.2}$$

significantly contribute to the downconverted field.

4.1.2 Joint Spectral Amplitude

The probability amplitude of generating a certain frequency combination of signal and idler fields via SPDC is given by the joint spectral amplitude (JSA) which is characteristic for the two-photon state. Thus, the analysis of the JSA reveals important properties of the emitted photon pair, such as the spectral bandwidth and the relative timing of the photons.

The biphoton part resulting from SPDC can be denoted by [26, 51, 52]

$$|\mathrm{SPDC}\rangle = \int \mathrm{d}\omega_1 \mathrm{d}\omega_2 \mathit{JSA}(\omega_1, \omega_2) \hat{a}^\dagger_\mathrm{H}(\omega_1) \hat{a}^\dagger_\mathrm{V}(\omega_2) \, |\mathrm{Vac}\rangle \tag{4.3}$$

with the joint spectral amplitude

$$\mathit{JSA}(\omega_1, \omega_2) \propto \alpha_p(\omega_1 + \omega_2) h(\omega_1, \omega_2) \tag{4.4}$$

$$h(\omega_1, \omega_2) = \mathrm{e}^{-\mathrm{i}\, L/2\, \Delta k(\omega_1, \omega_2)} \mathrm{sinc}\left(\frac{L}{2} \Delta k(\omega_1, \omega_2)\right) \tag{4.5}$$

and the creation operators $\hat{a}^\dagger_\mathrm{X}(\omega) \, |\mathrm{Vac}\rangle = |\omega\rangle_\mathrm{X}$ for the modes given by X, ω. The spectral amplitude of a narrow band pump field $\alpha_p(\omega)$ can be approximated by a delta distribution $\alpha_p(\omega) \approx \delta(\omega - \omega_\mathrm{p})$. Consequently, the biphoton part of the SPDC state simplifies to

$$|\mathrm{SPDC}\rangle_\mathrm{Narrow} = \zeta \int \mathrm{d}\omega_1 h(\omega_1, \omega_\mathrm{p} - \omega_1) \hat{a}^\dagger_\mathrm{H}(\omega_1) \hat{a}^\dagger_\mathrm{V}(\omega_\mathrm{p} - \omega_1) \, |\mathrm{Vac}\rangle \,, \tag{4.6}$$

with a normalization constant ζ. Since the narrow band pump field approximation applies very well to the source used, we will omit the label "Narrow" in the following. Equation 4.6 also assumes a plane wave pump field. The power spectral density $\mathit{PSD}(\omega)$ of the individual photons traced over the frequency of the respective partner photon can be calculated as

$$\begin{aligned} \mathit{PSD}_\mathrm{H}(\omega_\mathrm{H}) &= \int \mathrm{d}\omega' \, \langle\omega_\mathrm{H}|_\mathrm{H} \, \langle\omega'|_\mathrm{V} \, |\mathrm{SPDC}\rangle\langle\mathrm{SPDC}| \, |\omega'\rangle_\mathrm{V} \, |\omega_\mathrm{H}\rangle_\mathrm{H} \\ &\propto |h(\omega_\mathrm{H}, \omega_\mathrm{p} - \omega_\mathrm{H})|^2 = \mathrm{sinc}^2\left(\frac{L}{2} \Delta k(\omega_\mathrm{H}, \omega_\mathrm{p} - \omega_\mathrm{H})\right) \end{aligned} \tag{4.7a}$$

$$\begin{aligned} \mathit{PSD}_\mathrm{V}(\omega_\mathrm{V}) &= \int \mathrm{d}\omega' \, \langle\omega'|_\mathrm{H} \, \langle\omega_\mathrm{V}|_\mathrm{V} \, |\mathrm{SPDC}\rangle\langle\mathrm{SPDC}| \, |\omega_\mathrm{V}\rangle_\mathrm{V} \, |\omega'\rangle_\mathrm{H} \\ &= \mathit{PSD}_\mathrm{H}(\omega_\mathrm{p} - \omega_\mathrm{V}). \end{aligned} \tag{4.7b}$$

Those spectra have a global maximum at ω_H0 and $\omega_\mathrm{V0} = \omega_\mathrm{p} - \omega_\mathrm{H0}$, which is where the phase matching condition $\Delta k(\omega_\mathrm{H0}, \omega_\mathrm{p} - \omega_\mathrm{H0}) = 0$ is satisfied. Two separate spectral

bands with orthogonal polarization are observed if the difference $\omega_{\mathrm{H0}} - \omega_{\mathrm{V0}}$ is greater than the bandwidth of the SPDC photons $\Delta\omega_{\mathrm{bw}}$. Such states with $\omega_{\mathrm{H0}} \neq \omega_{\mathrm{V0}}$ are called non-degenerate. However, the spectra of the photons completely overlap if the state is degenerate ($\omega_0 = \omega_{\mathrm{H0}} = \omega_{\mathrm{V0}}$). Consequently, the polarization of the photons can no longer be predicted on the basis of the angular frequency, which is an indispensable prerequisite for the generation of polarization-entangled photons.

The joint power densities with the corresponding single-photon spectra are plotted in Figure 4.1 for the degenerate case (left) and the non-degenerate case (right).

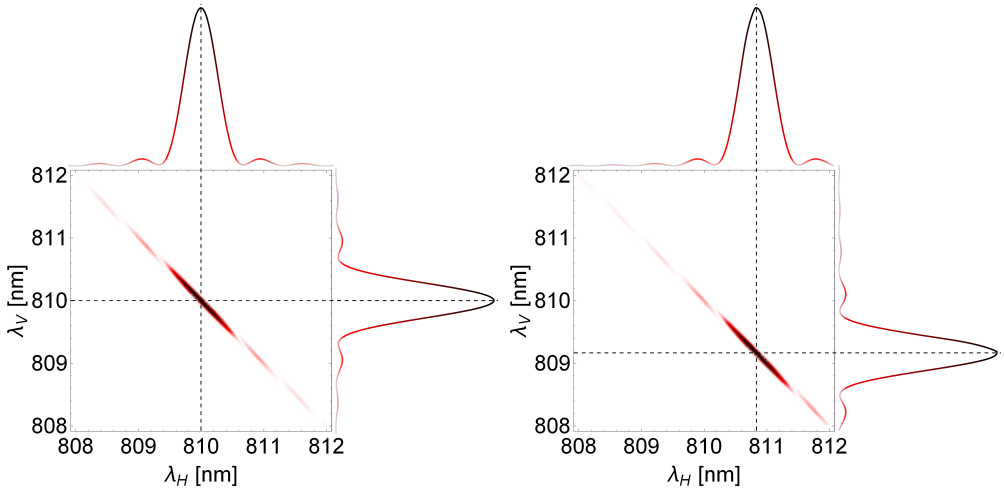


Figure 4.1 Joint power density $|JSA(\lambda_{\mathbf{H}}, \lambda_{\mathbf{V}})|^2$ for the degenerate case $\lambda_{\mathbf{H0}} = \lambda_{\mathbf{V0}}$ (left) and the non-degenerate case $\lambda_{\mathbf{H0}} \neq \lambda_{\mathbf{V0}}$ (right). The corresponding power spectral densities of the signal $PSD_{\mathrm{H}}(\lambda_{\mathrm{H}})$ and idler $PSD_{\mathrm{V}}(\lambda_{\mathrm{V}})$ fields are depicted outside the frame. The vacuum wavelength of the respective field is denoted by $\lambda_X(\omega) = 2\pi c/\omega_X$.

The bandwidth of the SPDC photons $\Delta\omega_{\mathrm{bw}}$ is determined by the FWHM of the squared sinc-function

$$\mathrm{sinc}^2\left(\frac{L}{2}\Delta k(\omega_0 + \frac{\Delta\omega_{\mathrm{bw}}}{2}, \omega_{\mathrm{p}} - \omega_0 - \frac{\Delta\omega_{\mathrm{bw}}}{2}\right) = \mathrm{sinc}^2(1.39) = 1/2 \tag{4.8}$$

and can be estimated using a Taylor series expansion of Δk around the point $\omega = \omega_0$

$$\begin{aligned}
\Delta k(\omega, \omega_{\mathrm{p}} - \omega) &= \Delta k(\omega_0 + \Delta\omega, \omega_{\mathrm{p}} - \omega_0 - \Delta\omega) \\
&= k_{\mathrm{p}}(\omega_{\mathrm{p}}) - k_{\mathrm{H}}(\omega_0 + \Delta\omega) - k_{\mathrm{V}}(\omega_0 - \Delta\omega) - \frac{2\pi}{\Lambda} \\
&\approx -\left(\mathrm{d}k_{\mathrm{H}}/\mathrm{d}\omega|_{\omega=\omega_0} - \mathrm{d}k_{\mathrm{V}}/\mathrm{d}\omega|_{\omega=\omega_0}\right)\Delta\omega \\
&\approx -D\Delta\omega = D(\omega_0 - \omega),
\end{aligned} \tag{4.9}$$

resulting in a bandwidth of $\Delta\omega_{\mathrm{bw}} = \frac{4\,1.39}{L|D|}$ or $\Delta\lambda_{\mathrm{bw}} \simeq \frac{2\pi c}{\omega_0^2}\frac{4\,1.39}{L|D|}$ where $D = \frac{1}{v_{\mathrm{H}}} - \frac{1}{v_{\mathrm{V}}}$ describes the difference of the inverse group velocities for the signal $1/v_{\mathrm{H}} = \mathrm{d}k_{\mathrm{H}}/\mathrm{d}\omega|_{\omega=\omega_0}$ and idler $1/v_{\mathrm{V}} = \mathrm{d}k_{\mathrm{V}}/\mathrm{d}\omega|_{\omega=\omega_0}$ waves.

4.1.3 Temporal Correlation

The orthogonally polarized photon-pair never leaves the birefringent crystal simultaneously. Thus, the polarization of the photons can be determined based on their relative timing. The indistinguishability of the photons, apart from their polarization is a prerequisite for most applications. With this in mind, we will examine the temporal behavior of the emitted photon pair in order to compensate its mean temporal walk-off.

The photons of a pair can be separated using a polarizing beam splitter. The relative timing of the photons $\Delta t = t_{\mathrm{H}} - t_{\mathrm{V}}$ could be measured by placing two detectors equidistant to the exit surface of the crystal ($x_{\mathrm{H}} = x_{\mathrm{V}} = x$). The probability of detecting a signal photon at time t_{H} if an idler photon was detected at time t_{V} is proportional to the intensity correlation function [53]

$$G^{(2)}_{\mathrm{SPDC}}(t_{\mathrm{H}}, t_{\mathrm{V}}) = \langle \mathrm{SPDC}|\, \widehat{E}^{\dagger}_{\mathrm{H}}(x, t_{\mathrm{H}})\widehat{E}^{\dagger}_{\mathrm{V}}(x, t_{\mathrm{V}})\widehat{E}_{\mathrm{V}}(x, t_{\mathrm{V}})\widehat{E}_{\mathrm{H}}(x, t_{\mathrm{H}})\,|\mathrm{SPDC}\rangle \tag{4.10}$$

where

$$\widehat{E}_m(x,t) = \frac{1}{\sqrt{2\pi}}\int \mathrm{e}^{-\mathbb{i}\omega_m(t-x/c)}\widehat{a}_m(\omega_m)\,\mathrm{d}\omega_m \tag{4.11}$$

is the positive frequency part of the electric field operator $\widehat{E}_m(x,t) + \widehat{E}^{\dagger}_m(x,t)$. In the calculation of $G^{(2)}_{\mathrm{SPDC}}$ we follow [26] and calculate first

$$\begin{aligned}
&\widehat{E}_{\mathrm{V}}(x_{\mathrm{V}}, t_{\mathrm{V}})\widehat{E}_{\mathrm{H}}(x_{\mathrm{H}}, t_{\mathrm{H}})\,|\mathrm{SPDC}\rangle \\
&\quad= \frac{\zeta}{2\pi}\int h(\omega, \omega_{\mathrm{p}}-\omega)\mathrm{e}^{-\mathbb{i}\omega(t_{\mathrm{H}}-x_{\mathrm{H}}/c)}\mathrm{e}^{-\mathbb{i}(\omega_{\mathrm{p}}-\omega)(t_{\mathrm{V}}-x_{\mathrm{V}}/c)}\mathrm{d}\omega\,|\mathrm{Vac}\rangle \\
&\quad= \frac{\zeta}{2\pi}\mathrm{e}^{-\mathbb{i}\omega_{\mathrm{p}}(t_{\mathrm{V}}-x_{\mathrm{V}}/c)}\int h(\omega, \omega_{\mathrm{p}}-\omega)\mathrm{e}^{-\mathbb{i}\omega(\Delta t-\Delta x/c)}\mathrm{d}\omega\,|\mathrm{Vac}\rangle \\
&\quad= \frac{\zeta}{2\pi}\mathrm{e}^{-\mathbb{i}\omega_0(2t_{\mathrm{V}}-2x_{\mathrm{V}}/c+\frac{L\,D}{2})}\int \mathrm{sinc}\left(\frac{L}{2}D(\omega_0-\omega)\right)\mathrm{e}^{-\mathbb{i}\omega(\Delta t-\Delta x/c-\frac{L\,D}{2})}\mathrm{d}\omega\,|\mathrm{Vac}\rangle \\
&\quad= \frac{\zeta}{L\,D}\mathrm{e}^{-\mathbb{i}\omega_0(2t_{\mathrm{V}}-2x_{\mathrm{V}}/c+\frac{L\,D}{2})}\mathrm{e}^{-\mathbb{i}\omega_0(\Delta t-\Delta x/c-\frac{L\,D}{2})}\Pi\left(\frac{\Delta t-\Delta x/c-\frac{L\,D}{2}}{L\,D}\right)|\mathrm{Vac}\rangle \\
&\quad= \frac{\zeta}{L\,D}\mathrm{e}^{-\mathbb{i}\omega_0(t_{\mathrm{H}}+t_{\mathrm{V}}+(x_{\mathrm{H}}+x_{\mathrm{V}})/c)}\Pi\left(\frac{\Delta t}{L\,D}-\frac{\Delta x}{L\,D\,c}-\frac{1}{2}\right)|\mathrm{Vac}\rangle
\end{aligned} \tag{4.12}$$

where we have used Equations 4.6, 4.5, 4.9, the commutation relation 2.54 and

$$\int \mathrm{sinc}(C_1 + C_2\,\omega)\,\mathrm{e}^{-\mathbb{i}\omega t}\mathrm{d}\omega = \frac{\pi}{|C_2|}\Pi\left(-\frac{t}{2C_2}\right)e^{\mathbb{i}\frac{C_1}{C_2}t} \tag{4.13}$$

with rectangular function

$$\Pi(X) = \begin{cases} 1 & \text{if } -\frac{1}{2} < X < \frac{1}{2} \\ 0 & \text{otherwise.} \end{cases} \tag{4.14}$$

From Equations 4.12 and 4.10, we find the $G^{(2)}_{\mathrm{SPDC}}$-function:

$$G^{(2)}_{\mathrm{SPDC}}(t_{\mathrm{H}}, t_{\mathrm{V}}) \propto \Pi\left(\frac{\Delta t}{L\,D} - \frac{1}{2}\right). \tag{4.15}$$

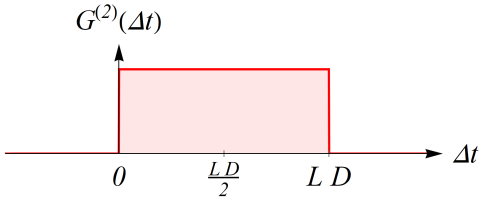


Figure 4.2 Second-order correlation function $G^{(2)}$ of signal and idler photons from SPDC vs. relative timing of the photons Δt. The maximal temporal delay acquired in the ppKTP is given by the crystal lengths L and the difference of the inverse group velocities D.

The intensity correlation function is zero for $\Delta t = t_{\mathrm{H}} - t_{\mathrm{V}} < 0$*. Consequently, we know that the V photon always reaches its detector first. This results from the different group velocity of the H and V polarized photons in the birefringent crystal. If the two photons are generated at the very beginning of the crystal, then the time difference of the emerging photons is given by $\Delta t = L\,D$. This difference would be zero if the two photons are generated shortly before leaving the crystal. But the H photon can never reach the detector first. Consequently, the polarization of the photons can be determined based on their time of arrival. In order to make the photons indistinguishable in terms of their arrival time, the mean time delay or temporal walk-off between the photons

$$\tau_{\mathrm{off}} = \frac{LD}{2}. \tag{4.16}$$

must be compensated. This is accomplished by placing an additional birefringent crystal behind the SPDC crystal so that the fast axis of the material coincides with the slow axis of the SPDC crystal. Such a compensation crystal delays the signal photon relative to the idler photon by τ. A perfect temporal overlap of the photons is achieved if the additional delay cancels the mean time delay of the photons [52]. The biphoton state after walk-off compensation can be denoted by

$$|\Pi_{\Delta\tau}\rangle = \zeta \int \mathrm{d}\omega\; h(\omega, \omega_{\mathrm{p}} - \omega) \mathrm{e}^{-\mathrm{i}\omega\tau} \hat{a}^{\dagger}_{\mathrm{H}}(\omega) \hat{a}^{\dagger}_{\mathrm{V}}(\omega_{\mathrm{p}} - \omega)\, |\mathrm{Vac}\rangle\,, \tag{4.17}$$

*if $D = \frac{1}{v_{\mathrm{H}}} - \frac{1}{v_{\mathrm{V}}}$ has a positive value

with $\tau = \frac{LD}{2} + \Delta\tau$. The parameter $\Delta\tau$ results from either insufficient walk-off compensation or a deliberately introduced delay between signal and idler photons. With perfect walk-off compensation ($\Delta\tau = 0$), the $G^{(2)}$-function is centered around $\Delta t = 0$, and the photons are indistinguishable in terms of arrival time.

$$G^{(2)}(t_\mathrm{H}, t_\mathrm{V}) \propto \Pi\left(\frac{\Delta t + \tau}{L\,D} - \frac{1}{2}\right) = \Pi\left(\frac{\Delta t}{L\,D}\right). \tag{4.18}$$

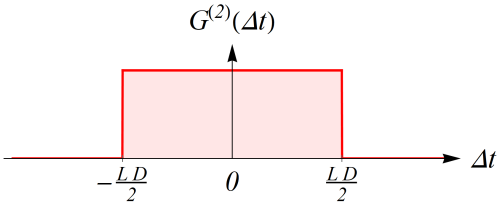


Figure 4.3 Second-order correlation function $G^{(2)}$ of signal and idler photons after walk-off compensation vs. relative timing of the photons Δt. The full width at half maximum of $G^{(2)}$ is given by the crystal lengths L and the difference of the inverse group velocities D.

4.2 Experimental Setup

A continuous-wave pump laser with a wavelength of $\lambda_\mathrm{p} = 405\,\mathrm{nm}$ is focused loosely into a periodically poled potassium titanyl phosphate (ppKTP) crystal. Signal and idler photons with horizontal and vertical polarization are generated via SPDC in a collinear type II configuration. The quasi-phase matching condition is satisfied for wavelength-degenerate photon pairs at a central wavelength of 810 nm. Two dichroic mirrors are used to divert the pump beam from the signal and idler photons which are subsequently coupled into a sole polarization maintaining single-mode optical fiber (PMF). The length of the PMF and an additional neodymium-doped yttrium orthovanadate (Nd:YVO_4) crystal are chosen to compensate for the temporal walk-off between the signal and the idler photons.

4.2.1 Pump Laser

The pump laser used is an Ondax diode laser (LM-405-40) with a central wavelength of $\lambda_\mathrm{p} = 405\,\mathrm{nm}$ and a nominal power of 40 mW. The actual output power was remotely controlled from a computer and set to 27.5 mW (diode current 60 mA) for most experiments. The manufacturer specifies a spectral line width of $\lambda_\mathrm{FWHM} = 0.08748\,\mathrm{pm}$, which is achieved by internal wavelength stabilization via volume holographic grating. Such a bandwidth corresponds to a coherence length of $l_{405} = \sqrt{\frac{2\log(2)}{\pi}}\frac{\lambda^2}{\Delta\lambda_\mathrm{FWHM}} = 1.25\,\mathrm{m}$ and a coherence time of $t_{405} = l_{405}/c = 4.15\,\mathrm{ns}$ [†].

[†] $\pm l_{405}$ will reduce the interferometric fringe visibility to 50%

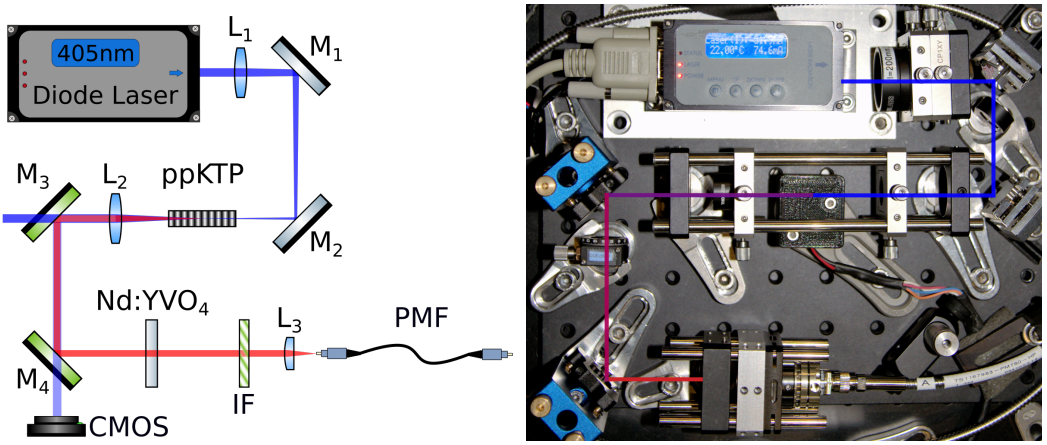


Figure 4.4 Sketch of the source: A continuous-wave pump laser with a wavelength of $\lambda_p = 405\,\text{nm}$ is focused loosely ($f_1 = 15\,\text{cm}$) into a ppKTP crystal, generating photon pairs which are subsequently coupled ($f_2 = 4\,\text{cm}$, $f_3 = 31\,\text{mm}$) into a sole polarization maintaining single-mode optical fiber (PMF) with numerical aperture $NA = 0.12\,\text{rad}$. An additional Nd:YVO_4 crystal is used to fine-tune the walk-off compensation. To prevent stray light, an interference filter (IF) was installed in front of the coupler.

The transverse mode of the laser beam is approximately Gaussian but with an elliptical cross section. Along the x axis a waist of $w_{405x} = 297\,\mu\text{m}$ ($\Delta x_{\text{FWHM}} = 350\,\mu\text{m}$) and along the y axis a waist of $w_{405y} = 240\,\mu\text{m}$ ($\Delta y_{\text{FWHM}} = 282\,\mu\text{m}$) were measured.

This beam is focused into the SPDC crystal with the lens L_1 of focal length $f_1 = 15\,\text{cm}$, which creates a waist of $w_{x0} = \frac{f_1 \lambda}{\pi w_{405x}} = 65\,\mu\text{m}$ and $w_{y0} = 80\,\mu\text{m}$ in the focal plane [54]. These waists correspond to a Rayleigh range (in vacuum $n = 1$) of $z_x = 3.2\,\text{cm}$ and $z_y = 5\,\text{cm}$. Consequently, the longitudinal alignment of the crystal along the beam is not very critical.

4.2.2 Crystal

The crystal is a periodically poled potassium titanyl phosphate crystal (ppKTP) manufactured (flux grown) by Raicol Crystals with a length of $L = 10\,\text{mm}$, a poling period of $\Lambda \sim 10\,\mu\text{m}$, and a rectangular cross section measuring $1\,\text{mm} \times 2\,\text{mm}$. It is mounted on an aluminum block, which is heated by a Peltier element. In addition, there is a temperature sensor in the aluminum socket, which is connected to a PID controller together with the Peltier element. With this system, the crystal temperature can be stabilized to a temperature range of $\pm 0.01\,°\text{C}$.

The pump laser (p) traverses the crystal along its x-axis with a polarization along the y-direction, producing signal (s) and idler (i) photons that are polarized along the y- and z-directions (horizontally and vertically), respectively. Potassium titanyl phosphate (KTP or $KTiOPO_4$) is an optically anisotropic crystal. Its wavelength-

dependent refractive indices (n_x, n_y, n_z) can be determined by the Sellmeier equation 4.19, and the associated coefficients measured by Fan *et al.* and Fradkin *et al.* (see Table 4.1) [55, 56].

$$n_{j0}(\lambda) = \sqrt{A_j + \frac{B_j}{1 - \frac{C_j}{(\lambda \times 10^6)^2}} + \frac{D_j}{1 - \frac{E_j}{(\lambda \times 10^6)^2}} - F_j\,(\lambda \times 10^6)^2} \tag{4.19}$$

	A_j	B_j	C_j	D_j	E_j	F_j
$j = x$	2.16747	0.83733	0.04611	0	0	0.01713
$j = y$	2.19229	0.83547	0.04970	0	0	0.01621
$j = z$	2.12725	1.18431	0.0514852	0.6603	100.00507	9.68956×10^{-3}

Table 4.1 Sellmeier equation coefficients for KTP [55].

Note that, $\lambda = 2\pi c/\omega$ describes the vacuum wavelength. The temperature dependence of these refractive indices has been studied by Emanueli and Arie [57]. For degenerate down-conversion with a pump wavelength of $\lambda_\mathrm{p} = \lambda_0/2$ ($\lambda_\mathrm{s} = \lambda_\mathrm{i} = \lambda_0 = 810\,\mathrm{nm}$), those results can be simplified to Equation 4.20 with the parameters from Table 4.2.

$$n_\mathrm{p}(\lambda, T) = n_{y0}(\lambda) + a_\mathrm{p}\ 10^{-8}(T - 25) + b_\mathrm{p}\ 10^{-6}(T - 25)^2 \tag{4.20a}$$
$$n_\mathrm{s}(\lambda, T) = n_{y0}(\lambda) + a_\mathrm{s}\ 10^{-8}(T - 25) + b_\mathrm{s}\ 10^{-6}(T - 25)^2 \tag{4.20b}$$
$$n_\mathrm{i}(\lambda, T) = n_{z0}(\lambda) + a_\mathrm{i}\ 10^{-8}(T - 25) + b_\mathrm{i}\ 10^{-6}(T - 25)^2 \tag{4.20c}$$

	p	s	i
a	24.7675	9.8180	16.2689
b	3.8172	-0.3156	2.6904

Table 4.2 Coefficients for a temperature-dependent description of the refractive indices in Equation 4.20

Where the variable T describes the temperature of the crystal in °C. Using those equations, the condition for degenerate down-conversion can be estimated via

$$\begin{aligned}\Delta k(\omega_0,\omega_0) &= k_\mathrm{p}(2\omega_0) - k_\mathrm{s}(\omega_0) - k_\mathrm{i}(\omega_0) - \frac{2\pi}{\Lambda} = 0 \\ &= \frac{2\pi\ n_\mathrm{p}(\lambda_0/2,T)}{\lambda_0/2} - \frac{2\pi\ n_\mathrm{s}(\lambda_0,T)}{\lambda_0} - \frac{2\pi\ n_\mathrm{i}(\lambda_0,T)}{\lambda_0} - \frac{2\pi}{\Lambda} \\ &\vdots \\ 0 &= 2\ n_\mathrm{p}(\lambda_0/2,T) - n_\mathrm{s}(\lambda_0,T) - n_\mathrm{i}(\lambda_0,T) - \frac{\lambda_0}{\Lambda}. \end{aligned} \tag{4.21}$$

The above condition is satisfied at a temperature T=44.87 °C, assuming a poling period of $\Lambda = 10\,\mu$m. The poling period and refractive indices change when the crystal is tilted. Therefore, the temperature at which a degenerate down conversion is achieved depends on the alignment of the source. We found the degenerate state experimentally at a temperature of T_0 =37.15 °C (see Figure 4.9). This can be explained by a slightly longer poling period $\Lambda_\mathrm{eff} = 10.023\,\mu$m[‡], which may result from manufacturing tolerances or a small tilt of the pump beam $\alpha_\mathrm{tilt} \sim 2°$. However, when the laser was switched on and off, variations of T_0 in the range of $\pm 1°C$ were observed, but during operation, the performance of the source was stable at a constant temperature. Presumably, these variations result from small changes of the pump wavelength and could be avoided with an optical isolator placed between the laser and L1. The thermal expansion of KTP along its x-axis is given by [57]

$$L(L_0,T) = L_0\ (1 + 6.7\times10^{-6}\ (T-25) + 11\times10^{-9}\ (T-25)^2) \tag{4.22}$$

and causes the poling period to change with temperature. Considering the expansion of the crystal, degenerate down-conversion is expected at a temperature of T=44.44 °C ($\Lambda_{44.44°C} = 10.0013\,\mu$m). Such a small change of the poling period can be neglected compared to deviations caused by manufacturing and alignment tolerances.

We use the effective poling period $\Lambda_\mathrm{eff} = 10.023\,\mu$m and the temperature T_0 =37.15 °C for all subsequent calculations. For parameter estimates or fitting functions, it may be helpful to approximate the wave vector mismatch $\Delta k(\omega_\mathrm{H}, \omega_\mathrm{p} - \omega_\mathrm{H}; T)$ by its partial derivatives at the point of degenerate down conversion

$$D = -\left.\frac{\mathrm{d}\Delta k}{\mathrm{d}\omega_\mathrm{H}}\right|_{\omega_\mathrm{H}=\omega_0,\omega_\mathrm{p}=2\omega_0,T=T_0} = \frac{1}{v_\mathrm{H}} - \frac{1}{v_\mathrm{V}} = -349.71\ 10^{-12} \tag{4.23}$$

$$D_T = \left.\frac{\mathrm{d}\Delta k}{\mathrm{d}T}\right|_{\omega_\mathrm{H}=\omega_0,\omega_\mathrm{p}=2\omega_0,T=T_0} = 196.17 \tag{4.24}$$

$$D_{\omega_\mathrm{p}} = \left.\frac{\mathrm{d}\Delta k}{\mathrm{d}\omega_\mathrm{p}}\right|_{\omega_\mathrm{H}=\omega_0,\omega_\mathrm{p}=2\omega_0,T=T_0} = 722.24\ 10^{-12} \tag{4.25}$$

[‡]$KTiOPO_4$ has a lattice parameter of ~ 1 nm, so this deviation corresponds to 23 crystallographic layers.

$$\Delta k(\omega_{\mathrm{H}}, \omega_{\mathrm{p}} - \omega_{\mathrm{H}}, T) \approx -D(\omega_{\mathrm{H}} - \omega_0) + D_T(T - T_0) + D_{\omega_{\mathrm{p}}}(\omega_{\mathrm{p}} - 2\omega_0) \tag{4.26}$$

A deviation of the pump wavelength of 0.1 nm from 405 nm corresponds to a temperature change of the crystal by 4.22 °C.

4.2.3 Fiber Coupling and Walk-off Compensation

The light leaving the crystal is collimated by lens L_2 with a focal length of $f_2 = 4\,\mathrm{cm}$. Subsequently, the downconverted photons are branched off from the pump beam by means of two dichroic mirrors. Behind the second of the two mirrors, a CMOS camera was installed to monitor the position of the pump beam. A laser beam coupler (Schäfter+Kirchhoff 60SMS-1-0-A3.1-02) with a focal length of $f_3 = 3.1\,\mathrm{mm}$ is used to thread the photons into a polarization maintaining single-mode optical fiber (PM780-HP) with a numerical aperture of $NA = 0.12\,\mathrm{rad}$[§] (mode field diameter $MFD = 5.3\,\mu\mathrm{m}$ @ 850 nm). This results in a collection waist in the center of the crystal of $34\,\mu\mathrm{m}$. An additional interference filter (Semrock LL01-810) was placed in front of the coupler to minimize stray light within the fiber.

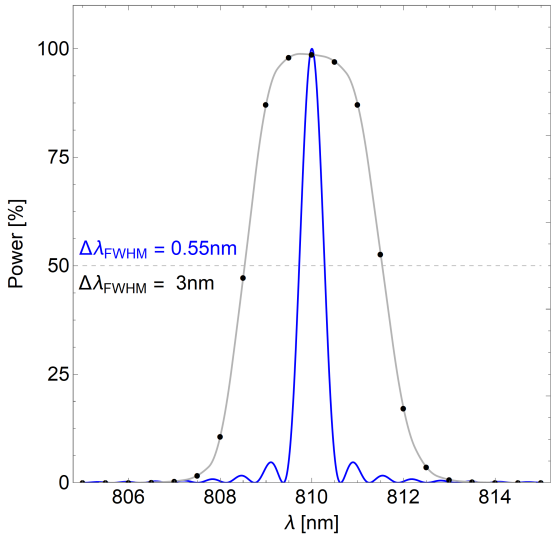


Figure 4.5 Transmission of the integrated interference filter (Semrock LL01-810). The polynomial interpolation (black line) of the measured transmission (black dots) has a full width half maximum of $\Delta\lambda_{\mathrm{FWHM}} = 3\,\mathrm{nm}$. In comparison, the expected spectrum of the down conversion (see Equations 4.7 and 4.26) with much smaller FWHM ($\Delta\lambda_{\mathrm{FWHM}} = 0.55\,\mathrm{nm}$) is plotted in blue.

In the PMF, two orthogonal polarization modes, one polarized along the fast axis and one along the slow axis, can propagate with very little cross talk ($< -40\,\mathrm{dB}$ @ 4m). When light is coupled into one of these modes, its polarization is maintained as it

[§]The numerical aperture $NA = 1.224\frac{\lambda}{\pi MFD/2}$ of a fiber is often measured as half-angle divergence of the 5% intensity level of the emerging light. The 5% radius of the emerging light cone is thus $r_{5\%}(z) = z\ NA$ at a distance z from the fiber. The waist $w(z)$ of a Gaussian beam is defined as the radius at which the intensity has dropped to $1/\mathrm{e}^2 = 13.5\%$. Therefore, $r_{5\%}$ is larger than the waist $r_{5\%}(z) = 1.224\ w(z)$.

passes through the fiber. However, to be able to use this feature, one must be careful when coupling so that the polarization of the light matches with one of the modes of the fiber.

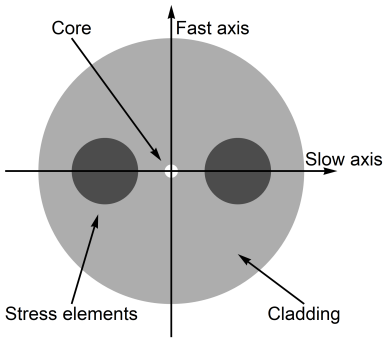


Figure 4.6 Cross-section of a PMF. This fiber type is often referred to as polarization maintaining and absorption reducing (PANDA) fiber. The stress elements create mechanical stress on the core, causing stress-induced birefringence $\Delta n_{\mathrm{PMF}} = n_{\mathrm{slow}} - n_{\mathrm{fast}}$.

According to the data sheet, the PMF used has a nominal birefringence of $\Delta n_{\mathrm{PMF}} = n_{\mathrm{slow}} - n_{\mathrm{fast}} = 3.5\ 10^{-4}$. With a fiber length of $L_{\mathrm{PMF}} = 1.3\,\mathrm{m}$, a temporal delay between the two modes of

$$\tau_{\mathrm{PMF}} \simeq \frac{L_{\mathrm{PMF}} \Delta n_{\mathrm{PMF}}}{c} = 1.52\,\mathrm{ps} \tag{4.27}$$

is expected. The temporal walk-off generated in the ppKTP crystal can be calculated with the length $L = 1\,\mathrm{cm}$ and the difference of the inverse group velocities $D = -0.35\ 10^{-9}$

$$\tau_{\mathrm{off}} = \frac{LD}{2} = -1.75\,\mathrm{ps}. \tag{4.28}$$

Thus, the PMF compensates most of the walk-off between the horizontally polarized signal and the vertically polarized idler photon. Due to the manufacturing tolerances of the fiber, an exact compensation would be possible with an iterative measurement and cutting process. However, to make the source as indestructible as possible, a fixed-length PMF with a metal jacket was used.

The remaining temporal difference of the photons was compensated with neodymium doped yttrium orthovanadate Nd:YVO_4 plates placed between the fiber coupling and the ppKTP. Based on the measurements of Zelmon *et al.* [58], the difference of the inverse group velocities of the ordinary and extraordinary ray in a Nd:YVO_4 crystal at room temperature ($T = 23\,^{\circ}\mathrm{C}$) and a wavelength of 810 nm results in $D_{\mathrm{YVO}} = 8.03\ 10^{-12}$. Thus, using a Nd:$YVO_4$ crystal with a length of $L_{\mathrm{YVO}} = 0.3\,\mathrm{mm}$ results in a temporal delay of

$$\tau_{\mathrm{YVO}} = L_{\mathrm{YVO}} D_{\mathrm{YVO}} = 0.24\,\mathrm{ps}, \tag{4.29}$$

which finally compensates for the walk-off between the signal and idler photons.

The thickness of the Nd:YVO_4 plates has a manufacturing tolerance of $\pm 30\,\mu$m. In order to achieve the best possible compensation, different plates were tested.

4.2.4 Alignment

Before starting the realignment of the source, the crystal temperature should be checked. The temperature at which the generated photons are transmitted by the interference filter cannot be missed if the crystal temperature is increased or decreased in increments of 2 °C. If no photons can be detected at the output of the PMF, the source must be realigned. This procedure works as follows:

1) Connect an alignment laser to the output of the PMF. If the interference filter in front of the coupler is not removed, a laser with a wavelength of $\lambda = 810\,\text{nm} \pm 1\,\text{nm}$ has to be used.

2) Adjust the mirror M_3 such that the light from the alignment laser passes through the crystal.

3) A short focal length lens ($f \sim 5\,\text{cm}$) can be inserted between the laser and L_1. The diverging light is used to illuminate the crystal. By adjusting the camera lens, the crystal can be imaged on the CMOS sensor. The center of the crystal must be marked on the monitor (water-soluble whiteboard marker) or in the software. After that, the inserted lens can be replaced by a pinhole.

4) The pump laser should be visible as a point on the camera if the exposure time is set correctly. Use the first mirror M_1 and aim the laser at the marked spot.

5) Due to the back reflection of the crystal surface, a spot should be visible on the back of the pinhole. With the second mirror M_2, this spot is set to the center of the pinhole.

6) Repeat the last two steps until both spots are in the correct position.

7) By adjusting the coupler, the light from the alignment laser can be directed to the center of the pinhole. Then the pinhole has to be removed.

After this procedure, photons should already be detected when the alignment laser is replaced with a single photon counter. The photon count rate can be maximized by adjusting M_3 and the coupler. M_4 is not needed for the alignment, and its holder has been replaced with a fixed mount.

4.3 Performance

4.3.1 Brightness and Heralding Efficiency

Photon pairs emerging from the PMF are separated by means of a PBS and subsequently detected. At a pump power 27.5 mW, we measured a total coincidence count rate of $R_c = 191\,\text{kcps}$, of which about $R_{\text{Acc}} = 3\,\text{kcps}$ were accidental coincidences. For each polarization, a detection event rate of $R_{\text{H}} \simeq R_{\text{V}} \simeq 951\,\text{kcps}$ was recorded. Both count rates where measured with a photon detection efficiency of $\eta_{\text{D}} = 0.64$ (data sheet of the manufacturer).

The probability that a detected photon has a partner, i.e. is accompanied by a detection event of the second detector, is referred to as heralding efficiency η_{h}, which can be calculated by the coincidence-to-singles ratio

$$\eta_{\text{h}} = \frac{(R_c - R_{\text{Acc}})}{R_{\text{H}}} = 0.20 \tag{4.30}$$

The singles count rates $R_{\text{H}} \simeq R_{\text{V}} \propto \eta_{\text{D}}\eta_{\text{A}}\eta_{\text{C}}$, coincidence count rates $R_c \propto \eta_{\text{D}}^2\eta_{\text{A}}^2\eta_{\text{C}}^2$, and thus also the heralding efficiency $\eta_{\text{h}} = \eta_{\text{D}}\eta_{\text{A}}\eta_{\text{C}}$, depend on the detection efficiency η_{D}, the transmission probability trough the analyzer η_{A}, and the coupling efficiency of downconverted photons into the PMF η_{C}. If the loss in the analyzer is neglected, the coupling efficiency of the source results in

$$\eta_{\text{C}} = \frac{\eta_{\text{h}}}{\eta_{\text{D}}} = 0.31 \tag{4.31}$$

4.3.2 Spectrum

The PMF can be connected directly to a single-photon spectrometer (Ocean Optics QE65000). When adjusting the crystal temperature, a shift in the spectrum is observed. A measurement (density plot Figure 4.7 left) shows that the spectra of the photons change with $\pm$ 0.20 nm/°C, which agrees very well with the value of $\pm$ 0.19 nm/°C determined from Equation 4.26 (yellow dashed line in Figure 4.7 left).

The spectra of the signal and idler photons overlap at a crystal temperature of about 37.4 °C. The spectrum measured at this temperature is plotted in Figure 4.7 (right) along with the spectrum predicted by Equations 4.7 and 4.26. The FWHM of the measurement is $\lambda_{\text{FWM}} = 0.76\,\text{nm}$ which is wider than the theoretically predicted value of $\lambda_{\text{FWM}} = 0.55\,\text{nm}$. The difference mainly results from the limited resolution of the spectrometer, which is specified by the manufacturer as 0.31 nm (FWHM).

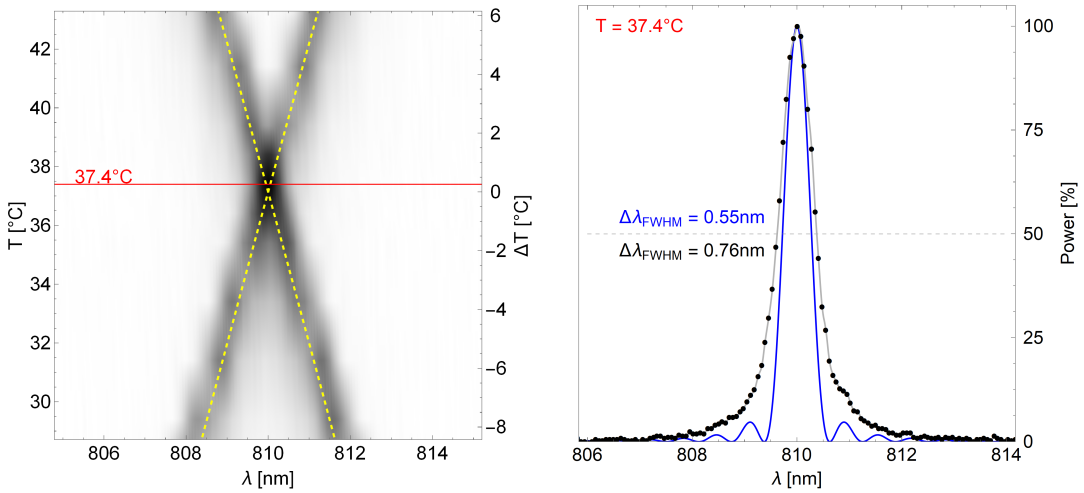


Figure 4.7 Left: measured power spectral density vs. crystal temperature T**.** The spectra of signal and idler photons overlap at a crystal temperature of about 37.4 °C. The yellow dashed line indicates the predicted central wavelengths (see Equation 4.26). This measurement was performed without the IF. **Right: Measured power spectral density at a crystal temperature of 37.4 °C.** The polynomial interpolation (black line) of the measurements (black dots) has a full width half maximum of $\Delta\lambda_{\mathrm{FWHM}} = 0.76\,\mathrm{nm}$. In comparison, the expected spectrum of the down conversion (see Equations 4.7 and 4.26) with a FWHM of $\Delta\lambda_{\mathrm{FWHM}} = 0.55\,\mathrm{nm}$ is plotted in blue.

4.3.3 Two-Photon Interference

Ideally, the photons generated by the source are orthogonally polarized but indistinguishable in all their other properties. The visibility of a two-photon interference experiment is a good measure of the indistinguishability of the photons involved. Such an experiment is performed by means of a HWP, followed by a PBS with single-photon detectors in each output mode (see Figure 4.8).

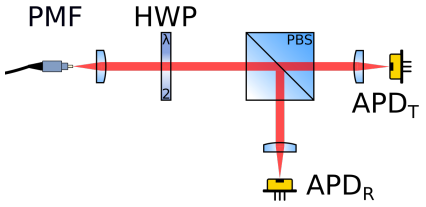


Figure 4.8 Arrangement of the detection module, as used to measure the temperature dependence of the HOM dip visibility. The HWP is rotated by an angle $\beta = \frac{\pi}{8}$, resulting in photon bunching at the PBS. The photons are detected in both outputs of the PBS by means of avalanche photodiodes (APD).

If the HWP is in a neutral position $\beta = 0$, the photons of a pair are split at the PBS. This leads to coincident events at the detectors with a coincidence count rate of $R_c(0)$. However, such setup mixes horizontal and vertical polarization modes if the half-wave plate is rotated by an angle $\beta = \frac{\pi}{8}$. Consequently, both photons bunch into the same output mode due to the Hong–Ou–Mandel effect. So if the two photons are

absolutely indistinguishable, no coincidences can be detected $R_{\min} = R_c(\frac{\pi}{8}) = 0$. But with distinguishable photons e.g., based on their wavelength, no interference occurs, resulting in a random splitting of the individual photons. In this case, 50% of the pairs will end up in the same output mode, and 50% will be split between the output modes. Therefore, a coincidence count rate of $R_{\max} = R_c(0)/2$ is expected. The visibility of such a Hong–Ou–Mandel dip is given by

$$\mathcal{V}_{\mathrm{HOM}} = \frac{R_{\max} - R_{\min}}{R_{\max}}, \tag{4.32}$$

which results in one only if the involved photons are absolutely indistinguishable ($R_{\min} = 0$). The probability of detecting a photon pair emitted by the source is proportional to the two-photon correlation function $G^{(2)}_{\mathrm{HOM}}$ integrated over the range of the detectors resolving time. For the detectors used, the resolving time is of the order of 1 ns and is thus much larger than $L\ D = 3.5\,\mathrm{ps}$. Consequently, we can extend the range of the integral to $\pm\infty$ in good approximation

$$\begin{aligned} P_c &\propto \int_{-\infty}^{\infty}\int_{-\infty}^{\infty} \mathrm{d}t_1\mathrm{d}t_2 G^{(2)}_{\mathrm{HOM}}(t_1,t_2) \\ &\propto \int_{-\infty}^{\infty}\int_{-\infty}^{\infty} \mathrm{d}t_1\mathrm{d}t_2 \left\langle \mathrm{II}_{\Delta\tau}\right| \widehat{E}^{\dagger}_{\mathrm{T}}(t_1)\widehat{E}^{\dagger}_{\mathrm{R}}(t_2)\widehat{E}_{\mathrm{R}}(t_2)\widehat{E}_{\mathrm{T}}(t_1) \left|\mathrm{II}_{\Delta\tau}\right\rangle , \end{aligned} \tag{4.33}$$

$$\widehat{E}_{\mathrm{T}}(t) = \cos(2\beta)\ \widehat{E}_{\mathrm{H}}(x,t) + \sin(2\beta)\ \widehat{E}_{\mathrm{V}}(x,t) \tag{4.34}$$

$$\widehat{E}_{\mathrm{R}}(t) = \cos(2\beta)\ \widehat{E}_{\mathrm{V}}(x,t) - \sin(2\beta)\ \widehat{E}_{\mathrm{H}}(x,t) \tag{4.35}$$

where $\widehat{E}^{\dagger}_{\mathrm{T}}(t)$ and $\widehat{E}^{\dagger}_{\mathrm{R}}(t)$ denote the field operators in the transmitted and reflected output mode of the PBS, respectively. The biphoton state $|\mathrm{II}_{\Delta\tau}\rangle$ and the operators $\widehat{E}_{\mathrm{H}}/\widehat{E}_{\mathrm{V}}$ are defined in Equations 4.17 and 4.11, respectively. The general solution of Equation 4.33 can be found in Appendix A (see Equation A.15). In the case of $\omega_{\mathrm{p}} = 2\omega_0$, $\beta = \frac{\pi}{8}$ and $\Delta\tau = 0$, the coincidence probability results in

$$P_c(T) \simeq \frac{1}{2}\left(1 - \mathrm{sinc}(LD_T(T - T_0))\right), \tag{4.36}$$

which leads to a temperature-dependent visibility of

$$\mathcal{V}_{\mathrm{HOM}}(T) = \mathcal{V}_0 \frac{\frac{1}{2} - P_c(T)}{\frac{1}{2}} = \mathcal{V}_0\ \mathrm{sinc}(LD_T(T - T_0)), \tag{4.37}$$

where L is the length of the crystal and D_T is defined in Equation 4.25. The parameter $\mathcal{V}_0$ takes into account that even with a perfectly stabilized crystal temperature the visibility is less than unity, e.g., resulting from accidental coincidences, polarization mismatch, the extinction ratio of the PBS, or insufficient walk-off compensation. Figure

4.9 shows the measured visibility as a function of the crystal temperature. The data is fitted with a function as in Equation 4.37. From the fitted function we find a temperature $T_0 = 37.150\,°\mathrm{C} \pm 0.003\,°\mathrm{C}$ and a visibility of $\mathcal{V}_0 = 97.54 \pm 0.09$. Furthermore, this measurement shows that a temperature variation of $\pm 0.1\,°\mathrm{C}/\pm 0.01\,°\mathrm{C}$ corresponds to a visibility loss of $\pm 0.66\%/\pm 0.01\%$, respectively. A similar calculation shows that the pump beam wavelength must be in a range of $405 \pm 0.008\,\mathrm{nm}$ if the visibility is to be kept in a range of $\pm 0.5\%$ (see Appendix A).

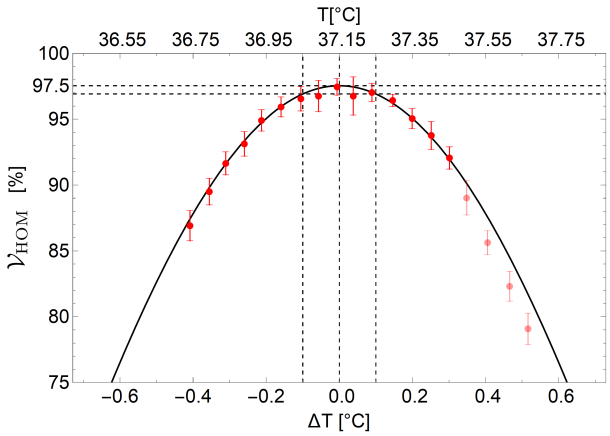


Figure 4.9 Visibility vs. crystal temperate T. The measurements (red dots) are fitted with a function as in Equation 4.37 (black line). The fitting results in a temperature $T_0 = 37.150\,°\mathrm{C} \pm 0.003\,°\mathrm{C}$ and a visibility of $\mathcal{V}_0 = 97.54 \pm 0.09$ .A temperature variation of $\pm 0.1\,°\mathrm{C}/\pm 0.01\,°\mathrm{C}$ (gray bars) leads to an uncertainty of visibility of $\pm 0.66\%/\pm 0.01\%$ (dashed lines). The error bars correspond to the shot noise of the count rate with an integration time of one second.

A relative delay $\Delta\tau$ between the photons can be generated by a Michelson interferometer (see Figure 4.10). A PBS splits the two photons, which subsequently traverse different paths of the interferometer. The polarization of the photons is rotated by an angle of $\pi/2$ by passing through the quarter-wave plates twice (back and forth). All photons entering port A will thus end up in Port E of the PBS. The relative delay $\Delta\tau$ can be changed via mirror M_1, which is mounted on a translation stage. The half-wave plate in port E is rotated by an angle $\beta = \pi/8$. So if $\Delta\tau = 0$, both photons will bunch into the same output mode of the second PBS.

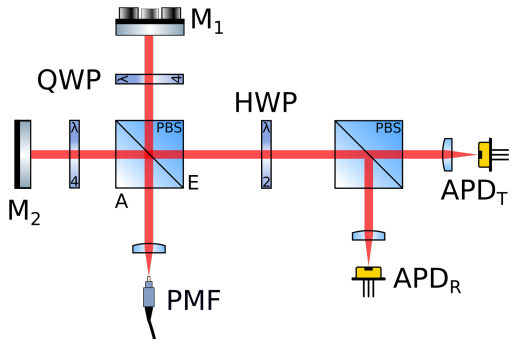


Figure 4.10 Michelson interferometer as used for the HOM dip measurement. One photon per pair is transmitted by the first PBS, and the other is reflected. The polarization of the photons is rotated by the QWPs so that both end up in port E. The HWP @ $\frac{\pi}{8}$ ensures bunching on the second PBS.

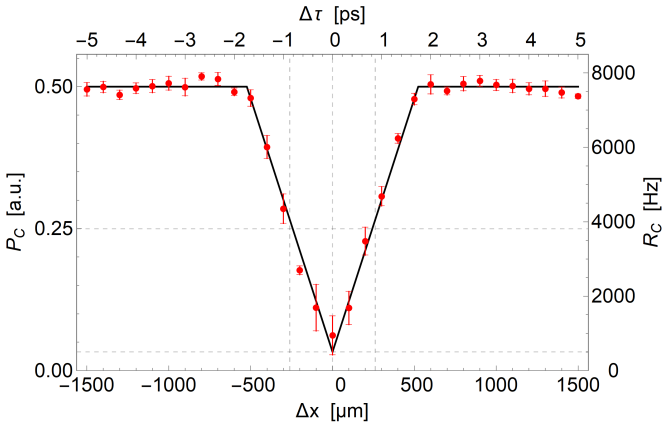
In such an experiment, the probability of detecting coincident events is given by

(see Equation A.15 with $\omega_p = 2\omega_0$, $\beta = \frac{\pi}{8}$ and $T = T_0$)

$$P_c(\Delta\tau) = \begin{cases} \frac{1}{2} & \text{if } \frac{L|D|}{2} < |\Delta\tau| \\ \frac{1}{2} - \mathcal{V}_{\mathrm{HOM}} \left(\frac{1}{2} - \frac{|\Delta\tau|}{L|D|} \right) & \text{otherwise.} \end{cases} \tag{4.38}$$

The measured HOM dip is shown in Figure 4.11, fitted with a function as in Equation 4.37. From the fitted function we find a visibility of $\mathcal{V}_{\mathrm{HOM}} = 93.4 \pm 0.3$ and the parameter $L'\,|D'| = (3.49 \pm 0.1)\ 10^{-12}$, which can be used to calculate the coherence time $L'\,|D'|\,/2 = 1.745 \pm 0.005\,\mathrm{ps}$, coherence length $cL'\,|D'|\,/2 = 523 \pm 1\,\mu\mathrm{m}$, and the spectral width $\Delta\lambda_{\mathrm{FWHM}} = 0.555 \pm 0.002\,\mathrm{nm}$[¶] of the photons.

Figure 4.11
Hong–Ou–Mandel dip The measured count rates (red dots) are fitted with a function as in Equation 4.38 (black line). The fitting results in a visibility of $\mathcal{V}_{\mathrm{HOM}} = 93.4 \pm 0.3$ and the parameter $L'\,|D'| = (3.49 \pm 0.1)\ 10^{-12}$, which can be used to calculate the coherence time $t_{\mathrm{coh}} = 1.745 \pm 0.005\,\mathrm{ps}$, coherence length $l_{\mathrm{coh}} = 523 \pm 1\,\mu\mathrm{m}$, and the spectral width $0.555 \pm 0.002\,\mathrm{nm}$ of the photons. The error bars correspond to the shot noise of the count rate with an integration one second.



[¶] $\Delta\lambda_{\mathrm{FWHM}} = \frac{(4\ 1.39)}{L'|D'|}\,\frac{2\pi c}{\omega_0^2}$



5 Entanglement in Accelerated Reference Frames

The content of this chapter is based on the publication "Experimental test of photonic entanglement in accelerated reference frames" [59]*.

5.1 Introduction

Entanglement is a resource for emerging applications such as quantum metrology and quantum cryptography, which are just making a leap from the laboratory into practice. In these promising applications, entanglement at the push of a button is required without worrying about its formation or stability. We have therefore developed a mobile plug-and-play testbed for quantum entanglement which is easy to use and can withstand adverse conditions. The result of our efforts is a crate containing a small quantum laboratory to go (QLTG), including all necessary optical and electronic equipment. This autarkic unit generates polarization-entangled photon pairs and verifies their entanglement. In order to test the stability of this mobile laboratory, we conducted experiments in free fall in a drop tower and under high stress due to acceleration forces in a centrifuge.

Such experiments are not aimed solely at the development of technologies and methods necessary for field applications. For the first time, the opportunity has arisen to systematically test entangled states in accelerated reference frames. The phenomenon of entanglement, on the basis of which EPR concluded the incompleteness of quantum mechanics, has since been at the center of extensive discussions that revolve around the non-local character of these spatial superposition states, which seems in conflict with the local nature of Einstein's theory of relativity. Experiments investigating the interplay of quantum entanglement and acceleration or gravity are therefore one scenario where new physical phenomena might potentially arise.

A remarkable, one-shot experiment was carried out where a correlated photon source was exposed to ultra-high acceleration during an explosion (when the rocket exploded

*Matthias Fink, Ana Rodriguez-Aramendia, Johannes Handsteiner, Abdul Ziarkash, Fabian Steinlechner, Thomas Scheidl, Ivette Fuentes, Jacques Pienaar, Timothy C. Ralph, Rupert Ursin, Experimental test of photonic entanglement in accelerated reference frames. *Nature Communications* **8**, 15304 (2017).

during the launch phase of the mission), but not during its operation [60]. In a subsequent launch this project ultimately succeeded in placing a correlated photon state on a cubesat into space[61]. Those experiments demonstrate very high stability of optical alignment under harsh mechanical and thermal conditions but do not directly relate to properties of entanglement under these conditions.

In the following experiments we investigate photonic quantum entanglement in the case of flat space-time, where the system experiences uniform acceleration ranging from 0.03 g in a drop tower to up to 30 g in a centrifuge. For this constellation, the expectations for the discovery of new physics are still subdued. However, these studies represent a first experimental approach to such challenges and demonstrate the technical maturity of quantum optics.

5.2 Experimental Setup

To provide entangled photons for real-world applications, we have developed a portable and ultra-stable system that generates and verifies polarization-entangled states. All the equipment required for this autarkic experiment was housed in a rigid three-level crate measuring (H×W×D) $45 \times 54 \times 37$ cm and weighing a total of 45 kg. (see Figure 5.1). The source discussed in Chapter 4 is screwed to the stable baseplate (level 1) while the detection module is installed at the more accessible level 3. A computer (zotac zbox) mounted on level 2, which can be accessed via an ad hoc wireless network, is used to remotely control the experiment and store the generated data. The total power consumption of the crate during the experiment is ~ 100 W. An uninterruptible power supply (UPS) serves as a battery which can operate the devices for approx. one and a half hours. This integrated crate design allowed flexible plug-and-play installation on the drop tower suspension and the centrifuge gondola.

5.2.1 Generation of Polarization-Entangled Photons

The source described in Chapter 4 generates horizontal (H) and vertical (V) polarized, but otherwise identical, signal and idler photons via SPDC in a degenerate collinear type II quasi-phase matching configuration. From such a state, polarization-entangled photon pairs can be generated by means of only one additional component. It should be noted that these were the first experiments carried out with this source and that a different temperature controller (Thorlabs TC200) was used at the time. With the TC200 the crystal temperature could be kept in a range of $\pm 0.1\,^{\circ}$C around $39.6\,^{\circ}$C for wavelength-degenerate quasi-phase matching at 810 nm.

A PM fiber guides the photons from the source to the detection module (see Figure 5.2). Subsequently, the photons are either transmitted (T) or reflected (R) at a non-

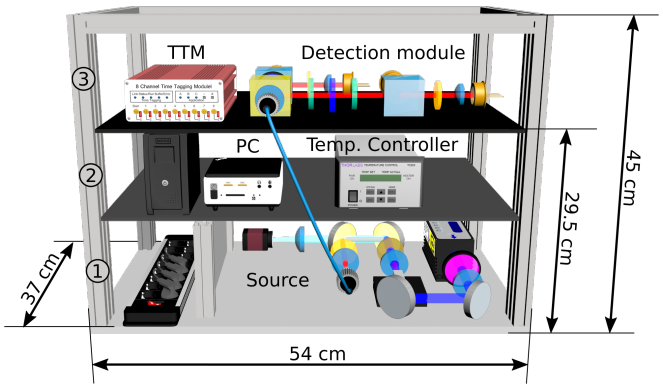


Figure 5.1 Sketch of the crate: Autarkic experiment, which generates and verifies polarization entangled states, housed in a rigid three-level crate measuring (H×W×D) 45 × 54 × 37 cm and weighing a total of 45 kg. Source (level 1) and detection module (level 3) are placed at different levels inside the crate and thus exhibit different g values in the centrifuge experiment. Revised version of Figure 1 in [59].

polarizing beam splitter cube (BS). At this point no interference occurs, since the photons are distinguishable by their polarization and impinge on the same surface of the BS. After the beam splitter, each photon is in an equal superposition of being in mode R and T.

$$\begin{aligned}
\left|\Psi^{\mathrm{PMF}}\right\rangle &= \hat{a}^{\dagger}_{\mathrm{H,PMF}}\hat{a}^{\dagger}_{\mathrm{V,PMF}}\left|\mathrm{Vac}\right\rangle \\
\left|\Psi^{\mathrm{PMF}}\right\rangle &\xrightarrow{\mathrm{BS}} \frac{1}{\sqrt{2}}\left(\hat{a}^{\dagger}_{\mathrm{H,T}}+\hat{a}^{\dagger}_{\mathrm{H,R}}\right)\frac{1}{\sqrt{2}}\left(\hat{a}^{\dagger}_{\mathrm{V,T}}+\hat{a}^{\dagger}_{\mathrm{V,R}}\right)\left|\mathrm{Vac}\right\rangle \\
&= \frac{1}{2}\left(\hat{a}^{\dagger}_{\mathrm{H,T}}\hat{a}^{\dagger}_{\mathrm{V,T}}+\hat{a}^{\dagger}_{\mathrm{H,R}}\hat{a}^{\dagger}_{\mathrm{V,R}}\right)\left|\mathrm{Vac}\right\rangle + \frac{1}{2}\left(\hat{a}^{\dagger}_{\mathrm{H,T}}\hat{a}^{\dagger}_{\mathrm{V,R}}+\hat{a}^{\dagger}_{\mathrm{H,R}}\hat{a}^{\dagger}_{\mathrm{V,T}}\right)\left|\mathrm{Vac}\right\rangle
\end{aligned} \tag{5.1}$$

Post-selecting events with one photon in each mode yields a polarization-entangled state [62]

$$\left|\Psi\right\rangle = \frac{1}{\sqrt{2}}(\left|\mathrm{H_T,V_R}\right\rangle + \mathrm{e}^{-\mathrm{i}\varphi}\left|\mathrm{V_T,H_R}\right\rangle), \tag{5.2}$$

where φ describes a polarization dependent phase difference between path T and R, which is accumulated over all optical elements in the respective paths. Due to post-selection 50% of the photon pairs are disregarded. The phase was set to $\varphi = \pi$ using a quarter-, half- and quarter-wave plate combination in path R. Thus, the rotationally invariant state $\left|\Psi^{-}\right\rangle$ (see Equation 2.35) was obtained.

5.2.2 Verification of Entanglement

In order to analyze the polarization of the photons, a PBS with detectors in both output modes was installed in each path. The measurement basis was set by means of

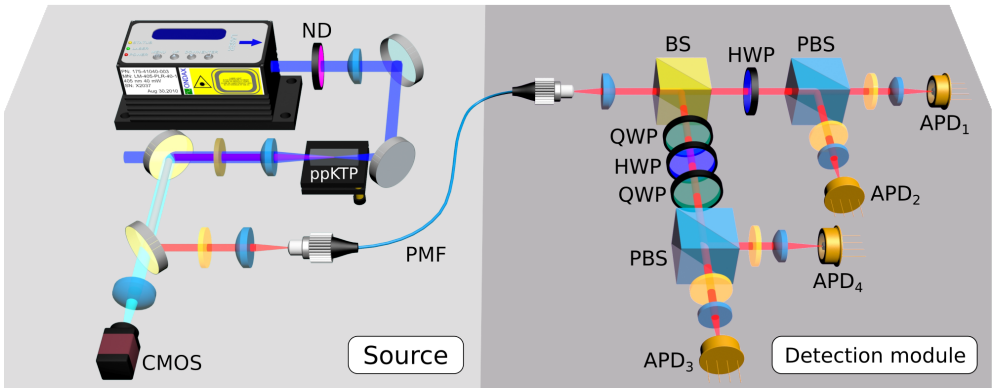


Figure 5.2 Arrangement of the optical elements: A polarization-maintaining fiber (PMF) guides the photons generated by the source (see Section 4) to a non-polarizing beam splitter (BS), which creates an equal superposition for reflection and transmission for each individual photon. A $|\Psi^-\rangle$ state is obtained by setting the relative phase using a quarter-, half- and quarter-wave plate (QWP, HWP, QWP) combination accordingly. The polarization of the photons is analyzed in each path by means of a polarizing beam splitter (PBS) with avalanche photodiodes (APD_1, APD_2, APD_3, and APD_4) in both output modes. Revised version of Figure 1 in [59].

motorized half-wave plates placed in front of each PBS. The passively quenched AIT detectors (see Section 3.1) used for single photon detection have a dead time of 10 μs. Therefore, the power of the pump laser had to be reduced in order to avoid saturation of the detectors. Such a reduction of the pump power to $\sim$ 2 mW was achieved by means of a laser diode current of 84.5 mA and a neutral-density filter (ND) with an optical density of 1.3. In addition, the APDs were protected against stray light by a colored glass filter and an interference filter (see Figure 3.1).

All four detectors were connected to a single time tagging module (TTM), which internally calculates the coincidence count rates within a coincidence window of $\sim$ 3 ns (FWHM) in real time. The counts were recorded on a connected PC using LabView. Typical count rates are summarized in Table 5.1.

The visibility of the generated polarization-entanglement of the photon pairs is measured as

$$\mathcal{V}_{\mathrm{Ex}} = \frac{N_{1,4} + N_{2,3} - N_{1,3} - N_{2,4}}{N_{1,4} + N_{2,3} + N_{1,3} + N_{2,4}}, \tag{5.3}$$

where $N_{\mathrm{x,y}}$ denotes the detected number of coincidences between detector x and y. The uncertainty of the count rate can be estimated via $\sqrt{N_{\mathrm{x,y}}}$, assuming Poisson noise of $N_{\mathrm{x,y}}$. The standard deviation of the visibility is derived via propagation of

	N_1	N_2	N_3	N_4
HV	40 k	39 k	39 k	41 k
DA	41 k	35 k	39 k	38 k

	$N_{1,4}$	$N_{2,3}$	$N_{1,3}$	$N_{2,4}$	$N_{1,2}$	$N_{3,4}$	$\mathcal{V}_{\mathrm{Ex}}$ [%]	$\sigma_{\mathcal{V}}$ [%]
HV	2979	2893	29	28	2916	2971	98.1	±0.253
DA	3041	2820	68	69	36	52	95.4	±0.386

Table 5.1 Typical number of counts per second for two different measurement settings, namely the horizontal/vertical (HV) and the diagonal/anti-diagonal (DA) basis. The number of single events at detectors 1-4 (see Figure 5.2) are indicated by N_1, N_2, N_3, and N_4, while $N_{\mathrm{x,y}}$ denotes the detected number of coincidences between detector x and y. Visibility is calculated using Equation 5.3, and the corresponding $\sigma_{\mathcal{V}}$ is estimated assuming Poisson statistics of the count rates.

uncertainty which results in

$$\sigma_{\mathcal{V}} = 2\sqrt{\frac{(N_{1,4}+N_{2,3})(N_{1,3}+N_{2,4})}{(N_{1,4}+N_{2,3}+N_{1,3}+N_{2,4})^3}}. \tag{5.4}$$

Table 5.1 shows the visibility for two different measurement settings, namely the horizontal/vertical (HV) and the diagonal/anti-diagonal (DA) basis. The visibility is limited, for instance, by polarization mismatch and accidental coincidences. The visibility in the DA basis depends additionally on the indistinguishability of the photons. Partial distinguishability can be caused by poor walk-off compensation or deviations from the wavelength-degenerate phase matching temperature. Therefore, the visibility observed in the DA basis is generally smaller than in the HV basis. The temperature of the crystal may fluctuate within a range of ±0.1 °C, and the associated visibility variation is 0.65 % (see Figure 4.9).

However, substituting these visibilities into the entanglement witness of Equation 2.53 yields a value of

$$\mathcal{W} = 1 - \mathcal{V}_{\mathrm{HV}} - \mathcal{V}_{\mathrm{DA}} = -0.935 \pm 0.005 \tag{5.5}$$

As discussed in Chapter 2, a measurement result of $\mathcal{W} < 0$ can only be achieved by entangled states. We have thus successfully proven that the photon pairs generated are entangled in polarization. This witness can be used to estimate a lower bound for the Bell-state fidelity [63]

$$\mathcal{F}_{\Psi^-} = \langle\Psi^-|\hat{\rho}_{\mathrm{exp}}|\Psi^-\rangle \geq \mathcal{F}^{\mathrm{M}}_{\Psi^-} = \frac{1}{2}(\mathcal{V}_{\mathrm{HV}} + \mathcal{V}_{\mathrm{DA}}) = \frac{1}{2}(1-\mathcal{W}) \tag{5.6}$$

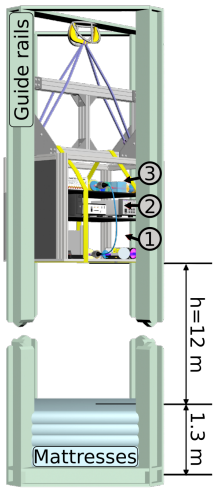


Figure 5.3 Drop tower at the Institute of Concrete Structures at the Technical University of Dresden. The crate was dropped from a height of $h = 19.6\,\mathrm{m}$ and $h = 12\,\mathrm{m}$ for a low-g (almost) free-fall flight in air. Guide rails kept the payload on track during flight and impact. A 1.3 m-high stack of mattresses was used to cushion deceleration phase on ground. Revised version of Figure 2 in [59].

5.3 Drop Tower

The drop tower experiment was carried out at the Institute of Concrete Structures at the Technical University of Dresden, whose drop tower is normally used for destructive material tests. Thus, there are no precautions at this facility to prevent the destruction of falling objects, but guide rails keep the payload on track during flight and impact (see Figure 5.3). In order to cushion the impact of the 80.5 kg-heavy crate (including suspension), we used a 1.3 m-high stack of foam mattresses. The first drop from a height of $h = 19.6 \pm 0.1\,\mathrm{m}$ was recorded with a high-speed camera with a frame rate of 2000 fps (see Figure 5.4). In this first test, the crate experienced a free fall for $2.1 \pm 0.1\,\mathrm{s}$ and had an impact velocity of approx. 60 km/h. During free fall, the guide rails and air resistance exerted a force on the crate, but shortly after the locking mechanism was opened, we were able to measure accelerations as low as $30 \pm 3\,\mathrm{mg}$. The subsequent impact caused misalignment of the source and damaged the battery, resulting in the loss of the recorded data.

The experiments were continued the next day with a new battery and restored alignment. The impact velocity was reduced to approx. 51 km/h by lowering the drop height to $h = 12 \pm 0.1\,\mathrm{m}$. In this configuration, two consecutive milli-g experiments, one with HV and one with DA measurement setting, were performed without the need for intermediate realignment. The evaluation of the accelerometer data shows a period of $1.5 \pm 0.1\,\mathrm{s}$ between the release and the impact of the crate. The subsequent impact saturated the accelerometer but did not damage the setup.

In each experimental run, we continuously measured the visibility (see Figure 5.5), yielding mean values of $\mathcal{V}_{\mathrm{HV}} = 97.3 \pm 0.1\,\%$ and $\mathcal{V}_{\mathrm{DA}} = 96.3 \pm 0.1\,\%$. Both experiments can be divided into three phases, in which the crate experienced rest (A), free fall (B), and impact with rebound (C). The individual visibility measurements are stable during all these phases within a range corresponding to the measurement tolerance.

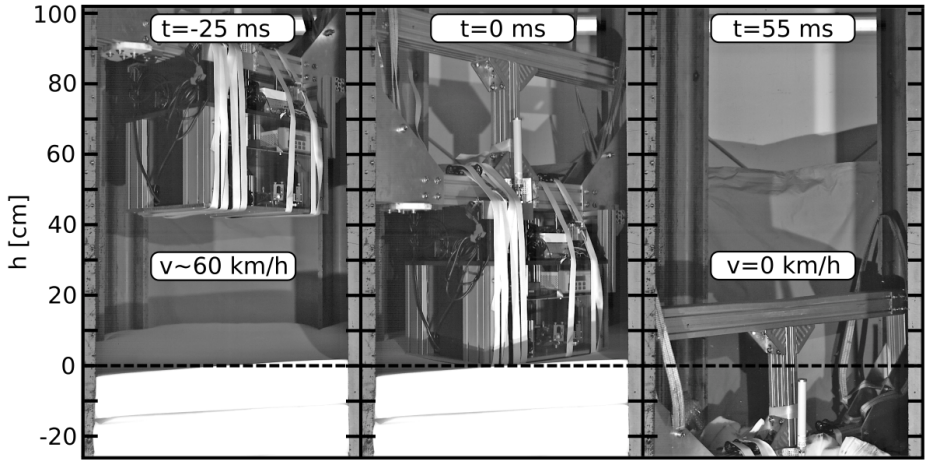


Figure 5.4 **Selected frames** from the high-speed camera video (2000 fps) of the $h = 19.6\,\mathrm{m}$ drop. The three images show the crate at the time the camera is activated (left, frame 1), when it hits the mattresses (center, frame 51), and when the movement of the crate is reversed (right, frame 161). The evaluation of the images results in an impact speed of approx. 60 km/h.

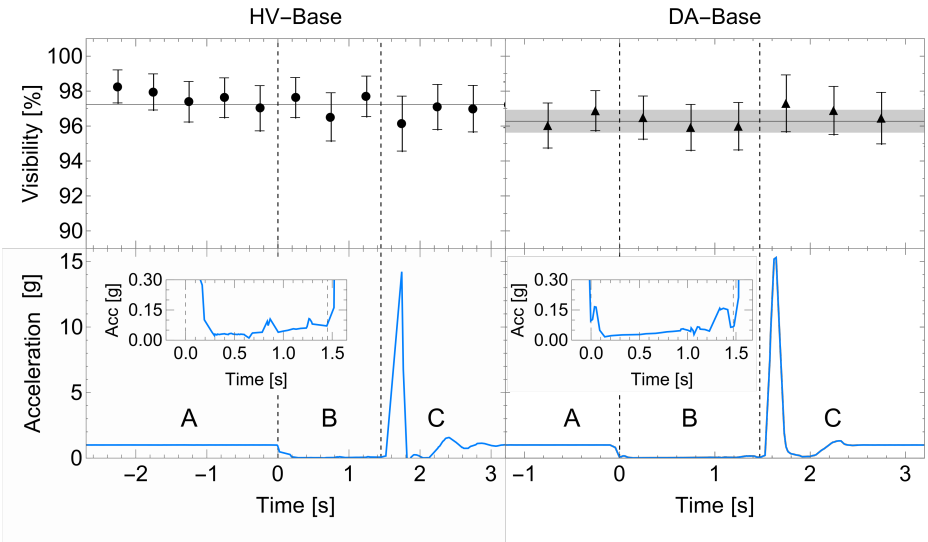


Figure 5.5 **Visibility and acceleration vs. time** during the drop tower experiments. The time-averaged visibility values (horizontal lines) are $\mathcal{V}_{\mathrm{HV}} = 97.3\,\%$ and $\mathcal{V}_{\mathrm{DA}} = 96.3\,\%$. The visibility was calculated every 500 ms (circles for HV and triangles for DA), the corresponding error bars indicate the expected uncertainty due to the Poissonian statistics of the count rates (3σ). The individual visibility measurements are stable, during the three phases (rest (A), free fall (B), impact and rebound (C)). In principle, the visibility in the DA measurement may vary within a range of 0.66 % (gray bar) due to possible temperature variations of the crystal. The g values measured at the same time are plotted in blue. The accelerometer was saturated on impact. Revised version of Figure 3 in [59]

5.4 Centrifuge

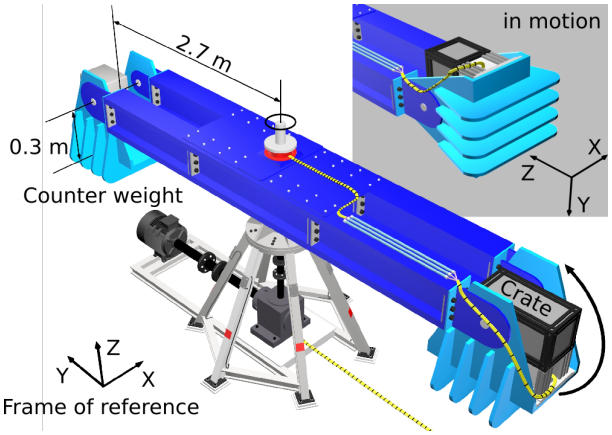


Figure 5.6 Centrifuge as installed at AMST in Ranshofen. The crate was screwed to one of the gondolas, which has a distance of approx. 3 m to the rotational axis. The gondolas swivel outwards in motion, thus the centrifugal force acts just like an additional gravitational force on the crate. The frame of reference (of the accelerometer) rests on the swing and is depicted for the cases in which the centrifuge is at rest and in motion. Revised version of Figure 2 in [59]

By means of a centrifuge, our experimental setup was exposed to strong acceleration in a controlled manner. The company AMST in Ranshofen operates a machine which has sufficient size and power for this purpose. This company was kind enough to make this machine available for our experiment. At full power, the centrifuge reaches a rotational speed of $N_{\mathrm{RPM}} = 94.5$ revolutions per minute. The two arms of the machine each have a total length of 3 m, at the end of which a centrifugal acceleration of maximum 30 g is achieved. At the maximum rotational speed, the gondolas at the end of the arms (see Figure 5.6) have a velocity of 107 km/h. The resulting air resistance prevented experimentation at higher speeds.

The crate was mounted on one of the two gondolas of the centrifuge which is equipped with Ethernet and 230 V mains connection via a sliding contact. Therefore, the battery and the WLAN antenna were removed in this experiment. The centrifuge was balanced with a counter weight of 37 kg on the opposite gondola. Since those gondolas swivel outwards when moving, the centrifugal force always acts just like an additional gravitational force on the crate (negative z-direction in the frame of reference of the swing).

During the experiment, the speed was increased in increments that corresponded to an additional acceleration of 5 g. After each step-wise increase of the rotational speed, a measurement was carried out in both, the HV and the DA bases. Figure 5.7 shows the angular deviation of the pump beam from its initial position α as measured by the CMOS sensor, along with the averaged single count rates R_{S} (sum of all detectors) and coincidence count rates R_{C} (sum over all detector combinations). The measured angle α is small compared to the $NA = 120\,\mathrm{mrad}$ of the PMF. Screwing the crate to the gondola probably caused a warp of the base plate, leading to a misalignment

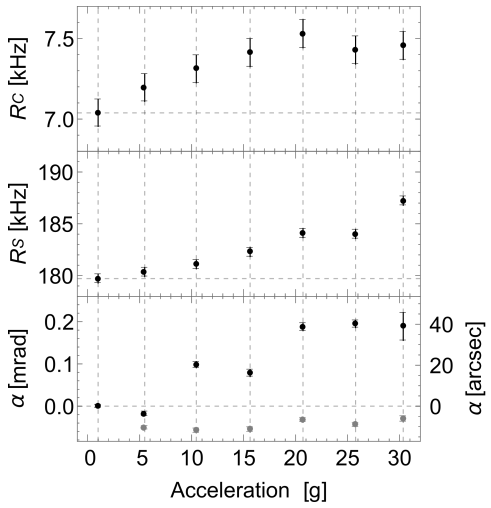


Figure 5.7 Angular deviation of the pump beam α vs. acceleration as measured by the CMOS sensor. The pixel size of the sensor is 5.2 μm, and the lens used as objective had a focus length of 5 cm. The given angles α are based on a Gaussian fit of the intensity distributions measured by the sensor. The measured misalignment of the pump beam correlates with the averaged detected count rates R_S (sum of all single detection events) and R_C (sum of coincident events between all detector combinations).

of the source. Fortunately, the deformation due to the additional centrifugal force counteracted this deformation. This leads to a slight increase in the count rate at a higher acceleration. However, the visibility of the polarization entanglement has not suffered from the misalignment (see 5.8).

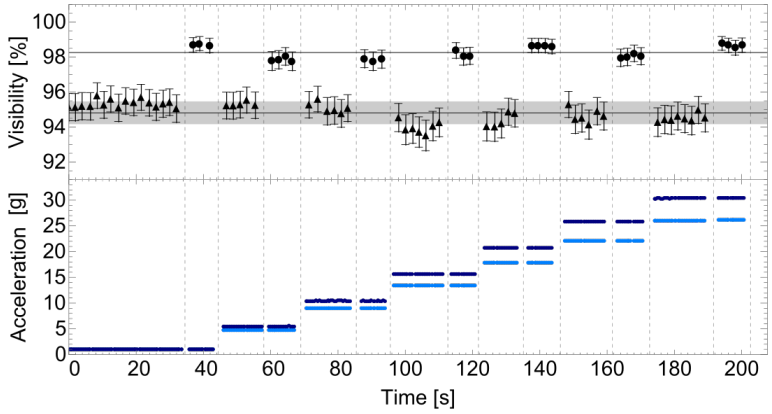


Figure 5.8 Visibility and acceleration vs. time during the centrifuge experiment. The time-averaged visibility values (horizontal lines) are $\mathcal{V}_{HV} = 98.3\,\%$ and $\mathcal{V}_{DA} = 94.8\,\%$. The visibility was calculated every 2 s (circles for HV and triangles for DA), the corresponding error bars indicate the expected uncertainty due to the Poissonian statistics of the count rates (3σ). The drop in visibility at 15 g is due to the effective cooling of the crystal. The expected variation of $\mathcal{V}_{DA}$ corresponds to a temperature change of $\pm 0.1\,°C$ is 0.66 % (gray bar). The lower g values (light blue) represent the measured data of the accelerometer at level 3 (detection) of the crate. Additionally, the calculated acceleration at level 1 (source) is plotted (blue). Revised version of Figure 2 in [59]

Since the source and the detection module are located on two different levels in the crate ($\Delta h = 29.5\,\text{cm}$), they were subjected to different centrifugal forces. Both accelerations are plotted in Figure 5.8. The small reduction of the DA visibility at

15 g stems from the effective cooling of the crystal during higher rotational speeds. The resulting deviation from the degenerate phase-matching temperature introduced distinguishability of the emitted photon pair and reduced the visibility in the DA basis (see Figure 4.9). Apart from these small deviations, the visibility was stable throughout the experiment.

5.5 Conclusion

The QLTG was subjected to various accelerations ranging from 0.03 g in the drop tower to 30 g in the centrifuge, while continuously measuring the visibility of the generated polarization-entangled photons. We have observed a slight change in count rates of 3 % at a centrifugal acceleration of 30 g, which we attribute to a deformation of the optomechanics. However, neither the measured visibility in the HV basis nor in the DA basis suffered from these deformations. An entanglement witness $\mathcal{W} = 1 - \mathcal{V}_{\mathrm{HV}} - \mathcal{V}_{\mathrm{DA}}$ can be calculated from the data collected at the respective acceleration. These values are summarized in Figure 5.9.

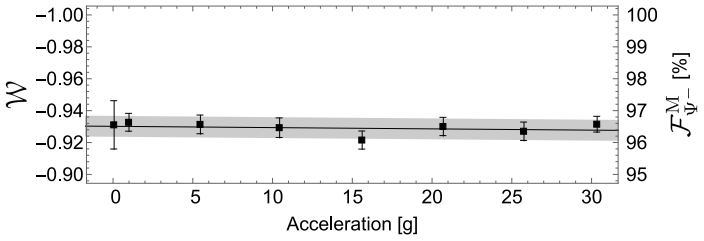


Figure 5.9 Entanglement witness $\mathcal{W}$ (fidelity $\mathcal{F}^{\mathrm{M}}_{\Psi^-}$) vs. acceleration : The right axis of the graph shows the estimated lower bound on Bell-state fidelity $\mathcal{F}^{\mathrm{M}}_{\Psi^-} = (1-\mathcal{W})/2$. All measured witness values (black squares) are below the limit for separable states ($\mathcal{W}_{\mathrm{sep}} > 0$). The error bars are calculated considering Poissonian statistics (3σ). The expected variation of $\mathcal{W}$ ($\mathcal{F}^{\mathrm{M}}_{\Psi^-}$) corresponding to a temperature change of $\pm 0.1\,^{\circ}\mathrm{C}$ is ± 0.0066 ($\pm 0.33\%$), which is represented as grey area around the linear fit (black line). Revised version of Figure 5 in [59].

The mean of the witness values $\overline{\mathcal{W}} = -0.929 \pm 0.004$ is well below the minimum for separable states ($\mathcal{W}_{\mathrm{sep}} > 0$), which testifies to the entanglement of the photon pairs generated at g-values ranging from 0.03 g to 30 g. From the measured visibilities a lower bound for the Bell-state fidelity $\mathcal{F}^{\mathrm{M}}_{\Psi^-} = (\mathcal{V}_{\mathrm{HV}} + \mathcal{V}_{\mathrm{DA}})/2 = (1 - \mathcal{W})/2$ can be calculated. The temperature of the SPDC-crystal significantly affects the visibility $\mathcal{V}_{\mathrm{DA}}$ and thus the fidelity. The deviation in fidelity to be expected due to temperature fluctuations of $\pm 0.1\,^{\circ}\mathrm{C}$ is shown in Figure 5.9 as a grey area around the linear fit and covers the deviation of the respective mean values.

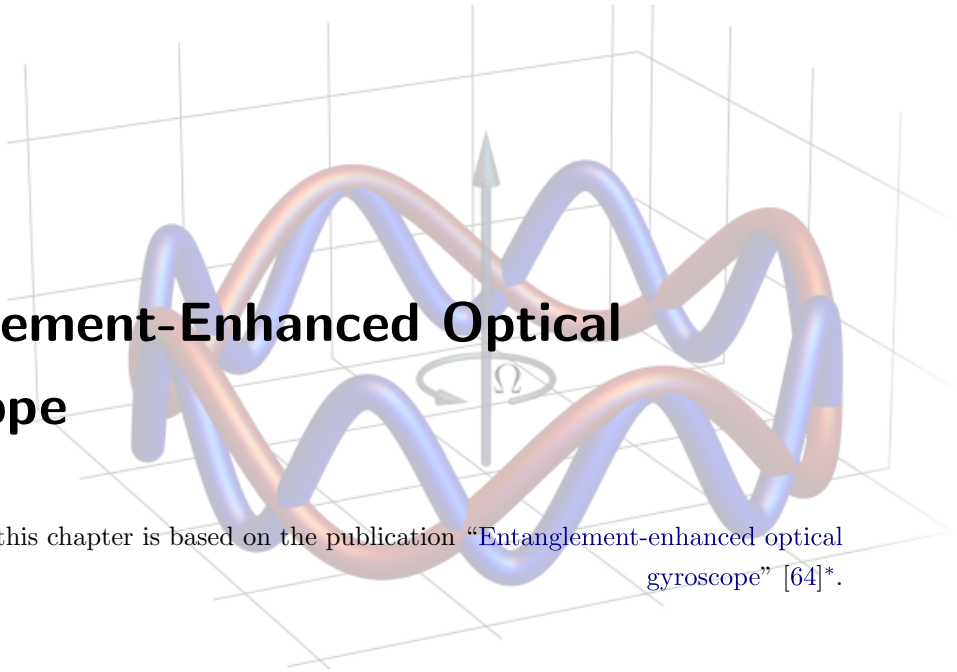
The linear fit shows a slope of $-0.0039\,\%/\mathrm{g} \pm 0.0066\,\%/\mathrm{g}$. These experiments thus

reduce a hypothetical influence on the polarization-entangled state by accelerated reference frames to a change in fidelity of less than $\pm 0.0105\,\%/\mathrm{g}$, and demonstrate the stability of the crate in a range from 0.03 g to 30 g.

The results achieved with the QLTG could be improved with its current version. Meanwhile, a new PID controller ensures a temperature stability of 0.01 °C. Thus, the variation of visibility in the DA basis is reduced to 0.01%. In addition, actively-quenched detectors have been installed whose shorter dead time of 20 ns instead of 10 μs increases the maximum count rate by a factor of ten and thus reduces the statistical error of the measurements.

The arms of the centrifuge can be shortened to 1.5 m. Due to the reduced air resistance, a rotational speed of up to $N_{\mathrm{RPM}} = 300$ revolutions per minute and thus an acceleration of 150 g can be achieved. However, the required test approval for the machine is costly and was therefore not applied for. Active source stabilization using piezo mirrors in a feedback circuit could be used to avoid loss of count rates at higher accelerations. Using such techniques, interferometric measurements on the centrifuge are also conceivable.

The conditions of the conducted experiments are close to those of a rocket launch, so our results could be relevant for emerging satellite missions. We have shown that our portable quantum optic laboratory involving entangled photons was not only capable of withstanding such severe stress, but also remained fully functional under these difficult operating conditions. Our experiment thus demonstrates the extent to which state-of-the-art quantum hardware can be exposed to such a harsh operational environment, with the intention of stimulating research on theories beyond the current paradigm which can be tested with the kind of experiments presented here.



6 Entanglement-Enhanced Optical Gyroscope

The content of this chapter is based on the publication "Entanglement-enhanced optical gyroscope" [64]*.

6.1 Introduction

Fiber optic gyroscopes (FOG) based on the Sagnac effect are instruments used to determine the absolute rotation Ω with respect to inertial space [65]. Such devices are valuable tools in sensing and navigation with applications ranging from spacecraft [66] and aircraft [67] to self-driving vehicles such as autonomous cars [68].

The Sagnac effect refers to the relative phase $\phi_S(\Omega)$ experienced by counter-propagating light waves in a rotating interferometer. This phase difference was discovered by Georges Sagnac in 1913 [69, 70] in an attempt to observe the "*relative circular motion of the luminiferous ether within the closed optical path*"[71, 72]. Along with the experiments of Michelson and Morley [73], it is considered one of the fundamental experimental tests of Einstein's theory of relativity [74]. There are still discussions about the relativistic correction for this effect [65, 75, 76, 77].

The precision of an optical gyroscope is determined by the phase response $\partial\phi/\partial\Omega$ as well as the minimum phase resolution $\Delta\phi$. The phase response $\partial\phi/\partial\Omega = S \propto A_{\circlearrowleft}/\lambda$, or scale factor S, is proportional to the area $A_{\circlearrowleft}$ enclosed by the counter propagating waves and inverse proportionality to the wavelength λ of the interfering wave. In commercial fiber optic gyroscopes (FOG), the phase response is amplified by increasing the effective area enclosed by the optical paths by using an optical fiber-coil. Another strategy to improve the precision is to use shorter wavelengths. Therefore, the Sagnac effect was examined with X-rays [78] as well as with de Broglie waves such as electrons [79], neutrons [80], and atoms [81, 82, 83]. The generation and guiding of such waves, however, is rather difficult in comparison to optical electromagnetic waves, and the area enclosed by such gyroscopes is rather small compared to the FOG.

The phase resolution of a FOG is limited by various sources of noise and depends

*Matthias Fink, Fabian Steinlechner, Johannes Handsteiner, Jonathan P Dowling, Thomas Scheidl, Rupert Ursin, Entanglement-enhanced optical gyroscope. *New Journal of Physics* **21**, 053010 (2019).

on the light source used. The most fundamental reason for limited precision is the shot noise of a number of individual photons, which is caused by the quantization of the electromagnetic field itself. For coherent states of light, the number of photons detected in a time interval τ follows a Poissonian distribution and thus varies — without phase change — with $\Delta M = \sqrt{M}$ (i.e. the standard deviation) around the average number of detected photons M. Moreover, this noise puts a fundamental boundary on the phase resolution $\Delta\phi > \Delta\phi_{\mathrm{SNL}} = 1/\sqrt{M}$ achievable with coherent or thermal states, which is called the shot-noise limit (SNL) [39]. While the phase resolution can obviously be enhanced by increasing the average photon rate, arbitrarily accurate measurements are prevented by additional phase noise resulting from detrimental effects like nonlinear Kerr effects or coherent back-scattering induced at high power levels [84, 85]. Consequently, a trade-off between these additional noise sources and the SNL has to be made to find the optimal operating point in any practical FOG.

Quantum metrology provides a route to improve the precision of measurement to levels which would be impossible with classical resources alone [14]. One strategy is to reduce the shot noise of the count rate by using photons with a "collective behavior" (entangled photons) in order to measure an optical phase with a higher precision per photon. The canonical example of such states are path-entangled NOON states. All $N > 1$ photons of such a state are in an equal superposition of being in either one of the two modes of an interferometer, resulting in a shortened de Broglie wavelength λ/N, where λ denotes the physical wavelength of the individual photons [16]. This leads to an increase of the interferometric fringe pattern frequency by a factor of N (super-resolution) without changing the physical wavelength of the photons. Thus, λ can be chosen for optimized transmission through optical single-mode fibers (SMF).

Only considering quantization noise, the phase uncertainty resulting from an average of M/N consecutively detected NOON states (i.e. M photons are detected in total) is given by $\Delta\phi_{\mathrm{NOON}} = 1/\sqrt{NM}$ [39]. This entanglement-enhanced phase precision is smaller by a factor $1/\sqrt{N}$ than the SNL $\Delta\phi_{\mathrm{SNL}} = 1/\sqrt{M}$. In particular, using NOON states the relative phase imparted on the interferometric modes can be determined with the same precision as if consecutive single photons with N-fold energy (N times shorter wavelength), or N times more photons were detected. The fundamental limit in quantum mechanics is the Heisenberg limit $\Delta\phi_{\mathrm{HL}} = 1/M$, which retains its validity for arbitrary photon states.

An improved resolution in interferometric phase measurements by using NOON states was proposed by Jacobson *et al.* [16], while the application in a Sagnac interferometer was proposed by Kolkiran and Agarwal [86]. The applicability of these non-classical states in metrology has already been widely demonstrated in other interferometric settings [15, 31, 87, 88, 89], while the measurement advantage, or quantum

enhancement, has not yet been used to measure a phase shift imparted by accelerated or rotational motion. Bertocchi *et al.* experimentally compared the resolution of a FOG fed either with coherent states or single-photon Fock states [90]. To our knowledge this was the first attempt to study the precision of FOG with non-classical states of light.

In this Chapter, we investigated the interference signal of the counter-propagating modes in the FOG at different rotational speeds and use the canonical example of a two-photon NOON state ($N = 2$) to provide phase sensitivity beyond the shot-noise limit. Subsequently, the effects of loss and the technical applicability of such a device are discussed.

6.2 Methods

6.2.1 Sagnac Effect

A Sagnac interferometer consists of a beam splitter whose output modes are connected by a closed optical path (see Figure 6.1). In case of FOGs this closed path is realized by a single-mode fiber coil of length L and radius r. Half of the light passes through the fiber in a clockwise direction. The remaining 50% of the light propagates counterclockwise in the interferometer before both spatial modes are superimposed at the same BS.

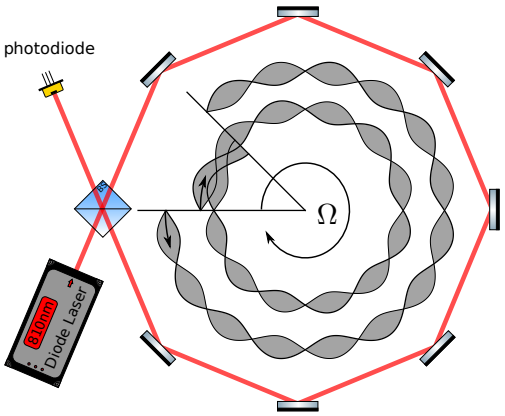


Figure 6.1 Bulk optics Sagnac interferometer: The light of a laser is split by a non-polarizing beam splitter cube. Half of the light propagates through the interferometer in a clockwise direction, and the other half propagates counterclockwise. Both modes are superimposed at the same BS and the resulting interference signal is measured by a photodiode.

If the interferometer is rotating with an angular velocity Ω, a phase shift $\phi_S \propto \Omega A_{\circlearrowleft}$ between counter propagating waves is accumulated. The effective area enclosed by the light path in a fiber coil $A_{\circlearrowleft} = N_W \, \pi r^2 = \frac{L\,r}{2}$ depends on the number of windings $N_W = L/(2\pi r)$. This effect is named after its founder Sagnac and applies to a kinematic effect of the special theory of relativity [74].

Grigorii B. Malykin derives this phase shift in the framework of the STR, as follows [65]. In the non rotating laboratory frame of reference K, the propagation time

difference $\Delta t(\Omega) = t^+ - t^-$ of the counter propagating waves can be calculated as

$$\Delta t(\Omega) = \frac{l^+}{v_{ph}^+} - \frac{l^-}{v_{ph}^-} = \frac{4\ A_{\circlearrowleft}\ \Omega}{c^2(1 - r^2\Omega^2/c^2)} = \frac{2\ L\ r\ \Omega}{c^2(1 - r^2\Omega^2/c^2)}. \tag{6.1}$$

The superscript + or − indicates a propagation of the light in or against the direction of rotation, respectively. The path lengths $l^\pm = L \pm r\Omega t^\pm$ of the counter-propagating waves differ because of the movement of the BS during the propagation of the light. The phase velocities are different due to relativistic velocity addition $v_{ph}^\pm = \frac{c/n \pm r\Omega}{1 \pm c/n\ r\Omega/c^2}$. It is worth mentioning that the resulting time difference $\Delta t(\Omega)$ is independent of the phase velocity, which makes FOGs independent of the refractive index of the fiber.

Since the photodiode co-rotates with the interferometer, one has to use the Lorentz transformation to calculate the time difference as observed in the rotating frame of reference K'.

$$\Delta t'(\Omega) = \sqrt{1 - \frac{r^2\Omega^2}{c^2}}\ \Delta t(\Omega) = \frac{2\ L\ r\ \Omega}{c^2\sqrt{1 - r^2\Omega^2/c^2}} \tag{6.2}$$

The measured phase difference of the counter propagating waves can be calculated via Equation 6.3 with the wavelength of the source λ' in the frame of reference K'.

$$\phi_{\mathrm{S}}'(\Omega) = \frac{2\pi\ c}{\lambda'}\Delta t'(\Omega) = \frac{4\pi\ L\ r\ \Omega}{\lambda'\ c\sqrt{1 - r^2\Omega^2/c^2}} \tag{6.3}$$

The Sagnac phase derived in this way does not consider the length contraction of the fiber coil. A more detailed discussion on this topic can be found in "*Relativistic Sagnac Effect and Ehrenfest Paradox*" by Ghosal *et al.* [76]. At low angular velocities $\sqrt{1 - r^2\Omega^2/c^2} \simeq 1$, however, Equation 6.3 can be approximated by

$$\phi_{\mathrm{S}}(\Omega) = \frac{4\pi\ L\ r}{\lambda\ c}\ \Omega = S\ \Omega, \tag{6.4}$$

with the scale factor

$$S = \frac{4\pi\ L\ r}{\lambda\ c}. \tag{6.5}$$

6.2.2 Experimental Setup

The basis of the experimental setup is the rigid three-level crate used in the centrifuge and drop tower Experiments (see Chapter 5). In order to measure the Sagnac effect, we developed a detection module which incorporates a fiber-based Sagnac interferometer (see Figure 6.3). The coil, consisting of a single-mode optical fiber (780-HP) with a length of $L = 270.5\,\mathrm{m}$ wound with a radius $r = 7.8\,\mathrm{cm}$ is passively stabilized against temperature drifts with a cardboard box and bubble wrap. The fiber coil is not perfectly circularly wound and has extra loops for the polarization controller and the PBS

connections. Therefore, Equation 6.4 with scale factor $S = 1.09$ is only a rough estimate of the expected phase shift.

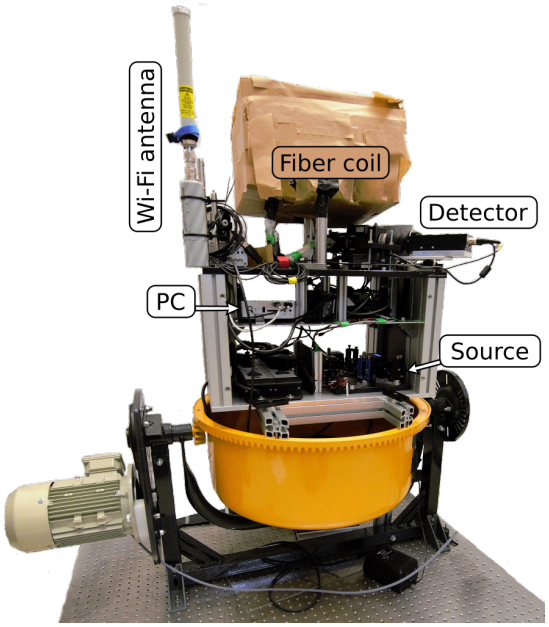


Figure 6.2 Rotation platform: A rigid three-level crate containing a photon source, a fiber based Sagnac interferometer, single photon sensitive detectors, and electronic equipment was mounted on a custom made rotation platform. A remotely controlled personal computer (PC) was used for data storage and to control the experiment. All electronics within the crate were driven via uninterruptible power supply. The optical fiber coil of the Sagnac interferometer was passively stabilized against temperature drifts with a cardboard box and bubble wrap. Revised version of Figure 1 in [64].

The crate containing the optical setup and the required electronic control equipment was mounted on a customized rotation platform (see Figure 6.2). All electronics within the crate were driven by an uninterruptible power supply (UPS). A computer which can be accessed via an ad hoc wireless network was used to remotely control the experiment and store generated data. The original motor of the mixer was replaced by a three-phase motor. We were able to adjust the rotational speed of the setup by controlling the motor by means of a variable-frequency drive. A commercially available gyroscope (Dytran Instruments Inc.) was used to log the rotational velocity.

6.2.3 Optical Setup

The source (see Chapter 4) generates horizontal (H) and vertical (V) polarized, but otherwise identical, signal and idler photons via SPDC in a degenerate collinear type II quasi-phase matching configuration at a wavelength of $\lambda = 810\,\mathrm{nm}$. For the following experiments we used a pump power of 27.5 mW (laser diode current of 60 mA without ND-filter). At the output of the PMF we measured a single-photon count rate of $R_\mathrm{H} \simeq R_\mathrm{V} \simeq 951\,\mathrm{kcps}$ for each polarization, of which $R_c = 191\,\mathrm{kcps}$ were detected in pairs. To be able to count such high photon rates, we used actively-quenched detectors (Excelitas SPCM-800 see Section 3.1). A polarization maintaining single-mode fiber collects the down-converted photons and guides them to the Sagnac interferometer.

The two-photon state $\left|\Psi^\mathrm{PMF}\right\rangle$ at the output of the polarization maintaining fiber is transformed by a half-wave plate (at 22.5°) to a NOON state in the polarization modes

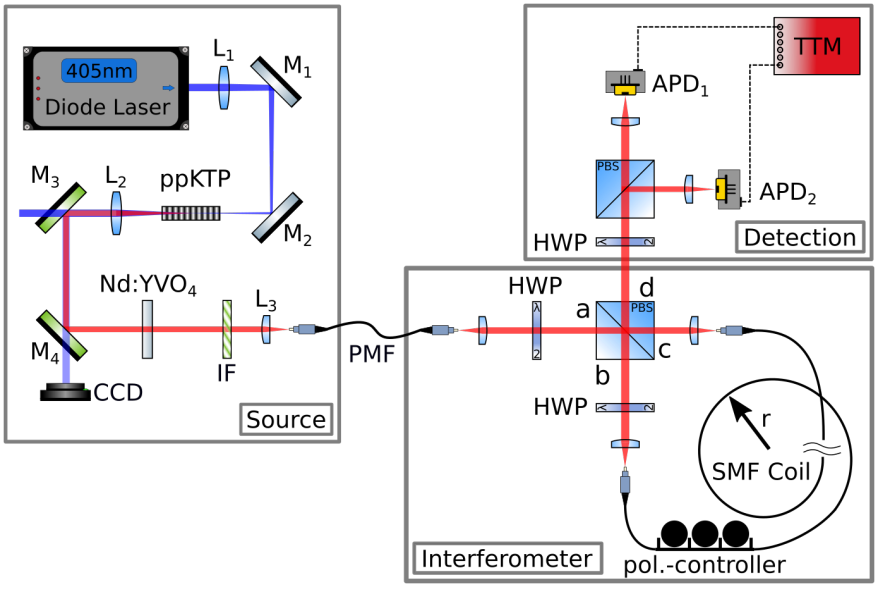


Figure 6.3 Scheme of the optical arrangement: The source (see Chapter 4) generates horizontal (H) and vertical (V) polarized signal and idler photons ($\lambda = 810\,\mathrm{nm}$). A polarization maintaining single-mode fiber (PMF) guides them to the Sagnac interferometer. A half-wave plate (HWP) at 22.5° rotates their polarization before they enter the interferometer. A polarizing beam splitter (PBS) with ports a,b,c, and d converts the polarization modes to spatial modes. The single-mode fiber (SMF) coil has a length of $L = 270.5$ m and is wound with a radius of $r = 7.8$ cm. A HWP within the loop and a fiber polarization controller are used to match the input and output polarization of the coil. The photons leaving the PBS through port d are measured in a mutually unbiased basis. Two avalanche photon diodes (APD) generate electrical pulses which are recorded by a time tagging module (TTM). Revised version of Figure 1 in [64].

H and V.

$$\left|\Psi^{\mathrm{PMF}}\right\rangle = |1_{\mathrm{H}}, 1_{\mathrm{V}}\rangle \xrightarrow{\mathrm{HWP}} |1_{\mathrm{D}}, 1_{\mathrm{A}}\rangle = \frac{1}{\sqrt{2}}(|2_{\mathrm{H}}, 0_{\mathrm{V}}\rangle - |0_{\mathrm{H}}, 2_{\mathrm{V}}\rangle) \tag{6.6}$$

In such state, either both photons are polarized horizontally or vertically. Additionally, for providing reference measurements with single photons, a one-photon state $|1_{\mathrm{H}}, 0_{\mathrm{V}}\rangle$ could be generated by inserting a horizontally oriented polarizer $\widehat{P}$ directly after the PMF. Subsequently, the HWP rotates the polarization of the photon to anti-diagonal.

$$\widehat{P}\left|\Psi^{\mathrm{PMF}}\right\rangle = |1_{\mathrm{H}}, 0_{\mathrm{V}}\rangle \xrightarrow{\mathrm{HWP}} |0_{\mathrm{D}}, 1_{\mathrm{A}}\rangle = \frac{1}{\sqrt{2}}(|1_{\mathrm{H}}, 0_{\mathrm{V}}\rangle - |0_{\mathrm{H}}, 1_{\mathrm{V}}\rangle)\,. \tag{6.7}$$

The PBS of the Sagnac interferometer converts the polarization modes to spatial modes, which are both coupled to the different ends of a single-mode fiber coil. Transmitted photons thus propagate in a clockwise (↻) and reflect in a counterclockwise (↺)

direction through the single-mode fiber. Thus, the state coupled to the SMF can be denoted in a generalized form

$$\left|\Psi^{\mathrm{in}}\right\rangle = \frac{1}{\sqrt{2}}\left(|N_{\circlearrowleft}, 0_{\circlearrowright}\rangle - |0_{\circlearrowleft}, N_{\circlearrowright}\rangle\right), \tag{6.8}$$

with N being either 1 or 2 in case of a measurement with or without the polarizer, respectively. In the fiber, the photons undergo a relative phase shift which is described by the operator $\widehat{U}(\phi) = \mathrm{e}^{\mathrm{i}\widehat{N}\phi}$, whereby $\widehat{N} = \widehat{\mathsf{a}}^{\dagger}\,\widehat{\mathsf{a}}$ represents the photon number operator. Consequently, the state at the output of the fiber can be written as

$$\left|\Psi^{\mathrm{out}}\right\rangle = \widehat{U}\ \left|\Psi^{\mathrm{in}}\right\rangle = \frac{1}{\sqrt{2}}(|N_{\circlearrowleft}, 0_{\circlearrowright}\rangle - \mathrm{e}^{\mathrm{i}N(\phi_{\mathrm{S}}(\Omega)+\phi_0)}\,|0_{\circlearrowleft}, N_{\circlearrowright}\rangle). \tag{6.9}$$

where ϕ_0 accounts for an initial offset caused by the SMF. Subsequently, the photons leave the interferometer in port d after passing the PBS a second time. A HWP within the loop and a fiber polarization controller are used to match the polarization accordingly. Thus, the modes $\circlearrowleft$ and $\circlearrowright$ convert to polarization modes H and V, respectively.

$$\left|\Psi^{\mathrm{d}}\right\rangle = \frac{1}{\sqrt{2}}(|N_{\mathrm{H}}, 0_{\mathrm{V}}\rangle - \mathrm{e}^{\mathrm{i}N(\phi_{\mathrm{S}}(\Omega)+\phi_0)}\,|0_{\mathrm{H}}, N_{\mathrm{V}}\rangle). \tag{6.10}$$

Performing a polarization measurement, in the HV basis, in port d, provides information about the propagation direction of the photons in the coil. Such which-way information ($\circlearrowleft/\circlearrowright$) is not accessible if the measurement is carried out in a mutually unbiased bases e.g., DA basis. Consequently, the interference of these modes becomes visible. Such a measurement is realized by means of a HWP at 22.5° followed by a PBS with two APDs, one in each output.

Using the optional polarizer, only single photons ($N = 1$) are guided through the interferometer. The probability that such a photon arrives at APD_1 (APD_2) is indicated by P_1 (P_2).

$$\begin{aligned} P_1 &= \left|\left\langle 1_{\mathrm{D}}, 0_{\mathrm{A}}\right|\left.\Psi^{\mathrm{d}}\right\rangle\right|^2 = \sin^2\left(\frac{1}{2}\left(\phi_{\mathrm{S}}(\Omega)+\phi_0\right)\right) \\ P_2 &= \left|\left\langle 0_{\mathrm{D}}, 1_{\mathrm{A}}\right|\left.\Psi^{\mathrm{d}}\right\rangle\right|^2 = \cos^2\left(\frac{1}{2}\left(\phi_{\mathrm{S}}(\Omega)+\phi_0\right)\right) \end{aligned} \tag{6.11}$$

Since we assumed ideal conditions when deriving $\left|\Psi^{\mathrm{d}}\right\rangle$ (e.g., perfect transmission, no background, ideal input state $\left|\Psi^{\mathrm{PMF}}\right\rangle$), the probabilities P_1 and P_2 become zero when removing the polarizer. In the case of the resulting two-photon state ($N = 2$), coincidences between the detectors occur with a probability of

$$P_{1,2} = \left|\left\langle 1_{\mathrm{D}}, 1_{\mathrm{A}}\right|\left.\Psi^{\mathrm{d}}\right\rangle\right|^2 = \cos^2\left(\phi_{\mathrm{S}}(\Omega)+\phi_0\right) \tag{6.12}$$

With the detectors used, the cases where both photons end up at the same APD

$$\begin{aligned} P_{1,1} &= \left|\left\langle 2_{\mathrm{D}}, 0_{\mathrm{A}} \middle| \Psi^{\mathrm{d}} \right\rangle\right|^2 = \frac{1}{2}\sin^2\left(\phi_{\mathrm{S}}(\Omega) + \phi_0\right) \\ P_{2,2} &= \left|\left\langle 0_{\mathrm{D}}, 2_{\mathrm{A}} \middle| \Psi^{\mathrm{d}} \right\rangle\right|^2 = \frac{1}{2}\sin^2\left(\phi_{\mathrm{S}}(\Omega) + \phi_0\right) \end{aligned} \tag{6.13}$$

cannot be distinguished from single events present in the experiment. However, as Ω increases, the probability $P_{1,2}$ and thus the count rate $R_{N=2} \propto P_{1,2}$ oscillate faster than $R_{N=1} \propto P_2$. This increase in fringe frequency is known as super-resolution.

6.3 Results

Two sequential measurement runs were performed using a one-photon state ($N = 1$) and a two-photon NOON state ($N = 2$), with and without the polarizer, respectively. For each run, the angular velocity was increased gradually from $\Omega = 0$ to $\Omega = 5.6\,\mathrm{rad/s}$, resulting in a full 2π phase shift according to Equation 6.10. For each setting of Ω we accumulated data for a total of $\sim 19\,\mathrm{s}$ and evaluated the one-photon (two-photon) count rates $R_{N=1}$ ($R_{N=2}$) with an integration time $\tau_1 = 5\,\mathrm{ms}$ ($\tau_2 = 20\,\mathrm{ms}$), leading to ~ 3800 (~ 950) data points per angular velocity setting. The different integration times used in the measurements account for the rarity of detected two-photon events compared to the one-photon events. Thus, in both measurements about the same number of detected photons per data point were processed. Figure 6.4(top) shows the single photon count rate $R_{N=1}$ of APD_2 during the first measurement run, whereas Figure 6.4(bottom) shows the two-photon coincidence count rate $R_{N=2}$ between APD_1 and APD_2 obtained in the second measurement run.

A comparison of the two graphs clearly shows the increased fringe oscillation frequency of $R_{N=2}$. The data of both measurements is fitted with the function

$$R_N(\Omega) = \frac{M_N}{N}\cos^2\left(\frac{N}{2}\left(S_N\,\Omega + \phi_{0N}\right)\right) + B_N \tag{6.14}$$

with $N \in \{1, 2\}$ and the fit parameters M_N, B_N, S_N and ϕ_{0N}, wheres M_N denotes the total number of photons detected per integration time τ_N, in the respective photon state. The amplitude in Figure 6.4(top) is about twice as large as in Figure 6.4(bottom), but M_N is approximately the same for both measurement runs (~ 2000). The scaling factor S_N is expected to be approximately equal to the value $S = 1.09$, as calculated in Section 6.2.2, and the phase shift caused by the fiber coil ϕ_{0N} was set to $\sim \pi/2 = 1.57$ using the fiber-polarization-controller. The background B_N results mainly from uncorrelated residual background counts but also from imperfect overlap of the counter propagating modes. The best-fitting parameters are presented in Table 6.1. The error estimation of the fit parameters was determined via bootstrapping.

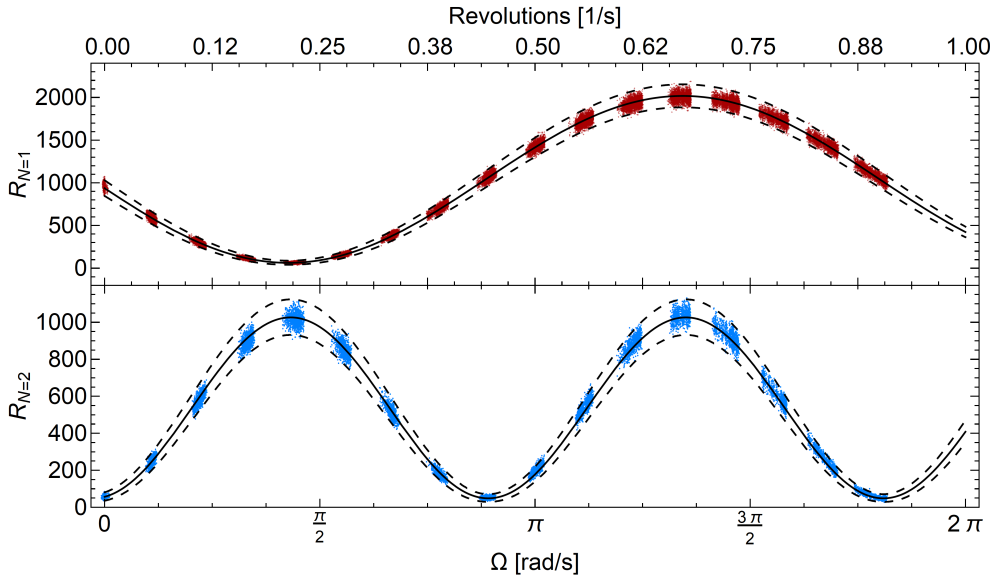


Figure 6.4 Count rate vs. angular velocity Ω: The red (blue) dots in the top (bottom) graph indicate the detected number of single- (two-) photon counts $R_{N=1}$ ($R_{N=2}$) per $\tau_1 = 5\,\text{ms}$ ($\tau_2 = 20\,\text{ms}$). The plotted measurement series consists of 64,688 (16,204) individual measurements of $R_{N=1}$ ($R_{N=2}$). The solid black line is a fit function of the form of 6.14. The dashed lines indicate the 99% confidence interval around the fitted function if only Poissonian error of the predicted count rate is assumed. Those lines contain 97.25% (95.88%) of the measured data, which is less than 99% due to unresolved phase errors. Revised version of Figure 2 in [64].

	M_N	B_N	S_N	ϕ_{0N}
$N = 1$	1955 ± 1	63 ± 1	$1.09179 \pm (0.09 \times 10^{-3})$	$1.6767 \pm (0.23 \times 10^{-3})$
$N = 2$	1956 ± 1	49 ± 1	$1.08903 \pm (0.15 \times 10^{-3})$	$1.6629\pm)0.47 \times 10^{-3})$

Table 6.1 Fit parameters of Equation 6.14 as plotted in Figure 6.4.

The vertical distribution of the individual measurements with respect to the fit function (see Figure 6.4) is caused by statistical count rate fluctuations. A Pearson chi square test was performed with the data collected at $\Omega = 0$ (see Figure 6.5). This test, with the null hypothesis of Poisson-distributed count rates, yielded a p-value of 0.78 (0.86) for the first (second) measurement run. These values correspond to the probability that a count rate distribution with even greater deviation from a Poisson distribution is observed, even if the source is perfectly Poisson. The observed count rate distribution is thus very well described by a Poisson distribution.

The horizontal distribution of the individual measurements in Figure 6.4, stems from variations in the rotational velocity of the modified cement mixer. The period of

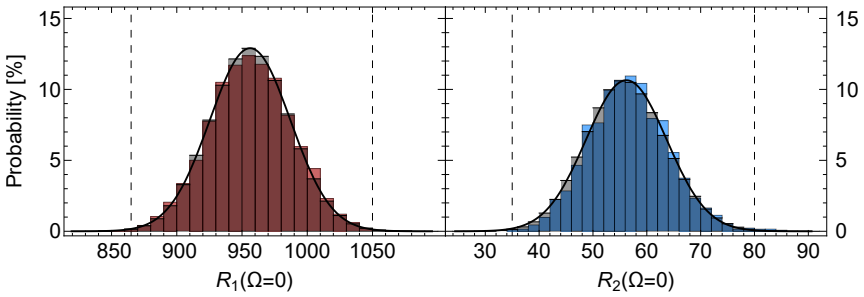
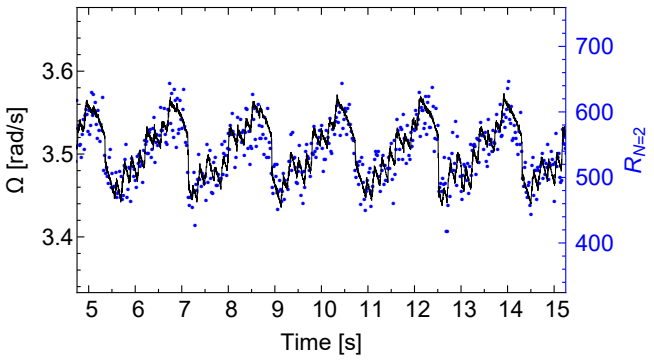


Figure 6.5 Histogram of the count rates measured at a rotational velocity of $\Omega = 0$. The red (blue) graph corresponds to the first (second) measurement run with $\Omega = 0$. The gray bars represent a Poisson distribution with a mean value of $M_1 = 956$ ($M_2 = 56$). The dashed grid lines indicate the 99.73% confidence interval of this distribution, which includes 99.77% (99.47%) of the measured data. A Pearson chi-square test with the null hypothesis of Poisson-distributed count rates, revealed a p-value of 0.78 (0.86). A normal distribution with the same mean value and a standard deviation $\sqrt{M_1}$ ($\sqrt{M_2}$) is plotted as black solid line.

the variation with the largest amplitude corresponds to the duration of one revolution of the rotation platform, while the duration of the second largest contribution corresponds to one revolution of the drive wheel (gear ratio of 11:1). This deterministic variation of Ω was measured with a commercial gyro sensor. By knowing the timing of individual detection events, we were also able to resolve those variations with the FOG. Therefore, this variation does not affect further error calculations. The correlation of the coincidence count rate and the rotational velocity, as measured by the commercial gyro sensor, is shown in Figure 6.6.

Figure 6.6 Coincidences $R_{N=2}$ and angular velocity Ω vs. time: The angular velocity Ω varies in time and was measured with a commercial gyroscope (black solid line). The blue dots indicate the coincidence count rate $R_{N=2}$, with integration time of 20 ms. The period of the variation corresponds to the duration of one completion revolution (1.8 s). Revised version of Figure 3 in [64].



6.4 Precision Beyond the Shot-Noise Limit

6.4.1 Estimation Based on Fitting Parameters

The shot-noise limit is a strict bound on the minimum phase shift $\Delta\phi > \Delta\phi_{\mathrm{SNL}} = 1/\sqrt{M}$ that is resolvable with a coherent state of light with a mean photon number M. The fundamental limit in quantum mechanics is the Heisenberg limit $\Delta\phi_{\mathrm{HL}} = 1/M$, which retains its validity for arbitrary photon states. With quantum devices one may exhibit sub-SNL phase sensitivity $\Delta\phi_{\mathrm{HL}} < \Delta\phi < \Delta\phi_{\mathrm{SNL}}$.

We are interested in the precision of the rotational velocity, which is proportional to the phase shift caused by the Sagnac effect $\Delta\Omega \propto \Delta\phi_{\mathrm{S}}$ (see Equation 6.4). Considering the coil geometry as given (fixed scaling factor S), we compare the precision, which was achieved with 2000 single ($N = 1$) or pairwise path-entangled ($N = 2$) photons. In order to get a measure of the rotational velocity Ω_E, we use the inverse function of Equation 6.14.

$$\Omega_E(R_N) = \frac{1}{S_N}\left(2/N\cos^{-1}\left(\sqrt{\frac{N(R_N - B_N)}{M_N}}\right) - \phi_{0N}\right) \tag{6.15}$$

The uncertainty in the measured velocity attributed to the Poisson distribution of R_N (see Figure 6.5) can be estimated via propagation of uncertainty $\Delta\Omega_E(R_N) = |\partial\Omega_E/\partial R_N|\sqrt{R_N}$. Usually, gyroscopes are operated at the point of best precision, which is called bias point. The expected count rate at such point R_N^{Bias} can be calculated by minimizing $\Delta\Omega_E(R_N)$ as a function of R_N, resulting in

$$\begin{aligned} R_N^{\mathrm{Bias}} &= \sqrt{B_N\left(M_N/N + B_N\right)} \\ &= \sqrt{R_N^{\mathrm{Min}} R_N^{\mathrm{Max}}} \end{aligned} \tag{6.16}$$

with

$$\begin{aligned} R_N^{\mathrm{Min}} &= B_N \\ R_N^{\mathrm{Max}} &= M_N/N + B_N. \end{aligned}$$

That ϕ_{0N} can be set such that R_N^{Bias} corresponds to any Ω of interest. The precision at the bias point is given by

$$\begin{aligned} \Delta\Omega_E(R_N^{\mathrm{Bias}}) &= \frac{1}{S_N\sqrt{NM_N}\sqrt{1 + 2N/M_N\left(B_N - \sqrt{B_N\left(M_N/N + B_N\right)}\right)}} \\ &= \frac{1}{S_N N\sqrt{R_N^{\mathrm{Max}} + R_N^{\mathrm{Min}} - 2R_N^{\mathrm{Bias}}}}. \end{aligned} \tag{6.17}$$

In the limit of zero background Equation 6.17 yields

$$\lim_{B\to 0} \Delta\Omega_E^{\text{Bias}} = 1/(S_N\sqrt{M_N N}), \tag{6.18}$$

which represents with $N = 1$ the SNL of the measurement system. Using the fit parameters of Table 6.1, results in a limit of $\Delta\Omega^{\text{SNL}} = 0.0207\,\text{rad/s}$. By using NOON states one expects improved precision which decreases towards the Heisenberg limit $\lim_{N\to M_N} \Delta\Omega^{\text{SNL}} = \Delta\Omega^{\text{HL}} = 1/(S_N M) = 469 \times 10^{-6}\,\text{rad/s}$.

The precision at the bias point of the first measurement run can be estimated with Equation 6.17 and yields a value of $\Delta\Omega_E(R_1^{\text{Bias}}) = 0.02478\,\text{rad/s}$. This value is slightly worse than $\Delta\Omega^{\text{SNL}}$ mainly because of the background. In the case of the second measurement run, Equation 6.17 yields $\Delta\Omega_E(R_2^{\text{Bias}}) = 0.01832\,\text{rad/s}$, which is an improvement in precision over the first measurement as well as against $\Delta\Omega^{\text{SNL}}$. This estimation of $\Delta\Omega$ based on the fit parameters thus confirms sub-SNL precision of the second measurement run.

	$\Delta\Omega^{\text{SNL}}$		$\Delta\Omega_E(R_N^{\text{Bias}})$		$\Delta\Omega^{\text{HL}}$
$N = 1$	0.0207	$\not>$	0.0248	$>$	469×10^{-6}
$N = 2$		$>$	0.0183	$>$	

Table 6.2 Comparison of the measurement precision achieved with $M = 1955$ photons detected on average. The precision at the bias point $\Delta\Omega_{\text{Bias}}^{\text{E}}$, is estimated via fit parameters of Table 6.1. $\Delta\Omega^{\text{SNL}} = 1/(S\sqrt{M})$, and $\Delta\Omega^{\text{HL}} = 1/(SM)$ is the shot-noise limit and Heisenberg limit of the measurement system, with a scale factor $S = 1.09$, respectively. All values are given in rad/s.

6.4.2 Estimation Based on Residuals

Equation 6.15 assigns a rotational velocity value to each measured count rate $\Omega_E(R_N^i)$. Those values deviate from the reference value Ω, as measured with an commercial gyro sensor. These residuals $(\Omega_E(R_N^i) - \Omega^i)$ are approximately normally distributed with a standard deviation $\Delta\Omega$ (see Figure 6.7), which yields the experimentally determined precision of a single measurement consisting of 2000 photons.

Notice that the precision of the reference sensor is $1.7\,\mu\text{rad/s}$ and therefore one order of magnitude smaller than the expected value of our device. We estimated $\Delta\Omega$ for each block of measurements with similar rotational velocity. The values are plotted along with the absolute values of the residuals in Figure 6.8. The uncertainty of the measured precision is calculated by bootstrapping.

The best precision $\Delta\Omega_{\text{min}}$ of the respective measurement run was determined with the data enlarged in Figure 6.8, which are close to the bias-point. The precision of

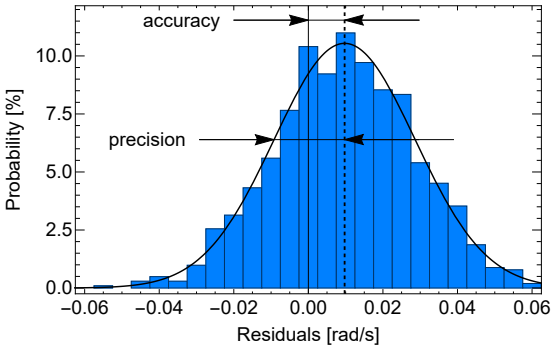


Figure 6.7 Histogram of residuals $\Omega_E(R_N^i) - \Omega^i$. The data used for the histogram are from the second measurement run and the block with the smallest precision measured (enlarged in Figure 6.8(bottom)). This data set has a precision of 0.0189 ± 0.0004 rad/s and an accuracy (systematic errors) of 0.0097 ± 0.0007 rad/s. A fitted normal distribution is plotted in black.

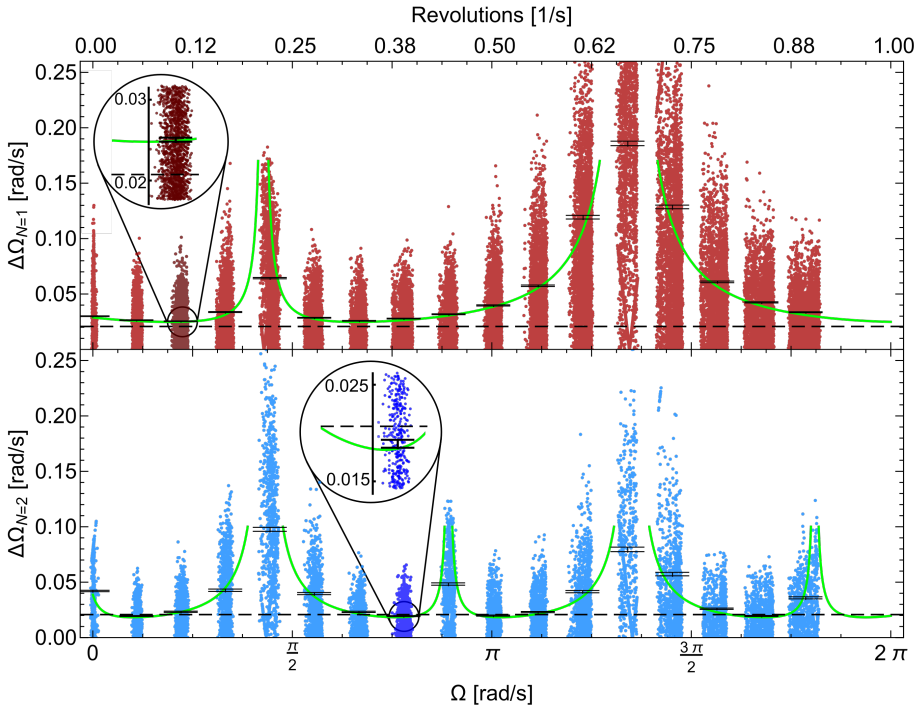


Figure 6.8 Measured precision $\Delta\Omega$ vs. rotational velocity Ω. The absolute values of the residuals $|\Omega_E(R_N^i) - \Omega^i|$ are plotted as red dots (blue dots) in the top (bottom) graph for the first (second) measurement run with $N = 1$ ($N = 2$). The measured precision —including uncertainty calculated by bootstrapping— of each measurement block is indicated by black error bars. The dashed line represents the shot-noise limit $\Delta\Omega^{\mathrm{SNL}}$. The uncertainty estimated via $\Delta\Omega_E(R_N(\Omega))$ is indicated by a solid green line. The measurement block with the best precision (darker colored) is magnified in the in-set. Revised version of Figure 4 in [64].

the NOON state measurement is, mainly due to background, slightly worse than the theoretical predicted limit $\Delta\Omega^{\mathrm{SNL}}/\sqrt{2} = 0.0146\,\mathrm{rad/s}$. Nevertheless, the measurement precision obtained with the two-photon state outperforms the one-photon state and is

below $\Delta\Omega^{\mathrm{SNL}}$ thus demonstrating sub-SNL precision.

	$\Delta\Omega^{\mathrm{SNL}}$		$\Delta\Omega_{\mathrm{min}}$	$\Delta\Omega_E(R_N^{\mathrm{Bias}})$		$\Delta\Omega^{\mathrm{HL}}$
$N=1$	0.0207	$\not>$	0.0250 ± 0.0002	0.0248	$>$	469×10^{-6}
$N=2$		$>$	0.0189 ± 0.0004	0.0183	$>$	

Table 6.3 Comparison of the measurement precision achieved with $M = 1955$ photons detected on average. $\Delta\Omega_{\mathrm{min}}$ denotes the best precision of the respective measurement run (enlarged in Figure 6.8). The precision at the bias point $\Delta\Omega^{\mathrm{E}}_{\mathrm{Bias}}$, is estimated via fit parameters of Table 6.1.$\Delta\Omega^{\mathrm{SNL}} = 1/(S\sqrt{M})$ and $\Delta\Omega^{\mathrm{HL}} = 1/(SM)$ represent the shot-noise limit and Heisenberg limit of the measurement system, with a scale factor $S = 1.09$, respectively. All values are given in rad/s.

6.5 Loss

So far we have used our gyroscope to investigate the precision of measurements consisting of $M \sim 2000$ detected photons. An equal number M for the two tested states was experimentally achieved by adjusting the integration time accordingly. Using path-entangled two-photon sates, we observed an advantageous effect on the measurement precision that cannot be achieved with classical resources alone. However, the presented FOG is not yet competitive with classical devices using brighter photon sources. Assuming NOON states with comparable brightness, a further disadvantage of these states would have to be considered. Such states are more susceptible to loss, since all N photons of such a state must be detected in order to obtain phase information. This vulnerability of the photonic states is of crucial importance when comparing measurements with an equal amount of photons at the input of the interferometer. For such scenarios, certain transmission thresholds required for actual sensor improvement can be calculated [37, 91, 92]. With the NOON state "chopping" strategy [39, 40], the state used for the measurement can be optimized for a limited total transmissivity of the system η (including detection efficiency). The key point of this strategy is to adjust the photon number N of a NOON state to $N < 1/(1-\eta)$. Thus, the inequality

$$\eta > 1 - \frac{1}{N} \tag{6.19}$$

indicates whether a NOON state consisting of N photons is the optimal choice for the measurement system. The transmission and detection probabilities of photons, of our FOG , are shown in Table 6.4. The transmissivity of the interferometer alone is close to the 50% limit for $N = 2$ states.

In the following, we will examine the conditions for NOON states to be advantageous

	Source	Interferometer	Detection	Total
η	0.319	0.485	0.64	0.1

Table 6.4 Probabilities of transmission and detection of photons in the FOG.

in FOGs. In doing so we assume a mean number of photons at the input of the interferometer M_0 and consider shot noise of the count rate, the transmissivity of the single-mode-fiber η_{SMF}, as well as the transmissivity of the remaining setup η_0 (including detection efficiency). Thus, a number of $M = M_0(\eta_0\ \eta_{\mathrm{SMF}}(\lambda, L))^N$ detected photons is expected. In the limit of zero background, Equation 6.17 yields a precision of

$$\begin{aligned}\Delta\Omega_E^{\mathrm{Bias}}(L,N) &= \frac{1}{S_N\sqrt{NM_0(\eta_0\ \eta_{\mathrm{SMF}}(\lambda,L))^N}} \\ &= \frac{\lambda\ c}{4\pi LR\sqrt{NM_0(\eta_0\ 10^{-\alpha(\lambda)\ 10^{-4}\ L})^N}},\end{aligned} \tag{6.20}$$

with the attenuation coefficient of the optical fiber $\alpha(\lambda)$ expressed in units of dB/km. This approximation predicts improved precision for arbitrarily larger radii and higher count rates. However, there is an optimum for the fiber length. At a wavelength of $\lambda = 1550\,\mathrm{nm}$, the attenuation coefficient α is about 0.18 dB/km [93]. Figure 6.9 shows the precision $\Delta\Omega_E^{\mathrm{Bias}}(L,1)$ and $\Delta\Omega_E^{\mathrm{Bias}}(L,2)$ for such wavelength as a function of L for both $\eta_0 = 1$ (solid lines) and $\eta_0 = 0.6$ (dashed lines).

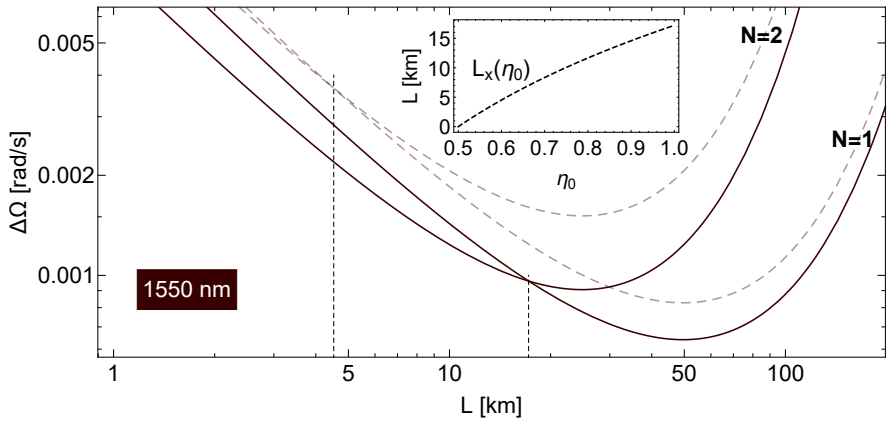


Figure 6.9 Precision vs. fiber length L ($\lambda = 1550\,\mathrm{nm}$): The precision $\Delta\Omega_E^{\mathrm{Bias}}(L, N = 1)$ and $\Delta\Omega_E^{\mathrm{Bias}}(L, N = 2)$ for $\eta_0 = 1$ (solid lines) and $\eta_0 = 0.6$ (dashed lines) are calculated by Equation 6.20 with $R = 0.1$ m, $\lambda = 1550$ nm, $\alpha = 0.18$ dB/km and $M_0 = 1000$. The dotted grid lines indicate the fiber length L_{X} at which the precision of $N = 1$ and $N = 2$ states are equal. The insert shows how L_{X} changes with η_0.

From Equation 6.20 and Figure 6.9 we conclude that the best precision is obtained

with one-photon states. This optimum is achieved with a fiber length of $L^{\mathrm{Opt}}(\lambda, N) = \frac{2\times10^4}{\alpha(\lambda)\ N\ \log(10)}$ which results in 49.6 km with $\lambda = 1550\,\mathrm{nm}$ and $N = 1$. The fiber length of commercially available gyroscopes is shorter than the calculated optimum. This is intended either to reduce the volume and weight [66] or to avoid additional phase noise (e.g., Shupe effect and Magneto-optic Faraday effect [85]), proportional to the fiber length but not considered in our model. Shorter fibers increase the overall transmission of the FOG, which in turn favors the use of NOON states. The precision of N and $(N-1)$ photon states perform equally well at a fiber length of

$$L_{\mathsf{X}}(\eta_0, N) = \frac{10^4 \log\left(\eta_0\ \frac{N}{N-1}\right)}{\alpha(\lambda)\ \log(10)}, \tag{6.21}$$

with $N \in \{\mathbb{N} \mid N \geq 2\}$. For shorter fiber lengths, however, the N-photon state is preferred. Thus, an improvement of the precision by using NOON states can be achieved if the length of the fiber coil is shorter than $L_{\mathsf{X}}(\eta_0, N)$. This statement is equivalent[†] to Equation 6.19 with $\eta = \eta_0\ \eta_{\mathrm{SMF}}$. Thus, if the transmissivity η_0 is less than 50%, L_{X} becomes negative, which means that the $N = 1$ state is a better choice regardless of the fiber length.

When deriving L_{X}, the same wavelength was assumed for both states. In fact, different wavelengths are ideal for different fiber lengths and given N-photon states. An optimal wavelength can be calculated numerically using Equation 6.20 and a toy model of the attenuation in a fused silica fiber [93]

$$\begin{aligned} \alpha(\lambda) &= \alpha_{Ray}(\lambda) + \alpha_{IR}(\lambda) \\ \alpha_{Ray}(\lambda) &= 1.7\ \left(\frac{0.85\times10^{-6}}{\lambda}\right)^4 \\ \alpha_{IR}(\lambda) &= 6\times10^{-11}\ \mathrm{e}^{-\frac{48\times10^{-6}}{\lambda}} \end{aligned} \tag{6.22}$$

with the attenuation coefficients α_{Ray} and α_{IR} attributed to the Rayleigh scattering and infrared absorption within the fiber, respectively. Figure 6.10 shows the precision calculated with the optimized wavelength $\Delta\Omega_E^{\mathrm{Bias}}(L, 1, \lambda^{\mathrm{Opt}}(L, 1))$ and $\Delta\Omega_E^{\mathrm{Bias}}(L, 2, \lambda^{\mathrm{Opt}}(L, 2))$ as a function of the fiber length for both $\eta_0 = 1$ (solid lines) and $\eta_0 = 0.8$ (dashed lines).

Figure 6.10 illustrates that wavelengths shorter than 1550 nm are advantageous for precision if the fiber length is less than 49.6 km. The optimized wavelength for states with $N > 1$ is shifted towards 1550 nm compared to states with $N = 1$ and the same fiber length. This is due to a higher loss at shorter wavelengths in the fiber.

[†] $\left(\frac{\Delta\Omega_E^{\mathrm{Bias}}(L,N-1)}{\Delta\Omega_E^{\mathrm{Bias}}(L,N)}\right)^2 = \frac{N(\eta_0\ \eta_{\mathrm{SMF}}(\lambda,L))^N}{(N-1)(\eta_0\ \eta_{\mathrm{SMF}}(\lambda,L))^{N-1}} = \frac{N}{N-1}(\eta_0\ \eta_{\mathrm{SMF}}(\lambda,L)) > 1$

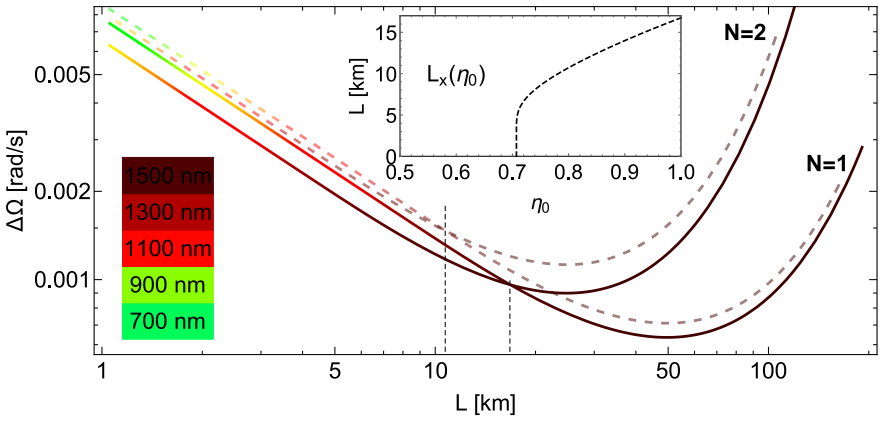


Figure 6.10 Precision vs. fiber length L with optimized wavelength: The precision $\Delta\Omega_E^{\text{Bias}}(L, N=1, \lambda^{\text{Opt}}(L, N=1))$ and $\Delta\Omega_E^{\text{Bias}}(L, N=2, \lambda^{\text{Opt}}(L, N=2))$ for $\eta_0 = 1$ ($\eta_0 = 0.8$) are represented by solid lines (dashed lines). The wavelength λ^{Opt} is indicated by the color of the lines. The precision is numerically calculated with $R = 0.1$ m, $M_0 = 1000$ and an attenuation coefficient given in Equation 6.22. The dotted grid lines indicate the fiber length L_{X} at which the precision of $N = 1$ and $N = 2$ states are equal. The insert shows how L_{X} changes with η_0.

For $L << L^{\text{Opt}}$ and thus short optimal wavelengths, the attenuation coefficient can be approximated by the contribution of Rayleigh scattering $\widetilde{\alpha}(\lambda) \simeq \alpha_{Ray}(\lambda)$. Since the optimum wavelength in this range is $\widetilde{\lambda}^{\text{Opt}}(L, N) \propto \sqrt[4]{L\,N}$, the ratio of the precision achieved with N and $(N-1)$ photon states given by

$$\frac{\Delta\Omega_E^{\text{Bias}}(L, N-1, \widetilde{\lambda}^{\text{Opt}}(L, N-1))}{\Delta\Omega_E^{\text{Bias}}(L, N, \widetilde{\lambda}^{\text{Opt}}(L, N))} = \sqrt{\eta_0 \sqrt{\frac{N}{N-1}}} \tag{6.23}$$

is independent of the fiber length. This equation represents the precision gain achieved, in an optimized FOG with practical fiber length ($L << L^{\text{Opt}}$), by using an N-photon state versus an $(N-1)$-state. If only the fiber loss of such a device is taken into account ($\eta_0 = 1$), Equation 6.23 shows that two-photon NOON states ($N = 2$) perform 1.19 times better than the one-photon state. This improvement in precision disappears as soon as

$$\eta_0 < \sqrt{1 - \frac{1}{N}}. \tag{6.24}$$

Thus, the best precision of optimized FOGs with limited fiber length ($L << L^{\text{Opt}}$) is also achieved with one-photon ($N = 1$) states if the transmissivity η_0 is less than $\frac{1}{\sqrt{2}} = 0.7071$.

6.6 Conclusion

In this chapter, a fiber-optic gyroscope was presented which can be used with both single photons and two-photon NOON states. We used this device to experimentally demonstrate the effect of super resolution. The increased fringe oscillation frequency of the coincidence count rate $R_{N=2}$ with respect to the single photon count rate $R_{N=1}$, referred to as super-resolution, is illustrated in Figure 6.4. The fringe period is reduced by a factor of $S_2/(\frac{1}{2}S_1) = 1.995 \pm (0.4 \times 10^{-3})$. The deviation from the theoretically expected value two is in the order of 10 standard deviation of the specified error (calculated from fit parameters). This deviation may be due to systematic errors such as variations of the scale factor S, e.g., due to changes of the enclosed area $A_{\circlearrowleft}$. Nevertheless, the inconsistency is rather small given the poor thermal and mechanical stabilization of the fiber. However, the ratio is significantly greater than 1, by means of 2487 standard deviations, which bears witness to super-resolution.

Furthermore we investigated the precision of measurements consisting of $M \sim 2000$ detected photons. An equal number M for the tested states was experimentally achieved by adjusting the integration time accordingly. Using path-entangled two-photon sates, we observed a precision close to the bias point $\Delta\Omega_{\min}$ (see Table 6.3) that is somewhat worse than the theoretically predicted limit $\Delta\Omega^{\mathrm{SNL}}/\sqrt{2} = 0.0146\,\mathrm{rad/s}$ mainly due to the background. Nevertheless, the measured precision of the two-photon NOON state performs better than the one-photon state, and is better than $\Delta\Omega^{\mathrm{SNL}}$. Such sub-SNL precision can never be achieved with coherent states of light.

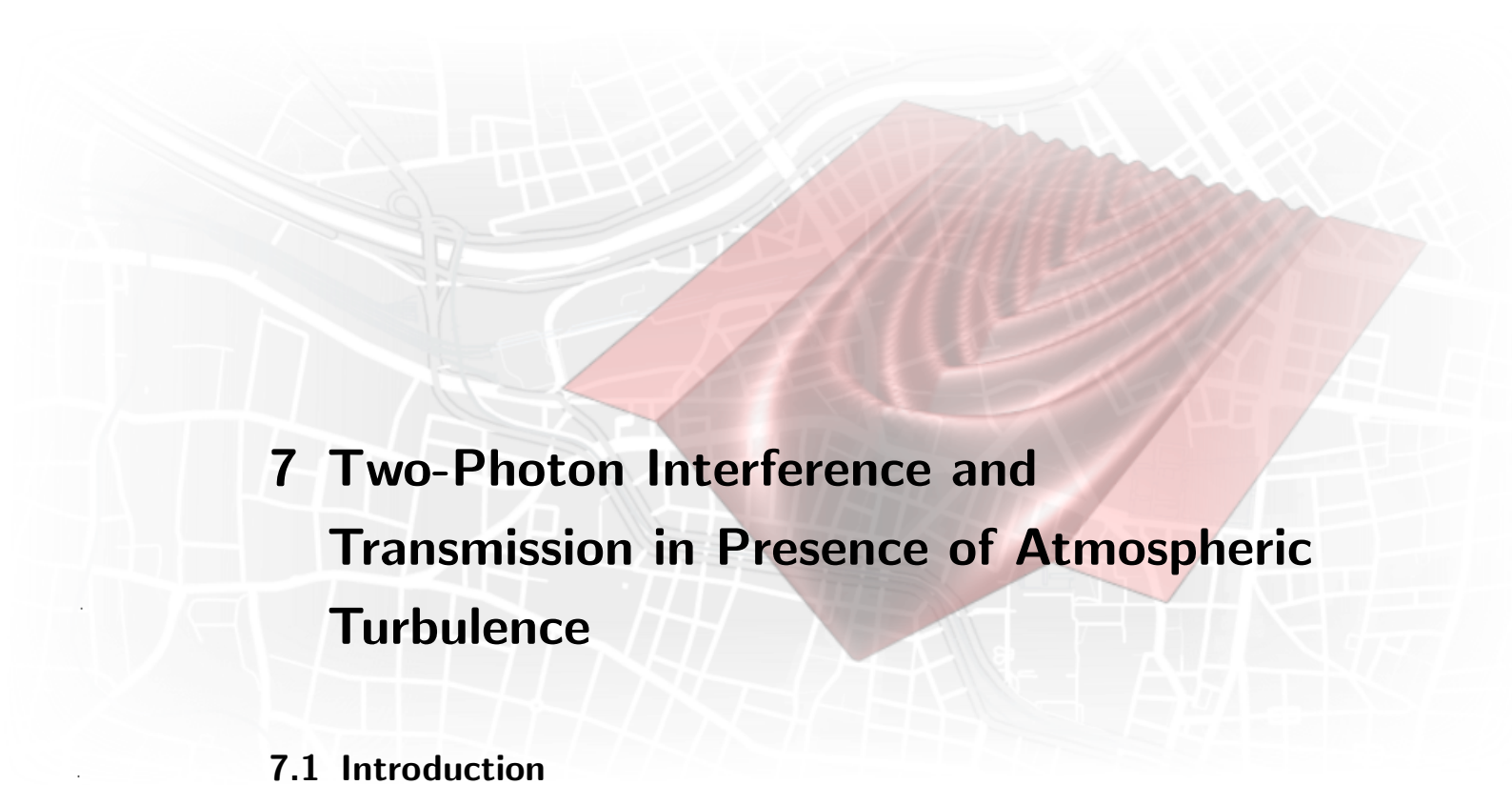
At this point we should stress, however, that the presented technology is not yet competitive with classical devices. Laser-driven FOG [84] uses an optical power of approx. $20\,\mu\mathrm{W}$, which corresponds to a rate of 156×10^{12} photons per second (at $\lambda = 1550\,\mathrm{nm}$). In contrast, the detected photon rate of the NOON state is 100×10^3 in our experiment. This relatively low photon rate was limited by the detectors used, whose efficiency decreases with increasing count rate.

In the last section of this chapter, we investigated the question of the extent to which a source of path-entangled photons with comparable brightness could provide a measurement advantage for FOGs. We discussed the vulnerability of the states due to loss, in conjunction with the fiber length, wavelength, and scaling factor of the gyroscope. Using a simple model for the loss mechanisms in an optical fiber and considering shot noise of the count rate and the transmissivity of the remaining setup η_0, we found an optimal configuration for FOGs that favors the use of one-photon states ($L = 49.6\,\mathrm{km}$, $\lambda = 1550\,\mathrm{nm}$ and $N = 1$). In practice, however, such long fibers are

avoided, as they have adverse effects (e.g., Shupe-effect and Magneto-optic Faraday effect) on the precision, which are not taken into account in our models [85]. Shorter fibers also serve the purpose of reducing the volume and weight of the device [66].

However, for fiber lengths $L < 16\,\mathrm{km}$ we were able to derive a measurement advantage based on NOON states. This improvement disappears if the transmissivity of the gyroscope η_0 (without fiber loss) is less than $\frac{1}{\sqrt{2}}$. Thus, the best precision of optimized FOGs with limited fiber length is also achieved with one-photon states ($N = 1$) if $\eta_0 < 0.7071$.

Finally, we would like to point out that the power circulating in the interferometer cannot be increased arbitrarily due to detrimental power-dependent effects such as coherent back-scattering [84] or nonlinear Kerr effects [85]. The interplay of noise sources and shot noise does not equate to a limitation of the number of photons used for the measurement. For FOGs, the key question is to what extent different photonic states respond to individual noise sources in order to verify whether the trade-off between these effects represents a net increase in precision. At the count rates we used, quantization noise is the dominant source of error. Thus, the minimal achievable phase resolution, which results from an interplay of all sources of noise cannot yet be measured. With the speed of ongoing developments in advancing detector technology and increasingly brighter photon sources such experiments may become feasible in the foreseeable future.



7 Two-Photon Interference and Transmission in Presence of Atmospheric Turbulence

7.1 Introduction

The distribution of entangled photons through turbulent atmosphere over terrestrial long distances with high fidelity has been proven in several experiments [11, 94, 95]. This pioneering work and the promise of an unconditional secure cryptographic key provided by shared entanglement [8] pushed research to first satellite experiments [96]. All of these proof-of-concept studies are optical direct connections, i.e. sharing photons directly between two parties. One way to create nodes in a quantum network is based on entanglement swapping [97, 98], which is a protocol that entangles independent photons via second-order interference.

So far, swapping has been demonstrated over a long distance between the Canary Islands of La Palma and Tenerife, with one photon being sent after the swapping protocol [99]. For a future global quantum network, a technology is required that allows the interference of two photons received from different directions. The challenge is to superimpose both photons on a beam splitter within their coherence time and ensure their indistinguishability. A technical solution to this issue can be expected in the near future.

In order to gain initial insights into the quality of multi-photon interference in the presence of turbulence, we conducted an experiment with a two-photon state traversing a 1.2 km-long, intra-city, free-space link. The receiver module used offers the possibility of generating a relative delay between the photons. Thus, we were able to measure a HOM dip of a collinearly transmitted photon pairs exposed to atmospheric turbulence. This experiment is not only a first step towards quantum interference between photons that have traversed independent atmospheric conditions, as required to perform the network-enabling entanglement swapping protocol with independent sources, but may also provide valuable insights into the transmission of multi-photon states for sensing and advancing quantum communication protocols with high-dimensional state encoding.

7.2 Methods

7.2.1 Optical Setup

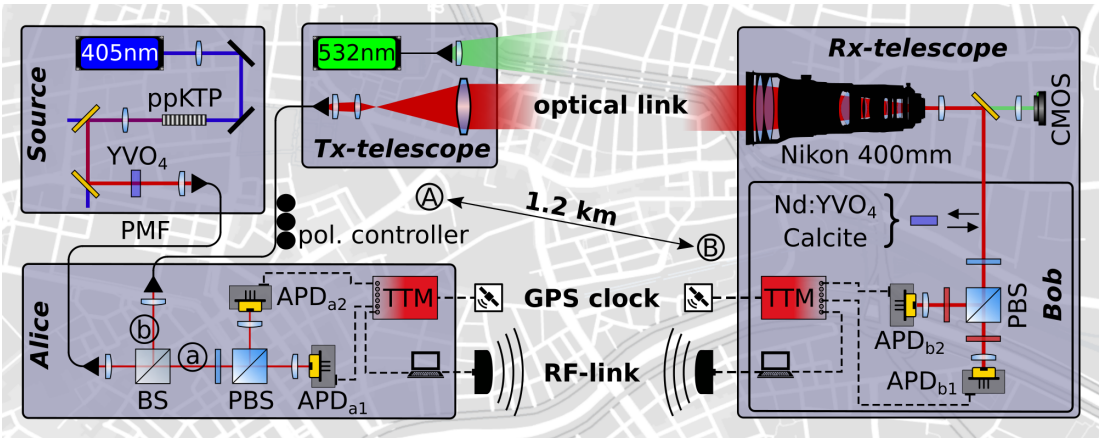


Figure 7.1 Experimental setup: Orthogonal polarized photon pairs are generated via SPDC (see Chapter 4) in a laboratory at IQOQI. A non-polarizing beam splitter (BS) — with otput modes a and b — within the Alice module creates a probabilistic splitting of the pairs. Photons in mode b are guided to a transmitter telescope on the roof of the institute and sent to Bob via a 1.2 km-long free-space link. The polarization of the photons collected using a telephoto objective is analyzed in Bob's measurement module, while photons in mode a are measured locally within the Alice module. Bob's measurement modules featured an additional polarization-dependent delay that could be inserted for HOM interference measurements.

The source generates horizontal and vertical polarized, but otherwise identical, signal and idler photons via SPDC in a degenerate collinear type II quasi-phase matching configuration at a wavelength of $\lambda = 810\,\mathrm{nm}$ (see Chapter 4). For the following experiments we used the same settings of the photon source as described in Section 4.3.1. A polarization maintaining single-mode fiber collects the down-converted photons and guides them to the Alice module. The non-polarizing beam splitter within this module generates an equal superposition of transmission (mode a) and reflection (mode b) for each individual photon (see Equation 5.1). Thus, the two-photon state $\left|\Psi^{\mathrm{PMF}}\right\rangle = |1_{\mathrm{H}}, 1_{\mathrm{V}}\rangle$ converts to

$$|\Psi\rangle = \frac{1}{2}\,|\Psi_{\mathrm{a,a}}\rangle + \frac{1}{2}\,\mathrm{e}^{-\mathrm{i}\varphi}\,|\Psi_{\mathrm{b,b}}\rangle + \frac{1}{\sqrt{2}}\,|\Psi_{\mathrm{a,b}}\rangle \tag{7.1}$$

with

$$|\Psi_{a,a}\rangle = \hat{a}^{\dagger}_{a,H}\hat{a}^{\dagger}_{a,V}\,|\mathrm{Vac}\rangle \tag{7.2a}$$

$$|\Psi_{b,b}\rangle = \hat{a}^{\dagger}_{b,H}\hat{a}^{\dagger}_{b,V}\,|\mathrm{Vac}\rangle \tag{7.2b}$$

$$|\Psi_{a,b}\rangle = \frac{1}{\sqrt{2}}\left(\hat{a}^{\dagger}_{a,H}\hat{a}^{\dagger}_{b,V} + \mathrm{e}^{-\mathbb{i}\varphi}\,\hat{a}^{\dagger}_{b,H}\hat{a}^{\dagger}_{a,V},\right)|\mathrm{Vac}\rangle \tag{7.2c}$$

where φ describes a polarization dependent phase shift between path a and b, which is accumulated over all optical elements in the respective paths. With a probability of $\frac{1}{2}$, both photons end up in the same mode. Therefore, 25% of the photon pairs can be detected in mode a as in mode b. The remaining 50% of the pairs lead to a polarization-entangled state, with one photon in each mode.

The photons in mode a, are guided to a local polarization measurement while mode b is optically connected to a transmitter telescope on the roof top via a 15-m-long single-mode fiber (780-HP). The phase shift φ was set to π by means of a fiber polarization controller, which was also used to match the polarization of Alice and Bob. Through the telescope, the photons are sent via an optical free-space channel to the receiver (Bob). The measurement modules of Alice and Bob each featured a polarization analyzer consisting of a half-wave plate, and a polarizing beam splitter, each equipped with avalanche photodiodes (Excelitas SPCM-800 see Section 3.1) in each output mode ($\mathrm{APD_{a1}}$, $\mathrm{APD_{a2}}$, $\mathrm{APD_{b1}}$, $\mathrm{APD_{b2}}$). Rotating the polarization of a photon in mode x, by means of a half-wave plate is described by the creation operator relation

$$\hat{a}^{\dagger}_{x,H} \xrightarrow{\mathrm{HWP}} \cos(2\theta_x)\,\hat{a}^{\dagger}_{x,H} + \sin(2\theta_x)\,\hat{a}^{\dagger}_{x,V} \tag{7.3a}$$

$$\hat{a}^{\dagger}_{x,V} \xrightarrow{\mathrm{HWP}} \cos(2\theta_x)\,\hat{a}^{\dagger}_{x,V} - \sin(2\theta_x)\,\hat{a}^{\dagger}_{x,H}, \tag{7.3b}$$

$$\tag{7.3c}$$

with θ_x denoting the angle between the horizontal polarization axes and the fast axes of the HWP. Subsequently, horizontally (vertically) polarized photons are transmitted (reflected) to mode 1 (2) of the PBS. Thus, the two-photon state in the output modes of Bob's detection module (b1, b2) is described by

$$|\Psi_{b,b}\rangle \xrightarrow{\text{HWP \& PBS}} \cos(4\theta_b)\,\hat{a}^{\dagger}_{b,1}\hat{a}^{\dagger}_{b,2}\,|\mathrm{Vac}\rangle + \frac{1}{2}\sin(4\theta_b)\,\left(\hat{a}^{\dagger}_{b,2}\hat{a}^{\dagger}_{b,2} - \hat{a}^{\dagger}_{b,1}\hat{a}^{\dagger}_{b,1}\right)|\mathrm{Vac}\rangle \tag{7.4}$$

Equation 7.4 only applies if the arriving photons differ only in their orthogonal polarization. In such a scenario, a HWP angle of $\theta_b = \pi/8$ results in a zero probability of detecting one photon in each mode $P_{b1,b2}(\theta_b) = \cos^2(4\theta_b)$. This effect results from HOM interference in polarization modes, i.e. two photons from different polarization

modes bunch into one mode. For the analysis of HOM interference, Bob's measurement module was equipped with the possibility of introducing an additional polarization-dependent delay via birefringent crystals of variable length. Such a delay $\Delta\tau$ reduces the temporal overlap of the down-converted photons and thus their indistinguishably [50, 52]. An explicit calculation for partially distinguishable photons (see Appendix A Equation A.13) yields a coincidence probability of

$$P_{\mathrm{b1,b2}}(\theta_{\mathrm{b}}, \Delta\tau) = \cos^2(4\theta_{\mathrm{b}}) + \frac{1}{2}\sin^2(4\theta_{\mathrm{b}}) \begin{cases} |\Delta\tau| / t_{\mathrm{coh}} & |\Delta\tau| < t_{\mathrm{coh}} \\ 1 & t_{\mathrm{coh}} \leq |\Delta\tau| \,. \end{cases} \tag{7.5}$$

From Equation 7.5 we find a random splitting of the photon pair $P_{\mathrm{b1,b2}}(\pi/8, \Delta\tau \geq t_{\mathrm{coh}}) = 1/2$ for temporal delays larger than the coherence time of the individual photons $t_{\mathrm{coh}} = 1.745 \pm 0.005\,\mathrm{ps}$ (see Section 4.3.3). Measurements with a neutral HWP position $\theta_{\mathrm{b}} = 0$ (HV basis) are unaffected by temporal delays $P_{\mathrm{b1,b2}}(0, \Delta\tau) = 1$, as long as the coincidence window $t_{\mathrm{coi}} = 2\,\mathrm{ns}$ is longer than the delay $\Delta\tau$.

During the experiment, the detection events at Alice and Bob were recorded relative to local 10 MHz GPS disciplined clocks and stored for post processing. Bob's measurement data was also streamed to Alice via an RF link where all combinations of two-photon detection events were monitored on-the-fly, while compensating for relative clock drifts [43]. Due to the detector jitter ($\sigma_t = 350\,\mathrm{ps}$*), using a coincidence window significantly smaller than $t_{\mathrm{coi}} = 2\,\mathrm{ns}$ leads to coincidence loss during post-processing (see Section 3.6).

7.2.2 Free-Space Link

The experiment depicted in Figure 7.1 was conducted with a transmitter (Tx) located at the Institute of Quantum Optics and Quantum Information† (IQOQI) and a receiving telescope (Rx) at the University of Natural Resources and Applied Life Sciences‡ (BOKU) in Vienna.

The photons from SPDC arrive at the Tx-platform via a single-mode fiber ($NA = 0.13\,\mathrm{rad}$). The divergent beam from the fiber is colliemiated by a lens ($f_{\mathrm{col}} = 18.4\,\mathrm{mm}$) and magnified ($M_{\mathrm{Tx}} = 11.2$) by a refractor consisting of two lenses ($f_1 = 25\,\mathrm{mm}$, $f_2 = 280\,\mathrm{mm}$, $\varnothing_2 = 70\,\mathrm{mm}$). Thus, the beam waist emitted by this telescope is $\omega_{\mathrm{Tx}} = 22\,\mathrm{mm}$, with a negligible divergence of $\Theta = 0.012\,\mu\mathrm{rad}$ (half angle). The photons from the source ($\lambda = 810\,\mathrm{nm}$) are additionally overlapped with an beacon laser ($\lambda \sim 532\,\mathrm{nm}$) for pointing, acquisition, and tracking (PAT). Both wavelengths are sent to a receiver telescope at BOKU via a 1.2 km-long optical free-space link.

*Standard deviation of detected arrival time of one detector

†Boltzmanng. 3, 1090 Vienna, Austria (48°13'16.52"N, 16°21'23.27"E)

‡Augasse 2-6, 1090 Vienna, Austria (48°13'54.05"N, 16°21'29.78"E)

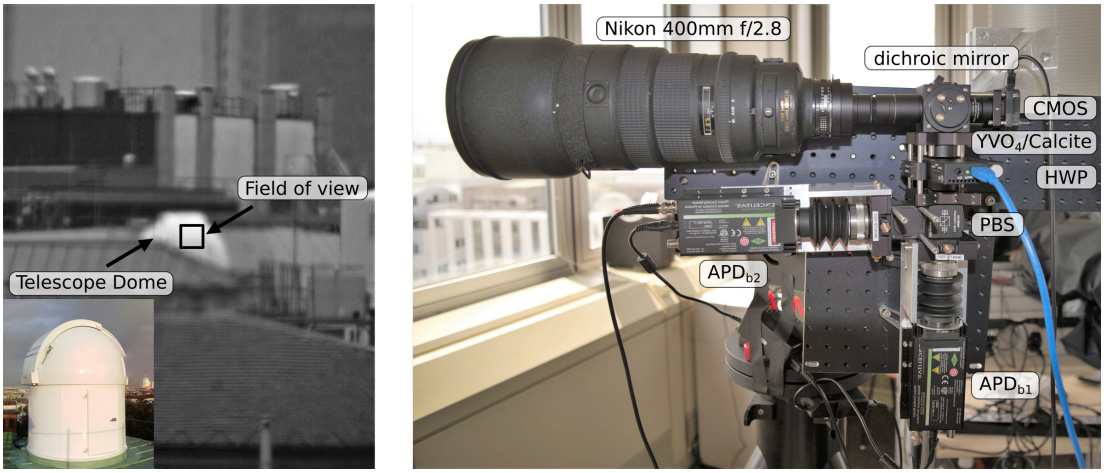


Figure 7.2 Dome of the Tx-Telescope (left) and Rx-Telecope (right). Right: A telephoto objective (Nikkor 400 mm f/2.8) at BOKU collects SPDC photons ($\lambda = 810\,\mathrm{nm}$) and light from an beacon laser ($\lambda \sim 532\,\mathrm{nm}$) sent from IQOQI. The two sent wavelengths are separated by a dichroic mirror, where the shorter wavelength is transmitted and subsequently focused on a CMOS camera, while the quantum signal is guided to Bob's measurement module depicted in Figure 7.1. **Left:** Image of the dome of the Tx-telescope, taken with CMOS camera at BOKU. The experimentally determined field of view of the single photon detectors ($\mathrm{APD_{b1}}$, $\mathrm{APD_{b2}}$) is framed in black.

The receiver telescope consists of a telephoto objective (Nikkor 400 mm f/2.8, $f_{\mathrm{Nik}} = 400\,\mathrm{mm}$ $\varnothing_{\mathrm{Nik}} = 142\,\mathrm{mm}$) and an additional collimation lens ($f = 25\,\mathrm{mm}$), resulting in a refractor with a magnification of $M_{\mathrm{Rx}} = 16$. Thus, the maximal diameter of the collimated beam within the Rx module is $\varnothing_{\mathrm{Rx}} = 9\,\mathrm{mm}$. The two sent wavelengths are separated by a dichroic mirror, where the green light of the beacon laser is transmitted and subsequently focused ($f_{\mathrm{cam}} = 40\,\mathrm{mm}$) on a CMOS camera (pixel size $5.2\,\mu\mathrm{m}$), while the photons from SPDC are guided to the detection module. The quantum signal is focused ($f_{\mathrm{APD}} = 50\,\mathrm{mm}$) on APDs with an active area of $\varnothing_{\mathrm{APD}} = 180\,\mu\mathrm{m}$ placed in each output mode of Bob's measurement module.

In order to reduce background counts from the city, the Rx-telescope was designed for a small field of view of the detectors $\mathrm{FoV} = \varnothing_{\mathrm{APD}}/f_{\mathrm{APD}}/M_{\mathrm{Rx}} = 255\,\mu\mathrm{rad}$ (see Figure 7.2). In addition, a long pass filter and interference filters (Thorlabs FGL665 and Semrock LL01-810 see Figure 3.1) are placed in front of each APD.

Besides being used for PAT, the camera also monitored the angle of arrival (AoA) fluctuations caused by atmospheric turbulence [100]. A series of short exposure time images were taken in order to estimate the full width half maximum of the AoA variation. The central position of each captured point spread function was determined by means of a Gaussian fit. The thus observed variation was in the order of $15.4\,\mu\mathrm{m}$ (FWHM) at the sensor, which corresponds to an AoA of $25\,\mu\mathrm{rad}$ and an atmospheric

Fried parameter of approximately $\lambda/\mathrm{AoA}_{\mathrm{FWHM}} \sim 2\,\mathrm{cm}$ ($\sim 3\,\mathrm{cm}$) at a wavelength of 532 nm (810 nm). Such turbulences resemble those of a 144 km free-space connection between the Canary Islands [11] and represents a worst-case scenario in a satellite-to-ground communication experiment. The angle of arrival fluctuations were significantly smaller than the detector's field of view.

7.2.3 Count Rate Normalization

Only a fraction of the photons generated via SPDC are recorded by time tag, i. e. some are lost on the way from the source to the APDs or not registered by the detectors. A common model for such a stochastic process is a beam splitter which reflects photons into a virtual mode with a certain probability. Thus, only the photons remaining in the original mode are available for data analysis. The expression η_{x} will be used to describe the overall probability of transmission in mode x. Due to the atmospheric turbulence in a free-space channel, the degree of transmission varies over time. Therefore, the recorded count rates must be normalized with respect to the actual condition of the link, in order to obtain a reasonable measurement result. Using the beam splitter model, the expected count rates are given by

$$R_{\mathrm{x}}(\theta_{\mathrm{x}}) = \frac{\eta_{\mathrm{x}}}{2} f(\theta_{\mathrm{x}}, \eta_{\mathrm{x}}) R \tag{7.6a}$$

$$R_{\mathrm{a1,a2}}(\theta_{\mathrm{a}}) = \frac{\eta_{\mathrm{a1}}\eta_{\mathrm{a2}}}{4} \cos^2(4\theta_{\mathrm{a}}) R \tag{7.6b}$$

$$R_{\mathrm{b1,b2}}(\theta_{\mathrm{b}}) = \frac{\eta_{\mathrm{b1}}\eta_{\mathrm{b2}}}{4} \cos^2(4\theta_{\mathrm{b}}) R \tag{7.6c}$$

$$R_{\mathrm{a1,b2}}(\theta_{\mathrm{a}}, \theta_{\mathrm{b}}) = \frac{\eta_{\mathrm{a1}}\eta_{\mathrm{b2}}}{4} \cos^2(2(\theta_{\mathrm{a}} - \theta_{\mathrm{b}})) R \tag{7.6d}$$

$$R_{\mathrm{a1,b1}}(\theta_{\mathrm{a}}, \theta_{\mathrm{b}}) = \frac{\eta_{\mathrm{a1}}\eta_{\mathrm{b1}}}{4} \sin^2(2(\theta_{\mathrm{a}} - \theta_{\mathrm{b}})) R \tag{7.6e}$$

$$R_{\mathrm{a2,b2}}(\theta_{\mathrm{a}}, \theta_{\mathrm{b}}) = \frac{\eta_{\mathrm{a2}}\eta_{\mathrm{b2}}}{4} \sin^2(2(\theta_{\mathrm{a}} - \theta_{\mathrm{b}})) R \tag{7.6f}$$

$$R_{\mathrm{a2,b1}}(\theta_{\mathrm{a}}, \theta_{\mathrm{b}}) = \frac{\eta_{\mathrm{a2}}\eta_{\mathrm{b1}}}{4} \cos^2(2(\theta_{\mathrm{a}} - \theta_{\mathrm{b}})) R, \tag{7.6g}$$

where R is the pair production rate of the source, R_{x} is the background subtracted rate of detection events, and $R_{\mathrm{x,y}}$ denotes the accidental corrected coincidence count rate between detectors (x,y) $\in$ {a1, a2, b1, b2}. The oscillation frequency with respect to the HWP rotation θ_{b} of the two-photon state is doubled compared to single photons sent. Such super-resolution in polarization is a common effect of the sent NOON state $|1_{\mathrm{bH}}, 1_{\mathrm{bV}}\rangle = 1/\sqrt{2}(|2_{\mathrm{bD}}, 0_{\mathrm{bA}}\rangle - |0_{\mathrm{bD}}, 2_{\mathrm{bA}}\rangle)$. It is also worth mentioning that if two photons hit the same detector at the same time ($R_{\mathrm{x,x}}$), only one "click" is generated by the detectors used. Therefore, a reduced number of time tags is recorded

for measurements in the DA basis, which is taken into account by the function

$$f(\theta_{\mathrm{x}}, \eta_{\mathrm{x}}) = 1 - \frac{\eta_{\mathrm{x}}}{4} \sin^2(4\theta_{\mathrm{x}}). \tag{7.7}$$

The total transmission of Alice's channels was stable due to laboratory conditions and could therefore be measured in advance.

$$\eta_{\mathrm{a1}} = 2\frac{R_{\mathrm{a1,a2}}(0)}{R_{a2}(0)} = 0.169 \pm 0.001 \tag{7.8a}$$

$$\eta_{\mathrm{a2}} = 2\frac{R_{\mathrm{a1,a2}}(0)}{R_{a1}(0)} = 0.161 \pm 0.001 \tag{7.8b}$$

Bob's detection events are susceptible to background photons from city lights despite extensive prevention measures. Therefore, the transmission in Bob's channels was calculated using accidental corrected coincidence events.

$$\eta_{\mathrm{b1}} = \frac{2\ R_{\mathrm{a1,b1}}\ f(\theta_{\mathrm{a}}, \eta_{\mathrm{a1}})}{R_{\mathrm{a1}}} + \frac{2\ R_{\mathrm{a2,b1}}\ f(\theta_{\mathrm{a}}, \eta_{\mathrm{a2}})}{R_{\mathrm{a2}}} \tag{7.9a}$$

$$\eta_{\mathrm{b2}} = \frac{2\ R_{\mathrm{a1,b2}}\ f(\theta_{\mathrm{a}}, \eta_{\mathrm{a1}})}{R_{\mathrm{a1}}} + \frac{2\ R_{\mathrm{a2,b2}}\ f(\theta_{\mathrm{a}}, \eta_{\mathrm{a2}})}{R_{\mathrm{a2}}}, \tag{7.9b}$$

With these values the normalized count rate of Bob's local coincidences can be calculated as

$$R^N_{\mathrm{b1,b2}} = \frac{4}{\eta_{\mathrm{b1}}\eta_{\mathrm{b2}}R} R_{\mathrm{b1,b2}} \tag{7.10}$$

with

$$R = \frac{R_{\mathrm{a1}}}{\eta_{\mathrm{a1}}\ f(\theta_{\mathrm{a}}, \eta_{\mathrm{a1}})} + \frac{R_{\mathrm{a2}}}{\eta_{\mathrm{a2}}\ f(\theta_{\mathrm{a}}, \eta_{\mathrm{a2}})} \tag{7.11}$$

being the estimated photon pair production rate of the source.

7.2.4 Stochastic and Deterministic Loss

We have neglected a distinction between stochastic and deterministic loss in the above calculations. The distinct impact of those loss mechanisms on quantum systems was studied by Rauch and Summhammer using different absorbers in neutron interferometers [101]:

- **Stochastic Loss:** *"An absorber is stochastic when the experimenter has no means, not even in principle, to predict whether the neutron will be absorbed or not at any given point in the absorber region at any given time."*

- **Deterministic Loss:** *"An absorber is deterministic when, in principle, it is known with certainty what will happen at any point in the absorber region at any time."*

Awaya *et al.* investigated this topic by means of single-photon interferometry with slow and fast beam choppers [102, 103]. The beam splitter model used in the above calculations only describes stochastic loss, whereas a chopper wheel produces deterministic loss. In free-space channels, atmospheric turbulence causes loss due to beam wandering at the receiving aperture [104]. Thus, from the two-photon state sent to Bob, either both or neither of the photons are lost, if the transmitted beam is deflected out of the Rx-aperture. Such a scenario is comparable to a chopper wheel and is classed under deterministic losses. The resulting variation in channel transmission cannot be observed directly if the deflection is shorter than the integration time t_I of the measured count rate. However, the signal is attenuated on average by the factor of $t_\mathrm{faid}/t_\mathrm{I}$, where t_faid is the time period within t_I for which the aperture is missed by the signal. This attenuation applies equally to single and multi-photon states and does not have a square effect on two-photon states like the stochastic loss. Thus, we have to rewrite Equation 7.6 to

$$R_\mathrm{bx}(\theta_\mathrm{b}) = \frac{\eta_\mathrm{det}\eta'_\mathrm{bx}}{2} f(\theta_\mathrm{b}, \eta_\mathrm{det}\eta'_\mathrm{bx}) R \tag{7.12a}$$

$$R_\mathrm{b1,b2}(\theta_\mathrm{b}) = \frac{\eta_\mathrm{det}\eta'_\mathrm{b1}\eta'_\mathrm{b2}}{4} \cos^2(4\theta_\mathrm{b}) R \tag{7.12b}$$

where $\eta_\mathrm{det} = 1 - t_\mathrm{faid}/t_\mathrm{I}$ describes the deterministic transmission probability of the free-space link and $\eta'_\mathrm{bx} \in \{\eta'_\mathrm{b1}, \eta'_\mathrm{b2}\}$ denotes the stochastic transmission. The heralding is not affected by deterministic loss. The transmission determined by Equation 7.9 does not distinguish between these values and measure both ($\eta_\mathrm{b1} = \eta_\mathrm{det}\eta'_\mathrm{b1}$, $\eta_\mathrm{b2} = \eta_\mathrm{det}\eta'_\mathrm{b2}$). This leads to an overestimation of the normalized count rate of Equation 7.10. With measurements in the HV basis, the extent of this overestimation can be determined, since the deterministic loss can be calculated by

$$\eta_\mathrm{det} = \frac{\eta_\mathrm{b1}\eta_\mathrm{b2} R}{4 R_\mathrm{b1,b2}(0)}. \tag{7.13}$$

7.3 Results

7.3.1 Setup Performance

A measurement with a neutral HWP position revealed a mean photon rate of $\overline{R}_\mathrm{a1}(0) = 421\,\mathrm{kcps}$ ($\overline{R}_\mathrm{a2}(0) = 402\,\mathrm{kcps}$) at Alice's detectors, including negligible dark counts ($\sim 100\,\mathrm{cps}$). From these events an average of $\overline{R}_\mathrm{a1,a2}(0) = 34.1\,\mathrm{kcps}$ accidental corrected

coincidences were observed. A comparative measurement in the DA basis resulted in a coincidence count rate of $\overline{R}_{\mathrm{a1,a2}}(\pi/8) = 159\,\mathrm{cps}$, subtracting 300 cps accidentals. From these measurements we can conclude that the visibility of undisturbed HOM interference was

$$\mathcal{V}_{\mathrm{a}} = \frac{R_{\mathrm{a1,a2}}(0) - R_{\mathrm{a1,a2}}(\pi/8)}{R_{\mathrm{a1,a2}}(0) + R_{\mathrm{a1,a2}}(\pi/8)} = 99.1 \pm 0.1\,\% \tag{7.14}$$

During night-time operation the background counts at the receiver were approximately $R^B_{\mathrm{b1}} \sim 800\,\mathrm{cps}$ and $R^B_{\mathrm{b1}} \sim 500\,\mathrm{cps}$, including 250 cps and 70 cps intrinsic detector dark counts. The background varied widely and was in the range of $R^B_{\mathrm{b1}} \sim 21.5\,\mathrm{kcps}$ and $R^B_{\mathrm{b1}} \sim 18.5\,\mathrm{kcps}$ at sunrise (4 May 2016 05:30:00 GMT+2) on a horizontal link facing south.

With measurement in progress, a mean count rate of $\overline{R}_{\mathrm{b1}}(0) = 87\,\mathrm{kcps}$ ($\overline{R}_{\mathrm{b2}}(0) = 103\,\mathrm{kcps}$) was observed before astronomical dawn. Due to atmospheric turbulence, the total transmission of Bob's channels varied around mean values of $\overline{\eta}_{\mathrm{b1}} = 3.5\,\%$ and $\overline{\eta}_{\mathrm{b2}} = 4.3\,\%$ (see Figure 7.3). Assuming the two measurement modules have roughly the same loss, we can estimate the link transmission to be 21 % (including the fiber link to the roof and Tx/Rx telescopes).

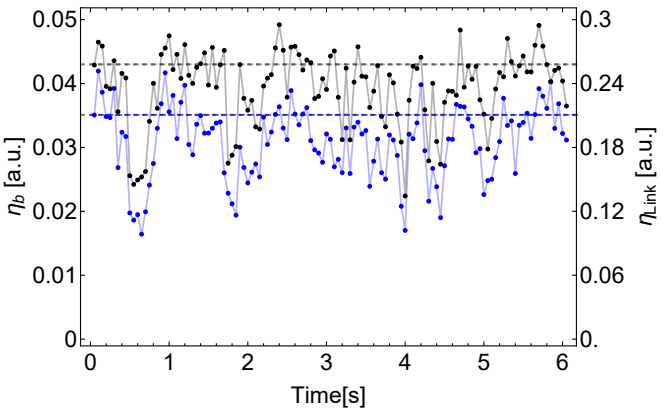


Figure 7.3 Overall transmission of Bob's channels vs. time. η_{b1} and η_{b2} are plotted in blue and black respectively. The difference results from unequal detector efficiencies. The right axis is scaled by the factor $2/(\eta_{\mathrm{a1}} + \eta_{\mathrm{a2}})$ in order to estimate the 1.2 km free-space link transmission. The plot shows a 10 s interval of the $\theta_{\mathrm{b}} = 0$, $\Delta\tau = 0$ measurement. The integration time per data point of this diagram is 50 ms.

A histogram of the transmission probability of two-photon states $4R_{\mathrm{b1,b2}}(0)/R$, as measured with neutral HWP position, is shown in Figure 7.4 (blue). In comparison, the quantity $\eta_{\mathrm{b1}}\eta_{\mathrm{b2}}$ determined from count rates in Equation 7.9 is plotted in gray. The ratio of these quantities corresponds to the deterministic transmission probability η_{det} (see Equation 7.13). However, no significant deviation can be detected from the histograms. The long-term mean $\overline{\eta}_{\mathrm{det}} = 1.005 \pm 0.002$ indicates that the atmospheric turbulence did not cause strong beam wandering. Thus, a possible overestimation of

the normalized count rate $R^N_{\mathrm{b1,b2}}$ caused by fading of the beam can be excluded.

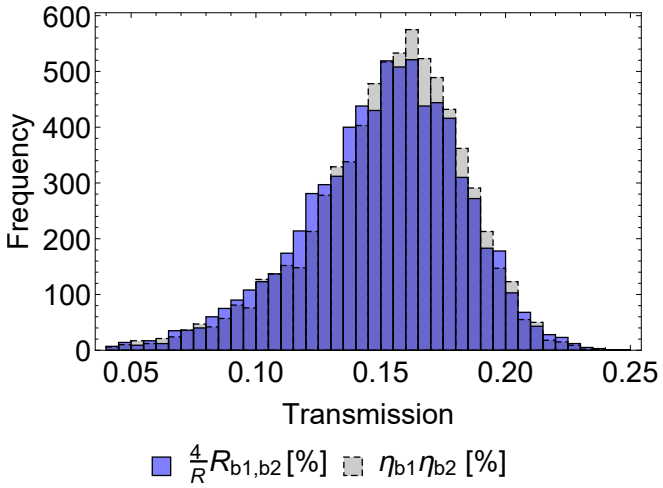


Figure 7.4 Transmission probability of two-photon states $4R_{\mathrm{b1,b2}}(0)/R$ in blue and the quantity $\eta_{\mathrm{b1}}\eta_{\mathrm{b2}}$ in gray. In the case of strong beam wandering at the free-space link, a deviation of the two histograms should be visible ($\eta_{\mathrm{b1}}\eta_{\mathrm{b2}} < 4R_{\mathrm{b1,b2}}(0)/R$). The integration time per measurement was 50 ms, and each histogram consist of 7410 data points.

7.3.2 HOM Interference

We performed five measurements in the DA basis, applying different relative delays $\Delta\tau$ to two-photon states exposed to a 1.2 km-long intra-city free-space link. The temporal delay between the horizontally and vertically polarized photons — with a coherence time of $t_{\mathrm{coh}} = 1.75$ ps — was realized by means of birefringent crystals. For this purpose we used a calcite plate with a thickness of 3 mm and a 1 mm-thick Nd:YVO_4 plate, which corresponds to propagation time delays between ordinary and extraordinary modes of $\Delta\tau_{\mathrm{calc}} = 1.8$ ps [105] and $\Delta\tau_{\mathrm{yvo}} = 0.8$ ps [58], respectively. Thus, by turning the plates by 90°, two measurement settings per plate, corresponding to $\pm\Delta\tau$ where observed. The fifth measurement was carried out without temporal delay ($\Delta\tau = 0$). In addition, three measurements in the HV basis were performed for reference, providing count rates unaffected by $\Delta\tau$. Each setting was recorded for ~ 300 s, and the normalized coincidence count rate $R^N_{\mathrm{b1,b2}}$ was calculated for each second of measurement time. The resulting mean values are compared to a HOM dip measurement carried out in the laboratory (see Section 4.3.3) and are depicted in Figure 7.5 as summarized in Table 7.1.

To guide the eye, the theoretically expected coincidence count rate $\propto P_{\mathrm{b1,b2}}(\frac{\pi}{8}, \Delta\tau)$ (see Equation 7.5) is plotted in Figure 7.5 (red line). The measured count rates — with an integration time of one second — agree with the prediction within the statistical error of the single measurements (error bars in Figure 7.5). The standard deviation of the seven mean values is smaller by a factor of $\sqrt{300} \sim 17$ and thus does not overlap with the prediction. Such systematic errors can be attributed to a polarization mismatch among Alice, Bob, and the birefringent crystal. This error is indirectly covered by the deviation of the one-second measurements, since the polarization alignment was carried

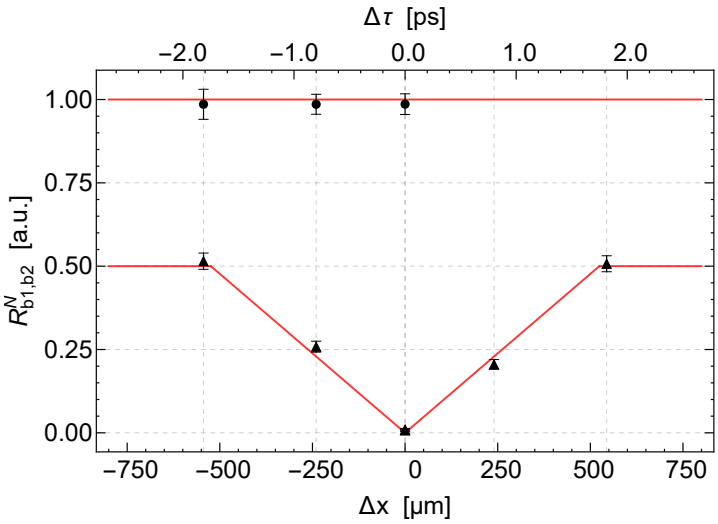


Figure 7.5 HOM dip measured after exposing the two-photon state to a 1.2 km free-space link. Normalized coincidence count rate $R^N_{\mathrm{b1,b2}}$ measured with different relative delays $\Delta\tau$. The circles • (triangles ▲) indicate the mean values of the HV (DA) basis measurements. The expected count rate due to the coincidence probability $P_{\mathrm{b1,b2}}(\theta_{\mathrm{b}}, \Delta\tau)$ (see Equation 7.5) is plotted in red. The error bars indicate the sample standard deviation of ~ 300 measurements with 1 s integration time. The expected standard deviation of the sample mean, which is smaller than the plotted symbols, can be found in Table 7.1. The visibility of the HOM dip is $\mathcal{V}_{\mathrm{b}} = 98.6 \pm 0.7$ %.

out based on them. However, the measurement without intentional delay ($\Delta\tau = 0$) reveals HOM interference of the photon pairs, exposed to the 1.2 km-long free-space link, with a visibility of

$$\mathcal{V}_{\mathrm{b}} = \frac{R^N_{\mathrm{b1,b2}}(0) - R^N_{\mathrm{b1,b2}}(\pi/8)}{R^N_{\mathrm{b1,b2}}(0) + R^N_{\mathrm{b1,b2}}(\pi/8)} = 98.6 \pm 0.7\,\%. \tag{7.15}$$

7.4 Conclusion

We developed a receiver module which was used in an urban area to receive single photons sent via an optical free-space channel. By using various precautions to suppress light pollution from the city, a background count rate of ~ 500 cps was achieved during nighttime. Shortly after sunrise (~ 5 min), however, the background count rate reached a level that prevented further measurements.

In order to obtain a reasonable measurement result a coincidence-count rate normalization was elaborated. Thus, we were able to distinguish variations of the count rates due to different transmission probabilities caused by atmospheric turbulence from a decrease of interference visibility. This normalization neglects the difference between

$\Delta\tau$ [ps]	$\overline{R}^{N}_{\mathrm{b1,b2}}(0,\Delta\tau)$ [%]	$\overline{R}^{N}_{\mathrm{b1,b2}}(\frac{\pi}{8},\Delta\tau)$ [%]	$P_{\mathrm{b1,b2}}(\frac{\pi}{8},\Delta\tau)$ [%]
-1.8	98.56 ± 0.26	51.49 ± 0.14	50
-0.8	98.56 ± 0.17	25.85 ± 0.09	22.9
0	98.61 ± 0.18	00.71 ± 0.02	0
0.8		20.54 ± 0.08	22.9
1.8		50.73 ± 0.14	50

Table 7.1 Normalized coincidence count rates $R^{N}_{\mathbf{b1,b2}}$ as depicted in Figure 7.5. The normalized count rate was recorded for $\sim 300\,\mathrm{s}$ for each setting. The specified uncertainty is the standard deviation of the sample mean. The uncertainty of measurements with an integration time of one second is $\sqrt{300} \sim 17$ times greater than the specified error and, in this case, more representative for the deviation from the coincidence probability $P_{\mathrm{b1,b2}}(0,\Delta\tau)$ (see Equation 7.5).

stochastic and deterministic loss. Thus, we have discussed the context of strong beam wandering and deterministic loss. Furthermore, it was verified that the loss experienced by the two-photon state was solely stochastic. To this end, we exploited the vulnerability to losses of the transmitted two-photon NOON state and used it to investigate link transmission in more detail. The absence of a deterministic loss despite the measured strong atmospheric turbulence can be attributed to the distance between transmitter and receiver. At longer distances, the phase front distortion leads to greater beam wandering and thus to more loss due to fading. A comparable experiment involving a larger free space transmission distance could reveal the impact of such loss.

Furthermore, we have demonstrated high visibility HOM interference of two photons both exposed to atmospheric turbulence. We found a HOM dip visibility of $\mathcal{V}_{\mathrm{b}} = 98.6 \pm 0.7\,\%$ after free-space transmission which is comparable to the visibility measured in a laboratory environment $\mathcal{V}_{\mathrm{a}} = 99.1 \pm 0.1\,\%$. This demonstrates, the unimpaired of second-order interference by a free-space channel with a Fried parameter of approximately 3 cm (at $\lambda = 810\,\mathrm{nm}$). Such turbulence resembles those of a 144 km free-space connection between the Canary Islands [11, 106] and is comparable to a satellite-to-ground communication experiment.

We want to emphasize that this experiment was successful without spatial filtering or adaptive optics at the receiver, since both photons traversed the same atmospheric channel. Second-order interference in general and HOM interference in particular play a major role in applications like quantum teleportation and entanglement swapping, which are fundamental nodes of future quantum networks. In order to realize large-

scale quantum networks, second-order interference of photon pairs, traversing different free-space channels, is a technological challenge which has to be mastered. Although we have not achieved this goal, the data presented underpins experimentally the feasibility of such projects. Furthermore, our experimental results put a very high upper limit on the visibility achievable with time-bin and hyperentangled states sent via a free-space link. [17].

8 Summary and Outlook

The presented photon source has undergone a continuous improvement process during all experiments and has proven its stability and constant performance. After the first setbacks at the centrifuge, we minimized the components of the source and adapted the adjustment process to such harsh conditions. In a second measurement campaign, the stability of the optical setup was sufficient to verify the entanglement of the generated photon pairs up to an acceleration of 30g. A temperature fluctuation of the crystal could be identified as the main cause of visibility variations of the entanglement. Consequently, the temperature control for the crystal was replaced, which not only resulted in more stable visibility but also made a better temperature resolution experimentally accessible. The impact of temperature on the indistinguishability of the down-converted photons was verified experimentally and — together with further relevant parameters — quantitatively described. These results concerning spontaneous parametric down-conversion with a periodically poled potassium titanyl phosphate crystal in a degenerate collinear type II quasi-phase-matching configuration, are useful as a rule of thumb in the design phase of such and similar sources. It should be noted that an optical isolator for the pump laser would probably be the most reasonable additional component, as the visibility reacts very responsively to mode jumps of the pump-wave.

We incorporated this source in a rigid crate which was utilized as an autonomous quantum laboratory. The two-photon state generated by the source can be used with great versatility. Such a NOON state in polarization modes shows super-resolution in polarization measurements. By means of a polarizing beamsplitter cube, this state can be converted into a path-entangled two-photon state and deployed in conventional interferometers. The random splitting at a beam splitter allows the generation of a polarization-entangled state in post-selection. The entangled state produced this way has pros and cons. In quantum key distribution applications, the bunching photon pairs prove to be a disadvantage as they cause an increased “uncorrelated” photon count rate and thus a higher quantum bit error rate. In the free-space experiment conducted, however, we were able to use the coincidences of six different detector combinations in order to measure the loss in a differentiated manner. Thus, deterministic loss by strong beam wandering at the free-space link could be excluded.

This versatile tool was used in three different experiments:

1) Entanglement in Accelerated Reference Frames

We verified the stable performance of our mobile quantum laboratory under sever stress in a centrifuge and a drop tower experiment. Those experiments allowed us to systematically test photonic quantum entanglement in accelerated reference frames. The crossroads between quantum mechanics and relativity is a gray area in which unexpected physical phenomena might potentially arise. We thus demonstrate to what extent this gray area can be accessed with state-of-the-art quantum hardware.

With the intention of stimulating the exploration of theories beyond the current paradigm that can be tested with such experiments, it should be mentioned that the acceleration in the centrifuge used is not limited to 30 g, but could be increased up to 150 g. Active components such as piezo mirrors can be used to avoid a misalignment of the setup. Using such techniques, interference measurements on the centrifuge are also conceivable. Concerning the drop tower, experiments are possible at a facility in Bremen, where a drop height of 100 m (drop time 4.7 s) can be achieved. A glass window in the drop capsule offers the possibility to retain an optical connection during the free fall, thus measurements of the photons of a pair in different reference frames would be possible.

2) Entanglement-Enhanced Optical Gyroscope

Inspired by the centrifuge, we constructed a quantum gyroscope. By integrating a fiber coil, our crate was turned into a fiber optic gyroscope which was operated with two-photon NOON states. With the super-resolution provided by such a photon state, we were able to measure the absolute rotation of the setup with respect to the initial space with sub shot-noise precision.

Furthermore, we discussed the photon losses in such a system and were able to identify the prerequisites for a real measurement advantage with such sensors. For fibre-optic gyroscopes, the key question is the extent to which different photonic states respond to individual noise sources associated with higher count rates. With the speed of ongoing developments in advancing detector technology and increasingly brighter photon sources, experiments exploring a minimum achievable phase resolution resulting from an interplay of several noise sources could become feasible in the foreseeable future.

3) Two-Photon Interference and Transmission despite Atmospheric Turbulence

We built a receiver module, suitable for optical free-space connections in urban areas. This receiver provides the possibility to impose a polarization-dependent time delay on the received photons and can thus be used to verify polarization and hyper-entanglement. We used this facility to demonstrate second-order interference of two

photons, both of which were exposed to atmospheric turbulence. The visibility of the Hong-Ou-Mandel-dip of the collinear transmitted photon pair was comparable to a reference measurement in a laboratory environment.

With regard to future quantum networks, these results experimentally underline the high visibility with which two-photon interference, time-bin, and hyper-entangled are usable despite atmospheric influences. Second-order interference of photon pairs traversing different free-space channels is a technological challenge which seems to be the next decisive step towards a quantum repeater.

Finally, we would like to point out that the use of a beam splitter source for quantum key distribution purposes in future applications should not be excluded from the outset in the planning phase. The influence of the disadvantage of an increased accidental count rate — between bunched photon pairs in Alice's and Bob's channels and uncorrelated background photons — decreases with the use of detectors with better temporal resolution and improved background suppression. In addition, the advantages of a polarization NOON state sent along may not be underestimated. With this the frame of reference of the spontaneous parametric down-conversion crystal is automatically being transmitted, which is advantageous for the polarization comparison of the link. Furthermore, knowledge about the total transmission can be derived from the locally measured heralding efficiency.

Bibliography

[1] J. Yin et al. Satellite-based entanglement distribution over 1200 kilometers. *Science*, 356:1140–1144, June 2017. [Cited on pages 1 and 15.]

[2] A. Einstein, B. Podolsky, and N. Rosen. Can quantum-mechanical description of physical reality be considered complete? *Physical review*, 47:777–780, May 1935. [Cited on pages 1 and 15.]

[3] J. S. BELL. On the Einstein Podolsky Rosen paradox. *Physics Physique Fizika*, 1:195, November 1964. [Cited on pages 1, 16, and 17.]

[4] M. Giustina et al. Significant-loophole-free test of Bell's theorem with entangled photons. *Physical Review Letters*, 115:250401, December 2015. [Cited on pages 1 and 18.]

[5] J. Handsteiner et al. Cosmic bell test: Measurement settings from Milky Way stars. *Physical Review Letters*, 118:060401, February 2017. [Cited on pages 1 and 18.]

[6] D. Rauch et al. Cosmic Bell test using random measurement settings from high-redshift quasars. *Physical Review Letters*, 121:080403, August 2018. [Cited on pages 1 and 18.]

[7] J. F. Clauser, M. A. Horne, A. Shimony, and R. A. Holt. Proposed experiment to test local hidden-variable theories. *Physical Review Letters*, 23:880–884, October 1969. [Cited on pages 1 and 17.]

[8] A. K. Ekert. Quantum cryptography based on Bell's theorem. *Physical Review Letters*, 67:661–663, August 1991. [Cited on pages 1 and 87.]

[9] W. K. Wootters and W. H. Zurek. A single quantum cannot be cloned. *Nature*, 299:802, October 1982. [Cited on page 1.]

[10] A. UN General. Universal Declaration of Human Rights. *UN General Assembly*, 217A, 1948. [Cited on page 1.]

[11] R. Ursin et al. Entanglement-based quantum communication over 144km. *Nature physics*, 3:481–486, July 2007. [Cited on pages 1, 87, 92, and 98.]

[12] S.-K. Liao et al. Satellite-Relayed Intercontinental Quantum Network. *Physical Review Letters*, 120:030501, January 2018. [Cited on pages 1 and 15.]

[13] J. Aasi et al. Enhanced sensitivity of the LIGO gravitational wave detector by using squeezed states of light. *Nature Photonics*, 7:613–619, July 2013. [Cited on page 2.]

[14] J. P. Dowling. Quantum optical metrology – the lowdown on high-N00n states. *Contemporary Physics*, 49:125–143, July 2008. [Cited on pages 2, 21, and 68.]

[15] P. Walther, J.-W. Pan, M. Aspelmeyer, R. Ursin, S. Gasparoni, and A. Zeilinger. De Broglie wavelength of a non-local four-photon state. *Nature*, 429:158–161, May 2004. [Cited on pages 2, 26, and 68.]

[16] J. Jacobson, G. Björk, I. Chuang, and Y. Yamamoto. Photonic de Broglie Waves. *Physical Review Letters*, 74:4835–4838, June 1995. [Cited on pages 2 and 68.]

[17] F. Steinlechner, S. Ecker, M. Fink, B. Liu, J. Bavaresco, M. Huber, T. Scheidl, and R. Ursin. Distribution of high-dimensional entanglement via an intra-city free-space link. *Nature Communications*, 8:15971, July 2017. [Cited on pages 3 and 99.]

[18] J. Audretsch. *Entangled Systems: New Directions in Quantum Physics*. John Wiley & Sons, 1 edition, February 2007. [Cited on page 5.]

[19] P. Hyllus, O. Gühne, D. Bruß, and M. Lewenstein. Relations between entanglement witnesses and Bell inequalities. *Physical Review A*, 72:012321, July 2005. [Cited on pages 5 and 19.]

[20] S. Bandyopadhyay, P. O. Boykin, V. Roychowdhury, and F. Vatan. A new proof for the existence of mutually unbiased bases. *Algorithmica*, 34:512–528, November 2002. [Cited on page 6.]

[21] I. Bengtsson. Three ways to look at mutually unbiased bases. In *AIP Conference Proceedings*, volume 889, pp. 40–51. AIP, March 2007. [Cited on page 6.]

[22] J. D. Franson. Bell inequality for position and time. *Phys. Rev. Lett.*, 62:2205–2208, May 1989. [Cited on page 11.]

[23] R. F. Werner. Quantum states with Einstein-Podolsky-Rosen correlations admitting a hidden-variable model. *Physical Review A*, 40:4277–4281, October 1989. [Cited on page 18.]

[24] M. Horodecki, P. Horodecki, and R. Horodecki. Separability of mixed states: necessary and sufficient conditions. *Physics Letters A*, 223:1–8, November 1996. [Cited on pages 19 and 20.]

[25] J. Barrett. Nonsequential positive-operator-valued measurements on entangled mixed states do not always violate a Bell inequality. *Physical Review A*, 65:042302, March 2002. [Cited on page 19.]

[26] Z.-Y. J. Ou. *Multi-Photon Quantum Interference*. Springer, 2007. [Cited on pages 21, 37, 39, and 41.]

[27] C. K. Hong, Z. Y. Ou, and L. Mandel. Measurement of subpicosecond time intervals between two photons by interference. *Physical Review Letters*, 59:2044–2046, November 1987. [Cited on page 21.]

[28] R. A. Campos, B. E. A. Saleh, and M. C. Teich. Quantum-mechanical lossless beam splitter: Su(2) symmetry and photon statistics. *Physical Review A*, 40:1371–1384, August 1989. [Cited on page 21.]

[29] A. Zeilinger. General properties of lossless beam splitters in interferometry. *American Journal of Physics*, 49:882–883, June 1981. [Cited on page 21.]

[30] P. Kok, A. N. Boto, D. S. Abrams, C. P. Williams, S. L. Braunstein, and J. P. Dowling. Quantum-interferometric optical lithography: Towards arbitrary two-dimensional patterns. *Physical Review A*, 63:063407, May 2001. [Cited on page 23.]

[31] V. Giovannetti, S. Lloyd, and L. Maccone. Quantum-Enhanced Measurements: Beating the Standard Quantum Limit. *Science*, 306:1330–1336, November 2004. [Cited on pages 23 and 68.]

[32] C. F. Wildfeuer, A. P. Lund, and J. P. Dowling. Strong violations of Bell-type inequalities for path-entangled number states. *Physical Review A*, 76:052101, November 2007. [Cited on page 23.]

[33] B. E. Kardynal, Z. L. Yuan, and A. J. Shields. An avalanche-photodiode-based photon-number-resolving detector. *Nature Photonics*, 2:425–428, June 2008. [Cited on page 24.]

[34] R. H. Hadfield. Single-photon detectors for optical quantum information applications. *Nature Photonics*, 3:696–705, December 2009. [Cited on page 24.]

[35] X. Tao et al. A high speed and high efficiency superconducting photon number resolving detector. *Superconductor Science and Technology*, 32:064002, April 2019. [Cited on page 24.]

[36] D. Šafránek. Simple expression for the quantum fisher information matrix. *Physical Review A*, 97:042322, April 2018. [Cited on page 25.]

[37] Y. M. Zhang, X. W. Li, W. Yang, and G. R. Jin. Quantum fisher information of entangled coherent states in the presence of photon loss. *Physical Review A*, 88:043832, October 2013. [Cited on pages 26 and 80.]

[38] I. Afek, O. Ambar, and Y. Silberberg. High-NOON states by mixing quantum and classical light. *Science*, 328:879–881, May 2010. [Cited on page 26.]

[39] U. Dorner, R. Demkowicz-Dobrzanski, B. J. Smith, J. S. Lundeen, W. Wasilewski, K. Banaszek, and I. A. Walmsley. Optimal Quantum Phase Estimation. *Physical Review Letters*, 102:040403, January 2009. [Cited on pages 26, 68, and 80.]

[40] R. Demkowicz-Dobrzanski, U. Dorner, B. J. Smith, J. S. Lundeen, W. Wasilewski, K. Banaszek, and I. A. Walmsley. Quantum phase estimation with lossy interferometers. *Physical Review A*, 80:013825, July 2009. [Cited on pages 26 and 80.]

[41] G. R. Jin, S. Luo, Y. C. Liu, H. Jing, and W. M. Liu. Polarization squeezing and multipartite entanglement of triphoton states. *Journal of the Optical Society of America B*, 27:A105–A109, June 2010. [Cited on page 28.]

[42] S. Cova, M. Ghioni, A. Lacaita, C. Samori, and F. Zappa. Avalanche photodiodes and quenching circuits for single-photon detection. *Applied Optics*, 35:1956–1976, April 1996. [Cited on page 29.]

[43] C. Ho, A. Lamas-Linares, and C. Kurtsiefer. Clock synchronization by remote detection of correlated photon pairs. *New Journal of Physics*, 11:045011, April 2009. [Cited on pages 31, 34, and 90.]

[44] F. Steinlechner. *Sources of Photonic Entanglement for Applications in Space*. Phd thesis, UPC-UNIVERSITAT POLIT'ECNICA DE CATALUNYA, 2015. [Cited on page 37.]

[45] J. Handsteiner. A transportable polarization-entangled photon source. Master thesis, TU Wien, December 2014. [Cited on page 37.]

[46] A. Rodriguez Aramendia. Photonic entanglement exposed to acceleration. Master thesis, Universität Wien, 2016. [Cited on page 37.]

[47] C. Couteau. Spontaneous parametric down-conversion. *Contemporary Physics*, 59:291–304, July 2018. [Cited on page 37.]

[48] Y. M. Mikhailova, P. A. Volkov, and M. V. Fedorov. Biphoton wave packets in parametric down-conversion: Spectral and temporal structure and degree of entanglement. *Physical Review A*, 78:062327, December 2008. [Cited on page 37.]

[49] K. Zielnicki, K. Garay-Palmett, D. Cruz-Delgado, H. Cruz-Ramirez, M. F. O'Boyle, B. Fang, V. O. Lorenz, A. B. U'Ren, and P. G. Kwiat. Joint spectral characterization of photon-pair sources. *Journal of Modern Optics*, 65:1141–1160, February 2018. [Cited on page 37.]

[50] M. H. Rubin, D. N. Klyshko, Y. H. Shih, and A. V. Sergienko. Theory of two-photon entanglement in type-II optical parametric down-conversion. *Physical Review A*, 50:5122–5133, December 1994. [Cited on pages 38 and 90.]

[51] A. Migdall, S. V. Polyakov, J. Fan, and J. C. Bienfang. *Single-photon generation and detection: physics and applications*, volume 45. Academic Press, 2013. [Cited on pages 38 and 39.]

[52] A. V. Sergienko, Y. H. Shih, and M. H. Rubin. Experimental evaluation of a two-photon wave packet in type-II parametric downconversion. *Journal of the Optical Society of America B*, 12:859–862, May 1995. [Cited on pages 39, 42, and 90.]

[53] M. W. Mitchell. Quantum Optics for the Impatient. ICFO - Institut de Ciències Fotòniques Castelldefels, Lecture Notes, 2015. [Cited on page 41.]

[54] H. Sun. Thin lens equation for a real laser beam with weak lens aperture truncation. *Optical Engineering*, 37:2906–2914, November 1998. [Cited on page 44.]

[55] T. Y. Fan, C. E. Huang, B. Q. Hu, R. C. Eckardt, Y. X. Fan, R. L. Byer, and R. S. Feigelson. Second harmonic generation and accurate index of refraction measurements in flux-grown KTiOP04. *Applied Optics*, 26:2390–2394, June 1987. [Cited on page 45.]

[56] K. Fradkin, A. Arie, A. Skliar, and G. Rosenman. Tunable midinfrared source by difference frequency generation in bulk periodically poled KTiOPO4. *Applied Physics Letters*, 74:914–916, February 1999. [Cited on page 45.]

[57] S. Emanueli and A. Arie. Temperature-Dependent Dispersion Equations for KTiOPO4 and KTiOAsO4. *Applied Optics*, 42:6661–6665, November 2003. [Cited on pages 45 and 46.]

[58] D. E. Zelmon, J. J. Lee, K. M. Currin, J. M. Northridge, and D. Perlov. Revisiting the optical properties of Nd doped yttrium orthovanadate. *Applied Optics*, 49:644–647, 2010. [Cited on pages 48 and 96.]

[59] M. Fink, A. Rodriguez-Aramendia, J. Handsteiner, A. Ziarkash, F. Steinlechner, T. Scheidl, I. Fuentes, J. Pienaar, T. C. Ralph, and R. Ursin. Experimental test of photonic entanglement in accelerated reference frames. *Nature Communications*, 8:15304, May 2017. [Cited on pages 55, 57, 58, 60, 61, 62, 63, and 64.]

[60] Z. Tang, R. Chandrasekara, Y. C. Tan, C. Cheng, K. Durak, and A. Ling. The photon pair source that survived a rocket explosion. *Scientific Reports*, 6:25603, May 2016. [Cited on page 56.]

[61] Z. Tang, R. Chandrasekara, Y. C. Tan, C. Cheng, L. Sha, G. C. Hiang, D. K. L. Oi, and A. Ling. Generation and Analysis of Correlated Pairs of Photons aboard a Nanosatellite. *Physical Review Applied*, 5:054022, May 2016. [Cited on page 56.]

[62] C. E. Kuklewicz, M. Fiorentino, G. Messin, F. N. C. Wong, and J. H. Shapiro. High-flux source of polarization-entangled photons from a periodically poled KTiOPO4 parametric down-converter. *Physical Review A*, 69:013807, January 2004. [Cited on page 57.]

[63] B. B. Blinov, D. L. Moehring, L.-M. Duan, and C. Monroe. Observation of entanglement between a single trapped atom and a single photon. *Nature*, 428:153–157, May 2004. [Cited on page 59.]

[64] M. Fink, F. Steinlechner, J. Handsteiner, J. P. Dowling, T. Scheidl, and R. Ursin. Entanglement-enhanced optical gyroscope. *New Journal of Physics*, 21:053010, May 2019. [Cited on pages 67, 71, 72, 75, 76, and 79.]

[65] G. B. Malykin. The Sagnac effect: correct and incorrect explanations. *Physics-Uspekhi*, 43:1229, 2000. [Cited on pages 67 and 69.]

[66] X. Wang, C. Zhang, J. Jin, and N. Song. Optimum Length of Fiber Coil in Space-Borne Interferometric Fiber Optic Gyroscope. In W. Hu, editor, *Advances in Electric and Electronics*, volume 155 of *Lecture Notes in Electrical Engineering*, pp. 683–688, Berlin, Heidelberg, 2012. Springer Berlin Heidelberg. [Cited on pages 67, 82, and 85.]

[67] S. J. Sanders, L. K. Strandjord, and D. Mead. Fiber optic gyro technology trends - a Honeywell perspective. In *2002 15th Optical Fiber Sensors Conference Technical Digest. OFS 2002(Cat. No.02EX533)*, pp. 5–8, May 2002. [Cited on page 67.]

[68] H. Kajioka, T. Kumagai, H. Nakai, T. Dohsho, H. Soekawa, and T. Yuhara. Commercial applications of mass-produced fiber optic gyros. In *Fiber Optic Gyros:*

20th Anniversary Conference, volume 2837, pp. 18–33. International Society for Optics and Photonics, November 1996. [Cited on page 67.]

[69] G. Sagnac. L'éther lumineux démontré par l'effet du vent relatif d'éther dans un interféromètre en rotation uniforme. *CR Acad. Sci.*, 157:708–710, 1913. [Cited on page 67.]

[70] G. Sagnac. The Luminiferous Ether is Detected as a Wind Effect Relative to the Ether Using a Uniformly Rotating Interferometer, translated by William Lone in The Abraham Zelmanov Journal. *Abraham Zelmanov Journal*, 1:74–76, 2008. [Cited on page 67.]

[71] G. Sagnac. Sur la preuve de la réalité de l'éther lumineux par l'expérience de l'interférographe tournant. *CR Acad. Sci.*, 157:1410–1413, 1913. [Cited on page 67.]

[72] G. Sagnac. Regarding the Proof for the Existence of a Luminiferous Ether Using a Rotating Inteferometer Experiment. *Abraham Zelmanov Journal*, 1:77–80, 2008. [Cited on page 67.]

[73] A. A. Michelson and E. W. Morley. On the Relative Motion of the Earth and of the Luminiferous Ether. *Sidereal Messenger*, 6:306–310, 1887. [Cited on page 67.]

[74] A. A. Logunov and Y. V. Chugreev. Special theory of relativity and the Sagnac effect. *Soviet Physics Uspekhi*, 31:861–864, September 1988. [Cited on pages 67 and 69.]

[75] G. B. Malykin. Sagnac effect in a rotating frame of reference. Relativistic Zeno paradox. *Physics-Uspekhi*, 45:907, August 2002. [Cited on page 67.]

[76] S. K. Ghosal, B. Raychaudhuri, A. K. Chowdhury, and M. Sarker. Relativistic Sagnac Effect and Ehrenfest Paradox. *Foundations of Physics*, 33:981–1001, June 2003. [Cited on pages 67 and 70.]

[77] S. J. G. Gift. Inconsistency in relativistic derivations of the Sagnac effect. *Physics Essays*, 31(2):228–232, June 2018. [Cited on page 67.]

[78] V. I. Vysotskii, V. I. Vorontsov, R. N. Kuz'min, P. A. Bezirganyan, and A. G. Rostomyan. The Sagnac experiment with X-radiation. *Physics-Uspekhi*, 37:289, March 1994. [Cited on page 67.]

[79] F. Hasselbach and M. Nicklaus. Sagnac experiment with electrons: Observation of the rotational phase shift of electron waves in vacuum. *Physical Review A*, 48:143–151, July 1993. [Cited on page 67.]

[80] S. A. Werner, J. L. Staudenmann, and R. Colella. Effect of Earth's Rotation on the Quantum Mechanical Phase of the Neutron. *Physical Review Letters*, 42:1103–1106, April 1979. [Cited on page 67.]

[81] F. Riehle, T. Kisters, A. Witte, J. Helmcke, and C. J. Borde. Optical Ramsey spectroscopy in a rotating frame: Sagnac effect in a matter-wave interferometer. *Physical Review Letters*, 67:177–180, July 1991. [Cited on page 67.]

[82] A. Lenef, T. D. Hammond, E. T. Smith, M. S. Chapman, R. A. Rubenstein, and D. E. Pritchard. Rotation Sensing with an Atom Interferometer. *Physical Review Letters*, 78:760–763, February 1997. [Cited on page 67.]

[83] T. L. Gustavson, P. Bouyer, and M. A. Kasevich. Precision Rotation Measurements with an Atom Interferometer Gyroscope. *Physical Review Letters*, 78:2046–2049, March 1997. [Cited on page 67.]

[84] J. N. Chamoun, A. Evans, F. A. Mosca, and M. J. F. Digonnet. Low noise and low drift in a laser-driven fiber optic gyroscope with a 1-km coil. In *Proc.SPIE 9157, 23rd International Conference on Optical Fibre Sensors*, volume 91570E, June 2014. [Cited on pages 68, 84, and 85.]

[85] H. C. Lefevre. *The fiber-optic gyroscope*. Artech House, British Library, 2 edition, October 2014. [Cited on pages 68, 82, and 85.]

[86] A. Kolkiran and G. S. Agarwal. Heisenberg limited Sagnac interferometry. *Optics Express*, 15:6798–6808, May 2007. [Cited on page 68.]

[87] K. Edamatsu, R. Shimizu, and T. Itoh. Measurement of the Photonic de Broglie Wavelength of Entangled Photon Pairs Generated by Spontaneous Parametric Down-Conversion. *Physical Review Letters*, 89:213601, November 2002. [Cited on page 68.]

[88] O. Steuernagel. de Broglie wavelength reduction for a multiphoton wave packet. *Physical Review A*, 65:033820, February 2002. [Cited on page 68.]

[89] A. N. Boto, P. Kok, D. S. Abrams, S. L. Braunstein, C. P. Williams, and J. P. Dowling. Quantum interferometric optical lithography: Exploiting entanglement to beat the diffraction limit. *Physical Review Letters*, 85:2733–2736, September 2000. [Cited on page 68.]

[90] G. Bertocchi, O. Alibart, D. B. Ostrowsky, S. Tanzilli, and P. Baldi. Single-photon Sagnac interferometer. *Journal of Physics B: Atomic, Molecular and Optical Physics*, 39:1011, February 2006. [Cited on page 69.]

[91] M. Kacprowicz, R. Demkowicz-Dobrzański, W. Wasilewski, K. Banaszek, and I. A. Walmsley. Experimental quantum-enhanced estimation of a lossy phase shift. *Nature Photonics*, 4:357–360, June 2010. [Cited on page 80.]

[92] N. Thomas-Peter, B. J. Smith, A. Datta, L. Zhang, U. Dorner, and I. A. Walmsley. Real-world quantum sensors: Evaluating resources for precision measurement. *Physical Review Letters*, 107:113603, September 2011. [Cited on page 80.]

[93] M. E. Lines. Can the minimum attenuation of fused silica be significantly reduced by small compositional variations? I. Alkali metal dopants. *Journal of Non-Crystalline Solids*, 171:209–218, August 1994. [Cited on pages 81 and 82.]

[94] A. Fedrizzi, R. Ursin, T. Herbst, M. Nespoli, R. Prevedel, T. Scheidl, F. Tiefenbacher, T. Jennewein, and A. Zeilinger. High-fidelity transmission of entanglement over a high-loss free-space channel. *Nature Physics*, 5:389–392, March 2009. [Cited on page 87.]

[95] X.-M. Jin et al. Experimental free-space quantum teleportation. *Nature Photonics*, 4:376–381, June 2010. [Cited on page 87.]

[96] J. Yin et al. Quantum Science Experiments with Micius Satellite. In *Conference on Lasers and Electro-Optics*, pp. JTu3G.4. Optical Society of America, May 2019. [Cited on page 87.]

[97] M. Żukowski, A. Zeilinger, M. A. Horne, and A. K. Ekert. "Event-ready-detectors" Bell experiment via entanglement swapping. *Physical Review Letters*, 71:4287–4290, December 1993. [Cited on page 87.]

[98] J.-W. Pan, D. Bouwmeester, H. Weinfurter, and A. Zeilinger. Experimental Entanglement Swapping: Entangling Photons That Never Interacted. *Physical Review Letters*, 80:3891–3894, May 1998. [Cited on page 87.]

[99] T. Herbst, T. Scheidl, M. Fink, J. Handsteiner, B. Wittmann, R. Ursin, and A. Zeilinger. Teleportation of entanglement over 143 km. *Proceedings of the National Academy of Sciences*, 112:14202–14205, November 2015. [Cited on page 87.]

[100] D. L. Fried. Statistics of a geometric representation of wavefront distortion. *Journal of the Optical Society of America*, 55:1427–1435, November 1965. [Cited on page 91.]

[101] H. Rauch and J. Summhammer. Neutron-interferometer absorption experiments in the quantum limit. *Physical Review A*, 46:7284–7287, December 1992. [Cited on page 93.]

[102] K. Awaya and M. Tomita. Stochastic and deterministic absorption in single-photon interference experiments. *Physical Review A*, 56:4106–4110, November 1997. [Cited on page 94.]

[103] K. Awaya, T. Ishigame, and M. Tomita. Single-Photon Interference Experiment with a Fast Chopper. *Soryushiron Kenkyu Electronics*, 98:173–178, December 1998. [Cited on page 94.]

[104] D. Vasylyev, A. A. Semenov, and W. Vogel. Atmospheric Quantum Channels with Weak and Strong Turbulence. *Physical Review Letters*, 117:090501, August 2016. [Cited on page 94.]

[105] G. Ghosh. Dispersion-equation coefficients for the refractive index and birefringence of calcite and quartz crystals. *Optics Communications*, 163:95–102, May 1999. [Cited on page 96.]

[106] T. Schmitt-Manderbach. *Long distance free-space quantum key distribution*. Phd thesis, LMU München: Fakultät für Physik, 2007. [Cited on page 98.]

Appendices

A HOM Interference Coincidence Count Rate

A plane-wave pump field with an angular frequency of ω_p generates a horizontally polarized signal and vertically polarized idler photons in a ppKTP crystal of length $L = 1\,\mathrm{cm}$. The biphoton-state after walk-off compensation ($\tau = \frac{LD}{2} + \Delta\tau$) emerging from the PMF can be denoted by (see Equation 4.17)

$$|\mathrm{II}_{\Delta\tau}\rangle = \zeta \int \mathrm{d}\omega\; h(\omega, \omega_\mathrm{p} - \omega) \mathrm{e}^{-\mathbb{i}\omega(\frac{LD}{2}+\Delta\tau)} \widehat{a}^\dagger_\mathrm{H}(\omega) \widehat{a}^\dagger_\mathrm{V}(\omega_\mathrm{p} - \omega)\, |\mathrm{Vac}\rangle\,. \tag{A.1}$$

with

$$h(\omega, \omega_\mathrm{p} - \omega) = \mathrm{e}^{-\mathbb{i}\frac{L}{2}\Delta k(\omega, \omega_\mathrm{p}-\omega)} \mathrm{sinc}\left(\frac{L}{2}\Delta k(\omega, \omega_\mathrm{p} - \omega)\right) \tag{A.2}$$

The parameter $\Delta\tau$ results from either insufficient walk-off compensation or a deliberately introduced delay between signal and idler photons. For small deviations from degenerate down-conversion ($\omega = \omega_0$, $\omega_\mathrm{p} = 2\omega_0$), the wave vector mismatch $\Delta k(\omega, \omega_\mathrm{p} - \omega)$ can be approximated by (see Equation 4.26)

$$\begin{aligned} \Delta k(\omega, \omega_\mathrm{p} - \omega) &\approx D(\omega_0 - \omega) + A(T, \omega_\mathrm{p}) \\ A(T, \omega_\mathrm{p}) &= D_T(T - T_0) + D_{\omega_\mathrm{p}}(\omega_\mathrm{p} - 2\omega_0) \end{aligned} \tag{A.3}$$

with T_0 =37.15 °C, $\omega_0 = \frac{c\,2\,\pi}{\lambda_0}$ and $\lambda_0 = 810\,\mathrm{nm}$. The state analysis is performed by means of a HWP, followed by a PBS with a single-photon detector in each output mode.

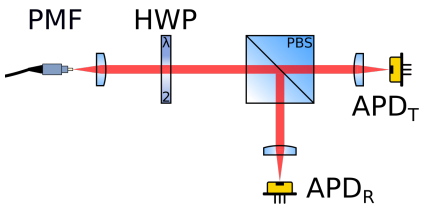


Figure A.1 Arrangement of the detection module. The HWP is rotated by an angle $\beta = \frac{\pi}{8}$, resulting in photon bunching at the PBS. The photons are detected in both outputs of the PBS by means of avalanche photodiodes (APD).

The field operators in the transmitted and reflected output mode of the PBS are denoted by

$$\widehat{E}_{\mathrm{T}}(t) = \cos(2\beta)\ \widehat{E}_{\mathrm{H}}(x,t) + \sin(2\beta)\ \widehat{E}_{\mathrm{V}}(x,t) \tag{A.4}$$

$$\widehat{E}_{\mathrm{R}}(t) = \cos(2\beta)\ \widehat{E}_{\mathrm{V}}(x,t) - \sin(2\beta)\ \widehat{E}_{\mathrm{H}}(x,t) \tag{A.5}$$

where β describes the rotation of the half-wave plate and

$$\widehat{E}_m(x,t) = \frac{1}{\sqrt{2\pi}} \int \mathrm{e}^{-\mathbb{i}\omega_m(t-x/c)} \widehat{a}_m(\omega_m)\ \mathrm{d}\omega_m \tag{A.6}$$

denotes the positive frequency part of the electric field operator $\widehat{E}_m(x,t) + \widehat{E}_m^{\dagger}(x,t)$. The two-photon correlation function in the output modes of the PBS can be calculated via

$$G^{(2)}_{\mathrm{HOM}}(t_1,t_2) = \langle \Pi_{\Delta\tau}|\ \widehat{E}_{\mathrm{T}}^{\dagger}(t_1)\widehat{E}_{\mathrm{R}}^{\dagger}(t_2)\widehat{E}_{\mathrm{R}}(t_2)\widehat{E}_{\mathrm{T}}(t_1)\ |\Pi_{\Delta\tau}\rangle\,, \tag{A.7}$$

where the right-hand part results in

$$\begin{aligned}
&\widehat{E}_{\mathrm{R}}(t_2)\widehat{E}_{\mathrm{T}}(t_1)\,|\Pi_{\Delta\tau}\rangle \\
&= \Big(\cos^2(2\beta)\ \widehat{E}_{\mathrm{H}}(x,t_1)\ \widehat{E}_{\mathrm{V}}(x,t_2) - \sin^2(2\beta)\ \widehat{E}_{\mathrm{V}}(x,t_1)\ \widehat{E}_{\mathrm{H}}(x,t_2)\Big)\,|\Pi_{\Delta\tau}\rangle \\
&= \frac{\zeta}{2\pi}\int \mathrm{e}^{-\mathbb{i}\omega(\frac{LD}{2}+\Delta\tau)} \Big(\cos^2(2\beta)\ \mathrm{e}^{-\mathbb{i}\omega(t_1-x/c)}\mathrm{e}^{-\mathbb{i}(\omega_{\mathrm{p}}-\omega)(t_2-x/c)} \\
&\qquad\qquad - \sin^2(2\beta)\ \mathrm{e}^{-\mathbb{i}\omega(t_2-x/c)}\mathrm{e}^{-\mathbb{i}(\omega_{\mathrm{p}}-\omega)(t_1-x/c)}\Big)\ h(\omega,\omega_{\mathrm{p}}-\omega)\mathrm{d}\omega\,|\mathrm{Vac}\rangle \\
&= \frac{\zeta}{2\pi}\int \Big(\cos^2(2\beta)\ \mathrm{e}^{-\mathbb{i}\omega\Delta t}\mathrm{e}^{-\mathbb{i}\omega_{\mathrm{p}}(t_2-x/c)} - \sin^2(2\beta)\ \mathrm{e}^{\mathbb{i}\omega\Delta t}\mathrm{e}^{-\mathbb{i}\omega_{\mathrm{p}}(t_1-x/c)}\Big) \\
&\qquad\qquad \mathrm{e}^{-\mathbb{i}\ (L/2\ (A(T,\omega_{\mathrm{p}})+D(\omega_0-\omega))+\omega\ \tau)}\mathrm{sinc}\left(\frac{L}{2}(A(T,\omega_{\mathrm{p}})+D(\omega_0-\omega))\right)\mathrm{d}\omega\,|\mathrm{Vac}\rangle \\
&= \frac{\zeta}{2\pi}\mathrm{e}^{-\mathbb{i}\ (L/2\ (A(T,\omega_{\mathrm{p}})+D\omega_0)+\omega_{\mathrm{p}}(t_2-x/c))}\int \Big(\cos^2(2\beta)\ \mathrm{e}^{-\mathbb{i}\omega\Delta t} - \sin^2(2\beta)\ \mathrm{e}^{-\mathbb{i}\Delta t(\omega_{\mathrm{p}}-\omega)}\Big) \\
&\qquad\qquad \mathrm{e}^{-\mathbb{i}\ \Delta\tau\ \omega}\mathrm{sinc}\left(\frac{L}{2}(A(T,\omega_{\mathrm{p}})+D(\omega_0-\omega))\right)\mathrm{d}\omega\,|\mathrm{Vac}\rangle \\
&= \frac{\zeta}{L\,|D|}\mathrm{e}^{-\mathbb{i}\ (L/2\ (A(T,\omega_{\mathrm{p}})+D\omega_0)+\omega_{\mathrm{p}}(t_2-x/c))}\left(\cos^2(2\beta)\ \mathrm{e}^{-\mathbb{i}(\frac{A(T,\omega_{\mathrm{p}})}{D}+\omega_0)(\Delta\tau+\Delta t)}\Pi\left(\frac{\Delta\tau+\Delta t}{L\ D}\right)\right. \\
&\qquad\qquad \left. - \sin^2(2\beta)\ \mathrm{e}^{-\mathbb{i}(\omega_{\mathrm{p}}\Delta t+(\frac{A(T,\omega_{\mathrm{p}})}{D}+\omega_0)(\Delta\tau-\Delta t))}\Pi\left(\frac{\Delta\tau-\Delta t}{L\ D}\right)\right)|\mathrm{Vac}\rangle \\
&= \frac{\zeta}{L\,|D|}\mathrm{e}^{-\mathbb{i}\ ((\frac{A(T,\omega_{\mathrm{p}})}{D}+\omega_0)(\frac{L\ D}{2}+\Delta\tau)+\omega_{\mathrm{p}}(t_2-x/c))}\left(\cos^2(2\beta)\ \mathrm{e}^{-\mathbb{i}(\frac{A(T,\omega_{\mathrm{p}})}{D}+\omega_0)\Delta t}\Pi\left(\frac{\Delta\tau+\Delta t}{L\ D}\right)\right. \\
&\qquad\qquad \left. - \sin^2(2\beta)\ \mathrm{e}^{\mathbb{i}(\frac{A(T,\omega_{\mathrm{p}})}{D}+\omega_0-\omega_{\mathrm{p}})\Delta t}\Pi\left(\frac{\Delta\tau-\Delta t}{L\ D}\right)\right)|\mathrm{Vac}\rangle
\end{aligned} \tag{A.8}$$

In the above calculation, we used the commutation relation from Equation 2.55 and

$$\int \mathrm{sinc}(C_1 + C_2\ \omega)\,\mathrm{e}^{-\mathbb{i}\omega t}\mathrm{d}\omega = \frac{\pi}{|C_2|}\Pi\left(-\frac{t}{2C_2}\right) e^{\mathbb{i}\frac{C_1}{C_2}t} \tag{A.9}$$

with rectangular function

$$\Pi(X) = \begin{cases} 1 & \text{if } -\frac{1}{2} < X < \frac{1}{2} \\ 0 & \text{otherwise.} \end{cases} \tag{A.10}$$

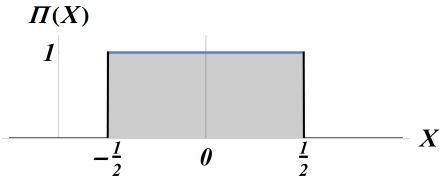


Figure A.2 Rectangular function $\Pi(X)$ as defined in Equation A.10.

With Equation A.8 the $G^{(2)}_{\mathrm{HOM}}$-function results in

$$\begin{aligned}
&G^{(2)}_{\mathrm{HOM}}(t_1, t_2) \\
&\propto \cos^4(2\beta)\ \Pi\left(\frac{\Delta\tau + \Delta t}{L\ D}\right) + \sin^4(2\beta)\ \Pi\left(\frac{\Delta\tau - \Delta t}{L\ D}\right) - \cos^2(2\beta)\ \sin^2(2\beta) \\
&\qquad \left(\mathrm{e}^{-\mathrm{i}(2\frac{A(T,\omega_\mathrm{p})}{D} + 2\omega_0 - \omega_\mathrm{p})\Delta t} + \mathrm{e}^{\mathrm{i}(2\frac{A(T,\omega_\mathrm{p})}{D} + 2\omega_0 - \omega_\mathrm{p})\Delta t}\right) \Pi\left(\frac{\Delta\tau + \Delta t}{L\ D}\right)\ \Pi\left(\frac{\Delta\tau - \Delta t}{L\ D}\right) \\
&\propto \cos^4(2\beta)\ \Pi\left(\frac{\Delta\tau + \Delta t}{L\ D}\right) + \sin^4(2\beta)\ \Pi\left(\frac{\Delta\tau - \Delta t}{L\ D}\right) - \cos^2(2\beta)\ \sin^2(2\beta) \\
&\qquad 2\ \cos\left((2\frac{A(T,\omega_\mathrm{p})}{D} + 2\omega_0 - \omega_\mathrm{p})\Delta t\right) \Pi\left(\frac{\Delta\tau + \Delta t}{L\ D}\right)\ \Pi\left(\frac{\Delta\tau - \Delta t}{L\ D}\right)
\end{aligned} \tag{A.11}$$

The probability of detecting coincidence events is proportional to the $G^{(2)}_{\mathrm{HOM}}$-function integrated over the range of the detectors resolving time. For the detectors used the resolving time is of the order of 1 ns and is therefore much larger than $L\ D = 3.5\,\mathrm{ps}$. Consequently, we can extend the range of the integral to $\pm\infty$ in good approximation.

$$P_c \propto \int_{-\infty}^{\infty}\int_{-\infty}^{\infty} \mathrm{d}t_1 \mathrm{d}t_1 G^{(2)}_{\mathrm{HOM}}(t_1, t_2). \tag{A.12}$$

In the case of $\omega_\mathrm{p} = 2\omega_0$ and $T = T_0$, the above integration yields the normalized probability

$$\begin{aligned}
&P_c(\Delta\tau, \beta) \\
&= \cos^4(2\beta) + \sin^4(2\beta) - 2\ \cos^2(2\beta)\ \sin^2(2\beta)\ \Theta\left(\frac{L\,|D|}{2} - |\Delta\tau|\right) \frac{2}{L\,|D|} \left(\frac{L\,|D|}{2} - |\Delta\tau|\right) \\
&= 1 - \frac{1}{2}\sin^2(4\beta) - \frac{1}{2}\sin^2(4\beta)\ \Theta\left(\frac{L\,|D|}{2} - |\Delta\tau|\right) \left(1 - \frac{2\ |\Delta\tau|}{L\,|D|}\right) \\
&= 1 - \frac{1}{2}\sin^2(4\beta) \left(1 + \ \Theta\left(\frac{L\,|D|}{2} - |\Delta\tau|\right) \left(1 - \frac{2\ |\Delta\tau|}{L\,|D|}\right)\right)
\end{aligned} \tag{A.13}$$

with Heaviside step function

$$\Theta(X) = \begin{cases} 1 & \text{if } 0 < X \\ 0 & \text{otherwise.} \end{cases} \tag{A.14}$$

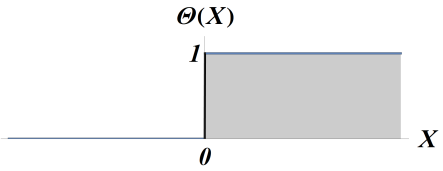


Figure A.3 Heaviside step function $\Theta(X)$ as defined in Equation A.14.

In the more general case, the integral of Equation A.12 results in

$$\begin{aligned} &P_c(\Delta\tau, \beta, T, \omega_\mathrm{p}) \\ &= 1 - \frac{1}{2}\sin^2(4\beta)\left(1 + \Theta\left(\frac{L\,|D|}{2} - |\Delta\tau|\right)\frac{2}{L\,|D|}\frac{\sin\left((2\frac{A(T,\omega_\mathrm{p})}{D} + 2\omega_0 - \omega_\mathrm{p})(\frac{L|D|}{2} - |\Delta\tau|)\right)}{2\frac{A(T,\omega_\mathrm{p})}{D} + 2\omega_0 - \omega_\mathrm{p}}\right) \\ &= 1 - \frac{1}{2}\sin^2(4\beta)\left(1 + \Theta\left(\frac{L\,|D|}{2} - |\Delta\tau|\right)\left(1 - \frac{2\ |\Delta\tau|}{L\,|D|}\right) f(\Delta\tau, \Delta T, \Delta\omega_\mathrm{p})\right) \end{aligned} \tag{A.15}$$

$$\begin{aligned} f(\Delta\tau, \Delta T, \Delta\omega_\mathrm{p}) &= \mathrm{sinc}\left((2\frac{A(T,\omega_\mathrm{p})}{D} - \Delta\omega_\mathrm{p})(\frac{L\,|D|}{2} - |\Delta\tau|)\right) \\ &= \mathrm{sinc}\left((\frac{2D_T}{D}\Delta T + \frac{2D_{\omega_\mathrm{p}} - D}{D}\Delta\omega_\mathrm{p})(\frac{L\,|D|}{2} - |\Delta\tau|)\right) \end{aligned} \tag{A.16}$$

$$\begin{aligned} V_\mathrm{HOM}(\beta, \Delta T, \Delta\omega_\mathrm{p}) &= \frac{P_c(\infty, \beta, T, \omega_\mathrm{p}) - P_c(0, \beta, T, \omega_\mathrm{p})}{P_c(\infty, \beta, T, \omega_\mathrm{p})} \\ &= \frac{\frac{1}{2}\sin^2(4\beta)}{1 - \frac{1}{2}\sin^2(4\beta)} f(0, \Delta T, \Delta\omega_\mathrm{p}) \\ &= \frac{\frac{1}{2}\ \sin^2(4\beta)}{1 - \frac{1}{2}\sin^2(4\beta)} \mathrm{sinc}\left(D_T\ L\ \Delta T + (D_{\omega_\mathrm{p}} - \frac{D}{2})\ L\ \Delta\omega_\mathrm{p}\right) \end{aligned} \tag{A.17}$$

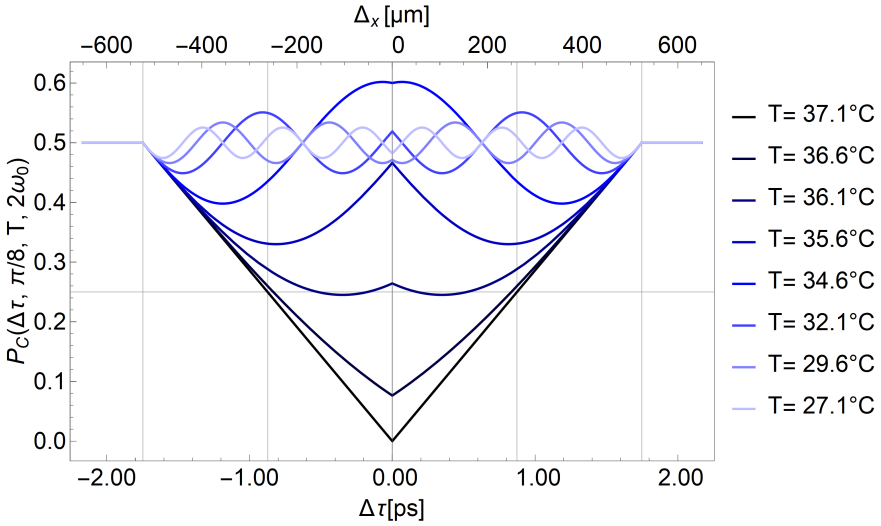


Figure A.4 $P_c(\Delta\tau, \pi/8, T, 2\omega_0)$ vs. $\Delta\tau$ @ different temperatures T.

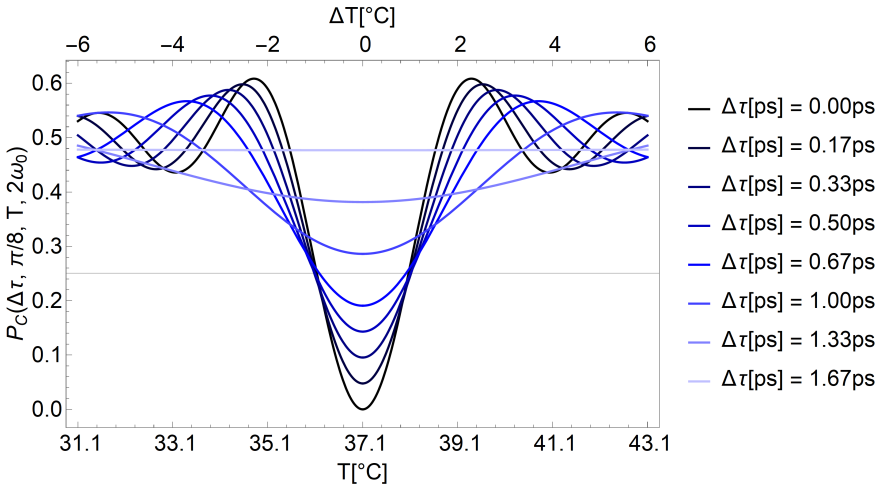


Figure A.5 $P_c(\Delta\tau, \pi/8, T, 2\omega_0)$ vs. temperatures T @ different time delays $\Delta\tau$.

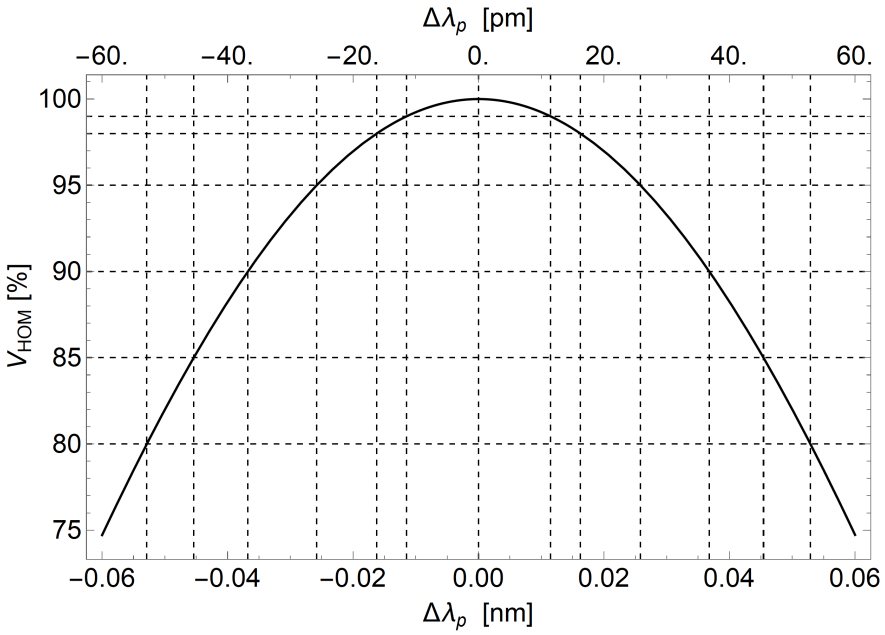


Figure A.6 $V_{\mathrm{HOM}}(\pi/8, 0, \frac{c2\pi}{\lambda_0+\Delta\lambda} - 2\omega_0)$ vs. pump wavelength offset $\Delta\lambda$

B First Author Publications

nature COMMUNICATIONS

ARTICLE

Received 22 Aug 2016 | Accepted 20 Mar 2017 | Published 10 May 2017

DOI: 10.1038/ncomms15304 OPEN

Experimental test of photonic entanglement in accelerated reference frames

Matthias Fink[1], Ana Rodriguez-Aramendia[1], Johannes Handsteiner[1], Abdul Ziarkash[1], Fabian Steinlechner[1], Thomas Scheidl[1], Ivette Fuentes[2], Jacques Pienaar[1,2,†], Timothy C. Ralph[3] & Rupert Ursin[1,4]

The unification of the theory of relativity and quantum mechanics is a long-standing challenge in contemporary physics. Experimental techniques in quantum optics have only recently reached the maturity required for the investigation of quantum systems under the influence of non-inertial motion, such as being held at rest in gravitational fields, or subjected to uniform accelerations. Here, we report on experiments in which a genuine quantum state of an entangled photon pair is exposed to a series of different accelerations. We measure an entanglement witness for g-values ranging from 30 mg to up to 30 g—under free-fall as well on a spinning centrifuge—and have thus derived an upper bound on the effects of uniform acceleration on photonic entanglement.

[1] Institute for Quantum Optics and Quantum Information—Vienna (IQOQI), Austrian Academy of Sciences, Boltzmanngasse 3, Vienna A-1090, Austria. [2] Faculty of Physics, University of Vienna, Boltzmanngasse 5, Vienna A-1090, Austria. [3] Centre for Quantum Computation & Communication Technology, School of Mathematics and Physics, University of Queensland, Brisbane, Queensland 4072, Australia. [4] Vienna Center for Quantum Science and Technology (VCQ), Vienna, Austria. † Present address: International Institute of Physics (IIP-UFRN), Avenida Odilon Gomes de Lima 1722, 59078-400 Natal, Brazil. Correspondence and requests for materials should be addressed to M.F. (email: Matthias.Fink@oeaw.ac.at) or to R.U. (email: Rupert.Ursin@oeaw.ac.at).

Einstein's relativity theory and quantum theory are two pillars of modern physics that have each been shown to work well in their respective regimes. All currently observed physical effects fall well within one regime or the other, and can be described by the respective theory to very high precision. Without the scientific insights from these two theories, a modern information society would not be imaginable, taking the global positioning system or semiconductor technology as two prominent examples.

The unification of Einstein's theory of relativity and quantum mechanics is a long-standing problem in contemporary physics. As long as these descriptions of nature remain confined to their own scope of application, they cannot contribute to a unified theory that captures physics at the boundary between these specialized regimes. In natural science, where theory becomes uncertain, new experimental data are needed. It is not unusual for the first steps into an uncharted experimental regime to yield unexpected results, as occurred in the historical black-body radiation[1] and Michelson–Morley[2] experiments.

One phenomenon whose limits have not been fully tested in all regimes is quantum entanglement of spatially separated quantum systems. Entanglement can spread quantum superpositions over macroscopic distances and has been experimentally found to exist over distances as large as 144 km (ref. 3). The non-local character of these superpositions then seems in conflict with the local nature of relativity. This raises the question of whether entanglement persists, when we consider non-inertial reference frames, such as those experienced by accelerated systems or systems in gravitational fields, as the space-time metric can vary with position in these cases. It is likely that the resolution of such questions will be a key piece in the puzzle leading to a full theory of quantum gravity. Hence, quantum entangled systems subjected to high- and low-accelerations is one regime, where new physical phenomena might potentially arise. It is known that experimental investigations involving simulated hyper- or milligravity can cause unexpected changes to physical phenomena[4]. Exposing physical systems to such extreme conditions can aid in the understanding of that system, and lead to a deeper understanding of the physical processes themselves.

It has been suggested that motion and gravity can both have observable effects on quantum entanglement[5–8]. However, experimental tests of quantum phenomena in these regimes is still sparse[9]. To date, first experiments have been performed using only single quanta, e.g., in the pioneering work of Colella *et al.*[10,11]. Apart from this, there has been no systematic experimental investigation of the effect of non-inertial motion or gravity on quantum entanglement.

Just recently a remarkable one-shot experiment was carried out where a correlated photon source was exposed to ultra high acceleration during an explosion (when the rocket exploded during the launch phase of the mission), but not during it's operation[12]. In a subsequent launch this project ultimately succeeded in placing a correlated photon state on a cubesat into space[13]. Those Experiments demonstrate very high stability of optical alignment under harsh mechanical and thermal conditions but do not directly relate to properties of

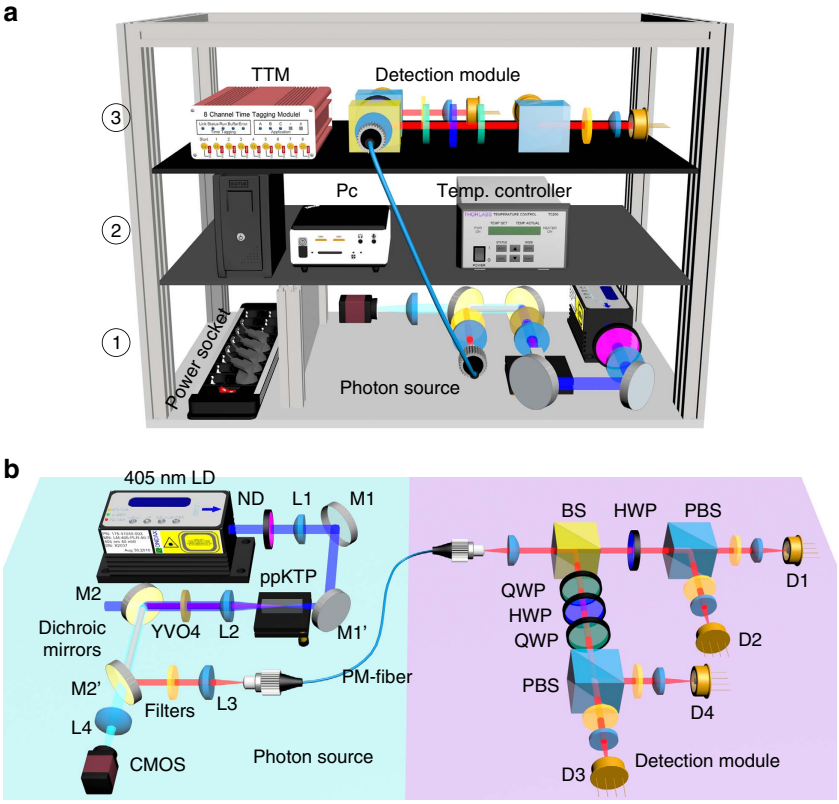


Figure 1 | Sketch of the source crate. (**b**) A laser diode pumps a ppKTP crystal heated by an oven, generating photon pairs collected in a polarization maintaining single-mode fibre. An additional Nd:YVO_4 crystal is used to fine-tune the walk-off compensation. A BS creates an equal superposition for reflection and transmission for each individual photon, which leads to an polarization-entangled state in postselection. Using various half- and quarter-wave plates (HWP, QWP) and PBS, the polarization correlations can be analysed in different measurement bases and measured in detectors (D1,D2,D3 and D4). (**a**) Source (level 1), electronics (level 2), as well as polarization analysis and detection module (level 3) are placed at different levels inside the crate and thus exhibit different maximal g-values.

entanglement under these conditions. However, with the onset of new technology, techniques now exist to transgress experimental barriers and begin to test quantum physics in non-inertial systems.

Following these lines we report on a series of experiments that test quantum theory in non-inertial reference frames by exposing a provably quantum state[14] of polarization-entangled photon pairs to various uniform accelerations. The acceleration is imposed by its motion, in free-fall, as well as on a centrifuge. In a first series of experiments, we dropped a crate containing an entangled photon source and two single-photon polarization detection units from 12 m in a drop tower to realize a milli-g environment, where we reached 30 mg. In the second series of experiment, the crate was mounted on an arm of a rotational centrifuge and accelerated to, as high as 30 g at a maximum angular speed of 9.9 rad s^{-1}.

Our results show that quantum entanglement is unaffected by non-inertial motion to within the resolution of our test-system. This represents the first experimental effort exposing a genuine quantum system to milli-g and hyper-g and extends the experimental regime in which quantum effects can be said to exist in harmony with relativity. Future experiments could be designed to investigate if the entangled state is transformed when the system undergoes non-uniform acceleration or much higher accelerations or massive gravitational fields.

Results

Entangled photon system. We developed an ultra-stable entangled photon system, comprising a source of polarization-entangled photons and detection setup. The optical setup and the electronic control equipment were mounted in a rigid three-level crate (Fig. 1a), which could withstand the high g-forces during the deceleration and acceleration phases in our intended drop-tower and centrifuge experiments. The integrated crate design also facilitated flexible plug-and-play installation at the drop-tower and centrifuge support structures.

The entangled photon source (Fig. 1) is based on spontaneous parametric down conversion (SPDC) in a degenerate collinear type-II quasi-phase matching configuration and postselection on a beam splitter (BS)[15]. A continuous-wave pump laser at 405 nm is focused loosely into a periodically poled potassium titanyl phosphate (ppKTP) crystal and creates pairs of signal and idler photons with horizontal (H) and vertical (V) polarization, respectively. The temperature of the nonlinear crystal is stabilized at 39.6 °C ± 0.1 °C for wavelength-degenerate quasi-phase matching at 810 nm. To monitor possible misalignment of the beam paths during acceleration, a fraction of the pump beam was imaged onto a CMOS camera that was placed behind one of the dichroic mirrors. The photon pairs were separated from the pump light using two dichoric mirrors and an interference filter, and coupled into a sole polarization maintaining single-mode optical fibre (PMSMF). The polarization axis of the PMSMF was carefully aligned to coincide with the optical axes of the nonlinear crystal. The length of the PMSMF and an additional neodymium-doped yttrium orthovanadate (Nd:YVO_4) crystal were chosen, such that the average longitudinal walk-off between the signal and idler photons due to the birefringence of the ppKTP crystal, was compensated. This ensures, that no information about the polarization of a photon can be obtained from the timing of the SPDC photons. The PMSMF also had the benefit of ensuring polarization stability even at high accelerations during an experimental run. The PMSMF guides the photon pairs to a non-polarizing BS, which creates an equal superposition of reflection (mode 1) and transmission (mode 2). When post-selecting events where one photon is detected in each of these two modes, one thus obtains the maximally polarization-entangled state:

$$|\Psi\rangle = 1/\sqrt{2}\left(|H_1V_2\rangle + e^{-i\phi}|V_1H_2\rangle\right) \quad (1)$$

where H (V) denote the horizontal (vertical) polarization states relative to the baseplate of the source. Note that the orientation of the baseplate changes relative to the laboratory frame during the experiment (Fig. 2b).

A combination of a quarter-, half- and quarter-wave plate is used to compensate polarization dependent phase shifts caused by the reflection at the BS and allows setting the phase ϕ. For the presented experiments the quarter-wave plate was set such that $\phi = \pi$ resulting in the rotationally invariant two-photon state $|\Psi^-\rangle = 1/\sqrt{2}(|H_1V_2\rangle - |V_1H_2\rangle)$. An additional motorized half-

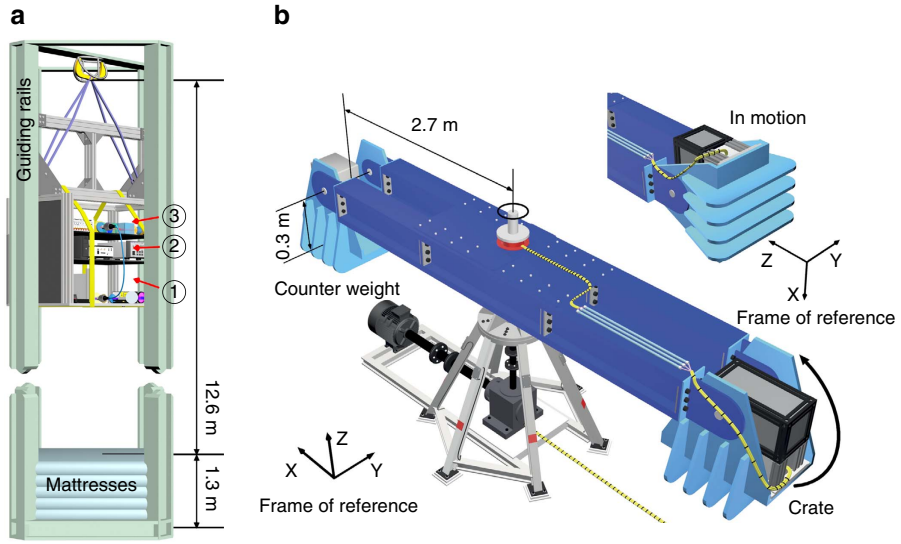


Figure 2 | Scheme of the experiments. (**a**) The crate was dropped from 12 m for a low-g (almost) free-fall flight in air of 1.4 s. A 1.3-m-high stack of mattresses was used to reduce deceleration on impact (Supplementary Movie 1). (**b**) The source crate was installed in one of the centrifuge gondolas at a distance of about 3 m from the axis, at full speed. The orientation of the accelerometer reference frame are shown when the centrifuge is at rest and in motion (Supplementary Movie 2).

wave plate followed by a polarizing beam splitter (PBS) is inserted in each output mode of the BS to analyse the polarization of the photons in any desired linear polarization measurement basis. Finally, the photons were detected using four passively quenched semiconductor avalanche photo diodes placed in every output mode of the two PBS. Coloured glass filters and additional interference filters were placed in front of the detectors in order to minimize background counts from the remaining pump photons and stray background light. The electronic detector signals are recorded by a time-tagging module, allowing to post-select simultaneous detection events in the two output modes of the 50/50 BS.

A lower bound on the Bell-state fidelity of the experimental state was established using the fidelity witness:

$$F_{\Psi^-}\left(\hat{\rho}_{\mathrm{exp}}\right)=\langle\Psi^-|\hat{\rho}_{\mathrm{exp}}|\Psi^-\rangle \geq F^{\mathrm{M}}_{\Psi^-}\left(\hat{\rho}_{\mathrm{exp}}\right)=\frac{1}{2}\left(V_{\mathrm{HV}}+V_{\mathrm{DA}}\right) \tag{2}$$

where V_{HV} and V_{DA} denote the visibilities of the two-photon correlation function measured in the horizontal/vertical (diagonal/anti-diagonal) basis[16]. The two-photon polarization-correlation functions were evaluated as:

$$V=\frac{N_{13}+N_{24}-N_{14}-N_{23}}{N_{13}+N_{24}+N_{14}+N_{23}} \tag{3}$$

where N is the number of coincidence detection events between detectors 1 and 2 for each measurement setting (HV, DA). For a pump power of $\sim$5 mW. The setup provides 280 kcps detected single counts in total and 7 kcps coincident counts, yielding a visibility of $V_{\mathrm{HV}}=97\%$ in HV basis and $V_{\mathrm{DA}}=96\%$ in the DA basis. Note that the visibility in the DA basis is lower, as it is affected by drifts in the alignment of polarization measurement bases, imperfect phase compensation, as well as the partial distinguishably of the two photons (for example, due to deviations from the wavelength-degenerate phase matching temperature).

The drop tower experiment. A drop from a height of 12 m provided us with an integration time of 1.4 s for the milli-g experiment (Fig. 2). Electrical power was provided by a battery built into the crate, and kept the source and detectors operational for about 1.5 h. A wireless network antenna provided data-connection to the crate, and was used to control the experiment. Guide rails kept the crate on track during flight and impact. Air resistance and the guide rails resulted in drag on the crate, which reached a maximum velocity of 55 km per h, enabling us to measure g-values, as low as 30 ± 3 mg after the electronic-mechanical locking mechanism was opened. To cushion the impact of the crate source, we placed a high-stack of foam mattresses at the base of the drop tower. This reduced deceleration enough to avoid permanent damage but still caused a saturation of our g-sensor at 16 g.

We observed no lasting degradation in count rates or source visibility after impact on the mattresses, and could repeat the experiment many times without the need for re-alignment between measurement runs. In each successive experimental run we measured the visibility either in the HV- or in the DA- measurement basis, as shown in Fig. 3. Each successive experimental run resulted in $\approx$400,000 single-photon detecion events in total, which were stored as time-tags on the local computer for later evaluation. During the free-fall phase the visibility never dropped below $V_{\mathrm{DA}}=96\%\pm2\%$.

The centrifuge experiment. For the strong acceleration regime, we used a centrifuge that rotates the crate around a fixed vertical axis, thus resulting in an outward oriented force perpendicular to the axis of rotation (Fig. 2b). The centrifuge consists of two 3-m-long arms with articulated platforms at either end (Fig. 2b). The platforms swing outwards at increasing angular velocities of the centrifuge. The crate was mounted in one of the two gondolas with a 37 kg counterweight on the other side. Electrical power and data-connection to the crate were provided by means of a sliding contact at the axis of the centrifuge to the control room.

The acceleration was varied from 1 g to up to 30 g in $\sim$5 g steps by increasing the angular velocity of the centrifuge. Despite the strong acceleration the optical setup remained stable throughout the experiment. The pump beam shifted by up to two pixels on the CCD camera, which corresponds to an angular deviation of $\sim$38 arcsec. This is well within the alignment tolerances of the PMSM-fibre coupling lens system and no drop in the count rates was observed. For each g value (set by the angular speed of the centrifuge) we evaluated the visibility in the complementary HV and DA measurement basis for several minutes (Fig. 4). Note that a small reduction of the DA visibility stems from the fact that the temperature of the crystal was not stable at high accelerations. This was due to high-wind speed of about 174 km per h, which effectively cooled the system as indicated by the temperature sensor of the oven. The resulting deviation from the degenerate phase matching temperature introduced distinguishability of the emitted photon pair, and reduced the visibility in the DA basis accordingly.

Discussion

We have conducted experiments with g-values corresponding to milli-g (drop tower) and hyper-g (centrifuge) settings. We used a genuine quantum mechanical system to evaluate whether the amount of entanglement is affected by non-inertial motion in accelerated reference frames. We implemented an entangled photon source together with a detection system and the required electronics in an autonomous source crate. We contiguously measured a witness, which imposes a bound on the minimum Bell-state fidelity, from the visibility of polarization correlations in two mutually unbiased basis (HV and DA).

Figure 5 summarizes the g-value versus the entanglement fidelity measured for experiments in the falling tower and the centrifuge. A Bell-state fidelity $>96\%$ was observed for all acceleration levels. Each data point was calculated using $>10{,}000$ coincidence counts leading to an 3σ error bar of 0.25%. The measured fidelity is limited by numerous sources of systematic errors such as accidental coincidence counts[17], and birefringence-induced transformations of the entangled photon state, temperature-dependent spectral characteristics of the SPDC process[18].

Our experiment can rule out any hypothetical variation of entanglement to within the precision of the current measurement apparatus. The resolution in our experiment was limited by the short experimental integration time, as well as residual drifts of the crystal temperature and alignment of the source. Note, however, that these were mainly due to wind speeds, and not correlated with the acceleration itself. The error bars shown in the graphs are calculated considering Poissonian statistics, as well as systematical errors. Due to temperature fluctuations of the nonlinear crystal (±0.1 °C) and gusts of cold air in the centrifuge, an additional error of $\pm0.6\%$ was observed in the DA-visibility. This corresponds to an uncertainty of $\pm0.3\%$ in the Fidelity, in addition to statistical errors. The total error is well within the average fidelity taking all acquired data into account.

Note that the sources of systematic errors could be reduced by automated opto-mechanical re-alignment and better temperature stabilization.

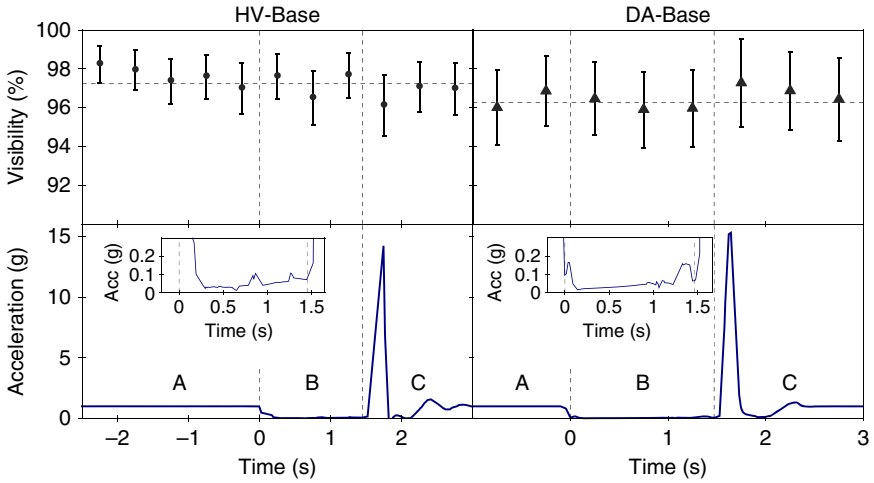


Figure 3 | Data for drop tower experiment. (A) Elapsed time at rest, (B) free-fall flight (C) and after impact versus HV- (left) and DA-visibility (right) measured in 500 ms slots compared to its average (denoted as horizontal dashed line). Each of data points shown consists of ≈3,500 coincident counts and $V_{DA} = 96\%$ on average. The error bars shown in the graphs are calculated considering Poissonian statistics, as well as systematical errors for DA measurements due to temperature fluctuations. The actual g-value shows the drag from contacts with the guiding rail and the wind at higher velocities. The impact (at 1.45 s) consisted of a 16 g deceleration phase (g-sensor saturated) and a rebound phase (at 2 s).

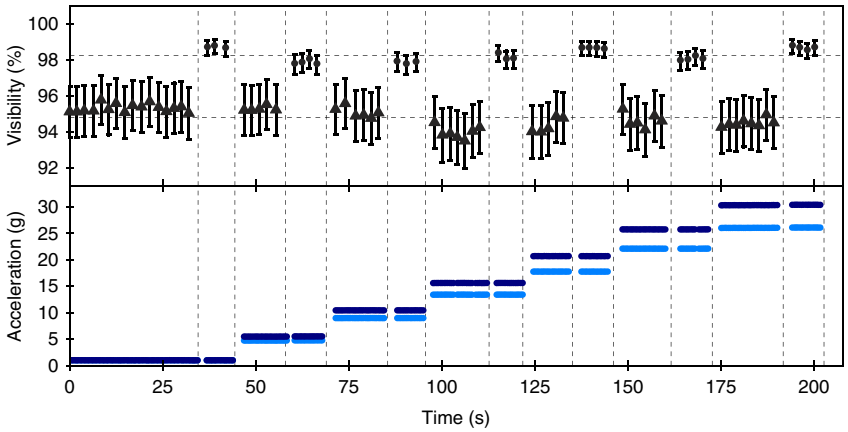


Figure 4 | Data from centrifuge experiment. Time elapsed versus g-force and visibility in the DA (triangles) and HV (circles) polarization measurement basis. The average of the visibilities is represented as horizontal dashed line (94.8 and 98.3%). Each of the points was calculated from ≈14,000 coincident counts. The error bars shown in the graphs are calculated considering Poissonian statistics, as well as systematical errors for DA measurements due to temperature fluctuations. The drop in visibility at 15 g is due to the effective cooling of the crystal during higher angular spinning speeds. The lower g-values (light blue) represent the measured data of the g-sensor at level 3 (detection) of the crate. In addition the calculated acceleration at level 1 (source) is plotted (blue).

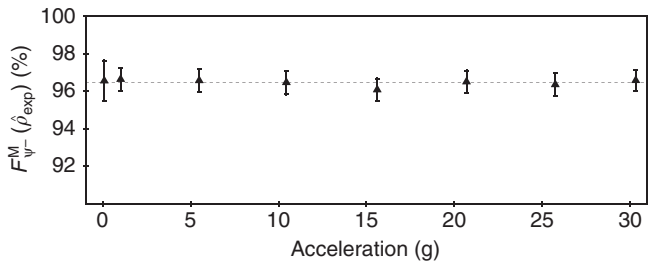


Figure 5 | Summary of experimental data. All data acquired during the experiments shown as the g-value versus lower bound on Bell-state fidelity $\left(F^{M}_{\Psi^-}(\hat{\rho}_{exp})\right)$, for g-values ranging from 3 mg to up to 30 g. The error bars shown in the graphs are calculated considering Poissonian statistics, as well as systematical errors for DA measurements due to temperature fluctuations. No deviation from the total average (96.45% represented as horizontal dashed line) for more than the estimated errors is visible.

In conclusion, we have used the techniques originally developed for quantum optics high-precision experiments, to search for first experimental indications of unexpected effects in quantum systems caused by acceleration. Using the entangled system in the milli-g and hyper-g experiments described above, we found no correlation between the phase of the entangled state or its degree of entanglement with the acceleration of its non-inertial reference frame. These experiments therefore rule out any influence on the polarization-entangled two-photon quantum state that could hypothetically cause a reduction in fidelity of $> 1.08\%$.

Our study tested photonic quantum entanglement in the case of flat space-time, where the system undergoes uniform acceleration. Within this experiment we have shown that quantum entanglement should persist in a variety of accelerated frames. Apart from the inherent novelty of testing entanglement under different accelerated conditions, the results of the experiment can also be extrapolated to analogous hypothetical experiments under different gravitational fields. If, for example,

the equivalence principle holds, then a local test of entanglement should not reveal the difference between uniform acceleration and a gravitational field[19]. We thus hope that the experimental work reported in this manuscript will help in the future to shed light on quantum mechanics in non-inertial frames, ultimately including gravity.

Note that similar conditions would also accompany a rocket launch into space and are thus also relevant to subsequent quantum optics experiments carried out in space. We have shown that a full quantum optics experiment involving entangled photons was not only capable to withstand such severe stress, but also remained fully functional in severe operating conditions. Our experiment thus demonstrates the extent to which state-of-the-art quantum hardware can be exposed to such harsh operational environment, with the intention of stimulating research on theories beyond the current paradigm which can be tested with the kind of experiments presented here.

Our experimental platform represents a testbed that can readily be upgraded for measurements with higher precision, by using a ultra-bright source of entangled photons[20], and higher-dimensional degrees of freedom, such as energy-time entanglement[21]. We also envisage bringing such a system very close to zero-g conditions for several tens of seconds and reaching hyper-g up to 150 g for many hours or even day's of operation. An interesting direction for future Earth and space-based experiments is to consider photonic states undergoing non-uniform acceleration, as theoretical studies predict that changes in acceleration and changes in the gravitational field strength produce observable effects on entanglement[5–8].

Data availability. The data sets generated and analysed during the current study are available from the corresponding author on reasonable request.

References

1. Rubens, H. & Kurlbaum, F. On the heat radiation of long wave-length emitted by black bodies at different temperatures. *Astrophys. J.* **14,** 335 (1901).
2. Michelson, A. A. & Morley, E. W. On the relative motion of the earth and the luminiferous ether. *Am. J. Sci.* **34,** 333–345 (1887).
3. Ursin, R. *et al.* Entanglement-based quantum communication over 144 km. *Nat. Phys.* **3,** 481–486 (2007).
4. Dreyer, M. The drop tower Bremen. *Microgravity Sci. Technol.* **22,** 461–461 (2010).
5. Bruschi, D. E. *et al.* Testing the effects of gravity and motion on quantum entanglement in space-based experiments. *New. J. Phys.* **16,** 053041 (2014).
6. Bruschi, D. E., Fuentes, I. & Louko, J. Voyage to alpha centauri: Entanglement degradation of cavity modes due to motion. *Phys. Rev. D* **85,** 061701 (2012).
7. Friis, N., Bruschi, D. E., Louko, J. & Fuentes, I. Motion generates entanglement. *Phys. Rev. D* **85,** 081701 (2012).
8. Alsing, P. M. & Fuentes, I. Observer-dependent entanglement. *Class. Quantum Gravity* **29,** 224001 (2012).
9. Amelino-Camelia, G. Gravity in quantum mechanics. *Nat. Phys.* **10,** 254–255 (2014).
10. Colella, R., Overhauser, A. W. & Werner, S. A. Observation of gravitationally induced quantum interference. *Phys. Rev. Lett.* **34,** 1472–1474 (1975).
11. Abele, H. & Leeb, H. Gravitation and quantum interference experiments with neutrons. *New J. Phys.* **14,** 055010 (2012).
12. Tang, Z. *et al.* The photon pair source that survived a rocket explosion. *Sci. Rep.* **6,** 25603 (2016).
13. Tang, Z. *et al.* Generation and analysis of correlated pairs of photons aboard a nanosatellite. *Phys. Rev. Appl.* **5,** 054022 (2016).
14. Bell, J. On the Einstein Podolsky Rosen Paradox. *Physics* **1,** 195–200 (1964).
15. Kuklewicz, C. E., Fiorentino, M., Messin, G., Wong, F. N. C. & Shapiro, J. H. High-flux source of polarization-entangled photons from a periodically poled ktiopo4 parametric down-converter. *Phys. Rev. A* **69,** 013807 (2004).
16. Blinov, B. B., Moehring, D. L., Duan, L.-M. & Monroe, C. Observation of entanglement between a single trapped atom and a single photon. *Nature* **428,** 153–157 (2004).
17. Takesue, H. & Shimizu, K. Effects of multiple pairs on visibility measurements of entangled photons generated by spontaneous parametric processes. *Opt. Commun.* **283,** 276–287 (2010).
18. Steinlechner, F. *et al.* Efficient heralding of polarization-entangled photons from type-0 and type-ii spontaneous parametric downconversion in periodically poled ktiopo4. *J. Opt. Soc. Am. B* **31,** 2068–2076 (2014).
19. Zych, M. & Brukner, C. Quantum formulation of the einstein equivalence principle. Preprint at https://arxiv.org/abs/1502.00971 (2015).
20. Steinlechner, F. *et al.* A high-brightness source of polarization-entangled photons optimized for applications in free space. *Opt. Express* **20,** 9640–9649 (2012).
21. Steinlechner, F. *et al.* Distribution of hyperentanglement via an intra city free-space link. Preprint at https://arxiv.org/abs/1612.00751 (2016).

Acknowledgements

We are especially thankful to Prof. Martin Tajmar and the Technical University Dresden (Germany) for their support in the drop-tower experiment. The centrifuge experiment was supported by Jens Schiefer and Clemens Greiner from AMST in Ranshofen (Austria). We would also like to thank FFG-ALR (contract no. 844360), ESA (contract no. 4000112591/14/NL/US), FWF (P24621-N27), as well as the Austrian Academy of Sciences for their financial support.

Author contributions

M.F. performed the experiments and analysed the data. T.S., J.H. and A.R.-A. designed the crate source. A.Z. assisted the drop tower experiment. F.S. provided experimental guidance on the entangled photon source and supervised the research. J.P., T.C.R. and I.F. provided advice and motivation regarding entanglement and the local nature of relativity. R.U. conceived the project, supervised the research and coordinated the project. All authors contributed to the writing of the paper.

Additional information

Supplementary Information accompanies this paper at http://www.nature.com/naturecommunications

Competing interests: The authors declare no competing financial interests.

Reprints and permission information is available online at http://npg.nature.com/reprintsandpermissions/

How to cite this article: Fink, M. *et al.* Experimental test of photonic entanglement in accelerated reference frames. *Nat. Commun.* **8,** 15304 doi: 10.1038/ncomms15304 (2017).

Publisher's note: Springer Nature remains neutral with regard to jurisdictional claims in published maps and institutional affiliations.

This work is licensed under a Creative Commons Attribution 4.0 International License. The images or other third party material in this article are included in the article's Creative Commons license, unless indicated otherwise in the credit line; if the material is not included under the Creative Commons license, users will need to obtain permission from the license holder to reproduce the material. To view a copy of this license, visit http://creativecommons.org/licenses/by/4.0/

© The Author(s) 2017

New Journal of Physics
The open access journal at the forefront of physics

Deutsche Physikalische Gesellschaft DPG
IOP Institute of Physics

Published in partnership with: Deutsche Physikalische Gesellschaft and the Institute of Physics



OPEN ACCESS

RECEIVED
22 January 2019

REVISED
9 April 2019

ACCEPTED FOR PUBLICATION
23 April 2019

PUBLISHED
8 May 2019

Original content from this work may be used under the terms of the Creative Commons Attribution 3.0 licence.

Any further distribution of this work must maintain attribution to the author(s) and the title of the work, journal citation and DOI.



PAPER

Entanglement-enhanced optical gyroscope

Matthias Fink[1,2,8], **Fabian Steinlechner**[1,2,7], **Johannes Handsteiner**[1,2], **Jonathan P Dowling**[3,4,5,6], **Thomas Scheidl**[1,2] **and Rupert Ursin**[1,2,8]

[1] Institute for Quantum Optics and Quantum Information—Vienna (IQOQI), Austrian Academy of Sciences, Vienna, Austria
[2] Vienna Center for Quantum Science and Technology (VCQ), Vienna, Austria
[3] Hearne Institute for Theoretical Physics, Department of Physics and Astronomy, Louisiana State University, Baton Rouge, LA 70803, United States of America
[4] CAS-Alibaba Quantum Computing Laboratory, USTC, Shanghai 201315, People's Republic of China
[5] NYU-ECNU Institute of Physics at NYU Shanghai, Shanghai 200062, People's Republic of China
[6] National Institute of Information and Communications Technology, Tokyo 184-8795, Japan
[7] Present address: Fraunhofer Institute for Applied Optics and Precision Engineering IOF, Jena, Germany
[8] Author to whom any correspondence should be addressed.

E-mail: Matthias.Fink@oeaw.ac.at **and** Rupert.Ursin@oeaw.ac.at

Keywords: Sagnac effect, fiber optic gyroscope, NOON-state, entanglement-enhanced, shot-noise limit, super-resolution

Abstract

Fiber optic gyroscopes (FOG) based on the Sagnac effect are a valuable tool in sensing and navigation and enable accurate measurements in applications ranging from spacecraft and aircraft to self-driving vehicles such as autonomous cars. As with any classical optical sensors, the ultimate performance of these devices is bounded by the shot-noise limit (SNL). Quantum-enhanced interferometry allows us to overcome this limit using non-classical states of light. Here, we report on an entangled-photon gyroscope that uses path-entangled NOON-states ($N = 2$) to provide super-resolution and phase sensitivity beyond the shot-noise limit.

1. Introduction

Among the many applications of optical interferometry, optical gyroscopes based on the Sagnac effect are an invaluable tool in sensing and navigation. First observed by Georges Sagnac in 1913 [1, 2]—in an attempt to observe the 'relative circular motion of the luminiferous ether within the closed optical path' [3, 4]—the Sagnac effect refers to the relative phase $\phi_S(\Omega)$ experienced by counter-propagating light waves in a rotating interferometer. To this day, this experiment, together with that of Michelson and Morley [5], is considered one of the fundamental experimental tests of the theory of relativity [6]. While the relativistic correction of the effect is still under discussion [7–10], a mass product has evolved from its application [11]. The effect allows us to determine the absolute rotation Ω with respect to inertial space [7] and has since found application in navigation systems for spacecraft [12] and aircraft [13] as well as self-driving vehicles such as autonomous cars [11].

The precision of an optical gyroscope is determined by the phase response $\partial\phi/\partial\Omega$ as well as the minimum phase resolution $\Delta\phi$. The phase response or Sagnac scale factor S_T, is proportional to the area $A_{\circlearrowleft}$ enclosed by the counter propagating waves and inverse proportionality to the wavelength λ of the interfering wave. In commercial fiber optic gyroscopes (FOG), the phase response is amplified by increasing the effective area enclosed by the optical paths by using an optical fiber-coil. Another strategy to improve the precision is to use shorter wavelengths. Therefore, the Sagnac effect was examined with x-rays [14] as well as with de-Broglie waves such as electrons [15], neutrons [16], and atoms [17–19]. The generation and guiding of such waves, however, is rather difficult in comparison to optical electromagnetic waves, and the area enclosed by such gyroscopes is rather small compared to the FOG.

The minimum phase resolution of a FOG is limited by various sources of noise. The most fundamental reason for limited precision is the so-called shot noise, which is caused by the quantization of the electromagnetic field itself. For coherent states, the number of photons detected in a time interval τ follows a Poissonian distribution and thus varies—without phase change—with $\sqrt{M}$ (i.e. the standard deviation) around the average number of detected photons M. Therefore, the shot-noise limit (SNL) $\Delta\phi_{\mathrm{SNL}} = 1/\sqrt{M} < \Delta\phi$

© 2019 The Author(s). Published by IOP Publishing Ltd on behalf of the Institute of Physics and Deutsche Physikalische Gesellschaft

constitutes a fundamental boundary for the phase resolution achievable wit coherent or thermal states. While the phase resolution can obviously be enhanced by increasing the average photon rate, arbitrarily accurate measurements are prevented by additional phase noise resulting from detrimental effects like nonlinear Kerr effects or coherent back-scattering induced at high power levels [20, 21]. Consequently, a trade-off between these additional noise sources and the SNL has to be made to find the optimal operating point in any practical FOG.

Quantum metrology provides a route to improve the precision of measurement to levels which would be impossible with classical resources alone [22]. Quantum interferometry thereby pursues the approach of using non-classical states of light in order to measure optical phases with a higher precision per photon. The canonical example of such states are path-entangled NOON-states, for which the resulting measurement advantage is based on the collective behavior of $N > 1$ photons. That is, all N photons are in an equal superposition of being in either one of the two modes of an interferometer, resulting in a shortened de-Broglie wavelength λ/N, where λ denotes the physical wavelength of the individual photons [23]. This leads to an increase of the interferometric fringe pattern frequency by a factor of N (super-resolution) without changing the physical wavelength of the photons, allowing the latter to be chosen for optimized transmission through optical single-mode-fibers (SMF).

Only considering quantization-noise, the phase uncertainty resulting from an average of $\nu_N = M/N$ consecutively detected NOON-states (i.e. M photons are detected in total) is given by $\Delta\phi_{\mathrm{NOON}} = 1/\sqrt{NM}$. This entanglement-enhanced phase precision is smaller by a factor $1/\sqrt{N}$ than the SNL $\Delta\phi_{\mathrm{SNL}} = 1/\sqrt{M}$. In particular, using NOON-states the relative phase imparted on the interferometric modes can be determined with the same precision as if consecutive single photons with N-fold energy (N times shorter wavelength), or N times more photons were detected. Note that the fundamental limit in quantum mechanics is the Heisenberg limit $\Delta\phi_{\mathrm{HL}} = 1/M$, which retains its validity for arbitrary photon states.

Quantum metrology usually assumes a restricted amount of photons available for the measurement (at the input of the interferometer). In such a scenario, the vulnerability to loss of the photonic states is of crucial importance and certain transmission thresholds required for actual sensor improvement can be calculated [24–28]. This assumption is generally not true for fiber optic gyroscopes, as the interplay of the noise sources does not equate to a limitation of the number of photons used for the measurement. For FOGs, the key question is the extent to which different photonic states respond to individual noise sources to verify that the trade-off between these effects represents a net increase in precision.

At the count rates we use, quantization-noise is the dominant source of error. Thus the minimal achievable phase resolution, which results from an interplay of all sources of noise cannot yet be measured. However, it is possible to verify experimentally the sub-SNL or entanglement-enhanced phase sensitivity of FOG using NOON-states at achievable count rates.

While the applicability of these non-classical states in metrology has already been widely demonstrated in other interferometric settings [29–33], the measurement advantage, or quantum enhancement, has not yet been used to measure a phase shift imparted by accelerated or rotational motion. In this work, we demonstrate an entanglement-enhanced phase sensitivity in a fiber optic gyroscope [34]. The gyroscope is based on a compact source of entangled photon pairs that was mounted together with a fiber coil on a rotating platform (see figure 1(a)). We investigated the interference signal of the counter-propagating modes in the FOG at different rotational speeds and use the canonical example of a two-photon N00N state ($N = 2$) to provide phase sensitivity beyond the SNL. Our work now demonstrates the experimental accessibility of entangled photon states in Sagnac interferometry and thus represents an important step towards reaching quantum-enhanced sensitivity of FOG.

2. Methods

A rigid three-level crate containing the optical setup and battery-powered electronic control equipment was mounted on a modified cement mixer (see figure 1(a)). A remotely controlled computer on board was used to store all relevant data and to control the experiment. By controlling the motor by means of a variable-frequency drive, we were able to adjust the rotational speed of the Sagnac interferometer. An additional commercial gyroscope (Dytran, VibraScout 6D, 5346A2) was mounted at the cement mixer to log the rotational velocity.

2.1. Photon source

The optical setup (see figure 1(b)) generates, detects, and analyzes photon pairs and has proven its stability in previous experiments [35]. A continuous-wave laser at 405 nm is focused into a periodically poled Potassium Titanyl Phosphate (ppKTP) crystal. The photons from the pump laser are converted within the crystal via spontaneous parametric down conversion (SPDC) into pairs of signal and idler photons with horizontal (H) and vertical (V) polarization, respectively. In order to guarantee wavelength-degenerate quasi-phase matching at

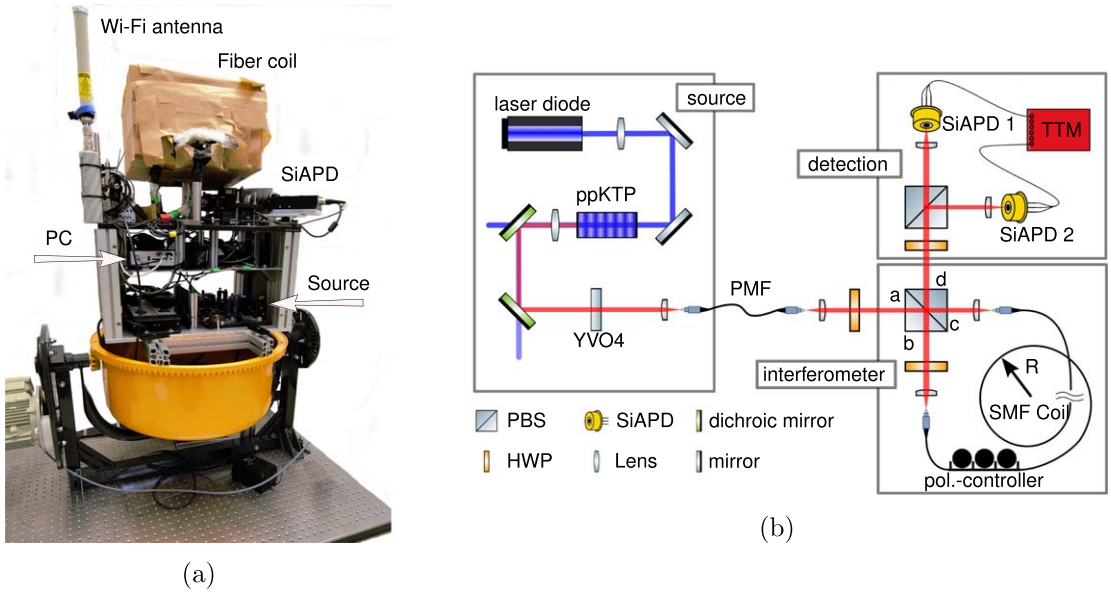


Figure 1. Experimental arrangement (a): a rigid three-level crate containing a photon source, a fiber based Sagnac interferometer and electronic equipment was mounted on a modified cement mixer. The optical fiber coil was passively stabilized against temperature drifts with a cardboard box and bubble wrap. Optical setup (b): light from the laser diode (405 nm) produces signal and idler photons at a wavelength of $\lambda = 810$ nm via spontaneous parametric down conversion (SPDC). A polarizing beamsplitter with ports a,b,c and d converts the polarization modes to spatial modes, which are coupled to the different ends of a single mode fiber (SMF) coil. The photons in port-d are measured in the DA-basis. Two silicon-avalanche photo diodes (SiAPD) generate electrical pulses which are recorded in time with a time tagging module (TTM).

810 nm, the temperature of the crystal is stabilized at 37.375° C ± 0.01° C. The wavelength-dependent splitting is realized with two dichroic mirrors. While the signal and idler photons are coupled into one polarization maintaining single-mode optical fiber (PMF). The birefringence of the ppKTP crystal leads to a longitudinal walk-off between the down converted photons. In order to create a NOON-State with two indistinguishable photons, one has to compensate this polarization dependent time delay with further birefringent components of the right length. For this purpose, we have used an additional neodymium-doped yttrium orthovanadate (Nd: YVO4) crystal, considering the birefringence of the PMF. This source produces a measured photon rate of 950 kcps at 810 nm with a pump power of 27.5 mW. Because of photon losses within the system, only a fraction of the photons leaves the PMF as a pair. We measure a photon pair rate of 191 kcps. Both rates are measured with a photon detection efficiency of $P_{\mathrm{SiAPD}} = 0.64$ (data sheet of the manufacturer).

2.2. Interferometer

A half-wave plate (HWP) at 22.5° transforms the two-photon state $|\Psi^{\mathrm{PMF}}\rangle = |1_{\mathrm{H}},\, 1_{\mathrm{V}}\rangle$ at the output of the PMF to a NOON state in polarization modes $1/\sqrt{2}\,(|2_{\mathrm{H}},\, 0_{\mathrm{V}}\rangle - |0_{\mathrm{H}},\, 2_{\mathrm{V}}\rangle)$, where both photons are either horizontal or vertical polarized.

Additionally, for providing reference measurements with consecutive single photons, the one-photon state $|1_{\mathrm{H}},\, 0_{\mathrm{V}}\rangle$ could be generated by inserting a horizontally oriented polarizer directly after the PMF. After the transmission through a HWP, the single photon is anti-diagonal polarized and its state can be written as a superposition of H and V polarization $|0_{\mathrm{D}},\, 1_{\mathrm{A}}\rangle = 1/\sqrt{2}\,(|1_{\mathrm{H}},\, 0_{\mathrm{V}}\rangle - |0_{\mathrm{H}},\, 1_{\mathrm{V}}\rangle)$.

The polarizing beamsplitter (PBS) of the Sagnac interferometer (see figure 1(b)) converts the polarization modes to spatial modes, which are both coupled to the different ends of a coiled fiber loop. Transmitted photons thus propagate in a clockwise ($^{\circlearrowright}$) and reflected in a counterclockwise ($^{\circlearrowleft}$) direction through the fiber. The resulting N-photon state in the Sagnac interferometer is given by

$$\frac{1}{\sqrt{2}}(|N_{\circlearrowright},\, 0_{\circlearrowleft}\rangle - |0_{\circlearrowright},\, N_{\circlearrowleft}\rangle), \tag{1}$$

with N being either 1 or 2 in case of a measurement with or without the polarizer, respectively. After traversing the fiber loop, the photons impinge on the PBS a second time, from where they are guided to output port-d. The polarization changes in the fiber-coil where compensate by an additional HWP and an in-fiber-polarization-controller (see figure 1(b)).

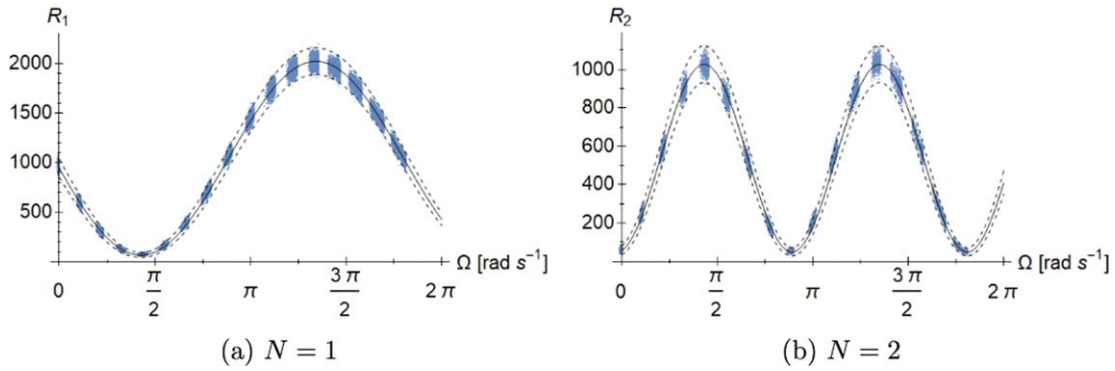


Figure 2. Count rate versus angular velocity: rate of one-/two-photon state detection events ((a)/(b)). The blue dots indicate the experimentally determined number of single-photon and two-photon counts per second. Each of the 64,688 (16,204) points was measured over $\tau_{N=1} = 5$ ms ($\tau_{N=2} = 20$ ms). The solid black line is a fit function of the form of equation (5). The dashed lines indicate the 99% confidence interval around the fitted function if only Poissonian error of the predicted count rate is assumed. Those lines contain 97.25% (95.88%) of the measured data.

2.3. Sagnac-phase

The rotation with an angular velocity Ω leads to a phase difference $\phi_S(\Omega)$ between counter propagating waves, called the Sagnac-phase. Typically $\phi_S(\Omega)$ is considered as a consequence of a kinematic effect of the special theory of relativity which ensues from the relativistic law of velocity composition [7, 36]. The difference in arrival time Δt at the PBS, between clockwise and counterclockwise propagating waves, reads:

$$\Delta t(\Omega) = \frac{2\,L\,r\,\Omega}{c^2\sqrt{1 - r^2\Omega^2/c^2}}, \tag{2}$$

where c denotes the speed of light, $r \sim 7.8$ cm is the radius of the fiber coil, and $L \sim 270.5$ m is the length of the fiber. Ignoring relativistic corrections due to the slow rotational velocity in our experiment, the Sagnac phase [10] is given by

$$\phi_S(\Omega) = c\frac{2\pi}{\lambda}\Delta t(\Omega) \simeq \frac{4\pi\,L\,r\,\Omega}{\lambda c} = S_T\,\Omega = 1.09\,\Omega, \tag{3}$$

where $\lambda = 810$ nm is the wavelength of the down-converted photons.

2.4. Detection

The final state after transmission through the Sagnac loop (in port-d of the PBS) reads:

$$|\Psi^{\mathrm{d}}(N)\rangle = \frac{1}{\sqrt{2}}(|N_{\mathrm{H}}, 0_{\mathrm{V}}\rangle - \mathrm{e}^{\mathrm{i}N(\phi_S(\Omega)+\phi_0)}|0_{\mathrm{H}}, N_{\mathrm{V}}\rangle). \tag{4}$$

where ϕ_0 accounts for an initial offset caused by the birefringence of the fiber coil. The detection module consists of a HWP at 22.5° followed by a PBS and two silicon-avalanche photo diodes (SiAPD), one in each output. This setup projects the state $|\Psi^{\mathrm{d}}(N)\rangle$ onto the diagonal/anti-diagonal (D/A) polarization basis. The which-way information ($^{\circlearrowleft}/_{\circlearrowright}$) is inaccessible in this basis, resulting in interference between the two modes. Note that the N-photon rate $R(N) \propto \cos^2(N/2(S\,\Omega + \phi_0))$ shows a linear increase of the fringe oscillation frequency $\omega(N) = (S\,N)/2$ with N.

3. Results

Two sequential measurement runs were performed using a one-photon state ($N = 1$) and a two-photon NOON-state ($N = 2$), with and without the polarizer, respectively. For each run, the angular velocity was increased step wise from $\Omega = 0$ to $\Omega = 5.6$ rad s^{-1}, resulting in a full 2π phase shift according to equation (4). For each setting of Ω we accumulated data for a total of ~19 s and evaluated the one-photon (two-photon) count rates $R_{N=1}$ ($R_{N=2}$) with integration time $\tau_{N=1} = 5$ ms ($\tau_{N=2} = 20$ ms), leading to 3800 (950) data-points per angular velocity setting. Note that using different integration times for measurements accounts for the different rates of detected one-photon and two-photon states and thus results in roughly the same number of detected photons per data point for both measurements. Figure 2(a) shows the one-photon count rate $R_{N=1}$ of SiAPD_2 obtained in the first measurement run, whereas figure 2(b) shows the two-photon coincidence count rate $R_{N=2}$ between SiAPD_1 and SiAPD_2 of the second measurement run. Comparison of the two graphs clearly shows the increased fringe oscillation frequency of $R_{N=2}$. Both count rates in figure 2 are fitted with the function

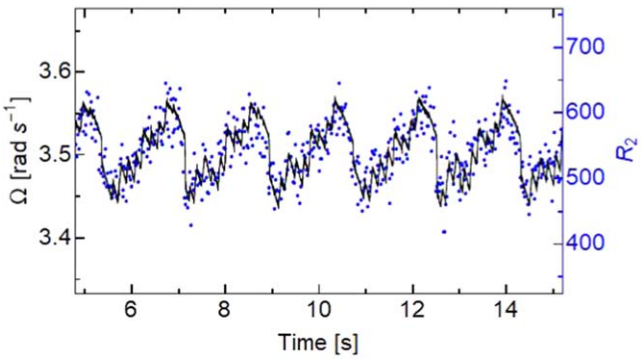


Figure 3. Two-photon count rate $R_{N=2}$ and angular velocity versus time: variation in time of the angular velocity Ω as measured with the commercial gyro-sensor (black solid line). The blue dots indicate the two-photon count rate $R_{N=2}$, with integration time of 20 ms.

Table 1. Fit parameters of equation (5) as plotted in figure 2.

N	M ($\tau^{-1}_{N=1(2)}$)	B ($\tau^{-1}_{N=1(2)}$)	S	ϕ_0 (rad)
1	1955	63	1.091(8)	1.676(7)
2	1956	49	1.089(0)	1.662(9)

$R(N)$ (see equation (5)) using the fitting parameters presented in table 1. The error estimation of the fit parameters was determined via bootstrapping and confirmed by Monte Carlo simulation.

$$R(N) = \frac{M}{N}\cos^2\left(\frac{N}{2}(S\,\Omega + \phi_0)\right) + B. \tag{5}$$

The phase shift caused by the fiber coil ϕ_0 was set to $\sim\pi/2$ using the fiber-polarization-controller. The background B results mainly from uncorrelated residual background counts but also from imperfect overlap of the counter propagating modes. Note that the amplitude in figure 2(a) is about twice as large as in figure 2(b), but $M \sim 2000$ is approximately the same for both measurement runs. Here, M denotes the total number of photons detected per integration time $\tau_{N=1(2)}$, in the respective photon state. The fiber coil is not perfectly circularly wound and has extra loops for the polarization controller and the PBS connections, therefore equation (3) is a rough estimation of the expected scale factor S_T, which agrees nicely with the fitted parameter S.

The vertical distribution of the individual measurements in figure 2 with respect to the fit function is mainly caused by statistical count-rate fluctuations. The horizontal distribution of the individual measurements stems from variations in the rotational velocity of the modified cement mixer (due to an imbalanced ball bearing mechanism). This deterministic variation of Ω was measured with the commercial gyro sensor. By knowing the timing of individual detection events, we were also able to resolve those variations with the FOG. Therefore, this variation does not affect further error calculations. The correlation of the coincidence count rate and the rotational velocity as measured by the commercial gyro sensor is shown in figure 3.

The uncertainty in the measured velocity attributed to Poisson noise of R_N can be estimated via propagation of uncertainty $\Delta\Omega^{\mathrm{E}}(R_N) = |\partial\Omega^{\mathrm{E}}(R_N)/\partial R_N|\sqrt{R_N}$, where $\Omega^{\mathrm{E}}(R_N)$ is the rotational velocity estimated via the inverse fit function (equation (5)). The uncertainty estimated in this way is plotted in figure 4 as a black solid line. Usually, such gyroscopes are operated at the point of best precision, which is called bias-point. The expected precision at the bias-point $\Delta\Omega^{\mathrm{E}}_{\mathrm{Bias}}$ is numerically compared to $\Delta\Omega^{\mathrm{SNL}} = 1/(S\sqrt{M})$ and $\Delta\Omega^{\mathrm{HL}} = 1/(SM)$ in table 2.

With the inverse fit function, a rotational velocity $\Omega^{\mathrm{E}}(R^{\mathrm{j}}_N)$ can be assigned to each measured count rate (blue points in figures 2(a) and (b)). Those values deviate from the reference Ω, as measured with the commercial gyro-sensor. The absolute value of those deviations are plotted in figure 4 (green points), together with the sample standard deviation (black error bars) of each block of measurements (measurements with similar rotational velocity). The block with the best precision of each measurement run is colored blue and the respective sample standard deviation $\Delta\Omega_{\mathrm{min}}$ can be found in table 2.

4. Discussion

In summary, we have demonstrated the effect of super-resolution in a FOG using two-photon NOON-states. The increased fringe oscillation frequency of the two-photon count rate $R_{N=2}$ with respect to the one-photon

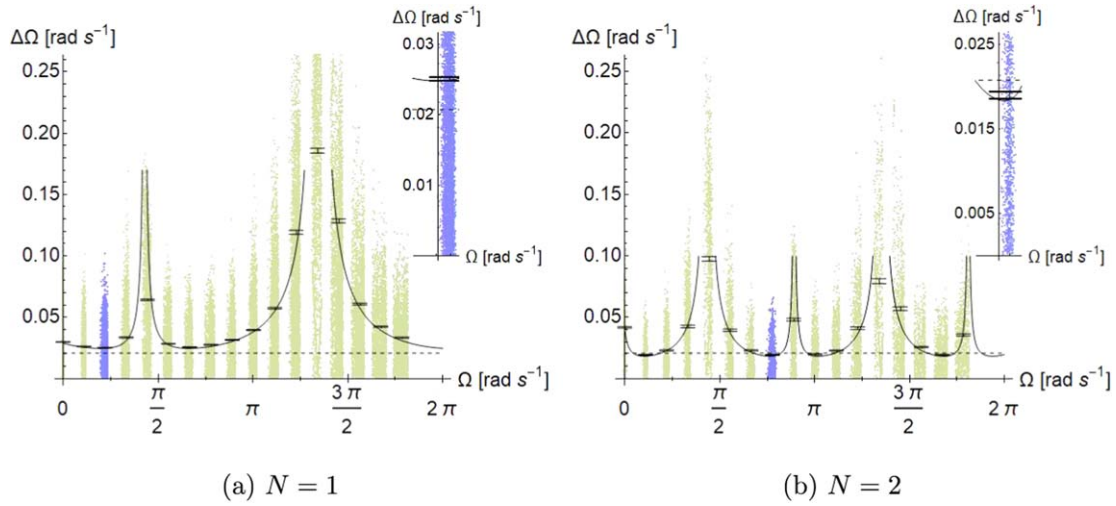


Figure 4. One-photon versus two-photon measurement precision. The precision of the rotational velocity, measured with the one-/two-photon state is shown in ((a)/(b)). Absolute value of the Deviation $|\Omega^{E}(R_N^j) - \Omega^j|$ (green dots). Sample standard deviation of $[\Omega^{E}(R_N^j) - \Omega^j]$ for each measurement block $\Delta\Omega$ with estimated errors (black error bars). SNL of the measurement system $\Delta\Omega^{SNL}$ (dashed line). Uncertainty estimated via fit function $\Delta\Omega^{E}(R_N(\Omega))$ (solide black line). The measurements with the smallest standard deviation $\Delta\Omega_{min}$ is colored blue. These data are shown enlarged in the upper right corner.

Table 2. Comparison of the measurement precision with $M = 1955$ photons detected on average. Standard quantum limit $\Delta\Omega^{SNL} = 1/(S\sqrt{M})$ and Heisenberg limit $\Delta\Omega^{HL} = 1/(SM)$ of the measurement system, with the scale factor $S = 1.09$. Best precision of the respective measurement run $\Delta\Omega_{min}$ (blue colored data in figure 4). Precision at the bias point $\Delta\Omega^{E}_{Bias}$, estimated via fit function. All values are given in rad s^{-1}.

N	$\Delta\Omega^{SNL}$		$\Delta\Omega_{min}$	$\Delta\Omega^{E}_{Bias}$		$\Delta\Omega^{HL}$
1	0.0207	$\not>$	0.025(0)	0.024 8	$>$	469×10^{-6}
2		$>$	0.018(9)	0.018 3	$>$	

count rate $R_{N=1}$, is shown in figure 2. From the fit parameters of table 2, a fringe oscillation frequency ratio of $\omega(2)/\omega(1) = S_{N=2}/(\frac{1}{2}S_{N=1}) = 1.995(\pm 0.4 \times 10^{-3})$ can be found. This value deviates from the theoretically expected value 2. The deviation is on the order of 10 standard deviation and therefore not fully covered by the specified error, which may be due to systematic errors such as drift of the birefringence of the fiber coil or scale factor S variations. Nevertheless, the inconsistency is rather small, given the poor thermal and mechanical stabilization of the fiber. However, the ratio is significantly greater than 1, by means of 2487 standard deviations, which bears witness of super-resolution.

Furthermore we have investigated the precision of the NOON-state measurements close to the bias-point $\Delta\Omega_{min}$ (see table 2). We found that, mainly due to background, it is slightly worse than the theoretical predicted limit $\Delta\Omega^{SNL}/\sqrt{2} = 0.014\,6$ rad s^{-1}. Nevertheless, the measured precision of the two-photon state performs better than the one-photon state, and is better than $\Delta\Omega^{SNL}$. Such sub-SNL precision can never be achieved with coherent states of light.

5. Conclusion

In conclusion our result suggest a possible improvement of the accuracy of FOG using non-classical states of light. In particular, when using NOON-states with large N, one can significantly reduce the de-Broglie wavelength of the photon state, without altering the wavelengths of the actual photons. Hence the de-Broglie wavelength can potentially be shifted outside of the transmission window of the FOG. At this point we should stress, however, that the presented technology is not yet competitive with a classical FOG. Laser-driven FOG [20] use an optical power of approx. 20 μW, which corresponds to a rate of 156×10^{12} photons per second (at $\lambda = 1550$ nm). In contrast, the detected photon rate of the NOON state is 100×10^{3} in our experiment. This relatively low photon rate was limited by the detectors used, whose efficiency decreases with increasing count rate.

Hence, while our sensor is not yet competitive with commercial gyroscopes, we believe that our work can be considered an important first step towards reaching the ultimate sensitivity limits in Sagnac interferometry. With experiments and applications becoming increasingly demanding—so does the severity of the limitation imposed by noise. Moreover, since power circulating in the interferometer cannot be increased arbitrarily, due to detrimental power-dependent effects such as to coherent back-scattering [20] or nonlinear Kerr effects [21], methods and techniques from quantum metrology will play a significant role in reaching the ultimate sensitivity limits of FOG and enable evermore demanding applications in fundamental science and technology. With the speed of ongoing developments in advancing detector technology and increasingly brighter photon sources, a technical application of such a system may become feasible in the foreseeable future. We hope that our work will inspire further research in this direction.

Acknowledgments

We would like to thank Roland Blach for preparing and testing the concrete mixer. Financial support from the Austrian Research Promotion Agency (FFG contract 854022, 866025 and 844360) as well as the Austrian Academy of Sciences is gratefully acknowledged. JPD would like to acknowledge support from the Air Force Office of Scientific Research, the Army Research Office, the Chinese academy of science, the Defense Advanced Research Projects Agency, the National Science Foundation, and the Northrop Grumman Corporation.

ORCID iDs

Matthias Fink https://orcid.org/0000-0001-7459-4508

References

[1] Sagnac G 1913 *CR Acad. Sci.* **157** 708–10
[2] Sagnac G 2008 *Abraham Zelmanov J.* **1** 74–6
[3] Sagnac G 1913 *CR Acad. Sci.* **157** 1410–3
[4] Sagnac G 2008 *Abraham Zelmanov J.* **1** 77–80
[5] Michelson A A and Morley E W 1887 *Sidereal Messenger* **6** 306–10
[6] Logunov A A and Chugreev Y V 1988 *Soviet Physics Uspekhi* **31** 861
[7] Malykin G B 2000 *Phys. Usp.* **43** 1229
[8] Malykin G B 2002 *Phys. Usp.* **45** 907
[9] Ghosal S K, Raychaudhuri B, Chowdhury A K and Sarker M 2003 *Found. Phys.* **33** 981–1001
[10] Gift S J G 2018 *Phys. Essays* **31** 228–32
[11] Kajioka H, Kumagai T, Nakai H, Dohsho T, Soekawa H and Yuhara T 1996 *Proc. SPIE* **2837** 18–33
[12] Wang X, Zhang C, Jin J and Song N 2012 Optimum length of fiber coil in space-borne interferometric fiber optic gyroscope *Advances in Electric and Electronics* (*Lecture Notes in Electrical Engineering*) ed W Hu vol 155 (Berlin: Springer) pp 683–8
[13] Sanders S J, Strandjord L K and Mead D 2002 Fiber optic gyro technology trends—a Honeywell perspective *15th Optical Fiber Sensors Conf. Technical Digest. OFS 2002(Cat. No.02EX533)* vol 1 pp 5–8
[14] Vysotskii V I, Vorontsov V I, Kuz'min R N, Bezirganyan P A and Rostomyan A G 1994 *Phys. Usp.* **37** 289
[15] Hasselbach F and Nicklaus M 1993 *Phys. Rev.* A **48** 143–51
[16] Werner S A, Staudenmann J L and Colella R 1979 *Phys. Rev. Lett.* **42** 1103–6
[17] Riehle F, Kisters T, Witte A, Helmcke J and Borde C J 1991 *Phys. Rev. Lett.* **67** 177–80
[18] Lenef A, Hammond T D, Smith E T, Chapman M S, Rubenstein R A and Pritchard D E 1997 *Phys. Rev. Lett.* **78** 760–3
[19] Gustavson T L, Bouyer P and Kasevich M A 1997 *Phys. Rev. Lett.* **78** 2046–9
[20] Chamoun J N, Evans A, Mosca F A and Digonnet M J F 2014 *Proc. SPIE* **9157** 91570E
[21] Lefevre H C 2014 *The Fiber-optic Gyroscope* (London: Artech House)
[22] Dowling J P 2008 *Contemp. Phys.* **49** 125–43
[23] Jacobson J, Björk G, Chuang I and Yamamoto Y 1995 *Phys. Rev. Lett.* **74** 4835–8
[24] Dorner U, Demkowicz-Dobrzanski R, Smith B J, Lundeen J S, Wasilewski W, Banaszek K and Walmsley I A 2009 *Phys. Rev. Lett.* **102** 040403
[25] Demkowicz-Dobrzanski R, Dorner U, Smith B J, Lundeen J S, Wasilewski W, Banaszek K and Walmsley I A 2009 *Phys. Rev.* A **80** 013825
[26] Kacprowicz M, Demkowicz-Dobrzański R, Wasilewski W, Banaszek K and Walmsley I A 2010 *Nat. Photon.* **4** 357–60
[27] Thomas-Peter N, Smith B J, Datta A, Zhang L, Dorner U and Walmsley I A 2011 *Phys. Rev. Lett.* **107** 113603
[28] Zhang Y M, Li X W, Yang W and Jin G R 2013 *Phys. Rev.* A **88** 043832
[29] Edamatsu K, Shimizu R and Itoh T 2002 *Phys. Rev. Lett.* **89** 213601
[30] Steuernagel O 2002 *Phys. Rev.* A **65** 033820
[31] Walther P, Pan J W, Aspelmeyer M, Ursin R, Gasparoni S and Zeilinger A 2004 *Nature* **429** 158–61
[32] Boto A N, Kok P, Abrams D S, Braunstein S L, Williams C P and Dowling J P 2000 *Phys. Rev. Lett.* **85** 2733–6
[33] Giovannetti V, Lloyd S and Maccone L 2004 *Science* **306** 1330–6
[34] Kolkiran A and Agarwal G S 2007 *Opt. Express* **15** 6798–808
[35] Fink M, Rodriguez-Aramendia A, Handsteiner J, Ziarkash A, Steinlechner F, Scheidl T, Fuentes I, Pienaar J, Ralph T C and Ursin R 2017 *Nat. Commun.* **8** 15304
[36] Vugal'ter G A and Malykin G B 1999 *Radiophys Quantum Electron.* **42** 333–41

C List of Publications

12. **Entanglement-enhanced optical gyroscope**
Matthias Fink, Fabian Steinlechner, Johannes Handsteiner, Jonathan P. Dowling, Thomas Scheidland and Rupert Ursin
New Journal of Physics **21**, 053010 (2019).

11. **Hong-Ou-Mandel interferometry on a biphoton beat not**
Yuanyuan Chen, Matthias Fink, Fabian Steinlechner, Juan P. Torres and Rupert Ursin
npj Quantum Information **5**, 43 (2019).

10. **Satellite-Relayed Intercontinental Quantum Network**
Liao Sheng-Kai, Cai Wen-Qi, Handsteiner Johannes, Liu Bo, Yin Juan, Zhang, Liang, Rauch Dominik, Matthias Fink, Ren Ji-Gang, Liu Wei-Yue, Li Yang, Shen Qi, Cao Yuan, Li Feng-Zhi, Wang Jian-Feng, Huang Yong-Mei, Deng Lei, Xi Tao, Ma Lu, Hu Tai, Li Li, Liu Nai-Le, Koidl Franz, Wang Peiyuan, Chen Yu-Ao, Wang Xiang-Bin, Steindorfer Michael, Kirchner Georg, Lu Chao-Yang, Shu Rong, Ursin Rupert, Scheidl Thomas, Peng Cheng-Zhi, Wang Jian-Yu, Zeilinger Anton and Pan Jian-Wei
Physical Review Letters **120** (3), 030501 (2018).

9. **Q^3Sat: quantum communications uplink to a 3U CubeSat—feasibility & design**
Sebastian Philipp Neumann, Siddarth Koduru Joshi, Matthias Fink, Thomas Scheidl, Roland Blach, Carsten Scharlemann, Sameh Abouagaga, Daanish Bambery, Erik Kerstel, Mathieu Barthelemy and Rupert Ursin
EPJ Quantum Technology **5**, 4 (2018).

8. **Nanobob: a CubeSat mission concept for quantum communication experiments in an uplink configuration**
Erik Kerstel, Arnaud Gardelein, Mathieu Barthelemy, Matthias Fink, Siddarth Koduru Joshi and Rupert Ursin
EPJ Quantum Technology **5**, 6 (2018).

7. **Cosmic Bell Test: Measurement Settings from Milky Way Stars**
Johannes Handsteiner, Andrew S Friedman, Dominik Rauch, Jason Gallicchio, Bo

Liu, Hannes Hosp, Johannes Kofler, David Bricher, Matthias Fink, Calvin Leung, Anthony Mark, Hien T Nguyen, Isabella Sanders, Fabian Steinlechner, Rupert Ursin, Sören Wengerowsky, Alan H Guth, David I Kaiser, Thomas Scheidl, Anton Zeilinger
Physical Review Letters **118** (6), 060401 (2017).

6. **Distribution of high-dimensional entanglement via an intra-city free-space link**
Fabian Steinlechner, Sebastian Ecker, Matthias Fink, Bo Liu, Jessica Bavaresco, Marcus Huber, Thomas Scheidl, Rupert Ursin
Nature Communications (8), 15971 (2017).

5. **Experimental test of photonic entanglement in accelerated reference frames**
Matthias Fink, Ana Rodriguez-Aramendia, Johannes Handsteiner, Abdul Ziarkash, Fabian Steinlechner, Thomas Scheidl, Ivette Fuentes, Jacques Pienaar, Timothy C Ralph, Rupert Ursin
Nature Communications (8), 15304 (2017).

4. **Twisted light transmission over 143 km**
Mario Krenn, Johannes Handsteiner, Matthias Fink, Robert Fickler, Rupert Ursin, Mehul Malik, Anton Zeilinger
Proceedings of the National Academy of Sciences **113** (48), 13648–13653 (2016).

3. **Twisted photon entanglement through turbulent air across Vienna**
Mario Krenn, Johannes Handsteiner, Matthias Fink, Robert Fickler, Anton Zeilinger
Proceedings of the National Academy of Sciences **112** (46), 14197-14201 (2015).

2. **Teleportation of entanglement over 143 km**
Thomas Herbst, Thomas Scheidl, Matthias Fink, Johannes Handsteiner, Bernhard Wittmann, Rupert Ursin, and Anton Zeilinger
Proceedings of the National Academy of Sciences **112** (46), 14202-14205 (2015).

1. **Communication with spatially modulated light through turbulent air across Vienna**
Mario Krenn, Robert Fickler, Matthias Fink, Johannes Handsteiner, Mehul Malik, Thomas Scheidl, Rupert Ursin, Anton Zeilinger
New Journal of Physics **16** (11), 113028 (2014).

Acknowledgements

First of all, I would like to thank my supervisor, Anton Zeilinger, whose dedication has significantly contributed to establishing Vienna as a prime hot spot for quantum research and who has given me the opportunity to work in this fascinating field. I would like to express my special thanks to Rupert Ursin for his patience, guidance, encouragement, and advice throughout my time as a student in his group.

This dissertation might have probably never seen light without the educational discussions with Fabian Steinlechner and Thomas Scheidl. I would also like to thank both of them for their valuable suggestions which have improved the readability of this work. Thanks also to the whole Ursin group, I had a lot of fun working with you.

I am particularly indebted to Roland Blach for all the customized construction solutions that were necessary to turn even the most bizarre ideas into experiments.

I owe my parents a great debt of gratitude for their immense support, trust, and patience they have shown me during my studies. Finally, I would like to thank my girlfriend Edith Ober, for all of her empathy, love, and support during the ups and downs of my research.